Title of Thesis:

Initial sedimentation processes and the early geological evolution of three maar craters, Hindon Maar Complex, Otago

A thesis

submitted in partial fulfilment

of the requirements for the degree

of

Masters of Science (Research) in Earth Sciences

at

The University of Waikato

by

CAITLIN MURPHY

THE UNIVERSITY OF
WAIKATO
Te Whare Wānanga o Waikato

2018

Abstract

The Hindon Maar Complex, located near Hindon, 25 km NW of Dunedin, consists of four volcanic craters infilled by lake sediments and mass flow deposits. The maars form part of the Waipiata volcanic group, which was active from 25–9 Ma. Drilling of Maar 1, Maar 3 and a sediment-filled depression between the inferred locations of Maar 2 and Maar 3 revealed up to 10 m of laminated biogenic lake sediments underlain by siliciclastic mass flow deposits. This project describes the siliciclastic deposits from these drill-cores and from limited outcrops of Maar 2. Physical properties, stratigraphic logs, X-ray fluorescence spectrometry, Also XRD, SEM and optical petrography are used to create a facies analysis and infer the processes of initial sedimentation into the maar craters following the maar-forming eruptions.

A total of 10 facies are identified within the Hindon Maar complex. Facies 1–6 show the progression of crater wall stabilisation from rockfalls which occurred weeks to years after the initial eruption to the formation of organic rich lake-sediment units which would have been deposited hundreds of years post eruption. Facies 1–6 have a high proportion of mica, quartz and schist grains, indicating extensive incorporation of the country rock. Nonconsolidated mottles are found throughout facies 2–5 and are interpreted as the remnants of weathered pyroclastic materials which were sourced from failures in the upper crater walls or tephra ring. Facies 1 is a laminated carbonaceous lake sediment consisting almost entirely of organic matter. Facies 2 is a nonconsolidated laminated silty clay formed by debris flows. Facies 3 is a consolidated silty fine sand with discrete gravel lenses and 5% mottles formed as a result of mass flows. Facies 4 is a fine gravel breccia comprising up to 35% mottles, which is formed by mass flows originating in the upper crater or tephra ring. Facies 5 is a poorly consolidated fine gravel breccia which formed as a result of turbidity currents. Facies 6 is loose schist and quartz grains of fine gravel to medium pebble size, formed by rockfalls into the early lake.

Facies 7 is a silty clay which is geochemically and mineralogically different to all other facies. Facies 7 exhibits convoluted bedding and is an example of a slump deposit occurring locally in Maar 3. Due to its significant differences to all other facies, it is assumed to have had a different parent material.

Facies 8–10 are found in the area of a major gravity anomaly associated with Maar 3. These deposits are composed of silt and clay sized particles and have elevated Fe. They have high magnetic susceptibility and density and are interpreted as weathered pyroclastic material of the tephra ring.

The infilling of Maar 1 occurred initially as a series of coarse-grained mass flows into the crater (Facies 6 and Facies 5). Once the crater wall began to stabilise and the occurrence of rockfalls decreased, Facies 4 was deposited, resulting from high crater wall collapse. This was followed by furthered, small cater wall collapse of Facies 3. Facies 2 was later deposited once crater wall failures halted, and resulted from the erosion, rather than the collapse, of the crater wall. Once the crater wall was fully vegetated, Facies 1 began to accumulate, forming thick organic rich deposits, indicating the maar lake was stratified and had an anoxic bottom layer.

The infilling of Maar 3 followed the same pattern. However, there is a significant lateral offset between some units of the same facies, which may indicate more complex processes, such as faulting. The exact history of Maar 3 cannot be determined with the information acquired.

Acknowledgements

First and foremost, I wish to thank my chief supervisor, Dr Beth Fox. You are an amazing supervisor and I could not have wished for anyone better. Thank you for supporting me through my Master's. Not only have you put up with my horrendous spelling, which belongs in a primary school, and my constant questions, but you have also provided me with an amazing Master's topic and you found funding so that I could undertake my thesis. I also thank you for organising the fieldwork in Dunedin; I cannot begin to comprehend the amount of work that must have required, and I am sure you would have much rather done anything else than spend 12 hours a day for 5 weeks with your students. Beth, you really have consistently gone above and beyond and for that I am immeasurably grateful.

To Dr Adrian Pittari, thank you for being such a wonderful second supervisor. Your volcanology expertise has been invaluable throughout this thesis, and I appreciate the many instances when you took the time to explain concepts to me in a way that I could understand.

To Dr David Lowe, thank you for taking the time out of your busy schedule to sit down and help me with clay mineralogy and XRD. You have been an immense source of knowledge, and have consistently provided references after explaining each topic to me. I really appreciate it.

I would also like to thank the technical staff: Helen Turner, Kirsty Vincent and Renat Radosinsky. This thesis has required multiple methods, most of which I had no idea how to perform; if it were not for the technical staff, there is no way I would have been able to complete this research. To Helen, thank you for teaching me SEM and the wonderful chats we have had. To Renat, thank you for your help with the thin sections and your words of encouragement. To Kirsty, thank you for walking me through XRD.

I would like to thank Nigel, Judy and Bernard for allowing us to drill at their farm and stay at their house for 5 weeks in 2016. You have all been incredibly kind and accommodating. Nigel and Bernard, thank you for your insight into drilling practices and the field area.

To Dr. Daphne Lee, thank you for allowing us to stay at your house while we were in Dunedin. I must also thank you for the support you have given us towards this project, and the wonderful company you are. I would also like to thank the University of Otago geology dept for their help in fieldwork logistics.

To all my friends, thank you for the unending support you have offered me over the last two years. To Andrew Douie, thank you for being so supportive, understanding and being the other dyslexic on the block. To Jamie Millar and Francesca Spinardi, thank you for always being there to help me let off steam. To Benjamin Campbell, thank you for hilarious conversations and support. To Thomas Robertson, a.k.a. Tom 2, Electric Boogaloo, thank you for being the best friend someone can have and always letting me crash on your floor for free. To Noel Bates and Frances Garrity, I am very lucky that my group included both of you; thank you for your support and camaraderie.

Finally, thank you to my family. Mum, I thank you especially for your support, understanding, and for proofreading my work until far too late into the night. I would have never passed High School if it were not for you. The fact that I am doing my Master's is nothing short of a testament to your support throughout my life. And to my loving husband, Thomas Petchell, my financial and emotional support: you've put up with a lot for the last two years and made a lot of sacrifices to enable me to undertake my Master's. Thank you, I love you.

Table of Contents

List of Figures

List of Tables

Chapter 1

Introduction

1.1 Background

Maars are the second most common type of volcano found on land (Lorenz, 2007; White & Ross, 2011). A maar forms as a result of the interaction between water and magma below ground level, resulting in a steep sided depression underneath the pre-eruptive surface (Lorenz, 1973; Ross et al., 2017). Maars are generally found in monogenetic fields and can accompany other volcanic types, such as on the flanks of composite cones (Coombs et al., 2008; White & Ross, 2011). Evidence of maar eruptions can be found throughout New Zealand, as they are common within active and extinct volcanic fields (Németh & White, 2003; Cassidy et al., 2007).

Very few maar eruptions have been witnessed in recorded history, therefore what is known about the eruption process and post eruption depositions is largely limited to field observations and laboratory experiments (Pirrung et al., 2008; Macorps et al., 2016). During the eruption phase, maars typically produce low angle tephra rings and once dormant, the crater fills with water (Lorenz, 1973; White & Ross, 2011). Lakes are infilled with post-eruptive material, mass flows, and, later, biogenic sediment (Pirrung et al., 2003; Lehndorff et al., 2015).

Research conducted into maars generally focuses on either: the eruption, including the eruption style, eruptive deposits and formation; the underlying diatreme; or the accumulation of varved sediments (Pirrung et al., 2008; White & Ross, 2011; Kurszlaukis & Fulop, 2013). Very little research has been conducted into the post-eruptive coarse-grained clastic sediments which accumulate in maars in the first few decades to centuries after eruption (Pirrung et al., 2008; Kaulfuss, 2017).

A handful of papers have researched the clastic accumulation of sediments in maar lakes, with only one conducted in New Zealand (Pirrung et al., 2003; Pirrung et al., 2008; Kaulfuss, 2017). Research into the area of maar sedimentation provides insight into the early infilling stage of the maar. It can also be used to determine some climate and environmental conditions, such as earthquakes and storm conditions, within the maar lake which would have otherwise been overlooked (Pirrung et al., 2008; Chassiot et al., 2016).

Early sedimentation in maars follows a general pattern of coarse grains transitioning into finer grains (Pirrung et al., 2008; Kaulfuss, 2017). The first deposits generally form breccias, because of debris flows and rock falls (Pirrung et al., 2008). This is often followed by a series of mass flows producing turbidites and densites (Pirrung et al., 2003). As the succession of sediments is consistent throughout previously studied maars, estimations of the age of the sediment in relation to a particular eruption can be made (Pirrung et al., 2003; Kaulfuss, 2017). Additional study into early maar sedimentation will confirm deposit successions and further the understanding of the eruption style and varved sediment accumulation (Pirrung et al., 2008).

1.2 Aims

The overarching aim of this study is to interpret sedimentation processes of early siliciclastic sediment accumulation of three maars within the Hindon Maar complex. Assessments will be made using five drill cores from Maars 1 and 3 and limited outcrop exposures of Maar 2. Analysis will be conducted with various methodologies, including visual assessment, grain size analysis, X-ray fluorescence spectrometry, scanning electric microscopy, optical petrography, XRD and Geotek analysis. These methods will be used to complete the following objectives:

- determine physical, sedimentological and geochemical properties of the sediments
- produce stratigraphic logs of cored sediments from Maars 1 and 3
- construct facies analysis for Maars 2 and 3
- determine initial sedimentation processes within Maars 1 and 3
- construct a model of maar evolution for Maars 2 and 3.

1.3 Thesis Layout

Chapter 2 of this thesis is a literature review. This covers the geological history of New Zealand with special reference to Otago, maar formation, and early sediments found within maars. Maar formation covers physical and structural features of maars, eruption mechanisms and eruptive deposits. The early sediments found within maars section, covers typical sediments and examines three case studies to establish the flow characteristics and deposit types found within maars.

Chapter 3 comprises the methods used within this thesis and background to these methods.

Chapter 4 contains the field and laboratory results obtained from the Hindon Maar complex. These include stratigraphic logs, petrographic analysis, scanning electric microscope images, X-ray diffraction analyses (XRD), portable X-ray fluorescence measurements (pXRF), a geomorphic map, grain size and Geotek analysis. Results are presented independently for each method and for each core.

Chapter 5 constructs a facies analysis based on the results, leading into the interpretation of the facies. From this analysis, depositional processes and deposit type are inferred.

Chapter 6 presents the evolution of the Hindon Maar complex, starting with eruption processes inferred from literature. This is follow by the evolution of Maar 1 and 3, supplemented with a proposed model for deposition. Finally, Chapter 6 presents minor interpretations for Maar 2 based on data acquired from this maar.

Lastly, Chapter 7 summarises all the findings from the Hindon Maar complex.

1.4 Site Location

The Hindon Maar Complex comprises four maars located in Hindon, near Dunedin, New Zealand (Figure 1 to Figure 4). The complex occupies an area of 16 km² and is located in a farmland setting. The greatest distance between maars is 3.6 km (between Maar 3 and Maar 4). Gravity anomaly previously used to identify the Hindon Maar complex shows estimated maar locations based on the gravity anomaly map produced by Glass Earth (2009) (and represented by Elliott (2015)) which was initially used to identify the locations, shape, and size of the four maars 2.8 Prior Research Conducted on the Hindon Maars). Maar 1 is slightly elliptical, Maar 2 and Maar 3 are close to one another, and Maar 4, located to the north-east, is outside the scope of this study.

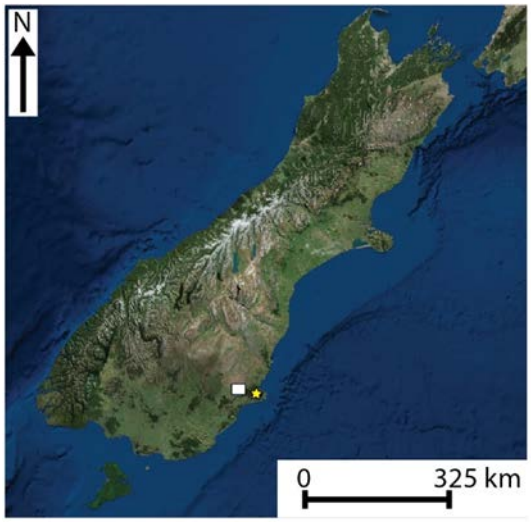

Figure 1: Shows the location of the Hindon Maar complex shown in a white square and its relation to the location of Dunedin in yellow. The white square approximates the size of the map in Figure 1

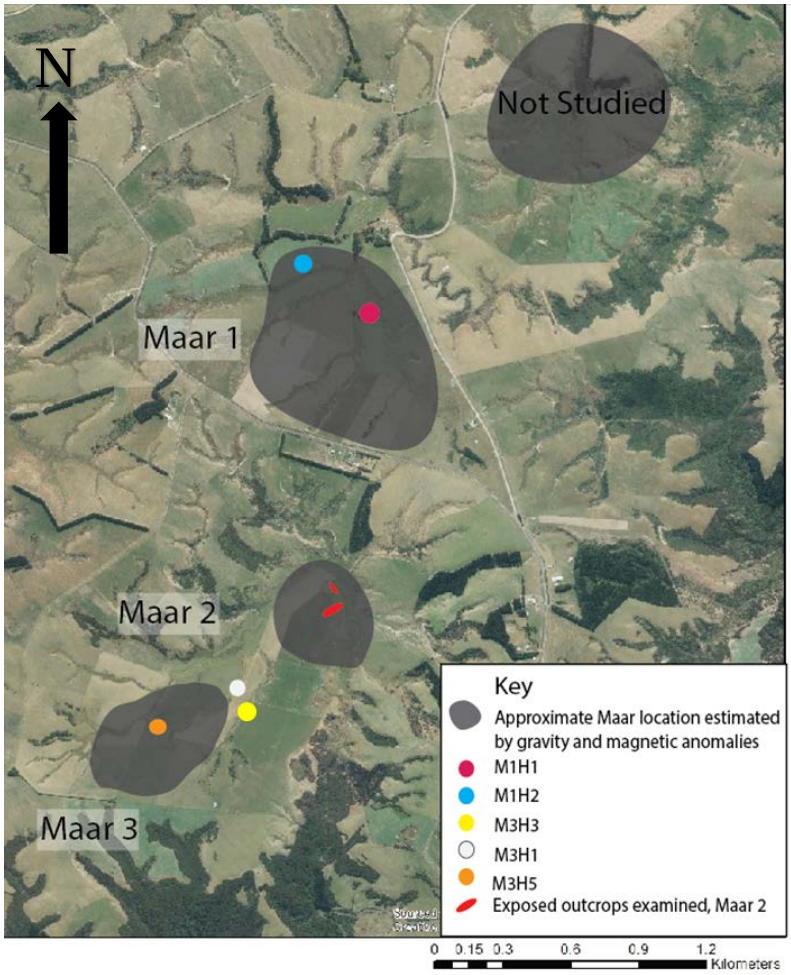

Figure 2: Shows the location of the four maars inferred by the gravity anomaly. Map also includes locations of the drill holes and exposed outcrops analysed within this thesis.

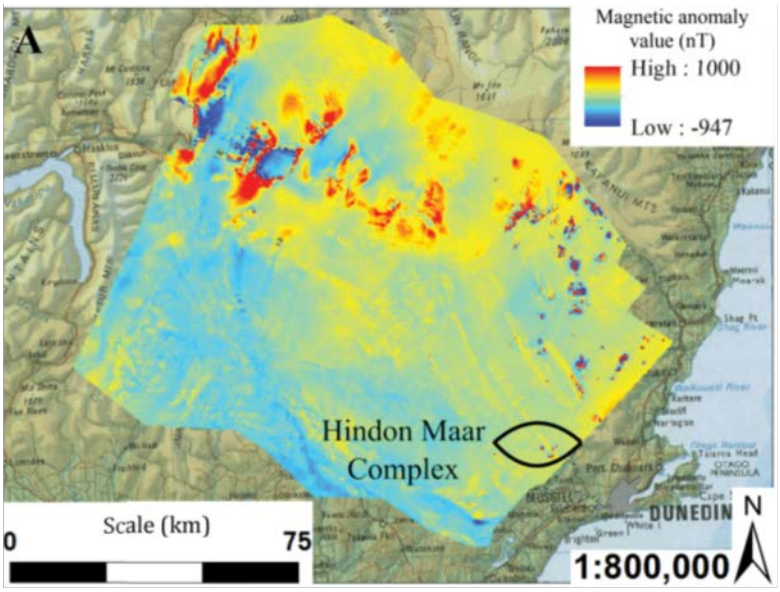

Figure 3: Shows the aeromagnetic survey of Otago, South East Area Survey. The Hindon Maar complex is circled and identified as an area of high magnetic intensity (Bowie, 2015).

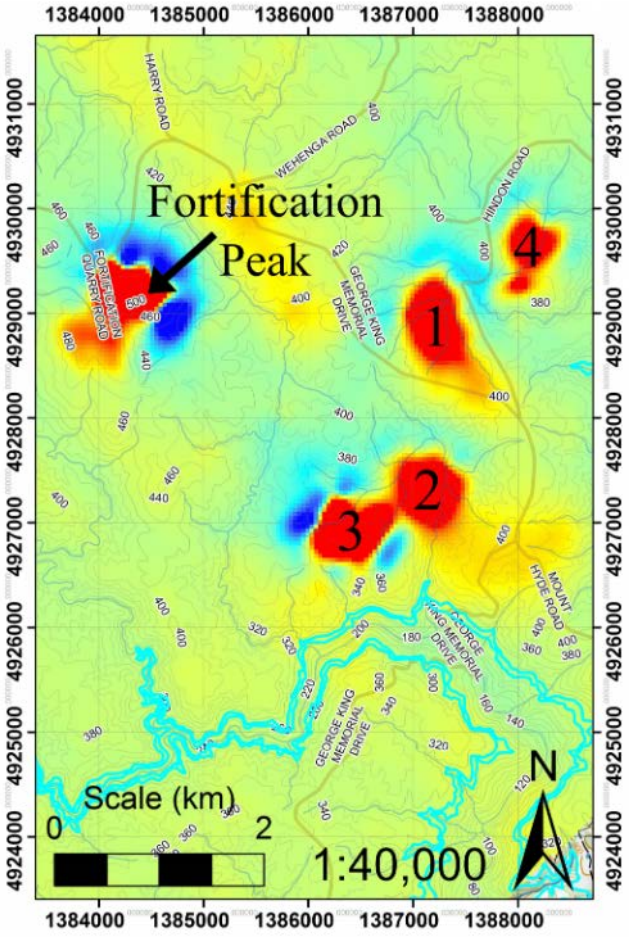

Figure 4: Close-up of the gravity anomaly used to identify the Hindon Maar complex (Bowie, 2015).

Chapter 2

Literature Review

This chapter coverers predominantly peer reviewed literature encompassing the topics of this thesis. The literature review is an overview of maar diatremes and early sedimentation processes within them, along with the geological history of the region. Special emphasis is given to maars and their formation, the sedimentation within maars using three case studies, the weathering of pyroclastic material, and previous studies conducted in the Hindon Maar Complex.

2.1 Geological Setting

New Zealand is the result of pre-Cenozoic allochthonous terranes which merged with the Gondwanan supercontinent (Figure 5; Scott, 2013). The terranes have been divided into the western and eastern provinces, which are separated by a long-lived subduction related batholith (Dalton et al., 2017; Okaya et al., 2013; van der Meer et al., 2016). During the Jurassic, as a result of subduction along the margin of Gondwana, Permian to Triassic sand and mudstones forming the Torlesse and Caples terranes collided with one another resulting in metamorphosis and gradual uplift (Forster & Lister, 2003; Glassey et al., 2003). This formed the basement rocks of much of the South Island as part of the Haast Schist group, comprised of the Otago Schist and the Alpine Schist (Coombs et al., 2008; Jugum et al., 2013). Through the Jurassic, gradual uplift occurred, exposing the Otago Schist by the mid-Cretaceous (Glassey et al., 2003; Jugum et al., 2013). The Otago schist forms a belt, predominantly green schist, extending from Dunedin to 300 km north-west towards where it merges with the Alpine schist (Adams & Graham, 1997; Mortimer, 2000).

Approximately 110 Ma, subduction along the Zealandia and Gondwana margin ended (van der Meer et al., 2016). Following this, extension occurred and by 84 Ma oceanic crust began to form between Zealandia and Australia, forming the Tasman Sea; as well as the Southern Ocean between Zealandia and Antarctica, over the period 83–79 Ma (Dalton et al., 2017; Larter et al., 2002; van der Meer et al., 2016;

Wright et al., 2016). The extension resulted in crustal thinning; and in the Dunedin region continental crust is <30 km thick (Németh & White, 2003b).

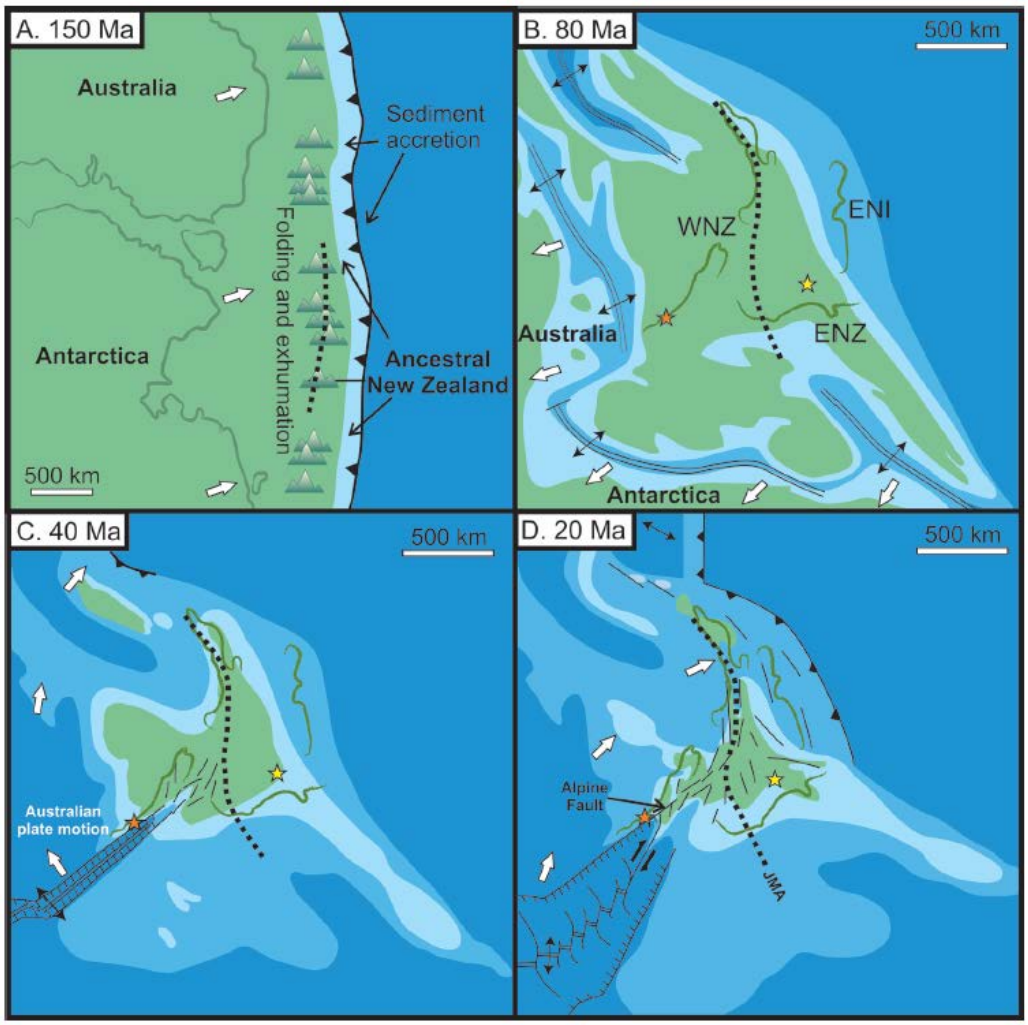

Figure 5: Series of paleogeographic maps showing the initial formation of New Zealand. At 150 Ma, Zealandia was forming along the coast of Gondwana. Rifting at 80 Ma resulted in the divergence of the Zealandian continent from Gondwana. At 40 Ma, rifting occurred south of Zealandia and at 20 Ma the Alpine Fault began to propagate throughout the proto-South Island (Scott, 2013).

During the late Cretaceous, non-marine fluvial sedimentary rocks were deposited over the wider Dunedin region (Glassey et al., 2003). This was followed by interbedded clay, silt, sand stone with conglomerates, and coal seams of the Taratu Formation (Glassey et al., 2003). Marine transgression began around 70 Ma, during the late Cretaceous, resulting in the accumulation of marine deposits of mud and fine sandstone (Abbotsford Formation), poorly indurated fine to medium sandstone (Green Island Sand), massive calcareous mudstone (Burnside Mudstone) and massive calcareous fine sandstone (Caversham Sandstone) (Glassey et al., 2003). Marine transgression in the area reached its maximum during the Oligocene, which

is consistent for the greater New Zealand area (Carter, 1988; Németh & White, 2003a). Uplift occurred because of the initiation of the Australian-Pacific plate boundary through New Zealand (Németh & White, 2003a). Because of the uplift, northeast-trending and northwest-trending faults and reverse faults began to form (Glassey et al., 2003). Extensive erosion occurred, resulting in the removal of much of the overlying sediments and exposing the Otago Schist. This formed the Waipounamu erosional surface (Landis et al., 2008; Glassey et al., 2003). Sedimentary cover sequences had been eroded due to regional uplift. The Waipounamu erosion surface formed a wave cut disconformity with the Haast Schist Group (Landis et al., 2008).

2.2 Regional Volcanism

During the Cenozoic, diverse intraplate volcanism occurred both temporally and spatially throughout the South Island (Hoernle et al., 2006). Cenozoic volcanism has been attributed extensively in the literature to continental rifting during the Mid-Cretaceous, or to a mantle hotspot (Adams, 1981; Sprung et al., 2007; Wellman, 1983). However, it has been argued that due to the irregular distribution, lack of age progression in relation to plate movements, and the temporal and geochemical variations found within Cenozoic volcanism, the volcanism may be due to lithosphere detachment (Hoernle et al., 2006; Timm et al., 2010).

The earliest volcanism recorded in the North Otago has been dated to the Palaeocene, which produced intraplate alkaline volcanism expressed in both on- and off-shore drill cores as a basaltic tuff (Moorhouse et al., 2015; Németh & White, 2003b). Emergent and submarine volcanoes were formed during the late Eocene to the early Oligocene and produced submarine lavas and tephra deposits (Coombs et al., 1986; Moorhouse et al., 2015; Németh & White, 2003b). Volcanism first occurred on land in the South Island at Oamaru around 40 Ma with the Waiareka-Deborah Volcanics (Coombs et al., 1986). Volcanism migrated southward towards the Dunedin area, resulting in the Dunedin Volcanic Group which is comprised of the Alpine Dyke Swarm (ADS), the Dunedin Volcanic Complex and the Waipiata Volcanic Field (WVF) (Coombs et al., 1986; Németh & White, 2003b). The Dunedin Volcanic Group covers an area of approximately 10,000 km², producing predominantly alkaline basalts (Coombs et al., 2008; Dalton et al., 2017). The overall geochemistry is heterogeneous and similar to Ocean Island basalts (Coombs et al., 2008; Dalton et al., 2017; Hoernle et al., 2006).

The ADS is located in northwest Otago and extends towards the Alpine Fault. It has produced lamprophyric dykes and diatreme swarms with a similar geochemistry and age (c. 22.9–31.9 Ma) to the Waipiata Volcanic Field (Coombs et al., 2008; Cooper et al., 1987).

The WVF erupted from 25 to 11 Ma (Figure 6) (Hoernle et al., 2006). The southernmost expression of the WVF is the Kaitangata coalfield, which extends northwards to Haughton Hill in Maniototo (Coombs et al., 2008). The WVF comprises at least 55 monogenetic volcanoes over an area of 5000 km² (Németh & White, 2003b). At least 38 scoria cones have been identified within the volcanic field, along with tuff rings and maars (concentrated near the centre of the volcanic field) and vent complexes such as nested maars and nested tuff rings (located on the north-western margin of the volcanic field) (Németh & White, 2003b). There is evidence that at least three volcanic edifices are polygenetic: Siberia Hill, Burns Point and Omimi (Coombs et al., 2008). The WVF initially produced phreatomagmatic eruptions, followed by Stromboli-styled eruptions, producing scoria cones, tuff ring maars, fissure vents and lava flows (Németh & White, 2003a). The total eruptive volume of the WVF is estimated to be between 9 and 40 km³ (Németh & White, 2003a). The Hindon Maar complex is part of the WVF (Möller et al., 2017). Pollen analysis conducted in Maar 1 of the Hindon Maar Complex indicates that the maar formed during the early Miocene, which is consistent with other eruptions of the WVF (Kaulfuss & Moulds, 2015). Furthermore, boulders on top of Maar 3 have been Ar-Ar dated to 14.603 ± 0.093 Ma (Lee, 2016). However, limited research has been conducted on the Hindon Maar complex and so the age is not well constrained.

Following the formation of the WVF, the Dunedin Volcanic Group became active from 16 to 10 Ma (Hoernle et al., 2006; Reichgelt et al., 2016). The Dunedin volcano forms a shield and has a complex eruption history (Coombs et al., 2008). The overall eruptive volume of the Dunedin Volcanic Group is greater than the entire eruptive volume of the WVF (Coombs et al., 2008).

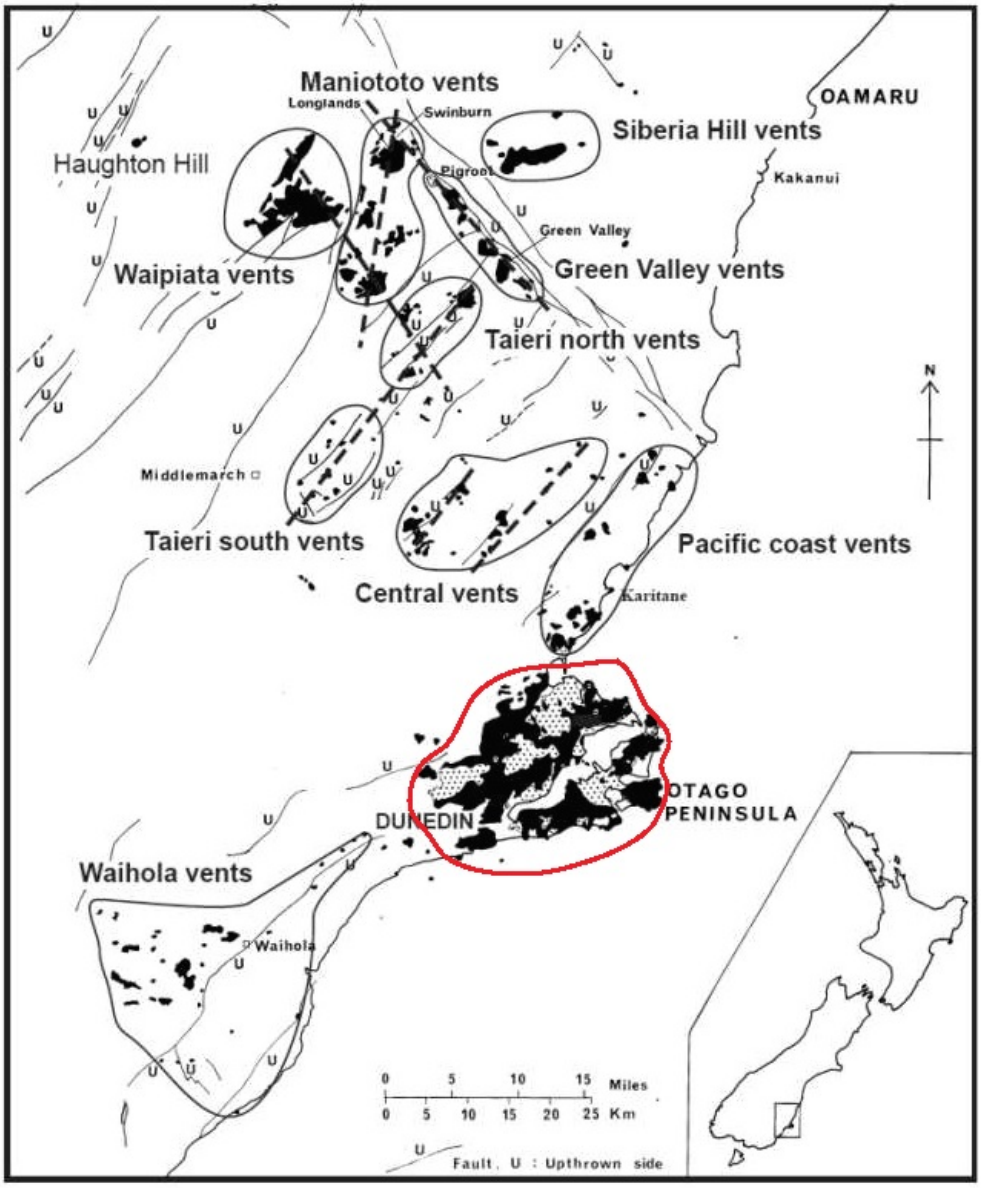

Figure 6: The Waipata Volcanic Field with the Dunedin Volcano circled in red (Nemeth & White, 2009).

2.3 Review of Maars

Maars are the second most common volcanic landform found on the Earth's surface and are generally found within monogenetic fields (Lorenz, 2003; Németh, 2010; Ross et al., 2017). Maars can also be found in relation to polygenetic volcanism, often on the foot plains of strata volcanoes, shield volcanoes and calderas (Boris et al., 2015; Lorenz, 2003; Németh & Kereszturi, 2015; Ross et al., 2017). Monogenetic fields are generally basaltic and volcanoes within them have an eruption period typically less than one year (Kurszlaukis & Fulop, 2013; Németh & Kereszturi, 2015). Monogenetic fields can be active for millions of years,

although the dense rock equivalent of individual volcanoes is only 1 to 2 times that of an average polygenetic volcano (Németh, 2010). However, the overall dense rock equivalent of a monogenetic field is similar to that of a composite cone (Németh, 2010).

Originally, the term ‘maar’ was loosely defined; an argument made for a rigid definition which included characteristics of maars such as diameter, shape and size was not made until 1967 (Ollier, 1967). More recently, the use of the term has been better defined. This has mostly arisen because kimberlite maars have traditionally been described using different terminology to other maars (White & Ross, 2011). More importantly, unlike other volcanic landforms, maars are not limited to a specific magma type or tectonic setting (Lorenz, 2007; Ross et al., 2017). Therefore, the definition of the term maar is related to the eruption process and volcanic landform produced (Lorenz, 2003). The most popular definition comes from Lorenz (1973) and is used often in literature (White & Ross, 2011).

> *“A large volcanic crater cut into country rock below general ground and possessing a low rim composed of pyroclastic debris (tuff or lapilli-tuff). Approximately 100 to 200 m wide; approx. several 10 to more than 200 m deep; height of rim above ground may reach a few metres to nearly 100 m.” Lorenz (1973).*

Within monogenetic fields, maars can be found to be ‘polycyclic monogenetic’ or ‘polymagmatic polycyclic monogenetic’ and vary slightly from typical monogenetic volcanoes (Boris et al., 2015; Németh et al., 2010). Polycyclic monogenetic volcanoes are volcanic edifices in which vents are nested or occur alongside one another with the distance between vents no greater than half the width of one individual volcanic edifice (Németh et al., 2010). Polymagmatic polycyclic monogenetic volcanoes differ from polycyclic monogenetic volcanoes only in that the edifices vary chemically from one another (Németh et al., 2010). An example of polycyclic volcanism can be found at Bandoro Volcano, of the Bakony–Balaton Highland Volcanic Field in Hungary, where a polycyclic monogenetic volcano has been identified as having multiple eruption episodes (Kereszturi et al., 2010). Another example of a polycyclic monogenetic volcano is the Barombi Mbo Maar, Cameroon. Here, the third eruptive episode occurred approximately 100,000 years after the second eruptive episode. The third eruptive episode was the result of a new feeder dike and new diatreme (Boris et al., 2015).

Coalescence of multiple maars can also occur. For example, Lake Purrumbete in south-eastern Australia is an example of multiple shallow craters forming a 3 km maar structure as a result of coalescence (Jordan et al., 2013). During the eruption the active vents migrated, and reactivation of early vents occurred during the later stage of the eruption (Jordan et al., 2013).

In recent years, the popularity of maars in research has increased due to two main factors: the exploration of kimberlite diatremes in Canada, and the use of varved lake sediments often found in maars for the reconstruction of paleoclimates (Kaulfuss, 2017; Kjarsgaard et al., 2006; Kurszlaukis & Fulop, 2013; White & Ross, 2011). As a result, much of the research has focused on these two factors, with much less research into sedimentation processes within maar craters (Pirrung et al., 2008).

2.4 Formation of Maar Diatremes

The driving force for the formation of maars is the interaction of magma with groundwater (Lorenz, 1986; Valentine et al., 2011; White & Ross, 2011). During a maar-forming eruption, as magma ascends through the country rock it encounters a groundwater source (Németh & Kereszturi, 2015). This interaction with water results in the rapid expansion of the water and fragmentation of the magma, resulting in a phreatomagmatic eruption (Kurszlaukis & Fulop, 2013; Lorenz, 2003). Water expands by 160%, resulting in a violent eruption consisting of ash, country rock fragments, steam, and water (Wang & Yang, 2014). The resultant eruption sends shockwaves through country rock, resulting in fragmentation (Lorenz, 2003; Ross et al., 2013). The landforms created by the eruption are governed by the amount of groundwater, with excess water deepening the conduit and limited water potentially forming a scoria cone or lava lake (Boris et al., 2015; Lorenz, 1985). Groundwater availability varies depending on whether the country rock substrate is a hard-rock or a soft rock and the height of the water table (Figure 7) (Lorenz, 2003).

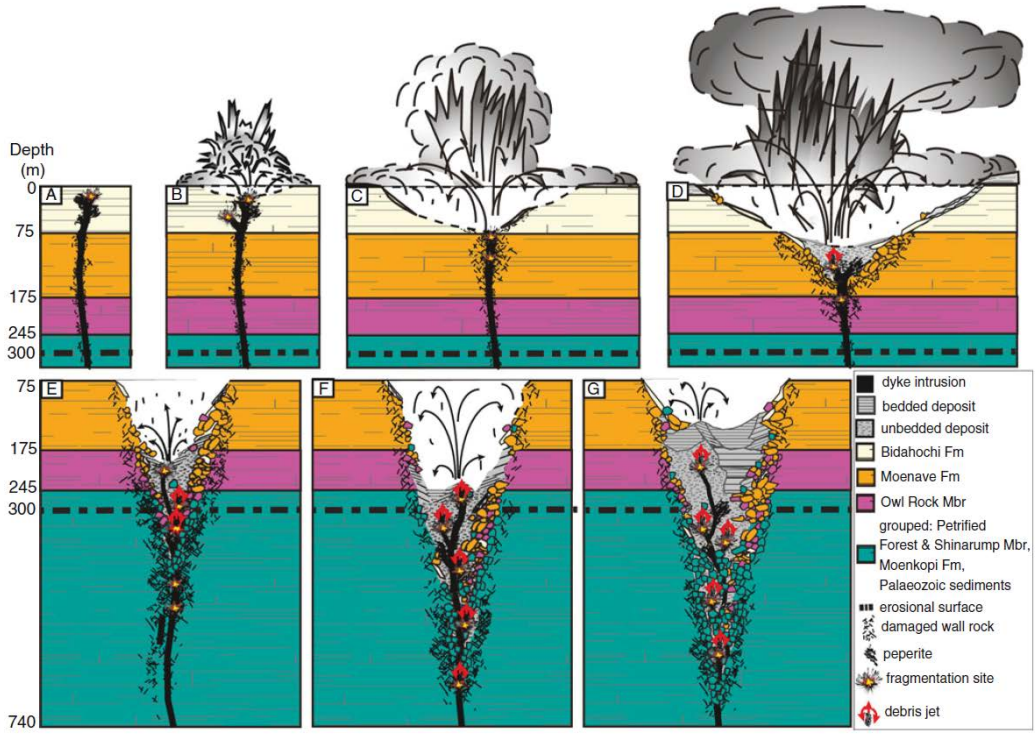

Figure 7: Diagram of the formation of the Standing Rock West diatreme. A) the dyke rises upward by hydraulic fracturing. B) the dyke interacts with groundwater, resulting in an explosion; C) explosion continues near surface and widens crater; D) un-bedded diatreme deposits begin to accumulate; E to G) eruption becomes more confined, debris streams begin to propagate, mixing diatreme deposits.(Lefebvre et al., 2013)

2.4.1 The Lorenz Model

The Lorenz model describes the interaction between ascending magma and groundwater in relation to the formation of maars. Within hard-rock environments, water availability is governed by hydraulically active faults and joints, and therefore also controlled by the orientation of the zones of weakness. Furthermore, maars found within these environments generally occur at valley floors; an example of this is Eifel Volcanic Field, Germany (Lorenz, 2003; Macorps et al., 2016). Maars found within soft substrates generally have a greater abundance of water available (Lorenz, 2003).

Due to the lithostatic pressure of above ground strata, water can only flash to steam, and thus explosively interact with magma, at 20 to 30 bar (Figure 8) (Lorenz, 1986). This is generally at a depth of 200 to 300 m. However, kimberlite diatremes have been found at depths up to 2,500 m, greatly exceeding this pressure range (Boris et al., 2015; Lorenz, 2003). The location at which the 20 to 30 bar pressure range occurs migrates downwards as the eruption proceeds (Lorenz, 2003; Lorenz et al.,

2017). The first explosive interaction between water and magma will occur at the highest possible point (Lorenz, 2003). The eruption will continue until the water can no longer replenish (Lorenz, 1986). By then, the pressure has been released enough that the 20 to 30 bar pressure range will now be below the first eruption (Lorenz, 2003). If there is water to explosively interact with the magma then it will do so deeper in the earth's surface (Lorenz, 2003). This process will continue until the water source has been fully extinguished, at which point there may be a transition into a different volcanic landform, such as a scoria cone. Alternatively, the eruption may stop.

One criticism of the Lorenz model is that it does not adequately account for the irregular distribution of lithics within ejecta rings (Valentine & White, 2012)(Boris et al., 2015). Furthermore, this model fails to account for the volumetric differences that have been observed in different eruptions between crater size, ejecta rings and diatreme deposits, or the relationship between crater size and thickness of tephra deposited (Boris et al., 2015).

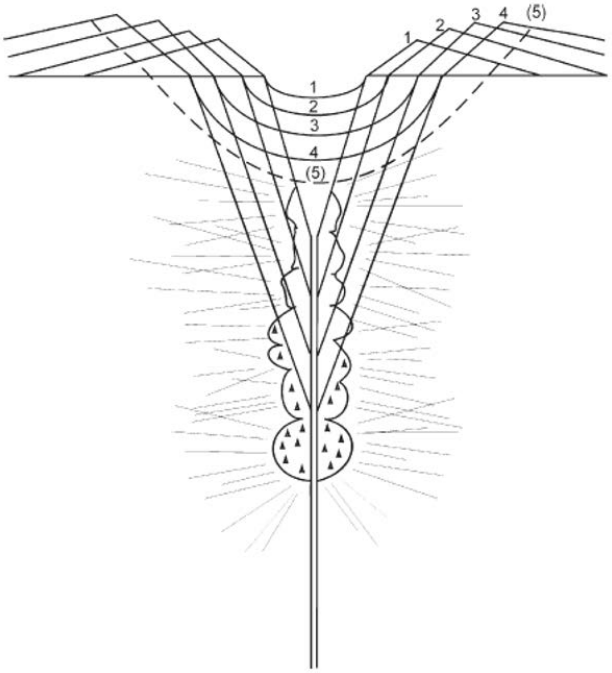

Figure 8: Diagram showing the growth of a maar diatreme using the Lorenz model. During the eruption, shockwaves fragment the country rock forming an explosion chamber, propagate downwards, increasing the size of both the maar crater and the diatreme (Lorenz, 2003).

2.4.2 Valentine & White model

A revision to the Lorenz model was made by Valentine and White in 2012. It differs from the Lorenz model in arguing that explosions, due to the interaction of magma

and groundwater, can occur at any depth below the critical pressure of water, and therefore the explosions occurring during the eruption may not necessarily propagate downwards in the fashion described in the Lorenz model (Figure 9)(Valentine & White, 2012).

The initial explosion damages the country rock, which can sometimes result in small craters (Valentine & White, 2012). At this point a proto-diatreme begins to form, consisting of breccia and peperite adjacent to the feeder dike. Following this, magma feeds into the proto-diatreme, with explosions continuing at any depth (Valentine & White, 2012). This model states that diatremes will grow wider at the top more quickly because the interaction of magma with water is more effective at lower hydrostatic pressures, and because rock strength increases with increasing lithostatic pressure. Furthermore, the closer the explosion is to the ground surface, the more the diatreme and crater walls will fail, propagating the crater (Valentine & White, 2012). Intra-diatreme dykes provide thermal energy for the eruption and follow irregular paths as opposed to vertical paths. However, as they extend upwards, the dykes favour upward widening of the diatreme. This model has been supported by experiments and field observations (Valentine & White, 2012). After the eruption, diatreme deposits are generally nonconsolidated and saturated. This is important because this model describes only two mechanisms in which country rock breccia can occur. The first is that explosions occurring within the diatreme result in jets of debris propagating upwards, mixing country rock with the diatreme. The second mechanism occurs when the diatreme walls fail further, mixing the country rock with diatreme deposits. This failure can result in the temporary liquification of diatreme fill, in which large country rock clasts can form floating reefs. These processes result in a mixing of diatreme fill (Valentine & White, 2012).

The revised model argues that the deepening of the maar crater due to loss of pressure at greater depths is not a necessary condition, as it is believed that the water table surrounding the diatreme remains relatively constant due to the permeability limitations of the substrate, preventing rapid drainage (Valentine & White, 2012). It is also believed that the diatreme remains heterogeneous and water saturated. It is argued that this allows for water recycling, allowing for the formation of peperite. The revised model hypothesises that the occurrence of scoria cones or other magmatic volcanic landforms or deposits are a result of transitions between magmatic and phreatomagmatic activity, and are a result of variations of magma

flux or water distribution (Valentine & White, 2012). These transitions may also show different eruptive processes from different vents within the maar.

The Valentine and White model proposes that magma fluxes can result in ascending magma having little to no interaction with the diatreme or having dikes underneath the eruptive surface (Valentine & White, 2012).

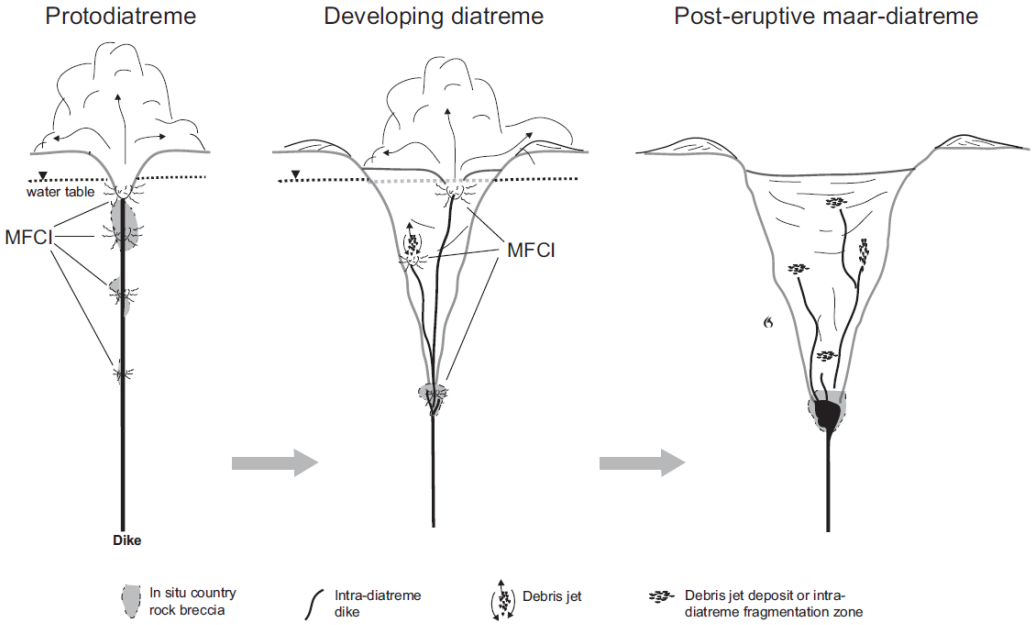

Figure 9: Valentine and White's revised model for maar diatreme growth, showing explosive molten fuel coolant interaction (MFCI) taking place at multiple depths resulting in the brecciation of country rock. Multiple MFCIs result in the formation of the maar and diatreme.

2.5 The maar as a volcanic landform

Most maar craters are approximately circular in shape, although this can be affected by aspects of the environment such as the country rock (Begét et al., 1996; Németh, 2010; Valentine et al., 2011). Maar craters range in diameter from 80 m to greater than 3 km, although they are generally 100 to 1500 m wide (Jordan et al., 2013; Lorenz et al., 2017; Pirrung et al., 2003). The largest maar crater on earth, Espenberg Maar in Alaska, is 8 km x 6 km wide, with a depth of 200 m. This is not typical, and the unusual size of this maar is associated with significant water availability due to permafrost that is 100 m thick in the area (Begét et al., 1996). The depth of a maar crater is related to the size of the eruption and the extent of infilling post eruption (Lorenz, 2003). Maar craters range in depth from 10 to 200 m deep, and crater depth has been related to explosive energy (Valentine et al.,

2017). Some authors have attributed large crater size to multiple eruptive events or coalescent maars (Begét et al., 1996; Jordan et al., 2013).

Maar craters are often separated into the lower crater, which exists below the pre-eruptive surface, and the upper crater, which exists above it (Lorenz et al., 2017). In hard-rock environments, the lower crater wall exposes country rock, whereas in soft substrates nonconsolidated tephra is exposed (Lorenz et al., 2017). The steepness of the crater wall is governed by the country rock, with more consolidated rocks forming steeper sided conduits. This is because soft sediment is more likely to flow towards the centre of the crater, resulting in shallow angle slopes (Lorenz, 2003; Pirrung et al., 2003).

Maar craters are surrounded by tephra rings (Lorenz, 1986; Valentine et al., 2017; White & Ross, 2011). Tephra rings extend from the crater for distances of normally between 2 and 5 km (Lorenz, 2007). Many young, small maars are surrounded by thinly bedded tephra rings, which are rich in accidental clasts (volcanic basement material). Tephra rings in small maars can consist of tens to hundreds of individual beds (Lorenz et al., 2017). Larger maars can have tephra rings 100 m in height and 2 km in diameter (Lorenz et al., 2017; White & Ross, 2011). In older maars, however, the tephra ring has often been eroded away (White & Ross, 2011).

Dip angles of tephra beds in the tephra ring are generally sub horizontal to 20°. White and Ross have stated that tephra rings are well stratified and are composed of up to 90% ash and lapilli (White & Ross, 2011). In contrast, Lorenz (2007) stated that maar tephra rings can contain up to 80 to 90% country rock (Lorenz, 2007). Massive tuff breccias, spatter clasts and ballistic projectiles along with ash and lapilli can be found in tephra rings (Valentine et al., 2017). When tephra rings are dominated by lithic-rich deposits, it may indicate short lived explosions over sustained eruption columns or fountains (Valentine et al., 2017).

Found underneath the maar crater is the diatreme, the subsurface feeder structure of a maar (Lorenz, 1986). Diatremes range in depth from <100 m to over 2.5 km. In hard-rock environments, cone-shaped diatremes occur, whereas, in soft rock environments, diatremes generally have a lower slope gradient and are larger. (Figure 10) (Lorenz, 1973; Lorenz et al., 2017; White & Ross, 2011).

Ring faults are concentric syn-depositional features commonly found in maars, formed by partial crater wall collapse (Jordan et al., 2013; Lorenz, 1986; Sohn & Park, 2005). For example, the Lake Purrumbete Maar, Australia, has two large faults tangential to the crater wall, and interspersed in a ring with a series of smaller

faults running both parallel and perpendicular to the crater wall (Figure 11) (Jordan et al., 2013).

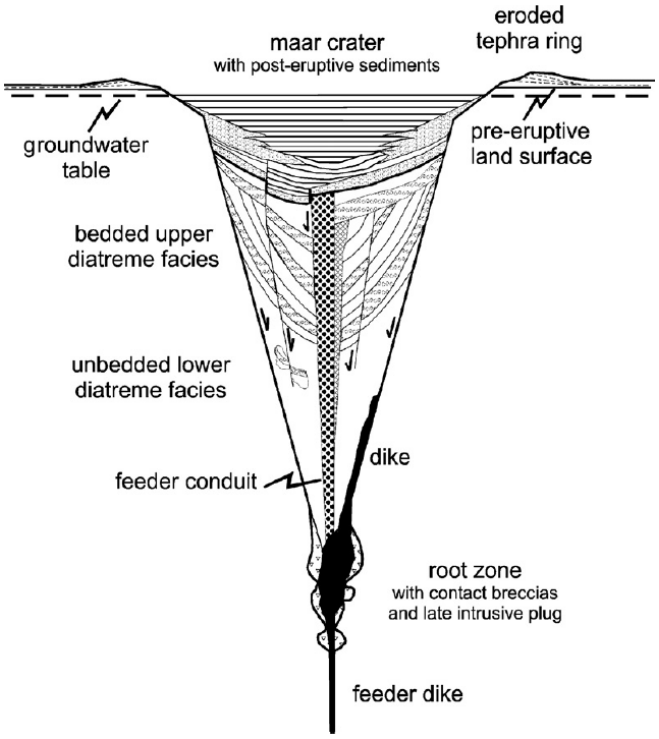

Figure 10: Diagram of an idealised maar with diatreme, including the feeder dike and root zone which supply magma for the eruption. The diagram shows both above-ground and below-ground features of the maar. The above ground topography of a maar generally has a low angle tephra ring. The maar crater sits below the tephra ring in the pre-eruptive surface. Within the diatreme there are a series of bedded facies and unbedded lower diatreme deposits (Lorenz, 2007).

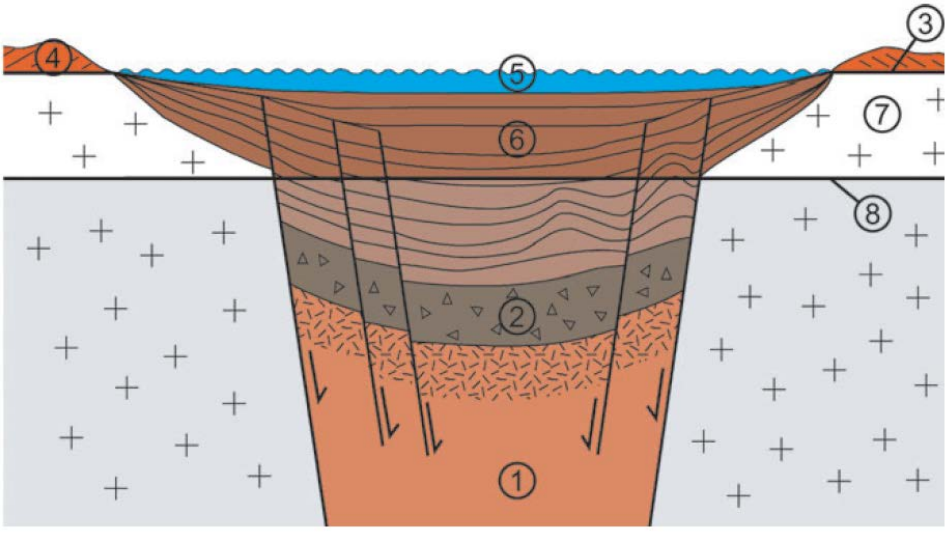

Figure 11: Diagram showing the post eruptive evolution below the maar crater. 1) diatreme deposits. 2) diatreme breccia 3) pre-eruptive surface 4) tephra ring 5) maar

lake 6) post eruptive sediments 7) depth of collapsing sediments due to subsidence (White & Ross, 2011).

2.6 Sediments found within maar craters

Maar craters form unique sediment traps which rapidly fill with water after the eruption (Pirrung et al., 2008). This is because there is generally no inflow and outflow of water; lakes are generally deep (10 – 100 m), and have a limited catchment area. (Nemeth et al., 2002; Pirrung et al., 2008; White, 1990). Studies conducted on the sediment found within maar craters primarily focus on annually accumulated biogenic rich material (Brauer et al., 1999; Czymzik et al., 2016; Fox et al., 2017; Lehndorff et al., 2015; Marchetto et al., 2015; Martin-Puertas et al., 2017; Rach et al., 2017). Very limited studies have focused on the sedimentary evolution of maars following the formation of the diatreme and before the final evolution phase of biogenic accumulation (Kaulfuss, 2017; Nemeth et al., 2002; Pirrung et al., 2008). This lack of studies has been attributed to the fact that clastic sediments are difficult to core, they contain little biogenic material, and precise chronologies are difficult to determine (Pirrung et al., 2008).

Clastic material which accumulates in maar craters is derived largely from material deposited on the tephra ring and crater wall (Lorenz et al., 2017; Pirrung et al., 2008). This material fails and is deposited within the maar crater as a series of flows (Bertrand et al., 2014; Pirrung et al., 2008). However, clastic material may also be found within beds of biogenic lake sediment and, in especially arid environments, be deposited by aeolian processes (Pirrung et al., 2008; Valentine et al., 2011).

2.6.1 Flows associated with clastic deposition in maars

Sediment gravity flows are the main mechanism for the transport of clastic sediment from the tephra ring and crater wall into the maar lake or to the lake edge (Nemeth et al., 2002; Pirrung et al., 2008; White, 1992). Sediment gravity flows are the movement of sediment in fluid down a slope due to gravity (Gani, 2004). The type of flow and the associated deposits depend on the interaction between the fluid and sediment (Gani, 2004; Khripounoff et al., 2012). The land equivalent of these sediment gravity flows are mudflows and pyroclastic flows; these two groups of flow have similar flow dynamics in different mediums: air and water (Talling et al., 2012).

There are four main factors which affect subaqueous sediment gravity flows. These factors are: sediment concentration, arguably the most important factor; sediment support mechanisms (matrix strength and fluid turbidity); flow state; and rheology (whether a flow is a Newtonian or non-Newtonian fluid) (Gani, 2004). The interaction between these characteristics results in different flow types and therefore different sedimentary deposits: turbidity currents (turbidites), debris flows (debrites), density flows (densites) and hyperpycnal flows (hyperpynites) (Liu et al., 2017; Talling et al., 2012). In maars, turbidity currents and debris flows are the most common subaqueous flow type (Nemeth et al., 2002; Pirrung et al., 2008; Pirrung et al., 2003; Smith, 1986; White, 1992).

2.6.1.1 Flow Types

Debris flows are movements of material in a hyper-concentrated flow (Nemeth et al., 2002). They generally thicken basin-ward and end abruptly, often pinching out at their extent (Gani, 2004). The flow is supported by a muddy matrix, which allows the transportation of large, outsized clasts (Gani, 2004; Talling, 2014; Xian et al., 2017). Debrites are generally massive, poorly sorted and often have very little post-depositional settling once the flow has finished propagating (Gani, 2004).

Turbidity currents are diluted; grains are fully supported within a turbulent flow (Meiburg & Kneller, 2010; Talling et al., 2012). Momentum in turbidity currents is due to gravity (Talling et al., 2012). Turbidites can be normally graded and can further settle after deposition (Talling et al., 2012). Normal grading results from waning flow, which also produces varying structures from incremental deposition (Delannay et al., 2017; Talling et al., 2012). Debrites and turbidites can be identified through different grading successions.

The Bouma Sequence (Fig. 12) is an idealised model for describing facies within turbidites (Bouma, 1962). This model was created by Bouma in 1962 and is popular throughout literature, although it has been described as overly simplistic (Talling et al., 2012). However, the Bouma Sequence has been found to accurately predict the deposits found within lakes (Covault et al., 2014; Liu et al., 2017). The Bouma Sequence is as follows: the lowermost facies is the T_A, which is a massive sandstone. This is overlain by the T_B facies, a laminated sandstone. The T_C facies is often laminated with ripples; this facies is generally of a finer sand than the TB. The T_D facies is characterised by laminated siltstone, and is overlain by the T_E facies, consisting of hemipelagic mud (Bouma, 1962).

Grain flows result from the failure comprised of cohesionless grains, which propulsion is the result of grain collision(Shanmugam & Wang, 2015). Subaerial grain flows form predominantly in sand and occur exclusively on slopes near the angle of repose (Lowe, 1976). They deposit thick units >5 cm as the flow freezes once the slope is less than the angle of repose (Lowe, 1976).

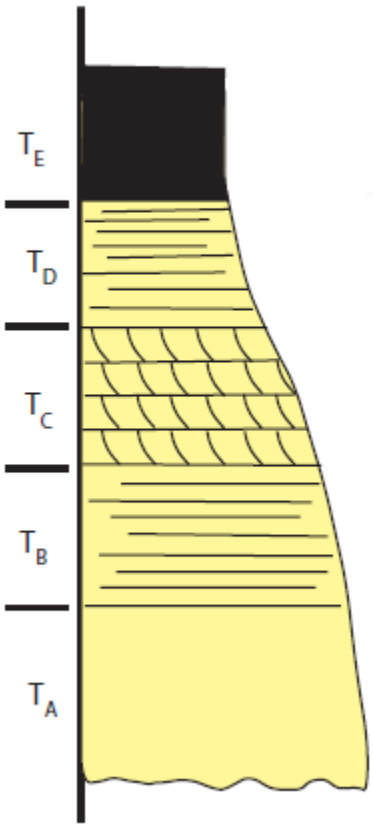

Figure 12: Bouma sequence: T_A is massive sand; T_B is laminated sand; T_C is cross ripple laminations; T_D is laminated mud; T_E is mud

Rock falls are the detachment of rock boulders from a steep cliff. These boulders fall through a free face in rotation (Dorren, 2003; Varnes, 1978). Within a rockfall, tailings are graded, and smaller grains are concentrated in the middle and at the top of the rockfall deposit (Varnes, 1978). In contrast, rock slides are characterised by failure along a shear plane, and boulders are transported without rotation (Varnes, 1978). It is important to note that not only can varying flows occur within maars, but multiple mass flow types can occur from a single failure, especially in a lacustrine environment (Liu et al., 2017).

2.6.2 Clastic Sediments in Maars

In general, the infilling of a maar crater follows a sequence of events from rock falls and debrites to turbidites and then later biogenic accumulation (Kaulfuss & Moulds, 2015; Nemeth et al., 2002; Pirrung et al., 2003). Understanding of these processes is restricted to interpretations of cores or rock outcrops (Kaulfuss, 2017; Pirrung et al., 2003). With a few exceptions, the best studied of maar is the Ukinrek East Maar which erupted in 1977 (Büchel & Lorenz, 1993; Pirrung et al., 2008). Since the Ukinrek Maars erupted, scientific observations have been made which have led to the unique opportunity of viewing early sedimentation processes into the maars (Lorenz, 2007; Pirrung et al., 2008).

2.6.3 Ukinrek East Maar

The Ukinrek Maars consist of two maar craters, East Maar and West Maar, which erupted during the months of March and April 1977 (Figure 13) (Kienle et al., 1980; Pirrung et al., 2008). The elevation of the West Maar crater rim was 72 m a.s.l, and it formed an elongated crater with a diameter of 168 m and an average depth of 32 m (Pirrung et al., 2008). The East Maar had a diameter of 307 m and a maximum depth of 71 m; the crater rim was approximately 83 m a.s.l (Kienle et al., 1980; Pirrung et al., 2008). A summary of the eruption is given by Kienle et al. (1980).

The following description of the early evolution of the East Maar is summarised from Pirrung et al (2008):

Morphologically the biggest changes to the crater post eruption were collapses to the crater wall producing rock falls and rock slides, the formation of localised slumps and the formation of a debris fans. Vertical escarpments were observed within the crater wall until at least August 1981. Observations made in August 1981 witnessed several rock falls per day. This continued until at least July 2004. Sporadic rock slides have also occurred, some of which produced several cubic metres of material. Rock slides decreased in frequency for the first few years post eruption.

In August 1977, failure in debris fans formed in grain flows. Early debris fans were separated by escarpments and sub aqueous grooves were observed in the fan. In 1977, debris fans failed frequently. By July 2004 debris fans had developed and were observed along steeper crater wall sections of the southern, western and northern crater walls. These developed debris fans extended from the crater rim to the crater floor and were more stable, with grain flows occurring rarely. In July

2004 coarse grains were concentrated near the shoreline of debris fans as fines were washed away via wave action.

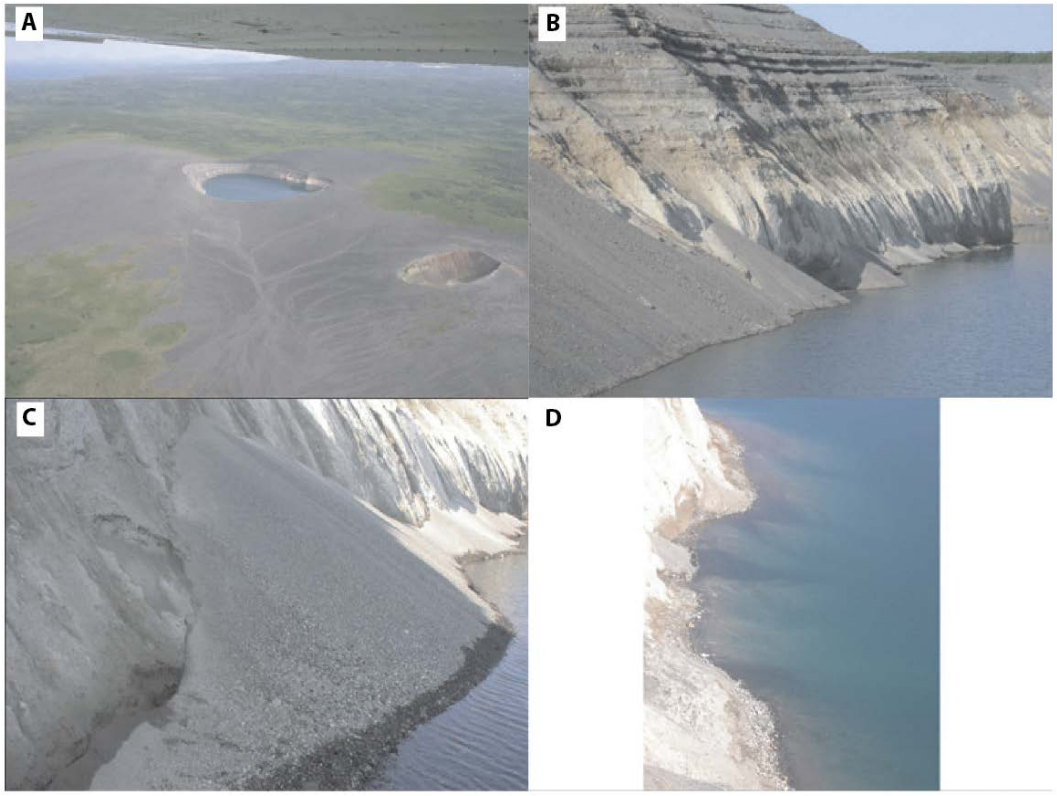

Figure 13: A series of pictures taken of the Ukinrek Maars. A-C were taken in July 2004. (A) shows the West Ukinrek Maar on the right and the East Ukinrek Maar to the left. (B) shows the southern shore of the East Maar with a near vertical escarpment. (C) shows a debris fan which is not connected to the upper crater wall. (D) shows a sub aqueous debris fan with grooves observed in August 1981 (Pirrung et al., 2008).

Marginal sedimentation events in the East Ukinrek

- The first phase of sedimentation produced breccia and rock falls/slides because of instability of the crater wall. These deposits could not be easily distinguished from syn-eruptive deposits.
- In the first few years following the eruption, subaerial debris fans formed. During storms debris fans would destabilise, resulting in mass flows.
- 13 years after the eruption the debris fans had enlarged both vertically and laterally and a lake had fully formed. The debris fan became stable but became more susceptible to wave activity

- The accumulation of sediments between 1977 and 1981 was estimated to be 37 m.
- The establishment of vegetation and the formation of soil on the maar crater greatly reduced the amount of flows into the maar by stabilising the crater wall.

Distal sedimentation events

- Distal lake sediments are the result of turbidites, aeolian deposition and ice rafted debris, resulting in the deposition of sandy to clayey silt with occasional gravel sized clasts.
- Turbidites produce horizontal laminations, normal grading and show the preferential fallout of heavier minerals such as magnetite.
- The propagation and formation of turbidites are independent of climate and may result from the compaction of the diatreme.
- Aeolian deposition occurs, has resulted in three inversely graded layers, and is believed to have resulted from dust storms.
- Clast size associated with ice rafted debris can be up to 3.3 cm in diameter. This exceeds the size of grains able to be transported into the centre of the lake by any other means.

2.6.4 Ekfeld Maar

Germany's monogenetic volcanic fields have been extensively studied, with over 150 scientific papers produced between 1990 and 2015 (Schindler & Wuttke, 2015). In the Eifel region, Germany, a study on the lithofacies of Eckfeld Maar has been conducted (Pirrung et al., 2003). Eckfeld Maar is part of the Palaeogene Hocheifel Volcanic Field and has a Ar/Ar date of 44.3±0.4 Ma (Mertz et al., 2000; Pirrung et al., 2003). Pirrung et al (2003) used cores to analyse the succession of lithofacies within the maar. This succession is summarised as follows.

- The lowermost unit formed a homogeneous breccia from rock falls consisting predominantly of country rock. This is believed to have formed some days after the eruption.
- Weeks to several years after the eruption, rock falls and sub aqueous debrites occurred. These produced assorted breccia, comprising juvenile pyroclastic and country rock.
- Following this, a further breccia was deposited, which consisted of juvenile pyroclastic and country rocks. Non-graded silt to gravel layers and well

sorted sandy layers are observed. This breccia is interpreted as being the result of rock falls, debris flows and turbidites. It is also assumed that due to the steep gradient of the crater wall, slumps occurred. This deposit formed some decades following the initial eruption.

- Hundreds to thousands of years after the eruption, laminated minerogenic deposits accumulated. These consisted of gravel and sandy layers. Some grading could be observed along with flame structures. The material is believed to have resulted from the erosion of the crater slopes after limited vegetation cover was established.
- Some tens of thousands of years after the maar eruption, biogenic/minerogenic lake sediments accumulated. These were similar to previous deposits; however, greater biogenic influences were observed.
- Still water sedimentation occurred, resulting in laminated biogenic and minerogenic deposits. This was followed by swamp deposits, which indicated the final maar infilling.

2.6.5 Foulden Maar

Foulden Maar is part of the Waipiata volcanic field and was active approximately 23 Ma (Fox et al., 2015; Mildenhall et al., 2014). Foulden Maar is ~30 km Hindon Maar and as a result it has been compared with the Hindon Maar complex (Figure 14) (Kaulfuss & Moulds, 2015). The topography of Foulden Maar today shows a 1000 x 800m depression, indicating the possible crater dimensions for the maar (Kaulfuss, 2017). Two cores were drilled at the centre of the maar, recovering 120.1 m and 183.48 m respectively of material (Kaulfuss, 2017). Numerous studies have be conducted on the Foulden Maar, with particular emphasis on the varved sediments for the purposes of paleoclimate reconstruction (Fox et al., 2015; Fox et al., 2017; Lindqvist & Lee, 2009; Mildenhall et al., 2014; Reichgelt et al., 2013). The clastic sedimentation of Foulden Maar has been analysed by Kaulfuss (2017); a summary of the findings are as follows.

The lowermost deposits found at Foulden Maar are a schist breccia. The breccia is composed mostly of schist; however pyroclastic fragments are also observed. No signs of weathering have been observed. This deposit has been interpreted as a concentrated density flow. The schist breccia accumulated on the crater floor, because of the collapse of the crater walls immediately to a few years after the eruption. This facies was deposited as a result of a debris flow. Overlying this is a

facies composed of massive breccia with additional normally graded composite beds and graded sand and mudstone. The massive breccia resulted from frequent gravity flows, which transitioned from a debrite to a hyperpycnite and then ultimately to a turbidite nearing the centre of the maar. Freshwater sponges had begun to accumulate, indicating the formation of the lake. This is interpreted as approximately 27 years after the eruption (Kaulfuss, 2017). Sub-horizontal bedding within the massive breccia has been interpreted as indicating that the crater floor was relatively flat. The massive breccia is distinguished from the underlying facies due to the finer grains and higher proportions of organic and biogenic siliceous material.

The overlying facies comprises graded beds and laminated sediments. This facies is distinguished from previous facies due to the finer grains and increased proportions of organic and biogenic siliceous material. The graded beds are associated with density flows.

Overlying the graded beds is a diatomaceous sandy mudstone, which is associated with turbidites. The upper section of this facies, which is laminated diatomite, is associated with background sedimentation within a lacustrine environment. The uppermost facies is predominantly diatomite and has been associated with a fully stratified lake.

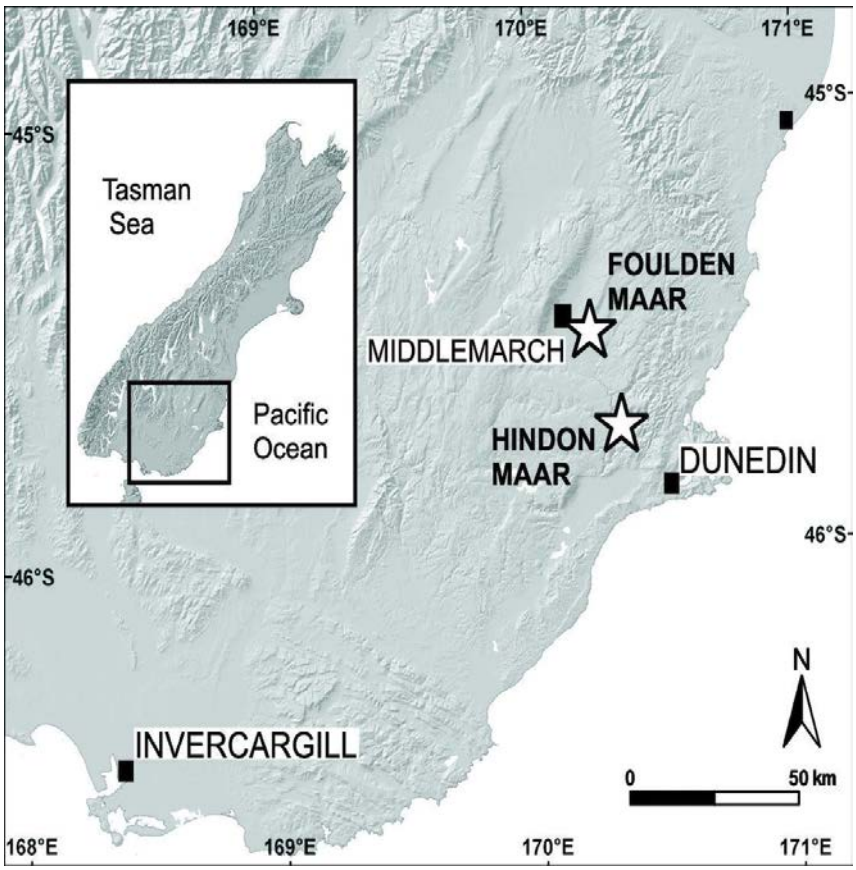

Figure 14: Map showing Foulden Maar in relation to the Hindon Maar Complex and their proximity to Dunedin (Kaulfuss & Moulds, 2015).

2.7 Weathering of pyroclastic material into clays

The weathering of the tephra ring will occur most rapidly in the volcanic glass fraction, followed by mafic minerals (Figure 15) (Churchman & Lowe, 2012; Schiffman et al., 2000; Vacca et al., 2003). The proportion of clay material found within a tephra deposit is related to the time since deposition and the time in which weathering can occur (Lowe, 1986). Studies conducted on intermediate to rhyolitic ash have found the proportion of clays to be approximately 5% of material after 3,000 years (Lorenz, 1986).

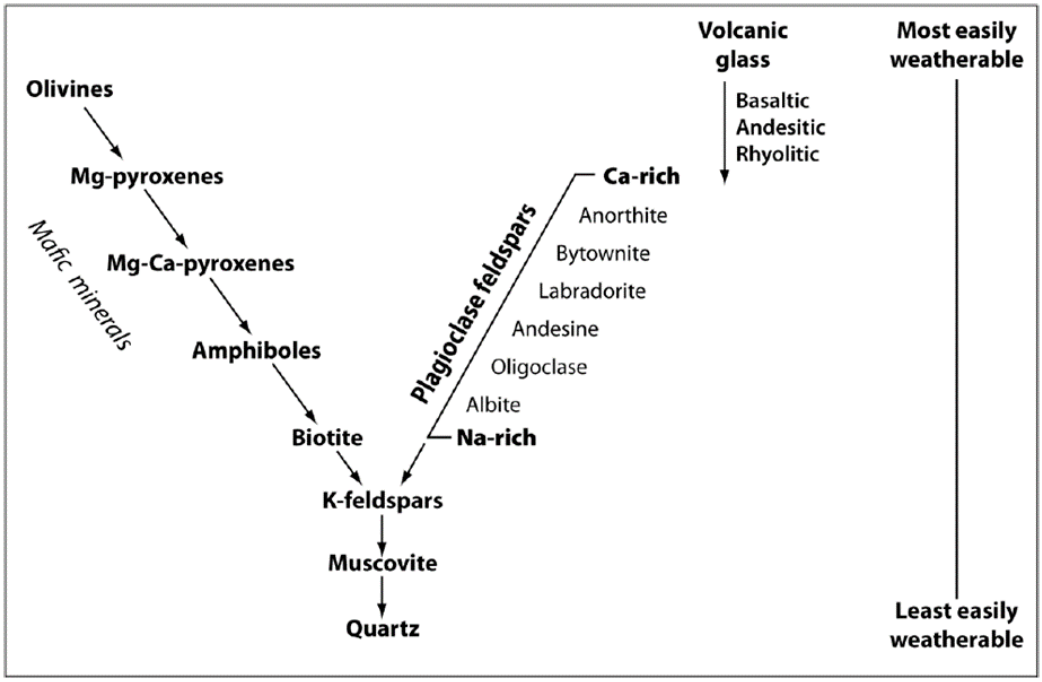

Figure 15: Shows the relative stability of clay-forming minerals found within pyroclastic deposits from most weatherable to least weatherable (Churchman & Lowe, 2012).

Nano-scale minerals such as allophane are a significant component of soils derived from weathered tephra (Churchman & Lowe, 2012). Other clay minerals such as kaolinite, smectite, hematite, and vermiculite are also found, although there is much less focus in research on these clay minerals because nano-scale minerals are responsible for the unique characteristics of tephra derived soils (McDaniel et al., 1999). Olivine, a mineral commonly found in mafic rocks, weathers to smectite from serpentine, although the weathering of olivine can also form kaolinite and halloysite (Churchman & Lowe, 2012; Churchman et al., 2016).

Weathering of tephra predominantly produces allophane and halloysite from the dissolution of aluminium (Al) (Churchman & Lowe, 2012; Filimonova et al., 2016; Lowe, 1986). Both allophane and halloysite have been found in basaltic-derived material (Churchman & Lowe, 2012; Joussein et al., 2005a; Ziegler et al., 2005). Allophane is a short range-order- aluminosilicate nano mineral (Filimonova et al., 2016; Kimsey et al., 2011). Halloysite is a di-octahedral 1:1 clay mineral from the kaolin group (Berthier, 1826; Joussein et al., 2005b). Studies conducted on rhyolitic and andesitic tephra found that halloysite forms in drier moisture conditions than allophane (Churchman et al., 2016). A study on basaltic ash in Hawaii found that moisture regimes must be much drier to form halloysite rather than allophane due to the lower silica content in basaltic ash (Churchman et al., 2016). Furthermore,

halloysite is far more likely to form in rhyolitic tephra than in basaltic tephra due to Si content (Joussein et al., 2005a).

A study conducted in Hawaii on the weathering of basaltic tephra found smectite, kaolinite, allophane and palagonitized glass (Ziegler et al., 2005). Soils analysed from Mount Gambia, which are basaltic, show kaolinite, illite, and smectite, along with stratified kaolinite-smectite and/or illite-smectite. Allophane and limited halloysite were also observed (Schiffman et al., 2000).

2.8 Prior Research Conducted on the Hindon Maars

Thorough research was conducted during the early 90s into diatomaceous sediments in Hindon Maar 1 (Youngson, 1993). But it was not until 2007, when Glass Earth and the Otago Regional Council conducted an aeromagnetic survey of Otago, that the maars were identified as such. This resulted in renewed interest in the area (Youngson, 1993). The Hindon Maar complex was identified by four near circular areas of high magnetic intensity (Figure 4) (Martin et al., 2007). In 2015, an unpublished study conducted into the geophysical characteristics of the Hindon Maar complex used ground-based magnetic, microgravity and seismic surveys in Maar 1 to interpret the size, depth, and extent of sediment infill. The study found that the Hindon Maar complex was 16 km², and concluded that Maar 1 contained 160–190 m of laminated sediments (Bowie, 2015).

The only published paper regarding the Hindon Maar complex concerns the identification of a new genus of primitive cicada (Kaulfuss & Moulds, 2015). Pollen analysis presented in this paper indicated that the maar was formed during the early Miocene, which is consistent with period of volcanism of the Waipiata volcanic field (Kaulfuss & Moulds, 2015). Fossilised plants indicate that the Hindon Maars are somewhat younger than the Foulden Maar. The fossils were dated by comparing them with fossils found elsewhere (Kaulfuss & Moulds, 2015). An unpublished Ar/Ar date has been made of basaltic lava found on top of Maar 3. The date indicates that the boulders are 14.603 ± 0.093 Ma, and the age of Maar 3 must be less then this (Lee, 2016).

Chapter 3

Methods

This chapter outlines the various field and laboratory methods utilized in this thesis. Standard methods were used where applicable. Field methods used were geological drilling and geomorphic mapping. Laboratory methods include Geotek measurements, geological logging, thin sections and X-ray fluorescence. Selected samples were also used in scanning electron microscope analysis, laser based particle size analysis and clay tests.

3.1 Selection of Core Sites

This chapter outlines the methods used to examine sediments of the Hindon Maars nominally numbered 1 and 3, between Maars 3 & 2, along with outcrops of Maar 2, including field and laboratory approaches. Most methods were based on generalised procedures, therefore highly detailed methods are not given here. The methods used are as follows: coring, field logging, geomorphic mapping, geological logging, Geotek MSCL analysis, portable/laboratory X-ray fluorescence, thin sections, laser sizer, X-ray diffraction and clay test. The methods used have aided in the understanding of the sedimentation processes that occurred within the maar following each eruption.

3.2 Field Methods

Prior to fieldwork commencing in July 2016, core sites were determined from information supplied by the University of Otago. This included gravity anomaly and magnetic susceptibility maps for Maars 1-3 and seismic interpretation of a seismic line from Maar 1. Previous trenching by the University of Otago also helped to determine ideal locations for obtaining maximum lake sediment thicknesses. For example, trenching in Maar 1, yielded diatomite; therefore, cores were taken close to the trenching fill area in order to uncover similar sediments. The ideal locations were then reviewed for accessibility upon entering the field. Consideration was given to geomorphology for determining where the maar depocentres were. However, as it is believed that the landscape has changed dramatically since the eruption, this was only a minor consideration. After each core was drilled, the information about subsurface stratigraphy was used in combination with all pre-

existing information to determine the next coring site. Multiple cores were drilled within Maars 1 and 3, and between Maars 2 and 3.

Prior to drilling it was hoped that diatomaceous lake sediments could be obtained to a depth of 30 m for paleoclimate reconstruction. However, it was found that the maars contained much less diatomaceous sediment and more mass flow deposits than was predicted by the seismic interpretation. Furthermore, drilling was terminated before 30 m and reached no deeper than 18.5 m due to increased consolidation/lack of suitable sediments. Therefore, the focus of research shifted to the mass flow deposits.

3.2.1 Core Drilling

Fieldwork was conducted in three separate campaigns: July 2016 (two weeks), November 2016 (three weeks) and August 8, 2017 (one day). The cores obtained during the field campaign of July 2016 yielded lake sediments through percussion coring and have not been used in this thesis. Percussion drilling was found to retrieve cores of lower quality than that of Rotary drilling. Very little of the deposits underlying the lake sediments was retrieved during July 2016. Therefore, as the July samples are of lesser quality and quantity, consisting predominantly of overburden and carbonaceous lake sediments, they were deemed unsuitable for mass flow and non-biogenic lake sediment analysis. The July campaign and associated cores will not be discussed further.

During November 2016, cores were obtained from Maars 1 and 3 through rotary drilling, with two and three cores obtained respectively. Cores were also obtained from the area between Maars 2 and 3. Only drill holes with non-biogenic sediment from the November campaign were used in this thesis. Cores such as M3H2 were not studied in this thesis, as only carbonaceous lake sediments were retrieved. The GPS coordinates for each hole and further information on core retrieval were noted in the field notebook (Chapter 4 Results). Notes were made within the field log about the core recovery. This included a brief description of the deposit along with the depth of the drilling. This was done to account for differences between the length drilled and the amount of core recovered. Geomorphic mapping was conducted on 8 August 2017.

3.2.2 Geomorphological Map

During the November 2016 campaign, cores were obtained using a LST1G+HD Lone Star portable rig adapted to perform rotary drilling, with equipment from

Blick Industrial to utilise a triple-tube wire line system (Figure 16). It was found that rotary drilling had a greater success at retrieving the samples with minimal disturbance of the core and was able to preserve structures within the cores. However, due to difficulties with the material being cored, voids within core were often disturbed and core recovery was not 100%. Core recovery ranged from 25 - 100% throughout the cores.

The drill was fitted with a tungsten drill bit and could drill to a depth of 30 m below ground level in suitable sediment. The drilling apparatus consisted of multiple parts: the portable Lone Star drilling rig, the drilling rod assembly, and the water pump.

Figure 16: Lone Star drilling rig in Maar 1.

The Lone Star drilling rig consisted of a trailer mounted drill rig which was attached to a four-wheel drive vehicle provided by the University of Otago so that the drill rig could be easily transported to the site. The drill rig came equipped with a petrol-powered Kohler 27-Horsepower Engine, auger drive head performing at 150-rpm at 10-gpmi, a 3,000-PSI hydraulic system; and a 20.3 cm diameter auger. The drill rig also came equipped with a fold down mast. Drilling equipment was lowered down the hole and retrieved using a pulley system with the cathead.

The rotary drill equipment consisted of 1.5 m drill rods (outer tube), a 1.5 m drill core barrel (inner tube), 1.5 m split core barrel, tungsten drill bit, sampler drive shoe, rotary head and the core retrieval unit. The outer tube, sampler drive shoe and tungsten drill bit were assembled and placed in position for drilling (outer assembly) (Figure 17). The inner tube with the split core barrel was locked inside the outer tube and lubricated with WD-40. The outer assembly remained inside the hole for the duration of drilling with new drill rods added to the top of the last drill rod when

necessary. Drill rods would protrude out of the ground and were drilled downwards using the rotary drill head until they were approximately 50 cm above the ground. The inner assembly was removed after every drilling sequence - approximately 1.5 m. The inner assembly was retrieved using the core retrieval unit, which was lowered down the hole via the cathead and would lock into place at the top of the inner assembly. The inner assembly was then pulled out of the hole, the core was removed, and the inner assembly was reassembled and placed back down the hole using the same process in reverse. The core was acquired as the outer assembly was drilled down the hole.

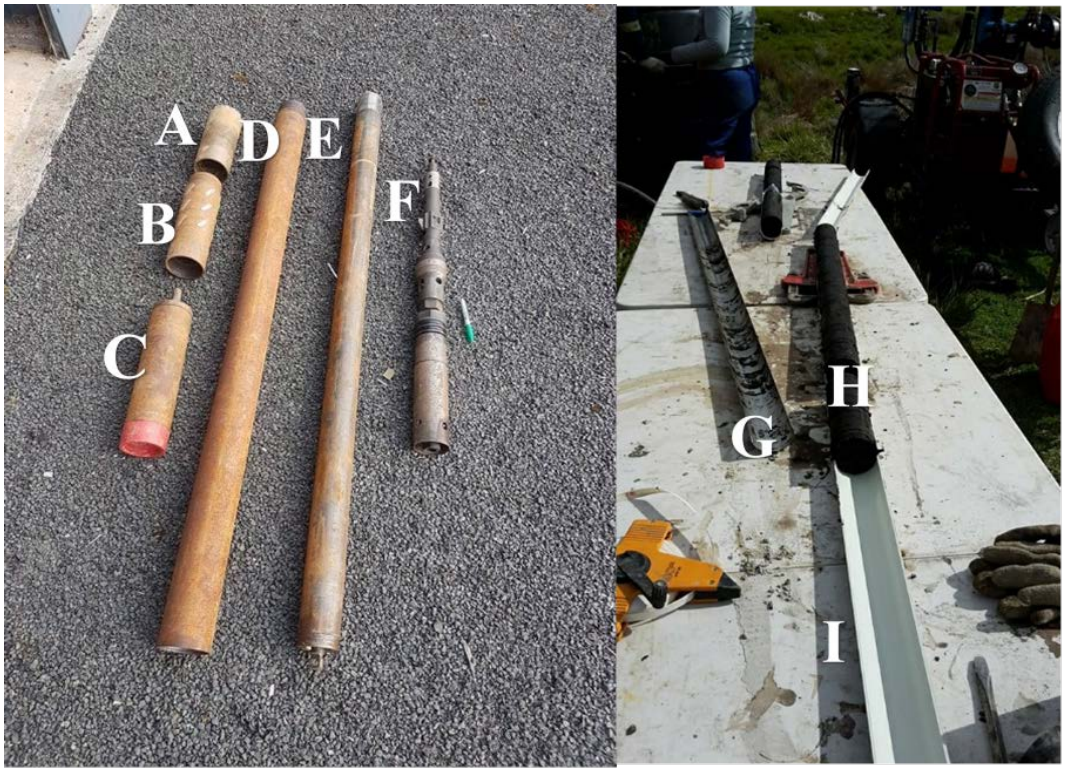

Figure 17: Photo of the core drill assembly and of the core being placed into the PVC pipe. A) drill bit, B), locking coupling, C) outer tube extension piece, D) 1.5 m drill rods (outer tube), E) 1.5 m drill core barrel (inner tube), F) knuckle head, G) split core barrel, H) core, and I) PVC pipe.

As drilling occurred, the drill bit cut around the exterior of the outer assembly and the core was pushed up into the split core barrel inside the inner assembly. The cuttings were comprised of drilled material that entered the cavity between the inner and outer assemblies. A water pump was used to remove cuttings from the whole; water was pumped down the hole to remove material from the drill rods. Using water to remove cuttings from within the hole resulted in better core retrieval. This was because drilling could be done continuously as cutting material did not clog up the drill hole or drill bit. As the drill bit was not being clogged up, the outer

assembly could remain within the hole, increasing efficiency by allowing greater core retrieval within the same timeframe. The water pump was also used to push the split core barrel out of the inner core assembly without damaging the core.

Initially, drillers' mud (Polyplus) mixed with farm water was used during drilling as a lubricant and to help lift the cuttings. Two pits were dug, along with a channel from the drill hole to the pits. The purpose of the first pit was to allow cuttings and sediment to settle out; the second pit was for the Polyplus to accumulate and be re-pumped down the hole (Figure 18). However, the viscosity of the Polyplus increased rapidly over time and would often exceed its recommended maximum of 34 m^2/s. As a result, additional water was constantly added to the Polyplus. It is unknown why the viscosity continuously increased, however, it is hypothesised that during drilling the Polyplus was continuously sheared which resulted in an increase in viscosity. As drilling continued it was found that use of the Polyplus increased the pressure down the hole significantly, resulting in water pooling at the ground surface in a 2 m radius of the hole. Therefore, the Polyplus was not used after M1H1. For M1H2 and subsequent holes, only water was used. Although the farm water had a lower viscosity than the Polyplus, the viscosity did not change nor did it increase the pressure down the hole significantly and it was found to successfully remove cuttings from down the hole. The hardness of the farm water was monitored throughout the process of drilling, and was found to be within acceptable limits. A minimum of three people were required to operate the drill rig. One person operated the penetration and rotation speed via the control valve panel. A second person ensured that the rods were drilling straight down, pulled the inner drill assembly in and out of the hole, and monitored the drilling. The third person assisted the second person in lifting the drill assembly into and out of the hole for each new run. After the mast was fully erected and the drill rig was placed in its location for drilling, the rear and front tracks levelled the rig and removed it from the four-wheel-drive. An auger assembly was used to drill the initial 1-1.5 m through the soil substrate. The outer drill assembly, shoe and drill bit length exceeded that of the drill rig mast, therefore some of the hole had to be predrilled so that the full drill assembly could fit below the rotary head. By pre-drilling some of the hole the likelihood of the drill not drilling straight down was also greatly reduced. The soil substrate was not used in this drilling project and therefore could be discarded. Cores were drilled until sediment hardness exceeded the capability of the drill rig, the depth at which this occurred ranged from 8 to 18.5 m.

Figure 18: Top left: close-up of the pump used in drilling. Top right: close-up of mast and pump fluid tubes. Bottom: pump connected to the drill rig drilling pits dug in M1H1.

Cores were drilled to a maximum of 1.5 m at a time. Once the core was retrieved it was removed from the core barrel using a plug and water pressure. The plug was placed within the core barrel and water was pumped in the top of the barrel, pushing the plug through the barrel and removing the core within the casing. The core was then carefully removed from the casing and placed in split PVC pipes which were a metre long. The core was logged and measured while drilling was occurring. Measuring the core was essential because sometimes the core would sometimes expand, for example 1.5 m of core would be drilled but 1.6 m of core would be

retrieved or the opposite could happen where 1.5 m of core was drilled but only 40 cm of core would be recovered. It is unclear why full core recovery was not achieved. There are two likely scenarios: first that the core fell out of the bottom of the split core barrel; second that the material fully liquidised and was pumped out of the core barrel assembly. Field logging was conducted as quickly as possible to prevent the core from drying out in the sun. This was because material within the core may change and alter its properties as a result of drying out, for example some clays decrease in volume significantly.

Notes were also made on all drilling conditions drilling by the main operator, including the ability of the rig to drill through the sediments, and the amount of water coming back up the drill hole. When the field notes were completed, the core was wrapped in Glad® Wrap two times and placed in a sealed plastic sleeve. Material that was significantly broken up or stuck within the core catcher was placed in plastic bags and labelled with its location within the core. This was because broken material could not be transported within the PVC carrier but needed to be retained at it could still be used to analyse the deposits within the Maar.

Cores were stored at first 4°C at the University of Otago and then at the University of Waikato because storage facility. The cores are stored in a fridge cooled to approximately 4 °C to prevent the cores drying out and increase their longevity (Figure 19).

Figure 19: Waikato University core storage facility

3.3 Laboratory Methods

Standard geomorphic mapping procedures were used to create a geomorphic map of the area. This was done through in-field mapping and with Google Earth to assess

the changes in elevation within the field area. Geomorphic mapping was conducted over a one-day period. Observations were made to illustrate the surrounding topography and landforms in and around the maars. Though active features such as slump scarps were observed and noted, the focus of mapping was to loosely infer the locations of the maars based upon the topographical evidence present. For Maar 1 this was done by observing depressions in the land and drainage patterns. For Maars 2 and 3, although in-field observations were important, elevation more heavily relied on. This was because where Maar 2 appeared in the aeromagnetic survey, the land relief is elevated in relation to its surroundings. In contrast, Maar 3 is located within a slope and does not appear to form a depression like Maar 1. The geomorphic maps were a minor component of this study, therefore 'basic' maps were chosen over analytical, derived or specialised geomorphic maps, as a high degree of investigation and detail was not necessary. Materials required for geomorphological mapping were: 1:16,000 base maps printed out on card, portable inclinometer, cell phone for GPS coordinates, pencils, and a geological notebook.

3.3.1 Geotek Measurements

During January 2017, physical properties of the core were logged using the multi-sensor core logger (Geotek MSCL) at the University of Otago by Noel Bates and Francis Garrity. The Geotek MSCL is a multi-sensor core logger that can complete various forms of down core analysis (Figure 20) (Geotek, 2014). Although the Geotek can perform some kinds of analysis on a whole core with plastic casting, all plastic was removed from the cores, except for the PVC acting as a holder, when analysis was performed to increase accuracy (Geotek, 2014). Prior to using the Geotek, the cores were split longitudinally by Noel Bates and Frances Garrity. Multiple analysis was performed on each of the cores to determine the density, magnetic susceptibility and colour of the core.

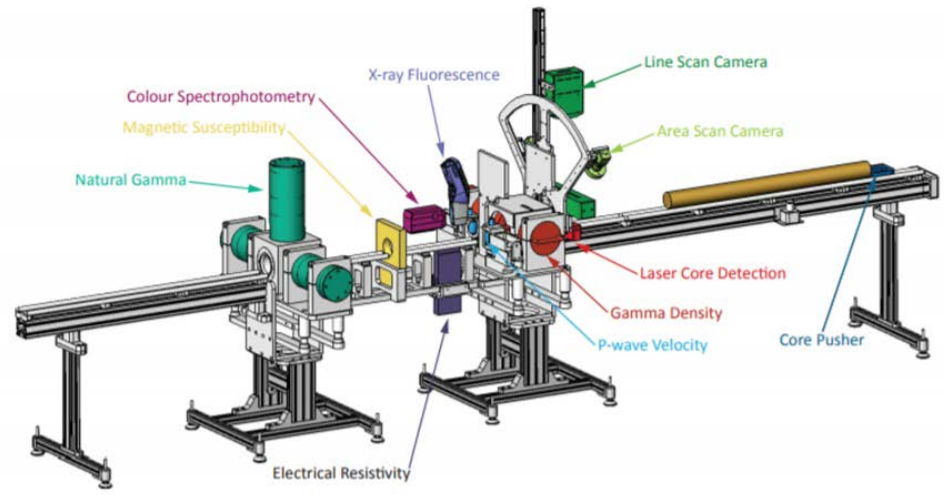

Figure 20: Diagram of the Geotek MSCL with instruments labelled (Geotek, 2014).

The Geotek consists of a core pusher and several sensors which take different measurements as the core is being pushed through the sensor assembly (Geotek, 2014). The Geotek can accurately measure the length of the core and it's position with respect to the sensor, therefore several measurements can be taken at different points of the core with the corresponding core depth recorded at the same time (Geotek, 2014). Not all measurements were used in this thesis due to time constraints. Measurements taken by the Geotek MSCL were; gamma attenuation density (every 5 mm), magnetic susceptibility (every 5 mm), reflectance (L*, a*, b*, X, Y, Z) and colour intensity (RGB) (every 2 mm). High-resolution line scan RGB photos were also taken of all the cores by the Geotek machine.

Notes were made for every core that was run through the Geotek. This was done to ensure that any changes or difficulties met in taking the measurements were accounted for. The notes covered the dates and start/finish times of the core, the Geotek section number, the length of the core measured by the Geotek, the top and bottom depth of the core as measured in the field and any comments of interest. Comments included whether there were sections of missing core, or if there were inconsistencies in Geotek measurement locations. Only material that was intact within the PVC pipes was measured. Samples that were entirely loose gravel or collected in sample bags were not tested.

3.3.1.1 Core Density

Density is the mass of a material within a given volume. This property is particularly important for sediments, as it can help determine the material that they are made from (Zolitschka et al., 2015). It is important to note the distinction between bulk density and gamma alteration density. Bulk density is derived from the mass of the sample divided by the total volume occupied (Abdullah & Geldart, 1999). Bulk density is often used with the study of nonconsolidated samples and is not performed by the Geotek (Geotek, 2014). Gamma density is a local measurement of bulk density (Geotek, 2014). For measuring gamma density with the Geotek the core is placed between a 10 milli-curie caesium-137 gamma-ray source and an electron conductor. Gamma rays are emitted from the caesium, pass through the core and are detected by the electron conductor. By measuring the amount of un-scattered electrons received by the conductor the density is determined (Geotek, 2014).

Core thickness must also be measured to calculate density. The core thickness is measured automatically by the Geotek. Because caesium has half-life of 30.2 years, the rate of gamma ray emission is calibrated at the beginning of every day (Geotek, 2014). The density of the core can be used to infer sediment compaction and mineralogy (Arnaud et al., 2006; McCanta et al., 2015). For example basalt has a greater density than quartz and an increase in density down the core may indicate an incorporation of basaltic minerals (Pirrung et al., 2001).

3.3.1.2 Magnetic Susceptibility

Magnetic susceptibility is a measurement of how magnetized a material becomes in a magnetic field (Mosher, 2007). The Geotek measures magnetic susceptibility by creating a low intensity magnetic field, using an oscillating circuit at a frequency of 0.565 kHz (Dearing, 1994). When material containing significant magnetic particles contacts the magnetic field produced by the sensor, it changes the oscillating cyclic frequency (Dearing, 1994). The oscillations will vary in relation to the proportion of magnetic material in the sensor space (Mosher, 2007). If the magnetic susceptibility is positive, it may indicate the presence of: paramagnetic, ferromagnetic or anti-ferromagnetic materials (Dearing, 1994). Conversely, if the material displays a negative magnetic susceptibility, it may be due to the occurrence of diamagnetic material, as the presence of diamagnetic material will weaken the magnetic field (Dearing, 1994). Changes in magnetic susceptibility down the core

have be used to identify mass flows in maar lake sediments, because material of high magnetic susceptibility and density can be concentrated at the bottom of each individual flow (Pirrung et al., 2008). Furthermore, magnetic susceptibility can be used to determine the makeup of lake sediments. Fe containing minerals have high magnetic susceptibility. In contrast, lake sediments comprising of organic matter have a low to negative magnetic susceptibility (Timperley & Allan, 1974; Rochette, 1987).

The changes in oscillation frequency are converted into magnetic susceptibility measurements by the Geotek software (Geotek, 2014). Because magnetic susceptibility is temperature sensitive, temperature measurements were made in conjunction with magnetic susceptibility so that the magnetic susceptibility measurements could be calibrated against temperature largely to check that drift was not outside acceptable limits (Geotek, 2014).

For the split cores analysis, a Bartington based model point sensor was used. The sensor was encased in a housing and was placed on top of the split core surface. The point sensor gives a high spatial resolution.

3.3.1.3 Spectrophotometer

The spectrophotometer is used to measure the reflectance of core and account for factors which affect colour, giving a true colour reading (Chapman & Shackleton, 1998). An example of a colour affecting factor is the environment in which the object is being viewed. The core colour is measured by the Konica Minolta spectrophotometer CM2600D, which takes measurements from the surface of the core. The reflectance of the core is measured from very near ultraviolet to very near infrared wavelengths using a xenon flash which illuminates the core (Geotek, 2014). The spectrophotometer measures the wavelengths produced and converts them into numerical value as either CIE colour space (L* a* and b*), XYZ or RGB values (Geotek, 2014). For this research project the L* a* and B* were used, as these are the values which closely represent how humans perceive colour. L* represents the lightness of the sample; when L*=0 the sample is black and when L*=100 the sample is white (Chapman & Shackleton, 1998). Positive and negative a* represent red and green respectively, while positive and negative b* represent yellow and blue (Geotek, 2014).

3.3.2 Geological Logging

The core was described as a sedimentary deposit if no clear pyroclasts were visible. Special care was taken to observe grading and sedimentary structures that had been preserved in the core. This was done by core observation and comparing and measuring the size of grains to a grain size scale. Other charts were used, such as compositional charts for estimating the percentage of composition; sorting and grain angularity charts found within the Rite in the Rain all Weather Geological Field Book. Other features of interest were contacts and weathering, which were determined by observation. Logging was conducted per metre of core and each core was logged independently of the others. This was to ensure a high level of detail and accuracy when logging. Though the cores were logged independently of each other, if a deposit continued over multiple cores, a note was made of this. A tape measure was kept beside the core so that every feature could be accurately described in relation to its position in the core. Core logging was conducted outside under natural light and cores were frequently sprayed with distilled water to keep them from drying out. Once logging was completed, the core was re-wrapped in two layers of Glad® Wrap and a plastic sleeve and placed back in the core fridge at the University of Waikato.

3.3.3 Thin Sections

Ideal samples for thin sectioning were identified through observation of the core and through the analysis of the Geotek data. The observation of the core helped identify changes in grain size, contact boundaries, and grading. Geotek data were used to identify anomalies in density and magnetic susceptibility that were not visible to the naked eye, which helped to identify potential thin section sample sites. Samples were also taken from deposits that appeared typical, so that both anomalies and generalised facies could be assessed on a microscopic scale.

3.3.3.1 Sample Preparation

Samples were collected and then air dried below a fume hood to prevent cracking of the sample, and to preserve any structure within the samples (Figure 21). Any remaining water left in the sample could greatly affect the ability of the sample to adhere to the glass slide, and therefore affect the quality of the thin section. To prevent this, the samples were left to dry out for a minimum of 48 hours. Initially, samples dried on a hot plate at 50 °C. However, rapid drying caused large cracks to

form in the samples, which destroyed the visible structures. Slower drying at room temperature limited the cracking of the samples. Samples that were cracked due to rapid drying were discarded and subsequently re-collected. Only samples from the boulder field and Maar 3 did not need resin put on the exterior of the samples. This is because the samples were fully consolidated rocks.

3.3.3.2 Forming Thin Section Blocks

The samples were difficult to make thin sections from because of their physical properties. The samples were weakly consolidated. This was problematic because solid blocks of the sample are required to make thin sections; if the sample is not consolidated then an artificial solid block of the sample must be made. Sample blocks were made one of two ways: either by placing nonconsolidated sample such as a loose sand into a square mould made of tinfoil, and pouring K 36 resin into the mould and allowing it to set; or by taking a semi-consolidated sample, heating it to 60 to 70°C, and applying resin to the exterior of the sample till the resin would no longer be absorbed by the sample.

3.3.3.3 Non-consolidated Samples

Making a block using a tinfoil mould was used only when the sample was fully nonconsolidated, as this technique destroying any structures and fabric in the deposit. Thus, the technique could only provide more information about grain morphology and composition. Once the impregnated sample had being heated at 60°C for a minimum of 12 hours, the bottom of the block was carefully cut off to remove the bottom of the tinfoil and to expose the sample. Following this, the block was heated to 60 to 70°C and resin was applied to the cut surface until it was no longer absorbed by the sample. The sample was then again cured on a hot plate at 60°C for a minimum of 12 hours. At this point the sample was ready to be ground.

3.3.3.4 Semi-consolidated Samples

The samples where resin was only applied to the exterior had a coloured line drawn on them indicating where the top of the sample was in relation to the core. This was done so that observations of features such as grading could be made. Before resin was added, the samples were heated to 60 to 70°C. The resin was applied evenly with a wooden spatula until an even colour was achieved and resin would no longer be absorbed by the sample. When the resin was no longer being absorbed, the

sample would begin to show a glossy finish, indicating too much resin was on the sample and no more would be absorbed. When this occurred, the excess resin was removed from the sample with the wooden spatula. This could take up to five attempts over the course of two days. However, it was preferable to impregnate the samples to saturation over the course of one day. In some cases, once resin had been applied, and had set, the sample was cut so that it would no longer exceed the size of the glass slide. Once the sample was an appropriate size, the sample was then heated to 40 - 60°C and resin was reapplied to the exposed surface until it was no longer absorbed. After resin had been applied to the sample to the point of saturation, the sample was left to cure for a minimum of 12 hours at 60°C on a hot plate. At this point the resin samples were ready to be ground.

3.3.3.5 Grinding and Smoothing Samples

The process of grinding off extra resin and smoothing off the blocks for both kinds of samples until they were perfectly flat, was very difficult. As a result, several samples had to be resined and ground several times until a successful sample was obtained. This was because the resin generally did not permeate through the sample fully, therefore, there was a fine line between too much and too little resin left on the block. Samples were ground down using a diamond disc sander and were finished off using a glass plate with grinding powder. The disc sander was used when samples had an excessive amount of resin on them, as the disc sander could grind down the samples faster. However, the disc sander was not used to finish off the samples because it was very easy to grind off all the resin, or to form grooves in the samples, resulting in the samples needing to be impregnated. Samples were deemed to be ready for block mounting when there was no glossy appearance of resin, it felt smooth to the touch, and when no marks were observable reflected in a film of water applied to the surface of the sample. Samples were then re-wetted with water to decrease the likelihood of anything such as grinding powder or fingerprints being left on the smoothed block surface. The samples were heated to 60°C, ready for block mounting.

Figure 21: 1) Samples drying out in tinfoil containers; 2) Thin sections that have been made, next to the parent sample; 3) Non-consolidated samples thst had been encased in resin

It is important to note that due to the difficulty of the material sampled, which contained features such as holes in the samples, not all the resin could be removed from some samples. Therefore, the samples were ground down to the best possible surface, and the slides were mounted on areas where the block was the best quality. This meant that in some cases the slides did not cover the entirety of the block, or only sections of the block were preserved in the thin section.

3.3.3.6 Frosting of Glass Slides

The Wards® glass slides used for block mounting were ground to the exact same thickness in the process of 'frosting the glass'. This process involved washing off any residue or dust from the slide, then manually grinding down the slide to a uniform thickness by pushing the slide across a grinding disc. This process would remove between 0.03 and 0.05 mm of glass from the surface. The slide was then re-washed and placed on a hot plate, frosted side up at approximately 40 °C to dry.

3.3.3.7 Block Mounting

A mixture of Hillquist® resin and harder at a ratio of 7:3 was used to mount the blocks to the frosted slides. The Hillquist mixture was heated to 60°C and mixed using a wooden spatula in a small plastic container. Once the mixture was heated and thoroughly combined, it was left for approximately one minute on the hot plate. Following this, a line of the Hillquist mixture was placed in the middle the frosted

side of the glass slides. The sample block was then placed on the glass slide and pressure was applied to the glass slide with two fingers, and moved around the sample block to remove any air bubbles. Pressure was then applied until resistance was felt between the glass slide and the block, indicating that the block had begun to adhere to the glass slide. This step was repeated for all samples. Glass mounted samples were then placed on a bench to cool for 12 - 36 hours. A minimum of 12 hours was needed to ensure that the slides and the blocks were stuck to one another. If left for more than 36 hours, then the glass slide could crack due to the weight of the block. Excess resin accumulated on the underside of the glass slide and around the block, which needed to be removed so that the glass slide surface was homogeneous. This was done by carefully scraping off excess resin with a blunt razor blade on the bottom surface and around the glass slide. After this the sample name, number, and, if applicable, line indicating the top of the slide were etched into the corner of the glass using a diamond tipped pen.

3.3.3.8 Grinding Down Thin Sections

The block was cut from the glass slide, leaving a millimetre-thick sample attached to the glass slide. The sample was then ground down to a satisfactory thickness 6 to 4.5 µm (Figure 22). This thickness was determined by the colour of feldspars observed down a polarised microscope. When the sample was the right thickness, feldspars present in the sample would become grey and black under crossed polar (first order birefringence colours). Therefore, during grinding, the slide was periodically checked underneath the microscope.

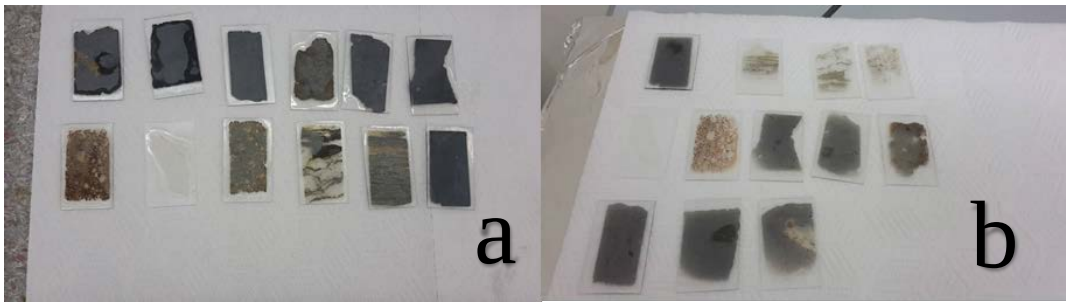

Figure 22: a) thin sections after the sample has been cut off from the glass. b) completed thin sections drying out.

3.3.3.9 Cover Slipping

Normally all thin sections are cover slipped, which involves gluing a thin piece of glass to the top of the slide to protect it from damage. However, this was only done

for samples taken from the outcrop in Maar 2. It was not done for any of the other samples, as it was found that the process would often lift the resin and sample from the slide, ruining the slide. Furthermore, several of the samples were analysed under the scanning electric microscope which could not occur if a coverslip had been applied.

3.3.3.10 Thin Section Analysis

Slides were observed under a microscope using both plane- and cross-polarised light at magnifications from 100x - 400x. Slide mineralogy was determined using standard petrographic procedures. These standard procedures include looking at the birefringence of the minerals and assessing whether pleochroism or twinning had occurred. In addition to this, grains were also analysed for their morphology and notes were made of any observed sedimentary structures. For example, when a quartz grain was identified, its abundance in relation to other minerals, along with its morphology, surface extra, size, and shape were noted. The overall sorting of grains and sedimentary structures such as bedding or grading were also observed.

3.3.4 Scanning Electron Microscope

The Hitachi S-4700 Field Emission Scanning Electron Microscope (SEM) with Quorum Technologies Cryo-system was used predominantly to determine the elemental composition and aid in determining the mineralogy of the thin sections, which were unable to be assessed with a standard petrographic microscope.

SEM can produce highly detailed images at very high magnifications; quantify elemental abundances across the entire sample surface; and qualify elemental abundances at a point(s) selected by the user (Joy, 2006). Back - scatter images can be used to identify differences within the sample not seen through normal SEM imaging, such as differences in density (Joy, 2006).

The SEM performs these analyses by scanning the top of a sample with electrons that interact with the sample (Goldstein et al., 2017). During this interaction, some electrons used in scanning the sample pre-scattered and along with electrons emitted during the interaction reach the detector (Reed, 2005). The number of electrons which reach the detector at a given point is determined by the topography and the atomic weight of said point, which results in the determination of both topography and elemental composition (Joy, 2006).

The choice of slides for SEM analysis was determined by observation of deposits made from both the geological logging and thin sections. Areas of interest were located by engraving the bottom of the thin section slide, and then photographed, followed by analysis of elemental distribution.

3.3.5 X-Ray Fluorescence

X-ray fluorescence (XRF) works by subjecting a sample to short wavelength x-rays and then measuring the secondary x-ray emitted from the sample (von Bohlen, 2009). This x-ray is emitted by the dislodging of electrons from the atom shell because of x-ray bombardment. Subsequently, an electron from a high energy order will replace the lost electron, but by doing so must drop to a lower energy state, which results in the release of x-rays (Kalnicky & Singhvi, 2001). Every atom will emit a unique x-ray, which then can be used to determine the elemental composition of a material (Loubser & Verryn, 2008; von Bohlen, 2009). XRF is a non-destructive method, and ideally samples should be examined using XRF when they are completely dry (Croudace et al., 2006). However, completely drying samples may alter their properties for later testing. Therefore, it was determined that the core would not be dried out as it can cause the core to crack. As a result, the samples were tested when they were water-saturated.

XRF measurements were taken using a The Olympus Delta Professional portable XRF (pXRF) every 5 cm or where visible changes in the core were observed. Such changes could be grain size, contact, or changes in the colour of the core. Where non-visible changes occurred, an XRF measurement was also taken. These non-visible changes were determined by the analysis of the Geotek data. XRF measurements were not performed where the core was not present, or the core was too narrow for the pXRF machine (just larger than the size of a $0.10 coin).

pXRF produces rapid analysis of samples and when tested against laboratory-based XRF machines are found to have good analytical precision (Goodale et al., 2012; Rouillon & Taylor, 2016). However, analytical inaccuracies are found between various models of pXRF and some elements are not as easily identified through this method. This is particularly the case for elements of low atomic number such as silicon, aluminium, magnesium and carbon which the majority of geological samples comprise of (Goodale et al., 2012). Therefore, there is a greater inaccuracy of results from lighter atomic numbers.

pXRF data obtained for M1H1, M1H2 and M3H1, M3H3, M3H5 was obtained using the elemental distributions of Yttrium (Y), Titanium (Ti), Manganese (Mn), Iron (Fe), Zinc (Zn), Rubidium (Rb), Strontium (Sr), Zirconium, Niobium (Nb), Molybdenum (Mo), and Lead (Pb). The samples have not been dried out and measurements were taken directly on the split core surface.

3.3.6 Laser Based Particle Size Analysis

Particle size analysis was used to measure the size distributions of nonconsolidated samples throughout the various maars. Traditionally, grain size has been determined by several methods, such as by the pipette method based on Stokes sedimentation rates (Konert & Vandenberghe, 1997). However, laser diffraction size analysis is now commonly used and is thought to be a far superior technique (Konert & Vandenberghe, 1997). Laser diffraction uses forward scattering of monochromatic coherent light to determine the grain size of particles in a liquid solution (Black et al., 1996).

A small amount of a sample is mixed with water and is then placed into the laser sizer. The laser sizer analysis is then performed and grain size distribution is calculated atomically. This is repeated with different sub-samples for a minimum of three instances per sample, and the average size and grain distribution is calculated.

3.3.7 Clay Test

The clays found within Maar 3 Hole 3 and Maar 3 Hole 5 were identified using XRD analysis on ceramic tiles, based on (Lowe & Nelson, 1983; Whitton & Churchman, 1987; Cunningham, 2012). This is a standard method used by the University of Waikato for identifying clays.

XRD is used for the identification of crystalline material such as clays. When crystalline atoms interact with x-rays they diffract in many specific directions, and the angles and intensities of the diffraction beams are used to determine the molecular and atomic structure of the crystalline substance (Kahle et al., 2002). Clays are made of tetrahedral silica sheets and octahedral aluminium sheets. For example, kaolinite and halloysite are one-to-one clays and made up of one tetrahedral and one octahedral sheet. However, the difference between these clays is the amount of inter-layer water bound between the clay layers. The structure the clay forms will be picked up by XRD analysis and therefore an identification can be made. By heating the clay and then re-measuring XRD, the presence of water

between the layers can be determined, and therefore a distinction between kaolin group minerals and halloysite can be made. This is because the change in size will be picked up by XRD and a comparison between the heated and non-heated sample can be made.

The method used to determine clay minerals involves measuring the sample XRD on five separate occasions after various treatments. Firstly, the clay fraction is removed from the sample by placing the sample in a centrifuge which spins at 800 rpm for three minutes, which results in the clay fraction becoming supersaturated within the water. The water containing clay particles is carefully removed and placed in a 50-ml beaker with 2 ml of magnesium chloride and one drop of hydrogen chloride. The beaker is then topped up with distilled water. Overnight the clay should flocculate and concentrate at the bottom of the beaker. After 12 to 24 hours, the water above the clay is fully removed. The beaker is then refilled with distilled water, approximately 50 ml, and the clay is left to settle overnight. The following day the water above the clay is removed.

The clay is then pipetted onto a ceramic tile to dry under a desiccator for 24 to 72 hours, after which the first round of XRD is performed within two days. Following this, two replicates of the sample are placed in a desiccator with 10 % ethylene glycol for minimum of 36 hours, followed by a further XRD test. Formamide is added to the remaining sample to test for halloysite. Samples tested with formamide are not reused. The ethylene glycol sample is placed in an oven at 110°C for at least an hour; followed by re-measurement of XRD. Samples were then placed in an oven at 550°C for one hour and cooled in a desiccator before undergoing a final round of XRD.

Chapter 4

Results

This chapter covers the results obtained through the methods described in the previous chapter. This comprises of core descriptions and thin sections of the five drill cores; geotek analysis of the density, magnetic susceptibility and CIELAB colours for the five drill cores; pXRF of suitable elements; scanning electron microscope, XRD and grain size analysis of various samples.

4.1 Core Description

Lithologies and sedimentological features are described in detail from visual assessments conducted on whole cores and split cores. Logs are produced for Maar 1, Holes 1 and 2 and Maar 3, Holes 1, 3 and 5. Except for M3H5, the Hindon Maar cores shared facies. However, individual units cannot be correlated across the cores. Comparisons can be made between M1H1, M1H2, M3H1, and M3H3, as these cores have comparable mineralogical characteristics and sedimentary successions.

4.1.1 Vesicular and Non-Vesicular Mottles

In Maar 1, Holes 1 & 2 and Maar 3, Holes 1 & 3, non-consolidated white to cream clasts are found within sections of the core, often surrounded by consolidated material. These deposits are here named ‘mottles’. Mottles range in size from medium sand to medium gravel and vary in shape from sub-rounded to angular, and from spherical to elongated. Larger mottles (fine to medium gravel in size) appear vesicular. The mottles range in concentration from <1% to 35% of the core by volume. The highest concentrations of mottles are found in M3H3, where they are characterised by discrete zones of high concentration, overlain by areas of approximately 2% concentration. Similar zones of high concentration can be observed in other holes, but they are less obvious. The overall shape, size and concentration varies throughout the different cores. It should be noted that the colour and consolidation of the mottles do not vary, allowing for them to be easily identified despite their varying morphologies. The mottles are not preserved well in the thin section. On the rare occasions that the mottles are preserved, they appear similar across thin sections.

4.1.2 M1H1

The lowermost deposit in this core is comprised of moderately consolidated breccia (B1) (Figure 23; Figure 45). The matrix is fine to coarse sand, with fine gravel to fine pebble sized schist and quartz clasts. All grains are angular to sub-angular and the deposit is poorly sorted. The breccia is characterised by unconsolidated vesicular mottles that are whitish-cream in colour. These mottles make up just over 1% of the breccia. Overall, this unit is normally graded.

Above the breccia is a layer of loose schist and quartz clasts (LSQ). The contact between these units was not preserved during coring. The loose schist and quartz range from fine gravel to medium pebbles in size. These grains are angular to sub-angular and are poorly sorted. The recovery of this deposit is poor: 1.5m was drilled but only 40 cm was recovered.

The loose schist and quartz unit is overlain by a second breccia (B2) (Figure 24). The contact between the two deposits is not observed. Unit B2 has a moderately consolidated, fine to coarse sand matrix, with fine to medium gravel clasts consisting of schist and quartz. Non-consolidated vesicular mottles are present, representing around 2% of the deposit.

Overlying Unit B2 is a weakly consolidated sandstone unit (STM) (Figure 25). The contact between these two units is gradational over 5 cm. Unit STM consists predominantly of fine to medium sand, with rare coarse sand layers (3 mm to 10 mm thick) comprising schist and quartz grains, which can be observed towards the top of the deposit. Overall the deposit is moderately sorted, although the bottom of this unit is poorly sorted. Throughout this unit, vesicular mottles can be observed, ranging in abundance from <1% up to 5%. The mottles found in this unit are medium sand to fine gravel in size, elongated, sub-angular to angular and have a rough surface texture. In conjunction with the mottles, fine gravel sized schist and quartz clasts are also present. These clasts are sub-angular to sub-rounded, with moderate sorting.

Overlying Unit STM is a very weakly consolidated sand unit (WCS) (Figure 26). The contact between STM and WCS is gradational over 3 cm. WCS is mostly massive, although discrete lenses of laminations can be observed at 14.15 m and 13.25-13.44 m. The overall grain size for WCS is a fine sand, although discrete zones of medium and fine gravel are observed at 13.94 m and 13.63–13.71 m. Rare vesicular mottles can be observed sporadically throughout this deposit. sharp

contacts or sudden changes in grain size are observed within this unit and shown in the stratigraphic log.

Above Unit WCS is a non-consolidated is silt unit (NCS) (Figure 27). The contact between WCS and NCS is sharp and flat. NCS is well sorted and is predominantly laminated (1 - 3 mm thick). It is important to note that through this deposit there appear to be multiple injections of drillers mud. Drillers mud was identified as horizontal zones of liquidised material which has a plastic feel.

Overlying NCS is a unit of black carbonaceous sediment (BCS) (Figure 28). The contact between the BCS and NCS is not observed. Clear laminations can be observed throughout BCS (0.5 - 5 mm), along with sand injections near the top of the deposit, likely a result of drilling.

Overlying BCS is a non-consolidated sand much like NCS. It appears that this deposit has been semi or fully liquidized. The deposit is a fine, well-sorted silt with no visible structure. It is possible that this section of the core may have been reworked by the drilling.

Figure 23: M1H1 18.29 – 18.44 m; unit B1; mottles circled in red.

Figure 24: M1H1 16.10 – 16.25 m; unit B2; mottles circled in red.

Figure 25: M1H1 14.45 – 14.60 m; unit STM; mottles circled in red.

Figure 26: M1H1 13.81 – 13.96; unit

WCS showing a mottle circled in red.

Figure 27: M1H1 12.6 – 12.75; unit NCS, with mud injections circled in red.

Figure 28: M1H1 10.60 – 10.75 m; unit BCS, showing black carbonaceous sediment with sand injections produced by drilling

4.1.3 M1H2

The lowermost unit in this core is a moderately consolidated breccia unit (B3) (Figure 29; Figure 46). The matrix consists of fine to coarse sand with fine to medium gravel-sized clasts of schist and quartz. Grains are angular to sub-angular and the deposit is very poorly sorted. Non-consolidated vesicular mottles are found throughout B3 with an overall abundance of 2%. The mottles are medium sand to medium gravel in size, have a rough surface texture and are spherical in shape. As in M1H1, fine to medium gravel sized schist and quartz clasts are found in association with the mottles. These clasts are sub-angular to sub-rounded, with a moderate surface texture.

Overlying B3 is a very weakly consolidated sand unit (WCS2) (Figure 30). The contact between B3 and WCS2 is not observed because approximately 1.1 m of core was not recovered between the two deposits. WCS2 is a massive fine sand which is well sorted and sub-angular to sub-rounded. The grains consist of schist and quartz, and the unit is also micaceous, as indicated by the glinting of cleavage planes.

Overlying Unit WCS2 is a non-consolidated silt deposit unit (NCS2) (Figure 31). There is an abrupt contact between WCS2 and the overlying NCS2. NCS2 is comprised of silt to fine gravel sized grains. These grains are angular to sub-rounded, but mostly sub-angular. At 15.0 to 15.4 m, the deposit is a fine to coarse sand. At 14.90 to 14.96 m the grain size increases from a medium gravel to fine pebbles with a medium to coarse sand matrix. At 14.48 m medium pebbles are present. At 14.35 to 14.34 m angular laminations within fine sand are observed. At 14.60 to 14.66 m, the deposit becomes a coarse sand to fine gravel with non-consolidated vesicular mottles present. The top of this deposit, from 13.46 to 13.26 m, has been liquefied and forms a poorly preserved contact between NCS2 and the black carbonaceous material above; therefore, the nature of this contact cannot be commented on.

Figure 29: M1H2 17.60 - 17.75 m; unit B3, mottles shown in red circles.

Figure 30: M1H2 15.5 - 15.30; unit WCS2 shows massive sand with small drillers mud injections indicated by red.

Figure 31: M1H2 13.7 - 13.85 m; unit NCS2, showing sand with gravel zones in red.

4.1.4 M3H1

The lowermost deposit in this core is a weakly consolidated breccia unit (B4) (Figure 32; Figure 47), comprising a medium to coarse sand matrix with medium gravel to coarse gravel and rare fine pebbles present. The clasts are made up of quartz and schist fragments. All grains are angular to sub-rounded and the deposit is poorly sorted and normally graded.

B4 is overlain by a weakly consolidated sandstone unit (WCS3) (Figure 33). The contact between Unit B4 and Unit WCS3 is sharp (1mm). WCS3 is a moderately sorted laminated fine sandstone with discrete beds of fine to coarse sand with normal grading. Coarser beds sometimes contain non-consolidated vesicular mottles which are most clearly seen at 5.31–5.4 m and 5.21–5.28 m. Where mottles occur, they make up <1% of the deposit. The mottles are medium to fine gravel in size, horizontally elongated and have a rough surface texture. Beds containing mottles are also found in conjunction with quartz and schist clasts. The quartz and schist clasts are medium to fine gravel in size, sub-angular to sub-rounded. The occurrences of coarser grained beds are concentrated near the bottom of the deposit. At 3.35–3.76 m the deposit becomes strongly laminated.

Overlying WCS3 is a soil deposit (Figure 34). Unlike previously described units, M3H1 does not have black carbonaceous sediment overlying the siliciclastic sediments. The contact between WCS3 and the soil is a sharp, angular contact with a small gravel lens just above WCS3.

Figure 32: M3H1 6.88 - 7.04 m; unit B4 showing the sand matrix with schist clasts.

Figure 33: M3H1 4.35 - 4.50 m; unit WCS3, showing bed of mottles circled in red.

Figure 34: M3H1 1.7 - 1.85 m; soil deposit.

4.1.5 M3H3

The lowermost deposit of this core is a weakly consolidated breccia unit (B4) (Figure 36; Figure 48). B4 has a fine to medium sand matrix with fine to coarse gravel schist and quartz clasts. Clasts are angular to sub-angular. Overall, this deposit is poorly sorted. Non-consolidated vesicular mottles are present within B5 at an abundance of 3%. From 16.03 – 16.12 m the mottles make up 5% of the core. The core containing Unit B4 is highly fragmented.

Above B5 is a weakly consolidated sandstone unit (WCS4) (Figure 37). The contact between B5 and WCS4 is a sharp dipping angular contact, although one medium-sized pebble can be found just above the contact at 15.95 m. The grain size of Unit WCS4 is fine to medium sand with angular to sub-angular grains and moderate sorting. Non-consolidated vesicular mottles can be found within this deposit at 15.65 – 16.03 m at an abundance of <1%. Between 15.53 and 5.65 m mottles make up 2% of the core.

Overlying WCS4 is a weakly consolidated sandstone dominated by mottles (MS) (Figure 38). The contact between WCS4 and MS is gradational over 5 mm. The

sand fraction of this deposit is fine to medium, although some fine gravel grains are present. The grains are angular to sub-angular and the deposit is poorly sorted in general. Mottles within this unit are medium sand to medium gravel in size, have a rough surface texture, are angular, elongated and occur at varying concentrations (Figure 35).

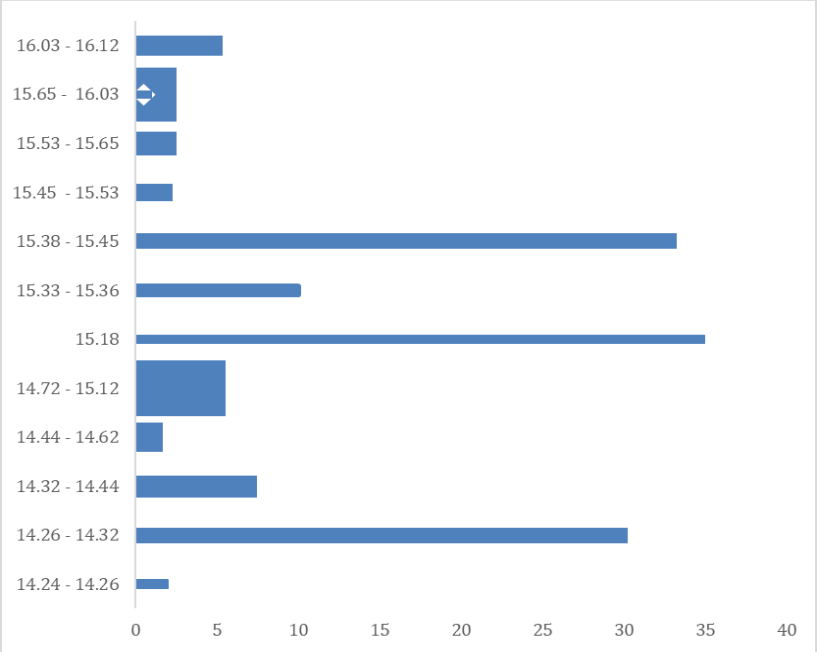

Figure 35: The percentage of mottles in M3H5

Figure 36: M3H3 15.99 - 16 .14 m; unit B5, mottles circled in red.

Figure 37: M3H3 15.7 - 15.85 m; unit WCS4 showing for small mottles in red.

Figure 38: M3H3 14.31 - 14.46 m; unit MS showing high concentration of mottles and mud injections labelled in red.

Above MS is a non-consolidated mud unit (NM) (Figure 39). The contact between Unit MS and Unit NM is abrupt and wavy. NM appears slightly laminated near the bottom of the unit and has a wavy slump structure near the top. The grain size is mud, and NM is well sorted.

Overlying NM is a continuation of Unit MS (Figure 40). The contact between these two deposits is dipping and wavy. The mottle concentration at this contact is approximately 10%, although mottles are smaller in overall size than the lower MS deposit, ranging from medium sand to fine gravel in size.

Above the MS continuation is a weakly consolidated sand unit (WCS5) (Figure 41). The contact between MS and WCS5 is sharp, occurring over 2 mm. WCS5 is a fine laminated sand comprised of mica and quartz grains. At 13.9 – 13.92 m the deposit contains fine to coarse sand. At 13.37 – 13.9 m ripples can be observed. This deposit also has evidence of organics as a small deposit of organic material can be seen incorporated into horizontal laminations. sharp contacts or sudden changes in grain size are observed within this unit and shown in the stratigraphic log.

Overlying WCS5 is a non-consolidated silt (NCS3) (Figure 42). The contact between these two deposits is not observed, as it occurs within the core catcher and therefore is not preserved. NCS3 is white in colour and very strongly laminated. It

is fine sand to mud sized and well sorted. This deposit has an abrupt horizontal contact with the black carbonaceous sediment above.

Figure 39: M3H3 14.05 - 14.20 m; unit NM showing swirly pattern as indicated by arrows.

Figure 40: M3H3 13.85 - 14.0 m; unit WCS5 with laminations overland with red lines and white line indicating bottom contact with MS.

Figure 41: M3H3 13.58 - 13.72 m; unit NCS3 showing transitional zone between black carbonaceous mud and sand base material..

4.1.6 M3H5

The lowermost unit of M3H5 is a non-consolidated, gravelly sand (NCS4) (Figure 42, Figure 49). NCS4 is fine to coarse sand with medium gravel fragments present. The unit is orange in colour and is massive. The grains are sub-angular to sub-rounded, and the overall deposit is poorly sorted.

Overlying NCS4 is a weakly consolidated mudstone unit (WCM) (Figure 43). The contact between WCM and NCS4 is sharp. WCM is highly fragmented and completely pulverised from 7.31 to 7.75 m, forming what appears to be a loose gravel comprised of WCM.

Above WCM is a weakly consolidated purplish mudstone unit (WCM2) (Figure 44). A green film is sometimes observed on the cut surface of this deposit. The green film also coats elongated voids within the deposit. The green film is believed to have formed following the core being split as it was not noticed before splitting. From 5.65–1.3 m, the deposit includes blueish-grey zones, which are more

consolidated and appear as rounded blobs within the core. The core has a green film and hollow voids thought
out it.

Figure 42: M3H5 7.45 – 7.60 m; bottom of the photo shows NCS4 as indicated by the red shape and WCM above.

Figure 43: M3H5 4.90 - 5.05 m; WCM showing minerals found in the deposit circled in red.

Figure 44: M3H5 1.47 - 1.53 m; WCM2, showing greenish film on the cut surface circled in red and voids in blue. Bluish-grey zones are shown in red

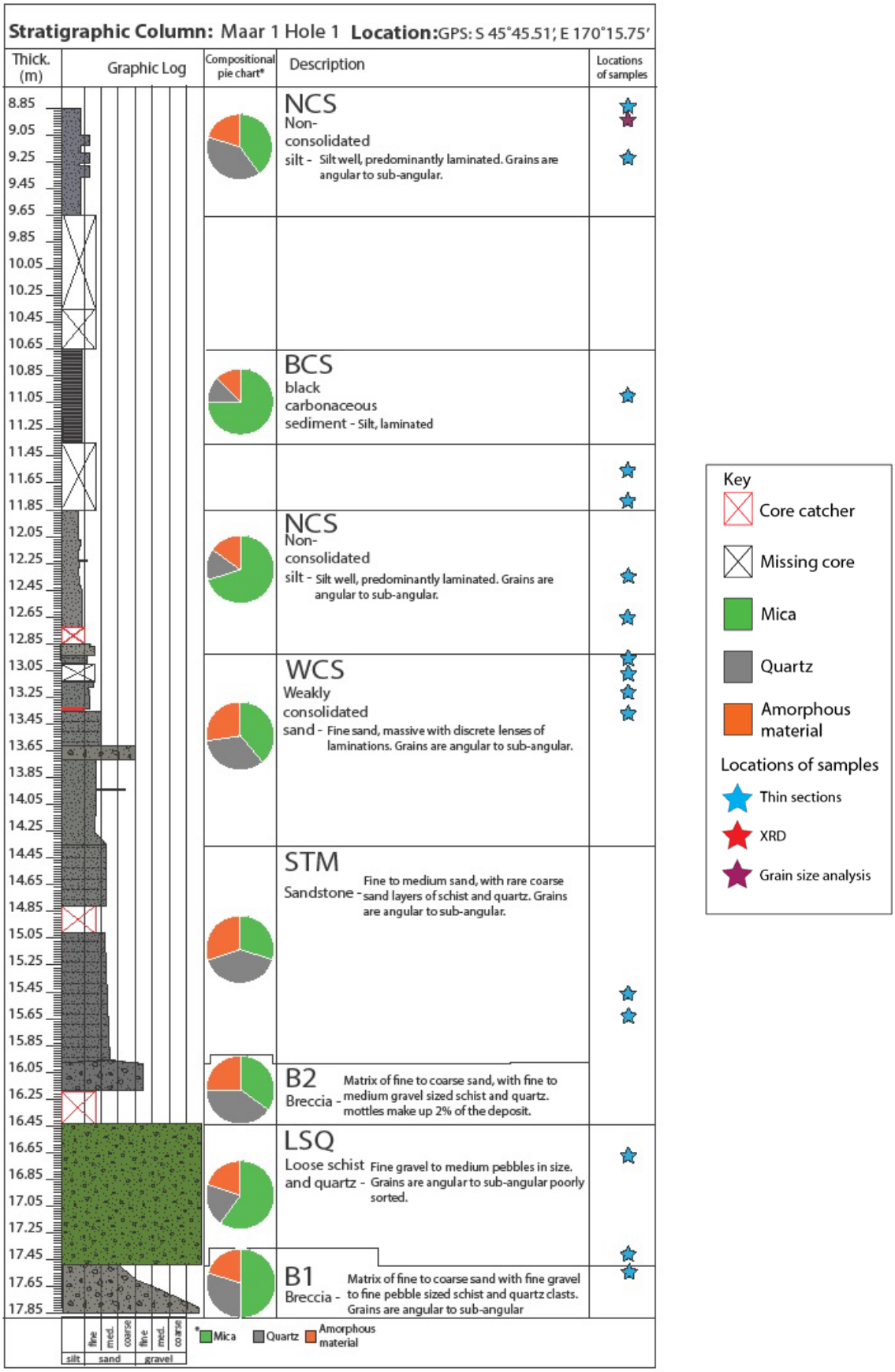

Figure 45: M1H1 showing stratigraphic log of units with brief descriptions, mineralogical composition, and locations for sampling.

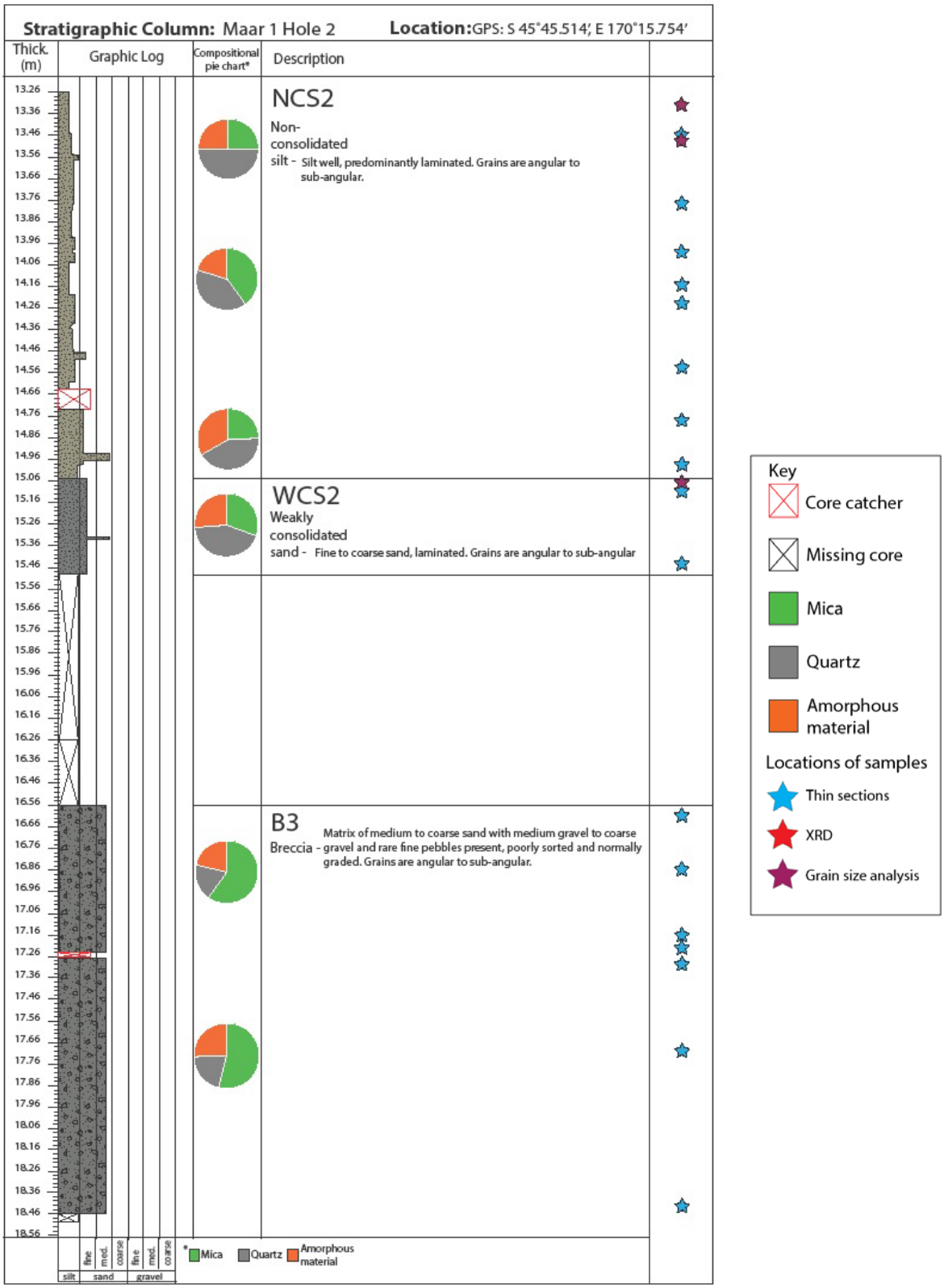

Figure 46: M1H2 showing stratigraphic log of units with brief descriptions, mineralogical composition, and locations for sampling.

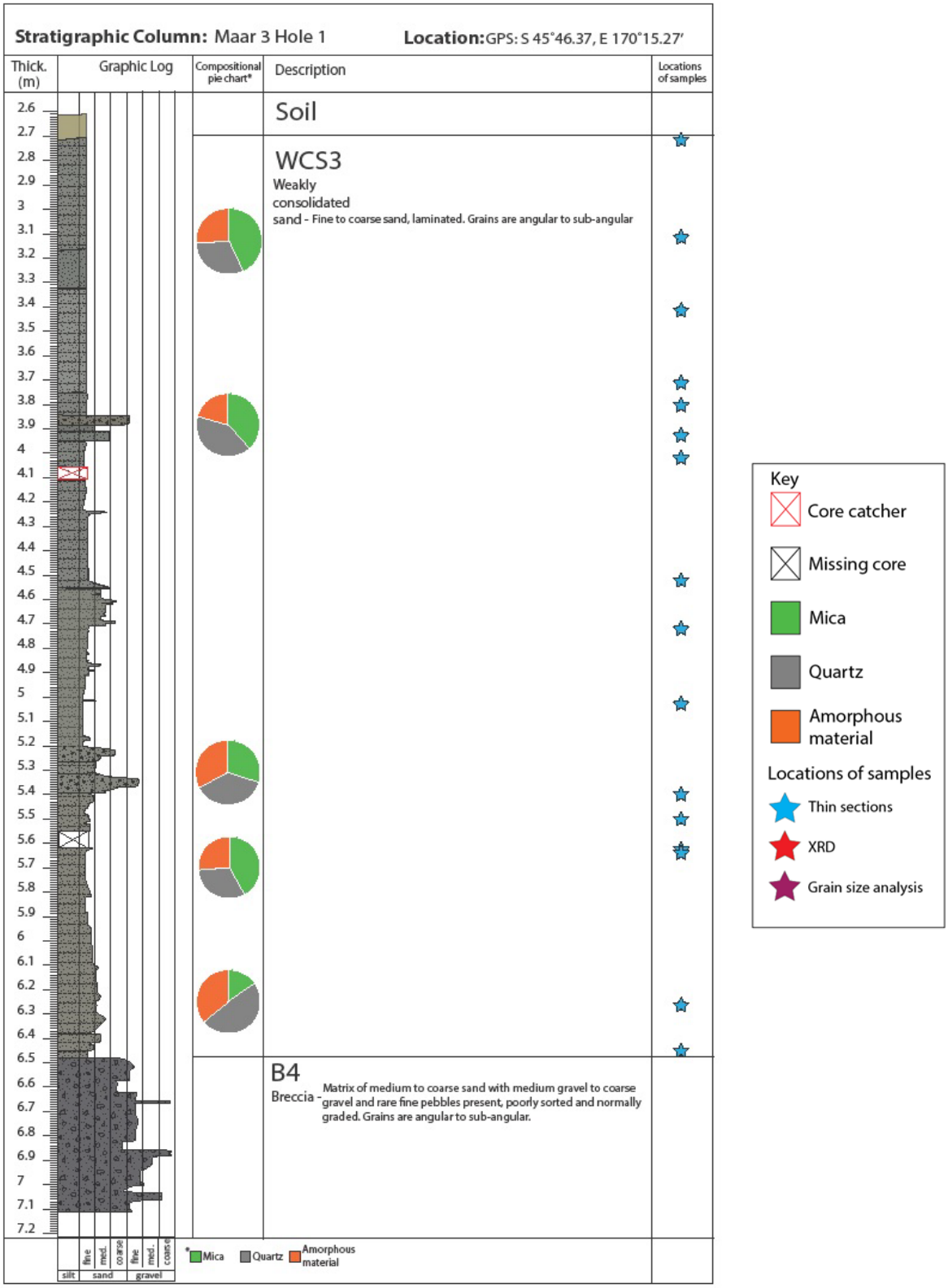

Figure 47: M3H1 showing stratigraphic log of units with brief descriptions, mineralogical composition, and locations for sampling.

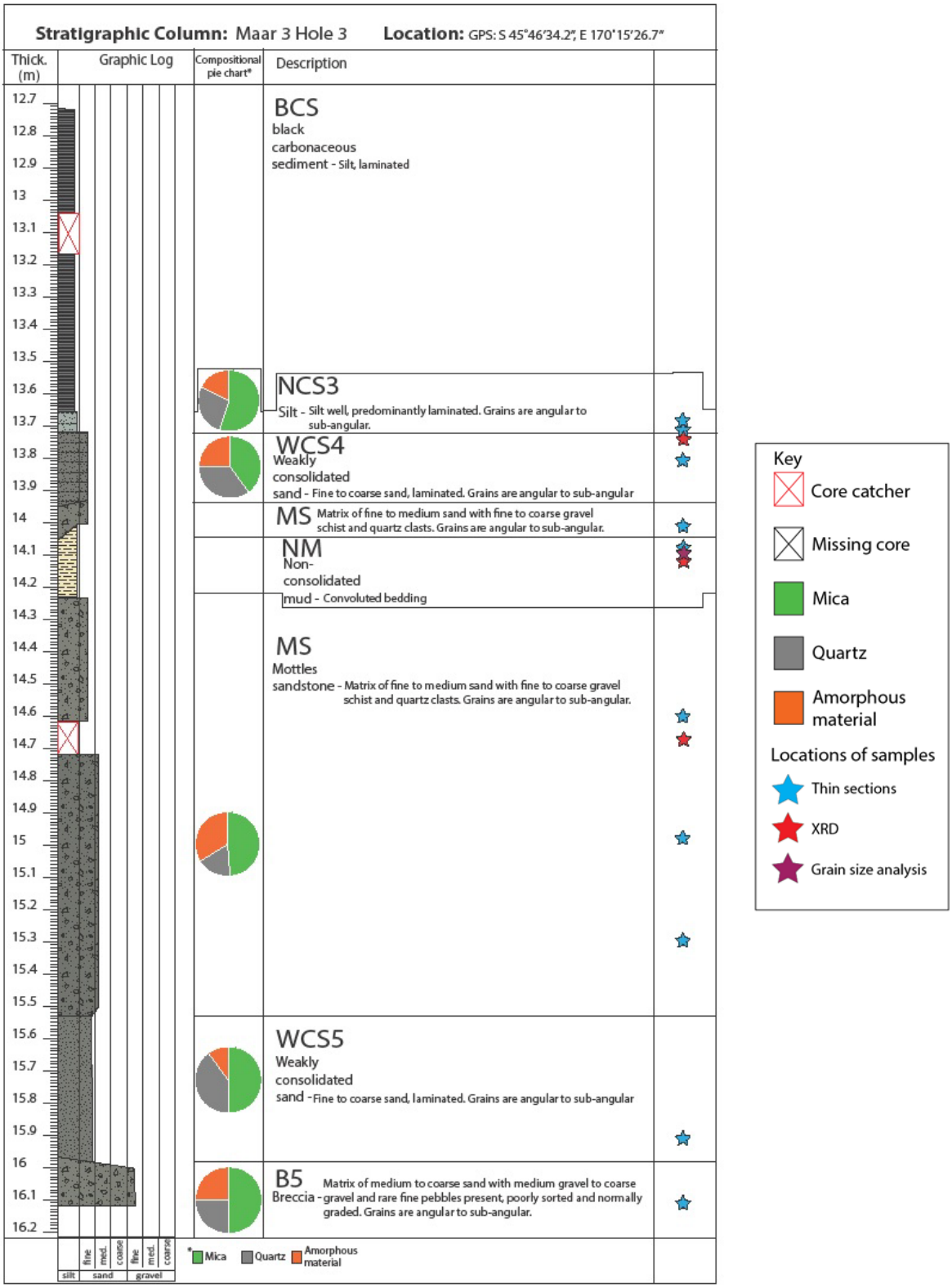

Figure 48: M3H3 showing stratigraphic log of units with brief descriptions, mineralogical composition, and locations for sampling.

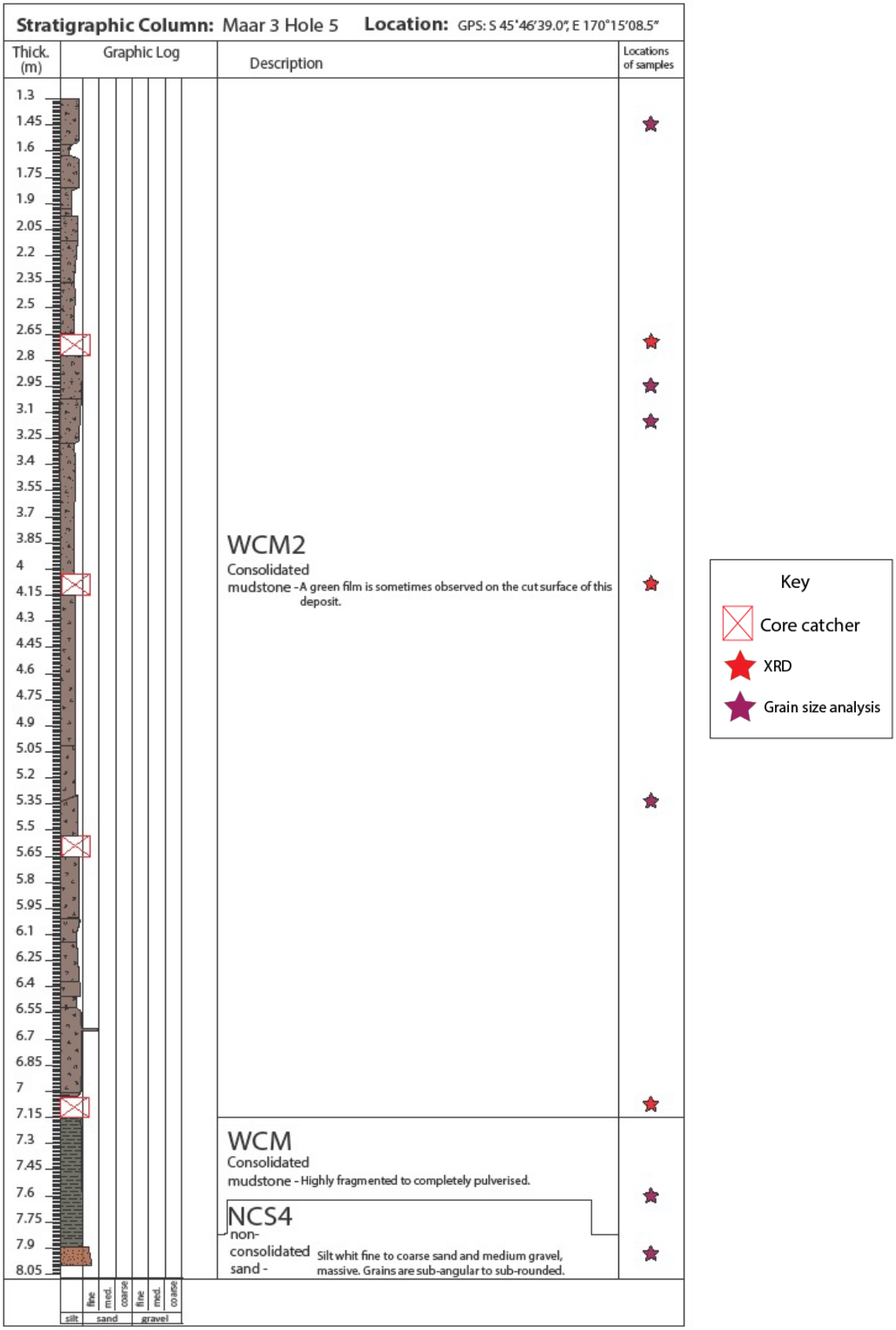

Figure 49: M3H5 showing stratigraphic log of units with brief descriptions, mineralogical composition, and locations for sampling.

4.1.7 Sediment Descriptions of Maar 2 Outcrops

The deposits found in Maar 2 were found in hill slope exposures within the Maar. As no core was obtained for Maar 2, it is likely that many of the deposits within this Maar have not been exposed in hill cuttings. Three dominant facies were observed within the hill cuttings, comprising two fine sand facies and one breccia facies. The results described below are a combination of field observations and sample analysis using optical microscopy.

4.1.8 Location 1

The GPS coordinates of location 1 are; S 45°46’26.9”, E 170°15’46.4” and the elevation is 337 m. Units at Location 1 are crudely interbedded with one another. Large schist boulders >40 cm in diameter are located within the section examined. Location 1 Sample 1 is a poorly consolidated bluish grey bedded sandstone (Unit 1) (Figure 50). Extensive weathering can also be seen throughout Unit 1 as orange staining. Unit 1 comprises fine to coarse sand. It is poorly sorted and angular to sub-rounded.

Underlying Unit 1 is Location 1 Sample 2 (Unit 2) (Figure 51). This unit is a poorly consolidated bluish grey massive sandstone with mottles. Unit 2 is weathered and comprises fine sand to fine gravel grains that are moderately sorted and sub-angular to sub-rounded.

4.1.8.1 Location 2

The GPS coordinates of Location 2 are: S 45°46’26.9”, E 170°15’47.00” and the elevation is 337m. Location 2 is 5-7 m closer to the centre of the maar than Location 1. Two different deposits are located at Location 2, Unit 1 and Unit 3, but a sample was only taken of Unit 3. No sample was taken of Unit 1 as it would have required climbing an unstable slope. At Location 2, Unit 1 is a consolidated bedded sandstone it is the same as Unit 1 identified in Location 1 except for the presence of pebbles and outsized schist boulders 20-40 cm in size found within the unit. Underlying Unit 1 is a nonconsolidated bluish-grey sandstone (Unit 3). Unit 3 is extensively weathered and comprised of fine sand grains that are well sorted and sub-angular to sub-rounded. Unit 3 is also micaceous.

4.1.8.2 Location 3

The GPS coordinates of Location 3 are: S 45°46’26.9”, E 170°15’47.05” and the elevation is 338 m. Location 3 is 5m closer to the centre of the maar than Location 2. The exposure of the outcrop of is approximately 3 m high with Location 3 Sample 3 at the top and Location 3 Sample 1 at the bottom (Figure 52). The exposure of the unit is not continuous. The lowermost deposit found in Location 3 is a poorly consolidated greyish red sandstone (Unit 4). Unit 4 is weathered and consists of fine to medium sand with fine to medium gravel grains that are poorly sorted and angular to rounded. The grains comprise quartz and schist lithics. Above Unit 4 is a large extremely weathered schist boulder encased by Unit 4. Above the schist boulder is Location 3 Sample 3, which is a poorly consolidated laminated sandstone (Unit 5). Unit 5 is weathered and comprises of fine sand grains that are well sorted and angular to sub-angular. The deposit is micaceous. Laminations found within Sample 5 dipped towards the centre of the maar.

4.1.8.3 Location 4

The GPS coordinates for Location 4 are: S 45°46’26.9”, E 170°15’47.05” and the elevation is 339 m. Location 4 was located 8 m further towards the centre of the maar from Location 3.

Location 4 Sample 1 is found at a similar elevation to the deposits at Location 3, although not the same unit. Location 4 Sample 1 is the lowermost deposit found at this location. Location 4 Sample 1 is a consolidated finely bedded sandstone (Unit 4). Unit 4 is weathered and comprises fine sand with minor fine gravel. Unit 4 is well sorted and sub-angular to sub-rounded. Lithics within this deposit are schist and quartz.

The contact between unit 4 and Unit 6 is not observed. Location 4 Sample 2 is a poorly consolidated breccia (Unit 6). Unit 6 is a light yellow-brown which had been moderately weathered; no grading could be observed. The matrix of Unit 6 consists of fine sand, while the coarse-grained component of this unit is fine gravel. Overall, the unit is poorly sorted sub-angular to sub-rounded and gravel comprises of schist and quartz lithics.

The lowermost deposit observed at this location was Location 4 Sample 3. However, the contact was not observed. Location 4 Sample 3 is a consolidated sandstone (Unit 2). Unit 2 is light bluish grey, has bright orange mottles, and is weathered. The grain

size of this deposit is fine sand with pebble to cobble sized schist. Overall, Location 4 Sample 3 is moderately sorted, angular to sub-rounded and micaceous.

4.1.8.4 Location 5

The GPS coordinates for Location 5 are: S 45°46’27.00”, E 170°15’47.05” and the elevation is 340 m. Location 5 is 10 m below the present-day surface of the maar deposit. The outcrop observed was 1.5 m wide and showed extensive iron oxide weathering. Within the deposit, discrete angular schist pebbles were observed. Location 5 Sample 1 is consolidated sandstone (Unit 3). The unit is brownish orange with white and brown mottles, weathered, massive (silt matrix with fine gravel, poorly sorted, sub-angular to sub-rounded), schist and quartz lithics.

4.1.8.5 Location 6

The GPS coordinates for Location 6 are: S 45°46’27.8”, E 170°15’44.0” and the elevation is 336 m. Location 6 Sample 1 shows a transition between fine grey sand of Unit 1 into a bluish grey sand of Unit 2. The transition was observed through the concentration of mottles are found in the outcrop as Unit 2 has mottles and Unit 1 does not. Location 6 Sample 1 is a consolidated sandstone (Unit 1). Unit 1 is orange and bluish grey and moderately weathered. Location 6 Sample 1 is fine sand, well sorted, sub-rounded and micaceous.

Location 6 Samples 2 and 3 were the uppermost deposits at this location. Both samples are poorly consolidated massive sandstones (Unit 2). The deposit was bluish grey with orange and white mottles. These samples were weathered, and the grains are fine sand to fine gravel, moderately sorted, sub-angular to sub-rounded. Lithics found in this deposit are quartz and schist.

4.1.8.6 Location 7

The GPS coordinates for Location 7 are: S 45°46’25.6”, E 170°15’43.9” and the elevation is 331 m. Location 7 Sample 1 is a poorly consolidated massive sand (Unit 2). The deposit is bluish grey with orange to white mottles. Location 7 Sample 1 comprised of fine sand to fine gravel, moderately sorted and is sub-angular to sub-rounded. Lithics in this deposit are quartz and schist.

4.1.8.7 Location 9

The GPS coordinates for Location 9 are: S 45°46’24.9”, E 170°15’44.0” and the elevation is 340 m. The exposure observed at Location 9 consisted of a frittery sandstone (Location 9 Sample 1) surrounded by breccia (Location 9 Sample 2). At this deposit, the first unit contained 5% clasts up to 10 cm. The entire exposure was 5 m wide.

Location 9 Sample 1 is a moderately consolidated massive sandstone (Unit 1). This deposit is light greyish brown and is moderately weathered. Location 9 Sample 1 is comprised of fine sand that is very well sorted and is sub-angular to sub-rounded. The deposit is frittery and has conchoidal fractures. (Figure 55)

Location 9 Sample 2 is a poorly consolidated breccia (Unit 6). The breccia is yellowish orange with zones of bluish grey and light-yellow mottles. No grading was observed in this deposit. Unit 6 comprises a fine sand matrix with coarse sand to medium gravel clasts. The deposit is poorly sorted and sub-angular to sub-rounded. Lithics found within the sample are schist and quartz.

Figure 50: Unit 1, Location 1 Sample 1. This sample is highly weathered.

Figure 51: Unit 1 Location 2 Sample 2. Consolidation was not preserved through acquisition.

Figure 52: Location 3 Sample 1. An example of schist clast found within surrounding unit 4. The schist is entirely weathered.

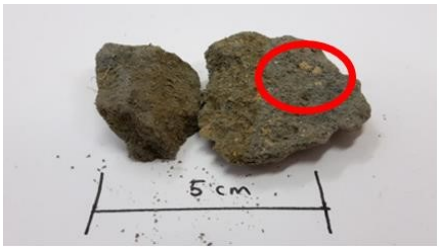

Figure 53: Location 1 Sample 2 Unit 2. Mottles circled in red.

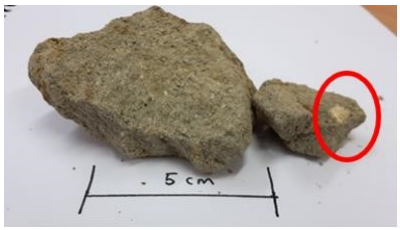

Figure 54: Unit 2 Location 7 Sample 2 showing mottles circled in red.

Figure 55: Unit 1 Location 9 Sample 1.

4.2 Thin Sections

4.2.1 M1H1

Unit B1 is visually identified as a fine gravel in thin section. The matrix of unit B1 is comprised of 50% quartz with an average grain size of silt. The grain size increases down the deposit to medium gravel at 15.95 m. Quartz grains are angular to sub-rounded. Mica comprises 30% of Unit B1, and has grain size varying from silt to medium gravel with grain-size variability increasing with depth. Mica grains are angular to sub-rounded. The overall sorting of this deposit decreases with depth from well sorted to poorly sorted.

Only one slide was made for Unit B2. The matrix of this deposit is identified as a silt, with mica making up the highest proportion of minerals at 40%. Mica grains were fine to coarse sand in size, horizontally elongated, and angular to sub-angular. Quartz grains make up 35% of the sample and are silt-sized. Quartz grains are angular to sub-rounded. Overall this deposit is poorly sorted.

Only one slide was made for Unit STM which is identified as a coarse sand comprising 40% mica grains and 30% quartz grains. Mica grains are fine to coarse sand-sized, angular to sub-angular. Quartz is fine to coarse sand, mostly medium sand. The quartz grains are sub-angular to sub-rounded. Overall this deposit is poorly sorted.

Unit WCS is identified as a fine sand composed of 39% quartz, which is silt to coarse sand-sized, but mostly fine sand sized. The proportion of sand size quartz grains increases down the unit. Quartz grains are sub-angular to sub-rounded. Mica makes up 34% of the unit and grains are silt to medium sand in size. Like the quartz grains, the proportion of sand size increases down the unit. The mica grains are sub-angular. From 12.9 to 13.03 m thin sections indicate that the deposit is well sorted. From 13.27m to the bottom of the deposit the unit is poorly sorted. Thin sections that are poorly sorted consist of

Unit NCS comprises 72% mica, which is silt-sized. The mica grains are sub-angular, horizontally aligned, forming laminations within many of the slides. Quartz makes up 13% of the unit and is also silt-sized. However, the proportion of fine sand increases down the unit 60 - 40%). Quartz grains are predominantly sub-rounded, although the angularity of the grains increases down the deposit. The unit is well sorted.

Unit BCS unit is largely composed of organic matter. Minerals found within this unit comprise 65% mica which is silt-sized and sub-angular. Mica grains are horizontally aligned forming beds 0.3 mm thick. Quartz grains comprise 12% of the sample and are silt-sized. The grain size increases slightly down the unit. Quartz grains are sub-rounded, becoming sub-angular towards the bottom of the unit. This unit is very well sorted.

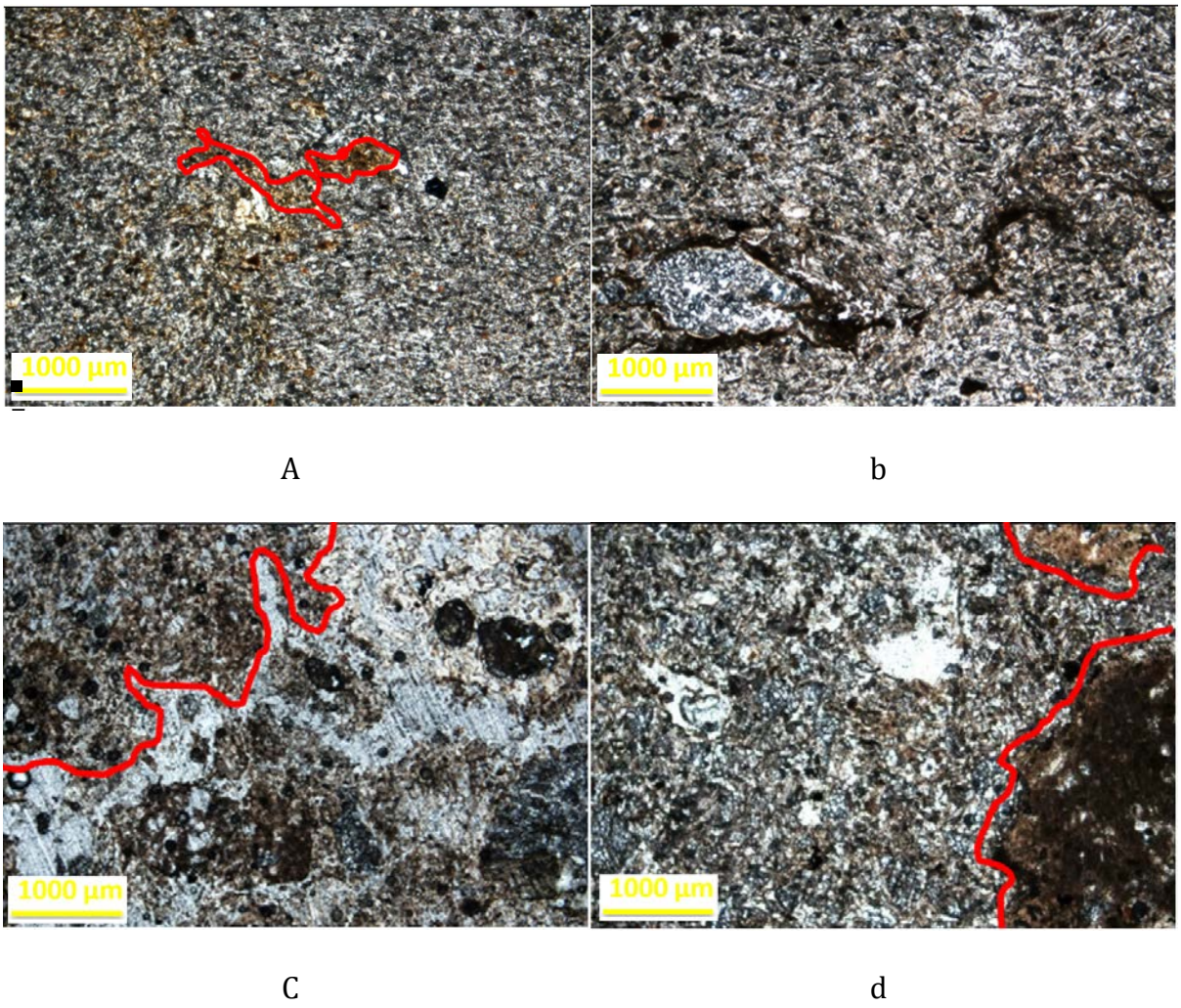

Figure 56: Selection of photos from M1H1 at 40x magnification; unidentified minerals are outlined in red; a) 12.18 m depth, showing mica, silt sized quartz, and unidentified minerals in orange patches; b) 13.34 m depth, showing large quartz grains among a silt sized matrix; c) 13.5 m depth, showing a sample with extensive unidentified minerals, which has led to difficulties with mineral identification in this slide; d) 14.4 m depth, showing poorly sorted sand with large areas of unidentified minerals, indicated in red.

4.2.2 M1H2

Unit B3 is a fine sand comprised of 22% quartz with an average grain size of silt. The quartz grains are predominantly sub-angular to sub-rounded. Mica makes up 59% of the unit and has an average grain size of silt. The mica is sub-angular. The sorting is predominantly poor; however, the unit is well sorted at 17.30 m and moderately sorted at 17.84 m. The thin section produced for Unit B3 comprised solely the matrix of this deposit.

Unit WCS2 is a fine sand comprising 30% quartz with an average grain size of very fine sand. The quartz grains are angular to sub-rounded. Mica makes up 63% of the unit and has an average grain size of silt. The mica is sub-angular. The unit is moderately sorted. Normal grading was observed at 15.10–15.13 m and two modal grain sizes (fine sand and coarse sand) were observed from 15.42–16.89 m.

Unit NCS2 comprises silt to medium sand-sized grains of which 43% is quartz. The quartz has an average grain size of fine sand, although grain size increases down the unit to medium sand. The quartz grains are angular to sub-rounded. Mica makes up 30% of the unit and is predominantly silt-sized grains. Most mica grains are sub-angular. The sorting of the deposit is poor to moderate. Normal grading was observed at 13.47–13.49 m. Alignment of mica grains were observed at 14.19–14.21m.

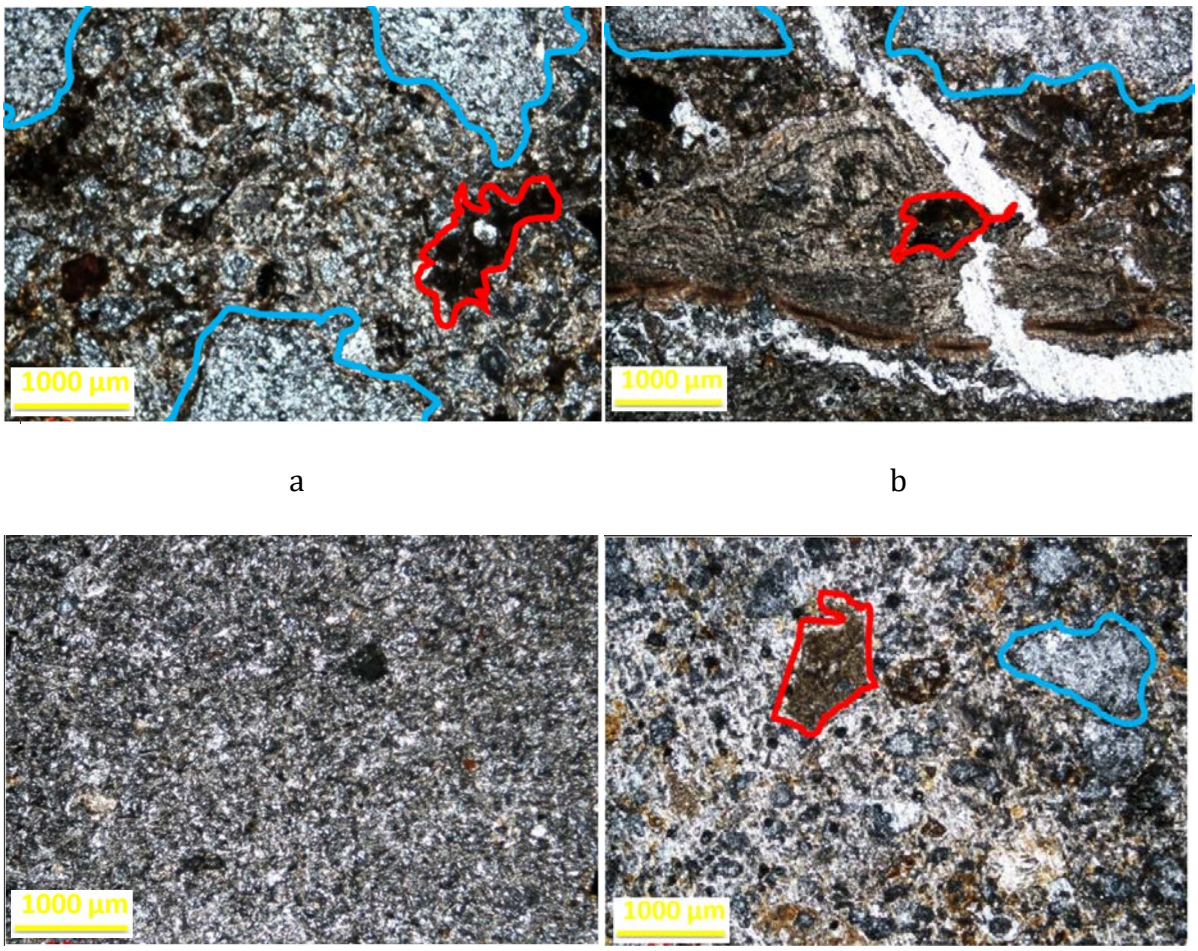

Figure 57: Selection of photos from M1H2 at 40x magnification; examples of quartz are outlined in blue and unidentified minerals are outlined in red; a) 13.43 m depth NCS2, showing large quartz grains and patches of unidentified minerals within a mica matrix; b) 14.65 m depth NCS2, showing a contact between coarse grained material and fine-grained material with some distortion of micaceous beds; c) 16.7 m depth B3, showing fine-grained material; d) 16.90 m depth B3, showing a poorly sorted deposit.

4.2.3 M3H1

Unit B4 the fine sand comprised of 40% quartz with an average grain size of fine sand. The quartz grains are angular to sub-rounded. Mica comprises 31% of the unit and has an average grain size of silt, although grain size increases to fine sand at 6.28 m. The mica grains are sub-angular to sub-rounded, although the grains become rounded at 6.49 m. Overall the unit is poorly sorted, although the interval at 5.63 m is very well sorted. Grain size transitions between silt at the top of the slide into a fine sand and then back into a silt is observed at 5.5 to 5.25 m.

Unit WCS3 is silt to fine sand comprising 38% quartz with an average grain size of silt, although grain size increases down the deposit. The quartz is subangular to sub-

rounded. Mica comprises 34% of the unit and has an average grain size of silt, with grain size increasing down the deposit. Fine sand is identified at 5.06 m. The mica grains are sub-angular to sub-rounded. Sorting is generally good; however, the unit becomes moderately sorted at 4.76 m. From 2.75–3.15 m and again at 3.72–3.75 m alignment of mica grains is observed.

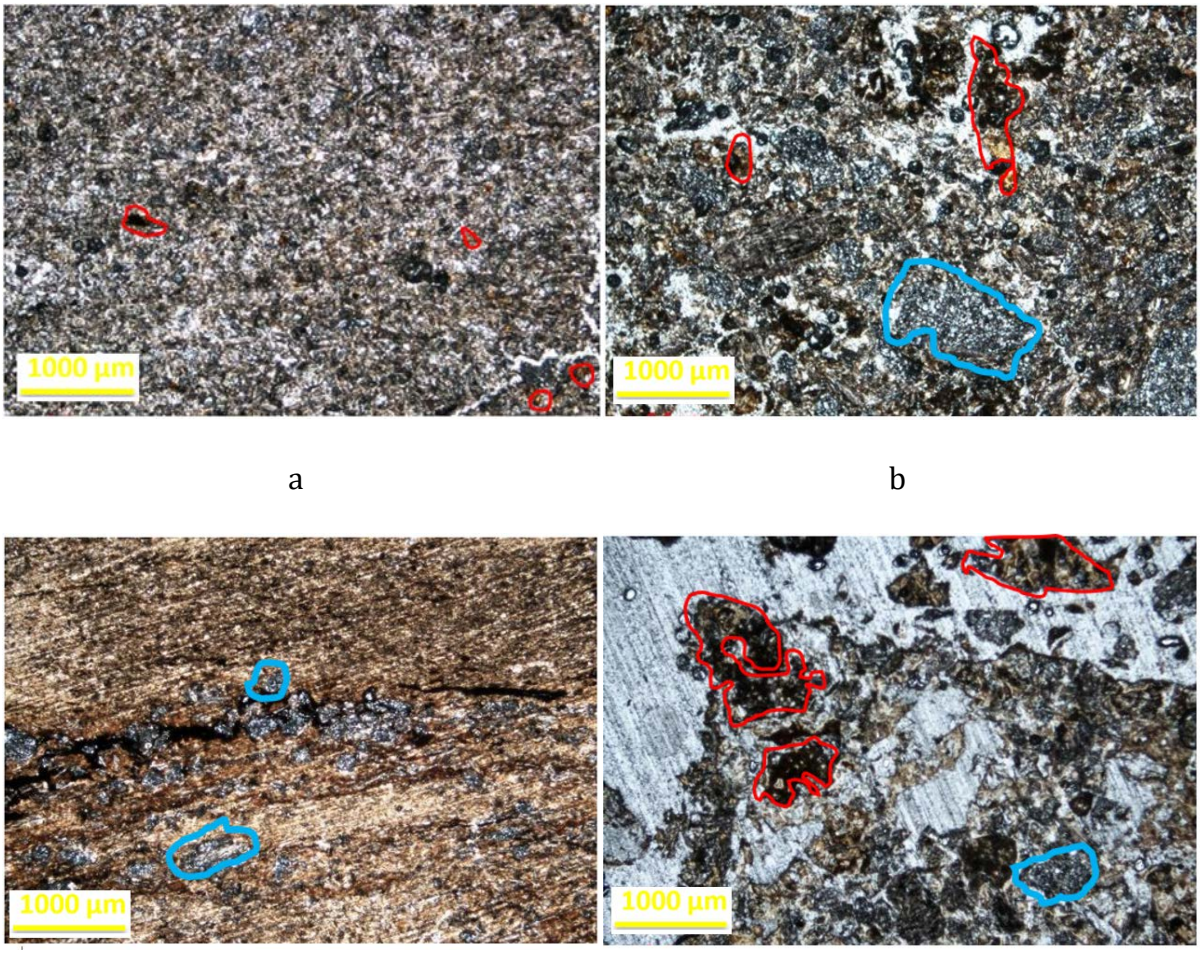

Figure 58: Selection of photos from M3H1 at 40x magnification; examples of quartz are outlined in blue and unidentified minerals are outlined in red; a) 4.15 m depth, showing a well sorted silt sized deposit; b) 5.39 m depth, showing a poorly sorted deposit with a dominance of quartz grains and unidentified minerals; c) 6.44 m depth, showing a deposit dominated by mica with coarser grained quartz beds. d) 7.50 m depth, showing a course grained deposit.

4.2.4 M3H3

The matrix of Unit B4 is a silt, comprising 25% quartz with an average grain size of silt. The quartz grains are angular to sub-angular. Mica makes up 50% of the unit

with an average grain size of silt. The mica grains are sub-angular to sub-rounded. The unit is well sorted.

Only one slide was made for unit WCS4, which comprised 40% quartz and 50% mica. The quartz grains are silt sized and angular to sub-angular. The mica grains are silt sized and sub-angular to sub-rounded.

Unit MS is a silt which comprises 18% quartz. The quartz grains are silt sized and are sub-angular to sub-rounded. Mica makes up 49% of the unit with silt sized grains. The mica grains are sub-angular to sub-rounded. Overall the unit is well sorted.

Only one slide was made for unit WCS5, which comprises 35% quartz and 40% mica. The quartz grains are silt sized and angular to sub-rounded. The mica grains are silt sized and sub-angular to sub-rounded. The unit is very well sorted. Alignment of mica grains is observed from 13.69–13.83 m.

Unit NCS3 is comprised of 28% quartz with an average grain size of silt. The quartz grains are sub-rounded at 13.69 m and become angular to sub-angular at 13.71 m. Mica makes up 55% of the unit with silt sized grains. The mica grains are sub-angular to sub-rounded. Overall the unit is well sorted.

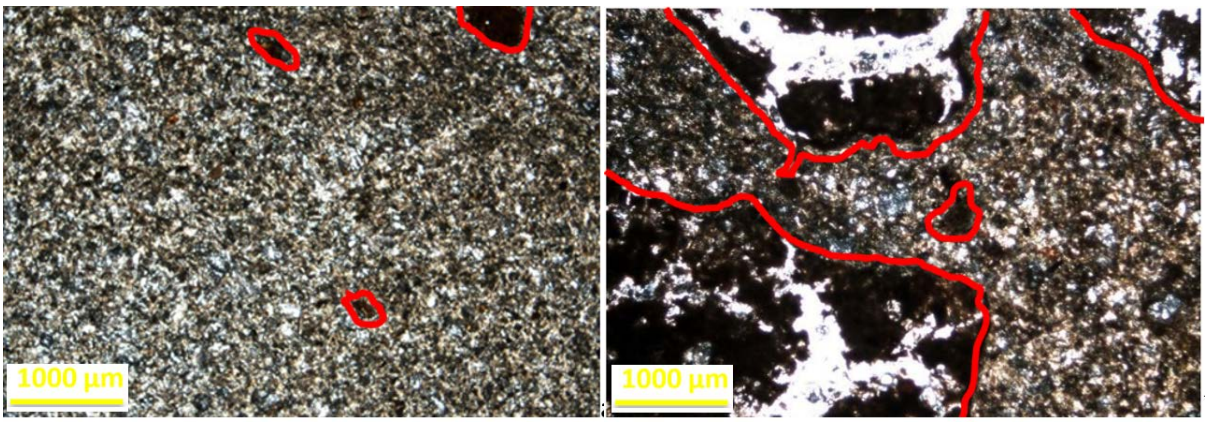

a b

Figure 59: Selection of photos from M3H3 at 40x magnification; examples of quartz are outlined in blue and unidentified minerals are outlined in red. a) 13.98 m depth, showing a silt deposit with small patches of unidentified minerals. b) 15.73 m depth, showing a deposit with extensive unidentified minerals. These patches of unidentified minerals are mottles.

4.2.5 M3H5

The minerals making up the main unit found in M3H5 could not be identified through thin section analysis. This is because the deposit is highly altered and the

material of which the deposit is comprised of is very fine-grained and possibly amorphous. Small black particles (5 to 20 µm) and clear yellow amorphous material (spherical and 0.2 – 0.5 µm) is observed at 400x magnification. From 1.3-4 m vesicles are lined with the yellow amorphous material. When hydrochloric acid is applied to infilled vesicles, no reaction occurs. In some thin sections, clear minerals are observed (under plane polarised light). These minerals are euhedral and triclinic with a low relief. Under PPL, they are reminiscent of feldspar. However, they are altered and an identification cannot be made as a result.

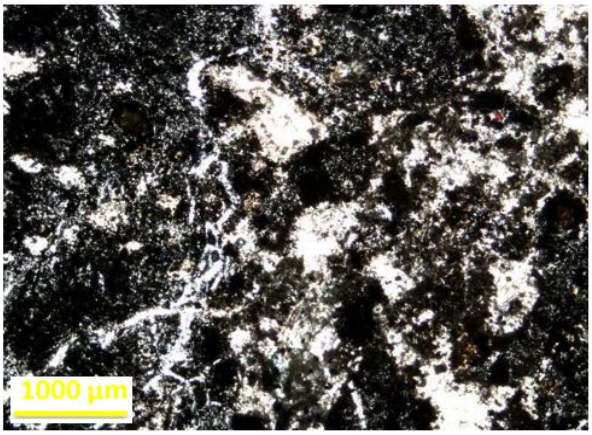

a

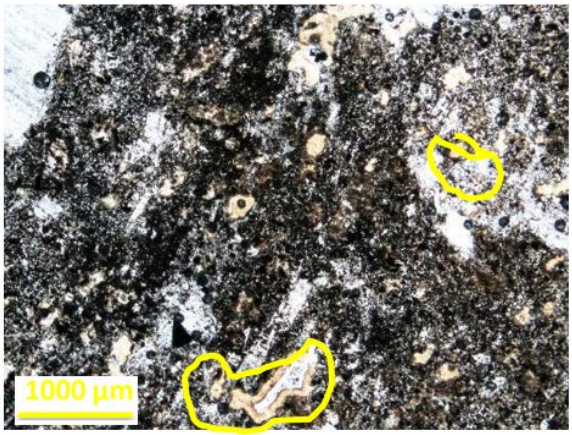

b

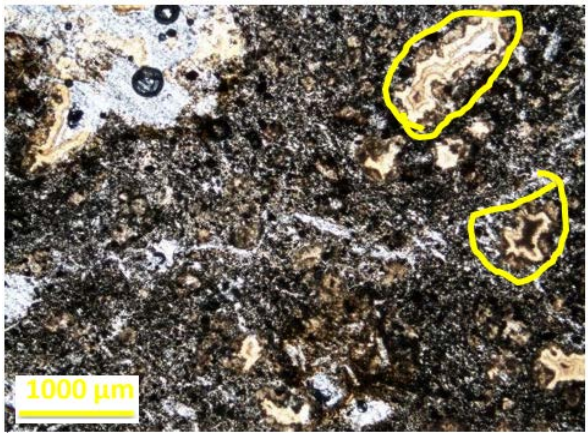

c

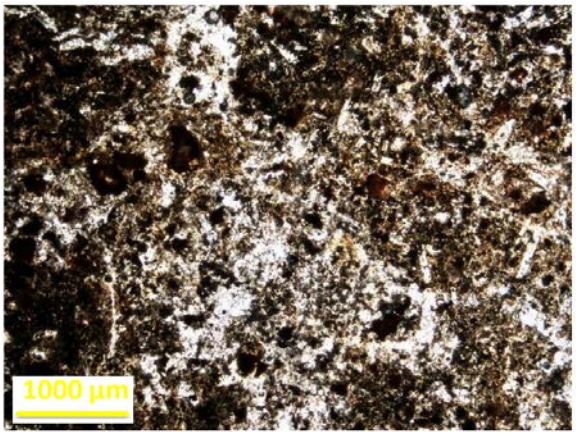

d

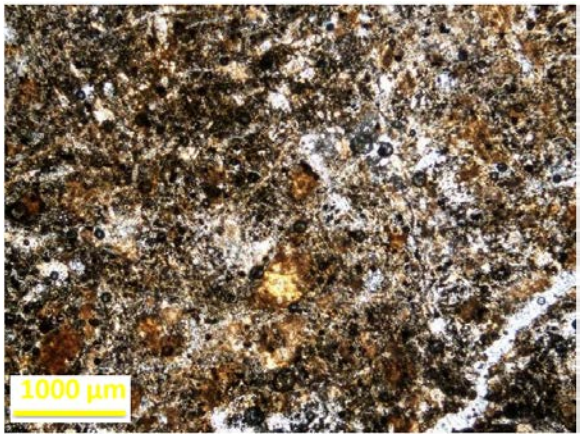

e

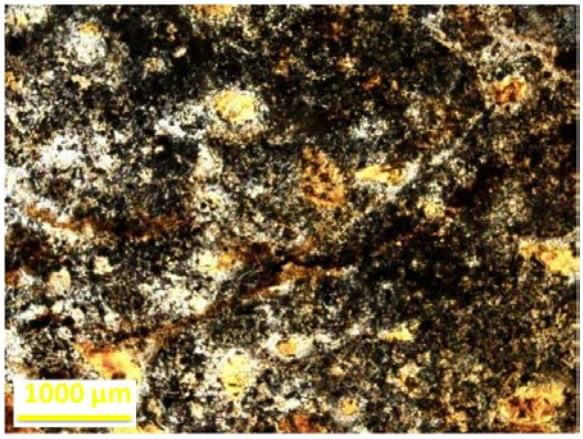

f

Figure 60: Selection of photos from M3H5 PPL; unidentified minerals are outlined in red and infilled vesicles are outlined in yellow. Little to no mineralogy can be observed. Patches of discoloration are easily observed.

4.2.6 Boulder Field

Approximately 70 m east of M3H5 was a field filled with basalt boulders, assumed to be the remains of a lava flow. The boulders ranged in size from 10 cm to 50 cm in diameter. The exteriors of the boulders were weathered and brownish red in colour. The interior of a freshly broken boulder was bluish reddish purple. The boulder in the hand specimen is fine-grained with less than 5% phenocrysts observed. Thin section analysis identified a porphyritic, holocrystalline basalt. Phenocrysts are medium grained and identified as olivine (10%), plagioclase (30%) and pyroxene (5%) (Figure 61). The groundmass of the lava had a similar mineralogy to the phenocrysts, with the addition of opaque material comprising up to 70% of the groundmass. Quartz xenocrysts at 1 cm were also observed in the thin sections with alteration rings around the clast. Infilling of vesicles is spherulitic.

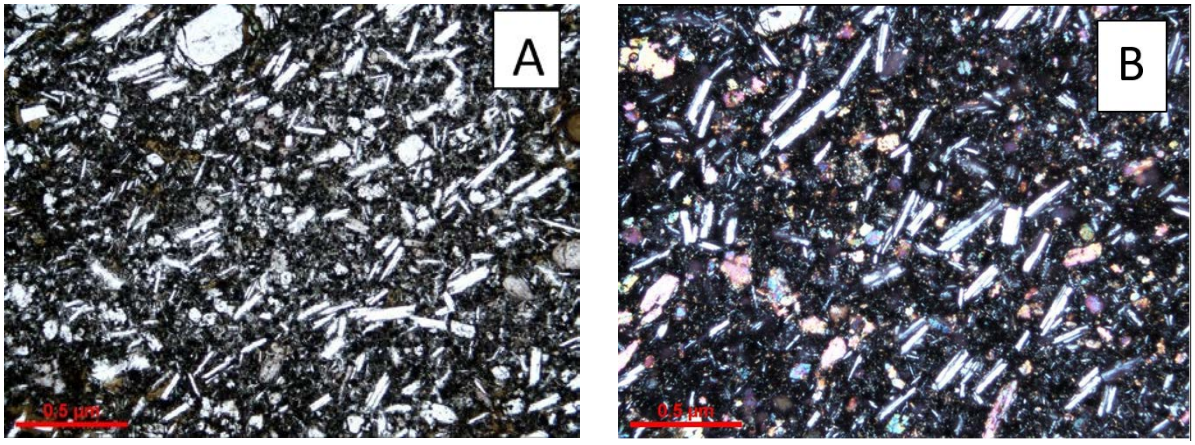

a b

Figure 61: Single view of a thin section of a boulder from the lava field under both plane light (a) and cross polarised light (b).

4.2.7 Maar 2

Unit 1 ranges in size from coarse sand to fine sand and is comprised of 52.5% mica which ranges in size from silt to medium sand. Mica grains found in Unit 1 are angular to sub-rounded and are generally horizontally elongated (Figure 62). On average the sample contains 31% quartz. Quartz grains range in size from silt to fine gravel with most of the quartz grains being fine sand. Quartz grains are sub-angular to sub-rounded and have a moderate surface roughness.

The sample taken from Unit 2 is a fine sand and comprised of 45% mica and 40% quartz. Mica grains range from silt to fine sand, but the majority are silt-sized. Mica grains are sub-angular to sub-rounded and horizontally elongated. Quartz grains

range from silt to fine gravel. Many of the quartz grains are fine sand and angular to sub-rounded.

Only one sample was taken from Unit 3. This is a silt and comprises 35% mica and 30% quartz. Quartz grains range from silt to medium sand, although most of the quartz grains are fine sand-sized. Most of quartz grains are sub-angular but ranged from sub-rounded to angular. Mica grains range from silt to fine sand and consist mostly of silt-size particles. Mica grains are sub-angular to sub-rounded and horizontally elongated.

Unit 4 consists of silt to fine sand particles comprising 40% mica and 35% quartz. Quartz grains range from silt to fine sand with most of the grains fine sand-sized. The morphology of the quartz grains is angular to sub-rounded. Mica grains range in size from silt to fine sand and mostly comprise fine sand particles. Mica grains are rounded to sub-rounded.

Unit 5 is a silt-sized sample which comprises 65% mica and 30% quartz. Quartz grains are fine sand-sized, angular to sub-rounded. Mica grains are silt-sized and sub-angular to sub-rounded.

Unit 6 consists of medium sand comprised of 50% quartz and 35% mica. Quartz grains range in size from silt to fine gravel with the majority of quartz grains medium sand-sized. While quartz morphology ranges from rounded to angular, most grains are sub-angular. Mica grains range from silt to coarse sand with most grains fine sand-sized. Mica grains are rounded to angular with sub-rounded grains predominant.

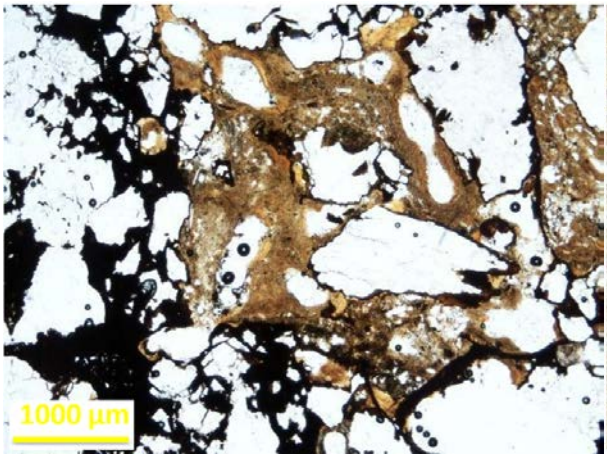

a

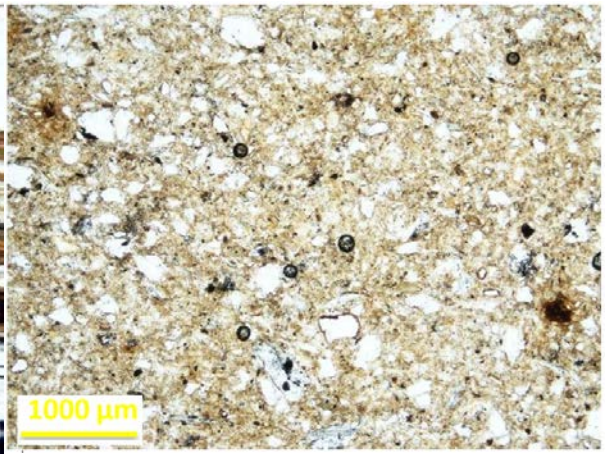

b

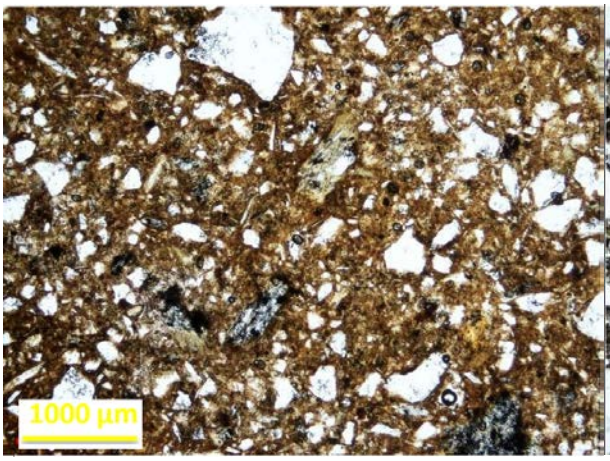

c

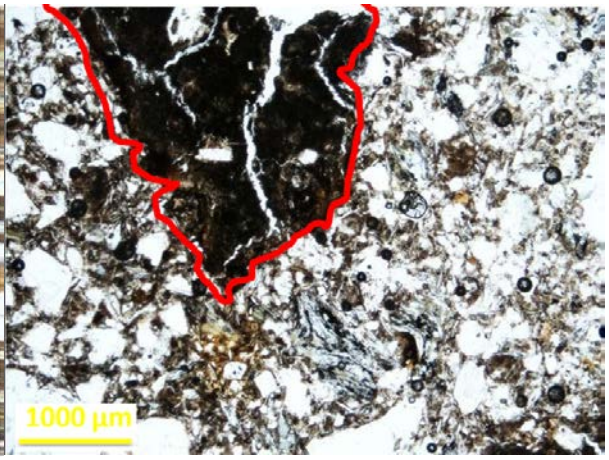

d

Figure 62: Selection of photos from Maar 2 mottles are outlined in red; a) breccia with a high proportion of quartz and unidentified minerals. b) sand deposit with unidentified minerals acting as a cement; c) has two modal grain sizes: distinct silt sized grains and sand sized quartz grains. This deposit is held together by orange unidentified minerals. d) showing a large area of unidentified minerals, which are mottles, like those found in other maars.

4.3 Geotek Results

The following graphs (Figure 63 to Figure 72) show the processed Geotek data for Maar 1 Holes 1 & 2 and Maar 3 Holes 1, 3, & 5. The data shown are from the split cores and include magnetic susceptibility, gamma attenuation, density, and reflectance (Chapter 3 Methods). Where the core is highly fragmented or missing, such as at the end of the core, the data are assumed to be inaccurate and have been removed.

4.3.1 M1H1

Changes in stratigraphic units are clearly seen in L*, a* and b* (Figure 64). The density determined by the Geotek varies throughout the hole (Figure 63). Data are removed from the graph when they show a negative density or a density higher than 10. The unaltered data can be found in Appendix-Geotek data.

The density of Unit B2 is significantly higher than other deposits and is assumed to be incorrect. The magnetic susceptibility is low and shows little variation. L*, a* and b* are extremely variable. However, L* and b* decrease slightly down the unit.

No Geotek analysis was undertaken on Unit LSQ. This is because the deposits are loose gravel and could not be placed in the Geotek. All physical properties increase in value down the unit.

Much of the data for Unit STM has been removed due to poor quality of the core. The top half of this deposit shows a density similar to that of Unit WCS, although there is increased variability. The very high absolute density at the bottom of Unit STM is believed to be a processing error. However, the pattern indicates a decrease in density over the lowermost extent of the unit. The magnetic susceptibility for STM is varied and, due to the removal of much of the data, no clear patterns can be determined. The bottom of Unit STM has a low magnetic susceptibility which is similar to the underlying Unit B2. L* a* and b* show significant variation. L* decreases from 15.5 m to approximately 15.75 m at which point the variance increases slightly. a* shows redness decreasing slightly until 15.75 m and then increasing to the bottom of the deposit. b* increases slightly towards the bottom of the deposit.

Unit WCS shows similar density to NCS; however, there is little overall variation in density and magnetic susceptibility within this deposit. The lack of variation in density and magnetic susceptibility is unique to this unit. The overall lightness of Unit WCS decreases slightly to 14 m or approximately the middle of the deposit. The a* values indicate that Unit WCS increases slightly in redness down the core; however, b* does not change. Compared to other units WCS has less variation.

Unit BCS had both low density and low magnetic susceptibility compared to other units from M1H1. The overall lightness in Unit BCS decreases over the unit (L*). BCS is significantly redder than other units in M1H1 (a*). Unit BCS is slightly bluer than other units, and this value decreases in variability down the core (b*).

The density of both NCS units shows some variation although overall the density of both units are similar to one another. The magnetic susceptibility shows

significant variation within the unit. This is particularly the case for the top NCS deposit. The CiELAB lightness (L*) of both unit NCS increases towards the middle (Fig 40). The overall red/green (a*) of the unit decreases (becomes less red) in the middle and then increases (becomes more red) towards the end of the unit NCS. Unit NCS varies in yellow/blue (b*) although there is no significant change of pattern down the unit. For the lower NCS unit, L*, a*and b* show little overall change throughout the unit although there is significant variance.

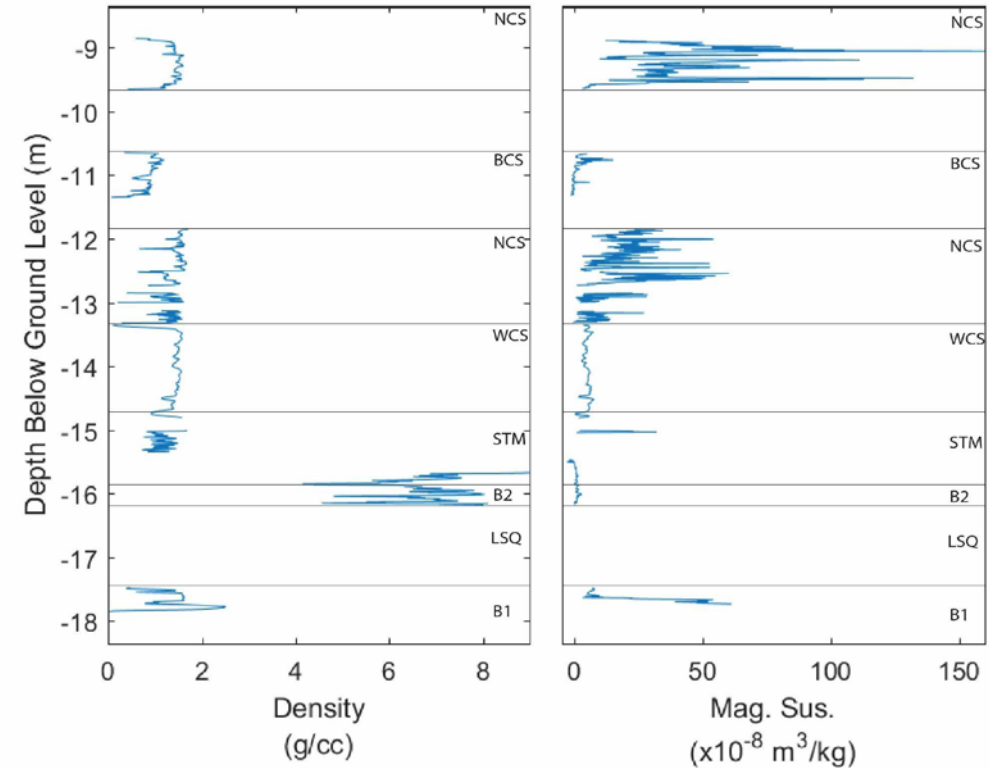

Figure 63: Geotek data for M1H1 showing density and magnetic susceptibility. Units within the core are labelled to the right of each graph

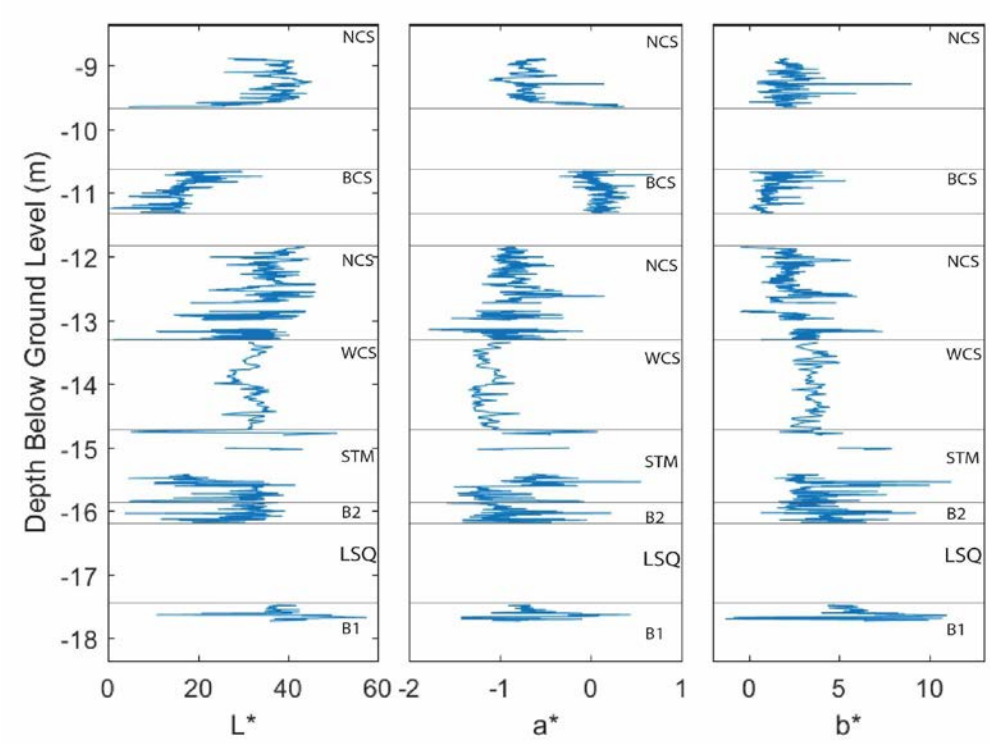

Figure 64: CIE values L*, a* and b* for M1H1. Lithological units are identified on the right of each the graphs

4.3.2 M1H2

Stratigraphic units are not easily identified within changes in the Geotek measurement. However, there are significant gaps in the data. Geotek measurements for M1H2 are shown in Figure 65 and Figure 66. From the top of Unit B3 to 17.25 m the density increases slightly. At 15.3 m the density increases significantly; thereafter, it decreases in both absolute values and variance to the base of the unit. The magnetic susceptibility from the top of B3 to 17.25 m is variable. At 17.3 m the magnetic susceptibility decreases significantly and then increases throughout the entirety of the rest of the unit. L* of the B3 unit decreases to 17.4 m at which point it increases slightly to 17.6 m and increases in variability for the remainder of the unit. a* increases over the entirety of the unit. b* increases to 17 m and then decreases until 17.35 m and then increases for the remainder of the unit.

Unit WCS2 has little overall variation in density, but at 15.1 m the density sharply decreases. The magnetic susceptibility of WCS2 is very variable and increases throughout the entirety of the unit. L* of WCS2 decreases to 15.1 m then remains relatively stable. At 15.15 m the overall a* of WCS increases slightly. b* variability decreases at 15.1 m.

Unit NCS2 shows a slight increase in density to 14.65 m, after which there is a section of missing core; density then increases significantly followed by a decrease to the bottom of the unit. The magnetic susceptibility of NCS2 is variable and does not show any overall pattern for the entire deposit. However, to approximately 14 m the magnetic susceptibility is stable, after which it increases to approximately 14.4 m and then decreases to the bottom of the unit. The overall brightness and red/green hue of the deposit as indicated by L*and a* respectively does not change significantly throughout the deposit. Variability increases at the bottom. b* shows a slight decrease until 14.5 m, at which point the b* value increases.

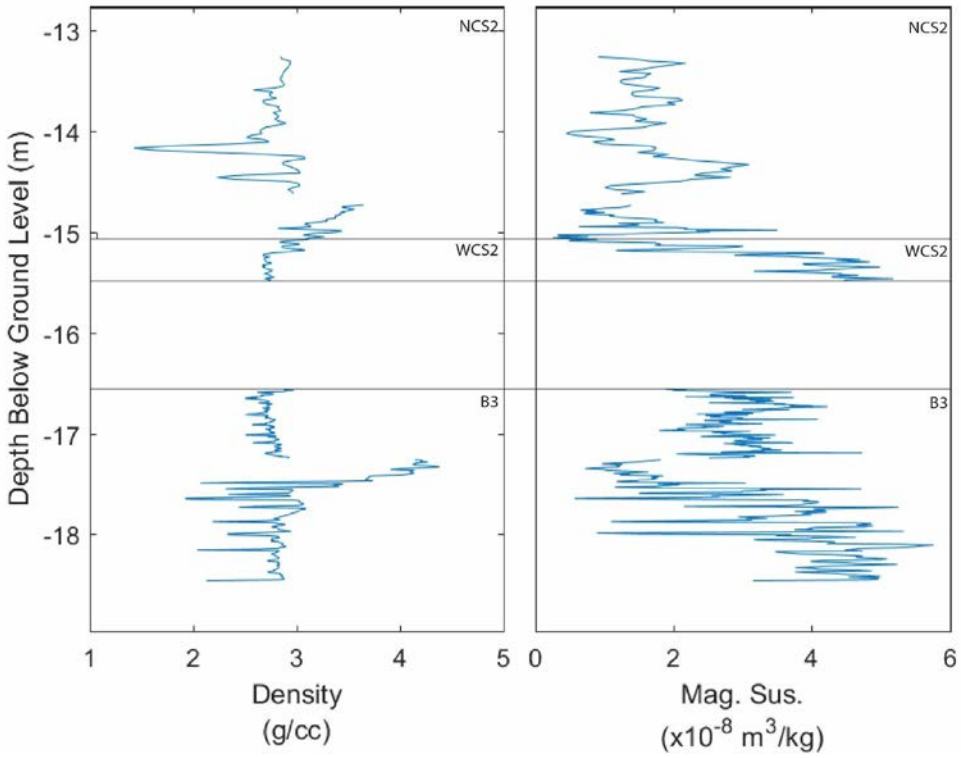

Figure 65: Geotek data for M1H2 showing density and magnetic susceptibility. Units within the core are labelled to the right of each graph.

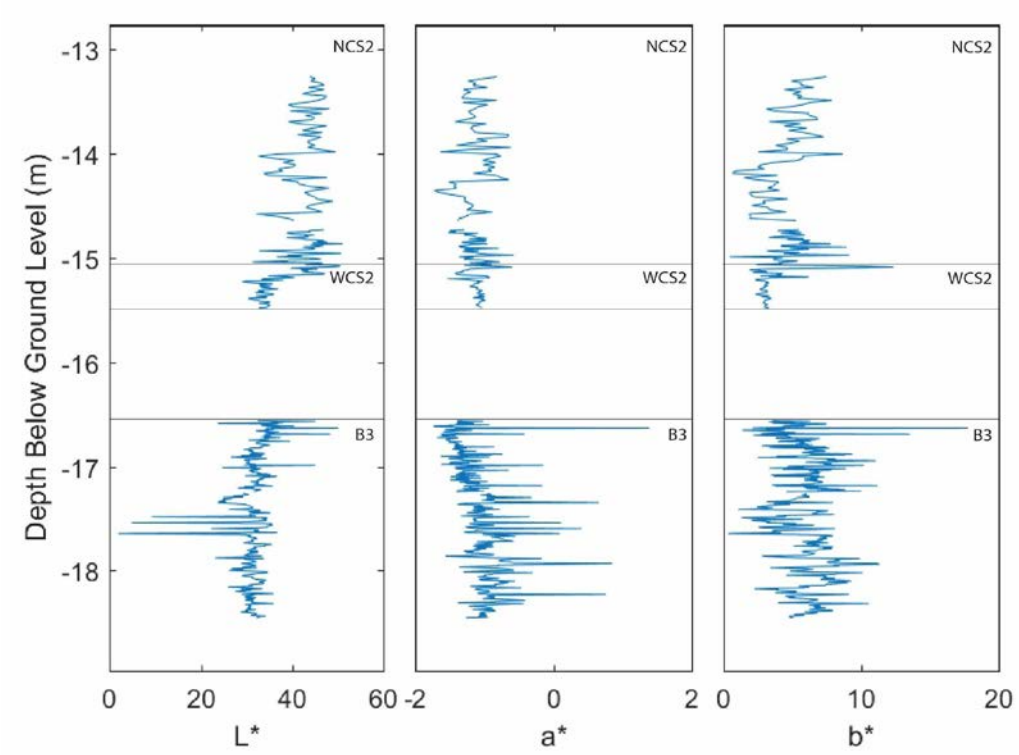

Figure 66: CIE values L*, a* and b* for M1H2. Lithological units are identified on the right of each the graphs.

4.3.3 M3H1

The density at the top of Unit B4 is variable. At 6.75 m, it decreases to 0.5 g/cc which corresponds to where the core is slightly fragmented. The magnetic susceptibility for B4 is extremely variable, overall the magnetic susceptibility increases then decreases (Figure 67). L* and b* also vary within Unit B4. L* increases to 6.75 m at which point it decreases slightly. a* remains relatively stable for the entirety of B4. b* increases to 6.8 m then decreases suddenly before increasing for the remainder of the core (Figure 68).

Most units show an abrupt change in Geotek data at unit contacts. The contact between the soil unit and WCS3 shows a transition between the units. The density of the top of Unit WCS3 is slightly lower than that of the soil unit; it then increases downcore to 3.35 m, where there is a notable decrease. The density increases at 3.55 m and again at 5.7 m. The magnetic susceptibility for WCS3 shows an opposite, but less pronounced pattern to density. However, at 5 m magnetic susceptibility increases and then decreases. The L* of WCS3 does not change significantly down the core. From the top of the unit to 3.4 m there is large variability within a* and b*. At 3.4 m, a* decreases significantly and then increases slightly over the

remainder of the unit. At 3.4 m, b* also decreases, but at 4.1 m there is a sudden increase then decrease. b* then decreases to 5 m and then increases slightly to the bottom of the core.

Overall density ranged from 0.5-1.5g/cc. Within the soil unit, the density is variable. Magnetic susceptibility increases, L* of the soil unit decreases and both a* and b*were highly variable but increase down the unit.

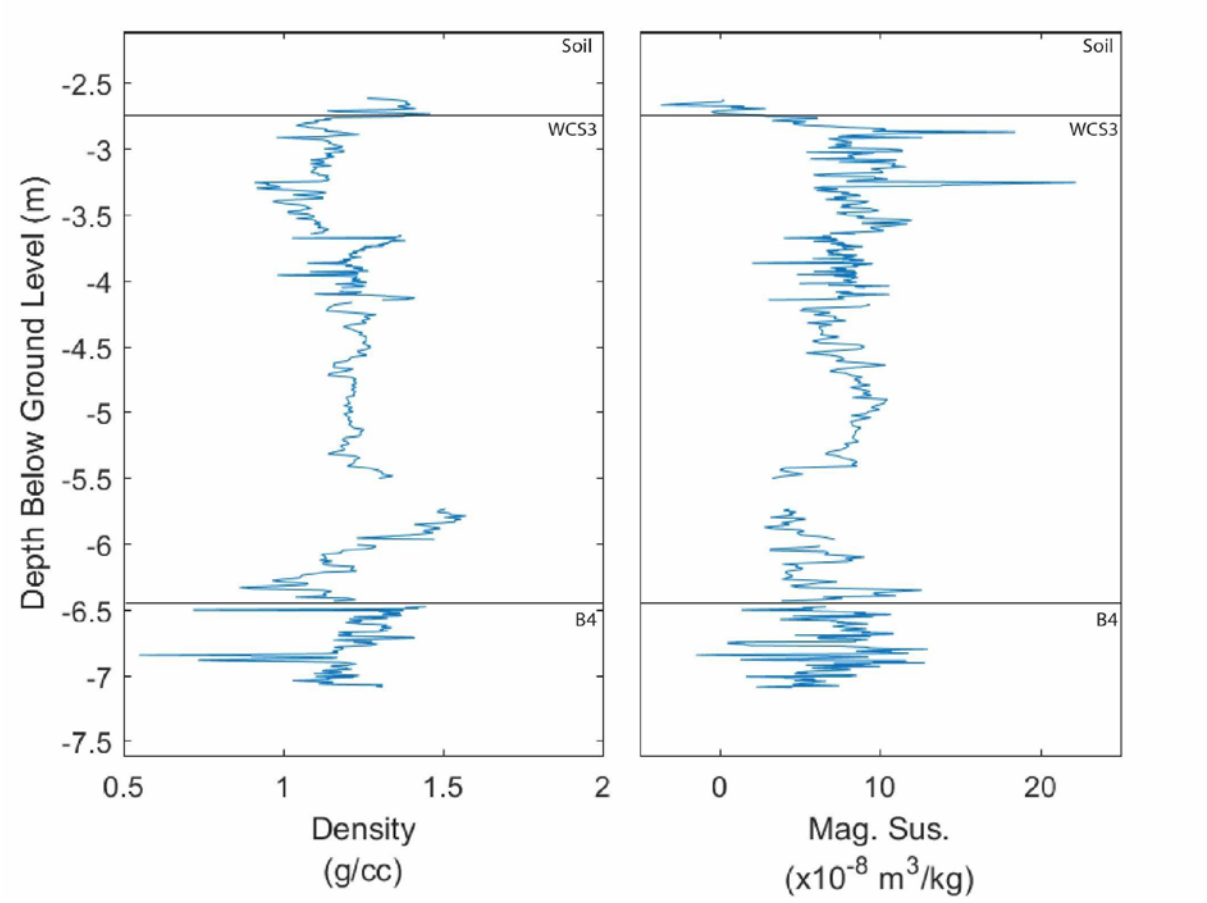

Figure 67: Geotek data for M1H3 showing density and magnetic susceptibility. Units within the core are labelled to the right of each graph.

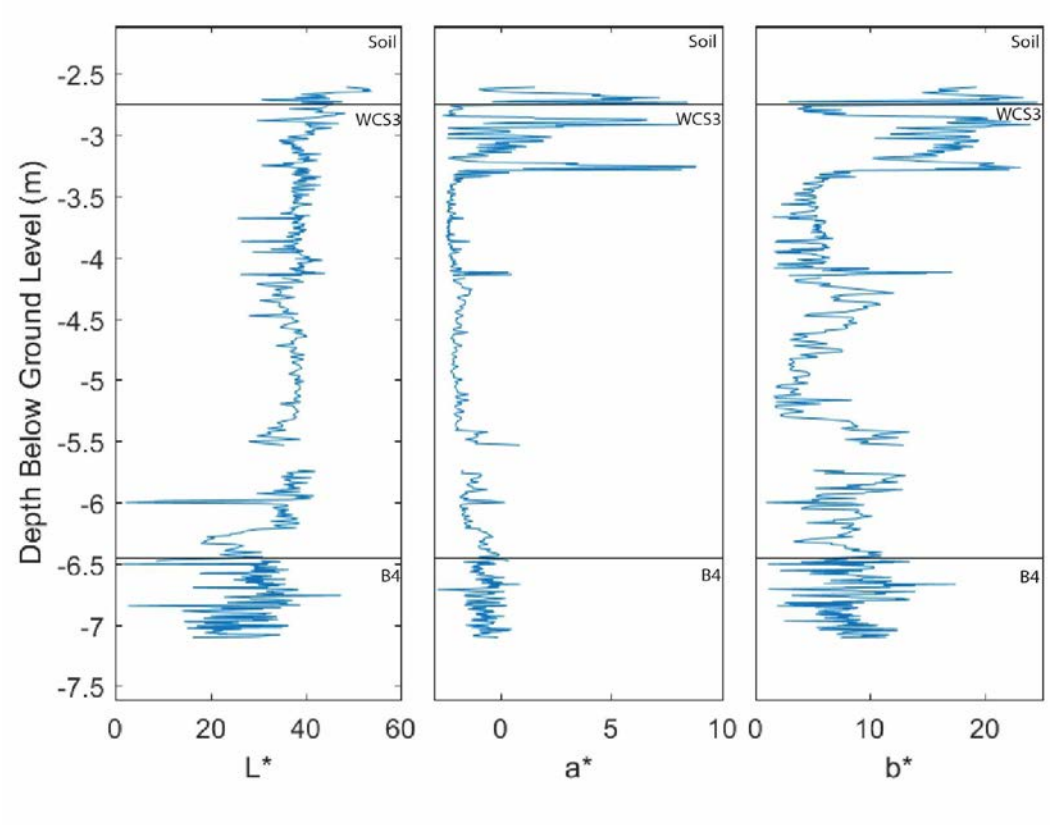

Figure 68: CIE values L*, a* and b* for M3H1. Units identified on the right of each the graphs.

4.3.4 M3H3

Overall there is little variation in the data between units, however changes in stratigraphic units are reflected by changes in the Geotek data. The overall density of Unit B4 is slightly greater than the overlying WCS. Down Unit B4, the density decreases, and magnetic susceptibility remains stable (Figure 69). Initially L* and b* of B4 decrease while the a* of the unit increases (Figure 70).

The density and magnetic susceptibility of WCS4 decrease slightly down the deposit. Both L* and a* are relatively stable down the deposit and show little variability. b* decreases down the core and shows much more variability than other CIE values.

The second MS deposit initially increases in density. There is a significant increase in density between where data have been removed. Following the sudden increase, the density decreases and stabilises. This decreased density is like that of the previous MS deposit. The magnetic susceptibility initially increases and then decreases slightly between the missing data and Unit MS. From Unit MS the magnetic susceptibility increases slightly over the remainder of the unit. L* of MS decreases slightly then between the missing data begins to increase slightly. Overall,

a* of the second MS deposit decreases down the core, whereas b* initially decreases, then subsequently increases.

The density for Unit NM decreases down the core and the magnetic susceptibility overall for the unit is low. The L* value for NM increases down the deposit. Both a* and b* increase initially and then decrease for the remainder of the unit.

The density of MS decreases down the unit. The magnetic susceptibility also decreases over the deposit and there is little variation within values. L* of MS increases throughout the deposit. a* of MS initially increases and then decreases throughout the deposit, while b* increases.

All data from NCS3 were removed for density and magnetic susceptibility due to poor core quality. Very few data points remain for L*, a*, and b*. These data points follow a similar pattern as the unit above and below. The density and magnetic susceptibility of WCS5 decrease down the deposit. However, the variation in the magnetic susceptibility is extreme. L* of Unit WCS5 decreases to 13.4 m at which point it increases slightly. a* of WCS5 is stable until 14.4 m, it increases slightly to 14.45 m then decreases suddenly. This decrease is very close to the contact between WCS5 and the following unit. b*of WCS5 decreases down the core to 13.4 m at which point it increases slightly.

Due to the quality of the core retrieved from M3H3, much of the data for the top few metres are removed from Unit BCS. This is because it is highly fractured. The overall density and magnetic susceptibility of this unit increases downcore. L* of Unit BCS increases down the deposit, along with b*, until 13.5 m where it decreases. The opposite trend was observed in a*.

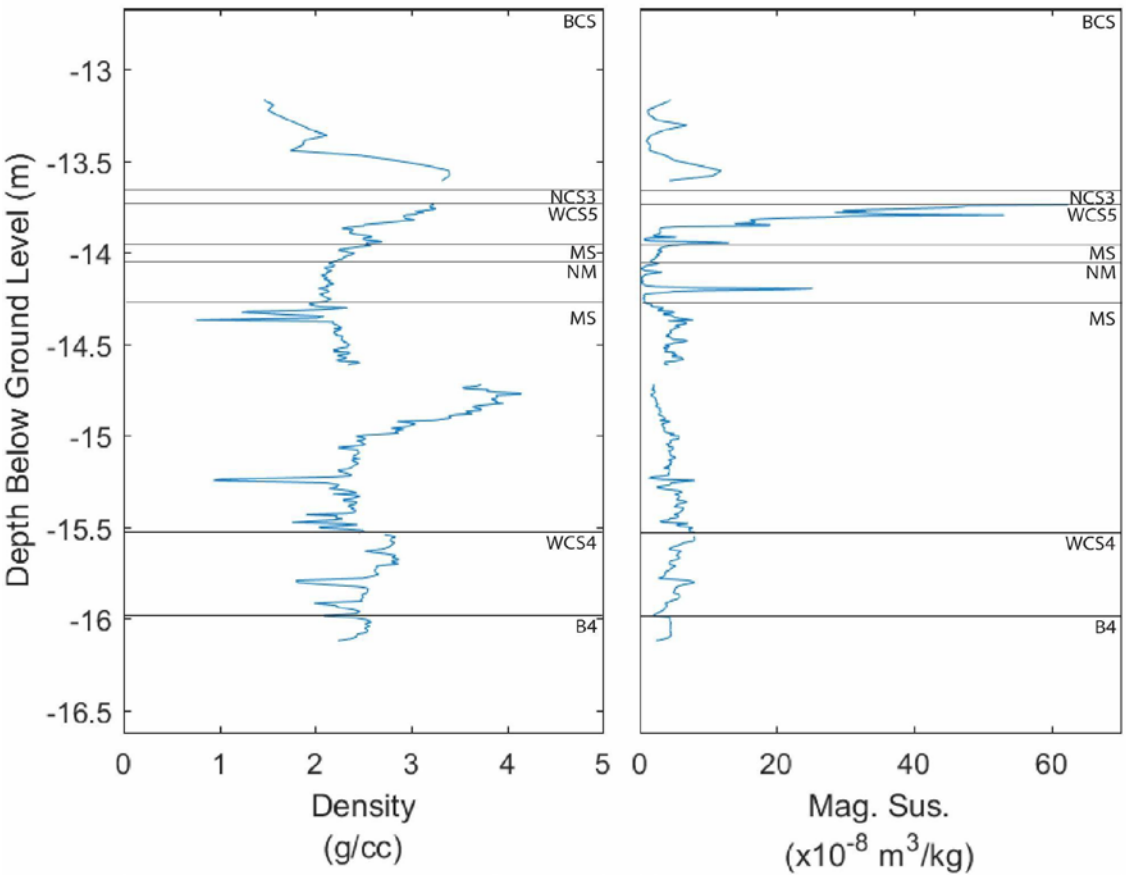

Figure 69: Geotek data for M3H3 showing density and magnetic susceptibility. Units within the core are labelled to the right of each graph.

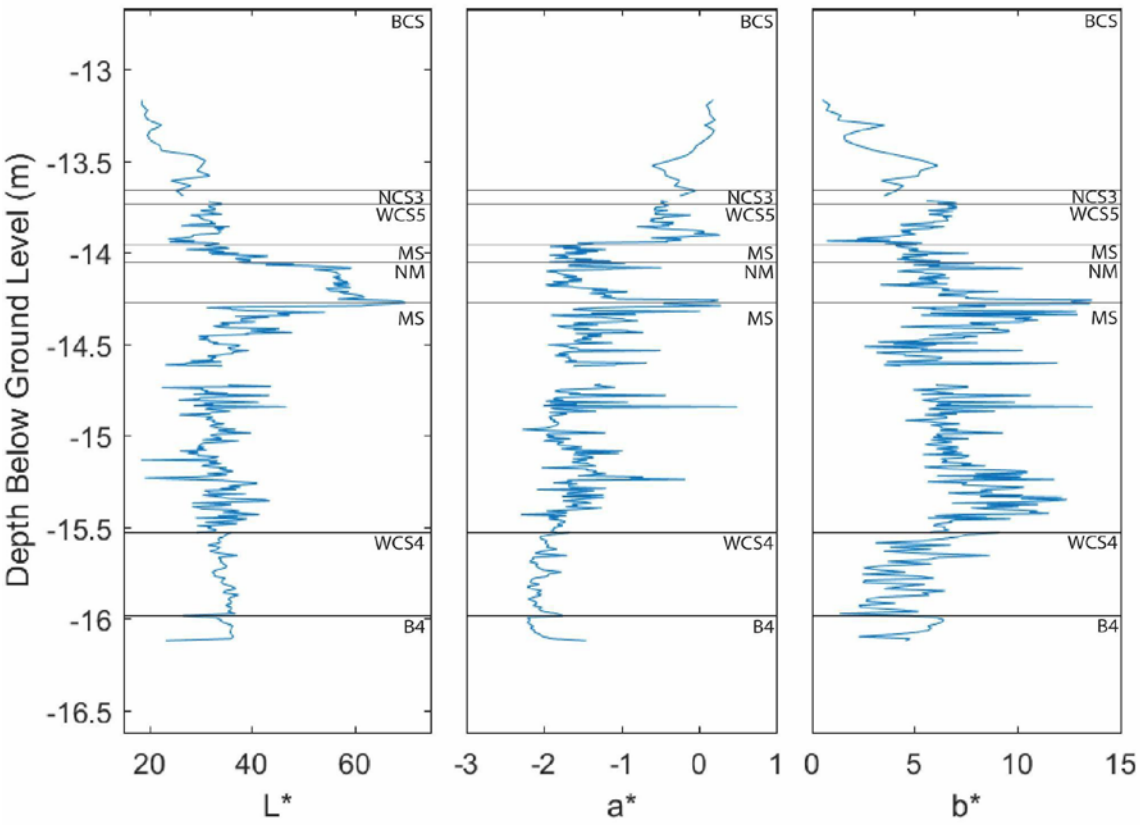

Figure 70: CIE values L*, a* and b* for M3H3. Units identified on the right of each the graphs.

4.3.5 M3H5

The Geotek data for M3H5 is significantly different to the other four cores. This is clearly seen in density, but also in L*, a* and b*. The contact between WCM2 and WCM is seen in a change in results. The density of WCM2 increases slightly down the core. The density spikes at the start and end of each core run. The spike increase can be up to 10 g/cc (Fig 47), density greater than 4g/cc is likely a calibration error. The density increases until approximately 5.8 m and then decreases. The magnetic susceptibility for WCM2 increases in variability down the deposit. The overall magnetic susceptibility is stable to 2.8 m at which point the magnetic susceptibility increases and then decreases to 3.5 m. At 3.5 m the magnetic susceptibility increases. At approximately 5.5 m, the magnetic susceptibility decreases and then increases until 6 m. At 6 m the overall variability in the data ranges from 0 to 270 x 10^{-8} m3/kg (Figure 71). Overall, there is not a significant change in L* in WCM2, although at 4.1 m L* deceases and increases at 5.75 m. a* increases in redness to 4.6 m, at which point it decreases slightly for the remainder of the unit. b* increases down the unit to 6.1 m at which point it decreases slightly (Figure 72).

The density of WCM is variable. Initially, the density increases to 7.6 m and then sharply decreases to 7.6 m and then increases for the remainder of the unit. The variability of magnetic susceptibility within WCM is significantly less than WCM2. Initially, it decreases to 7.45m and then increases again. L* of WCM decreases until 7.35 m then increases sharply at 7.8 m. a* of the deposit increases down the unit. b* of WCM follows a similar pattern to L*.

NCS4 was such a thin unit that only a few readings were recorded with the Geotek. They showed that the density of NCS4 is greater than the density of WCM and the magnetic susceptibility, L*, a* and b* are similar to the values at the bottom of WCM.

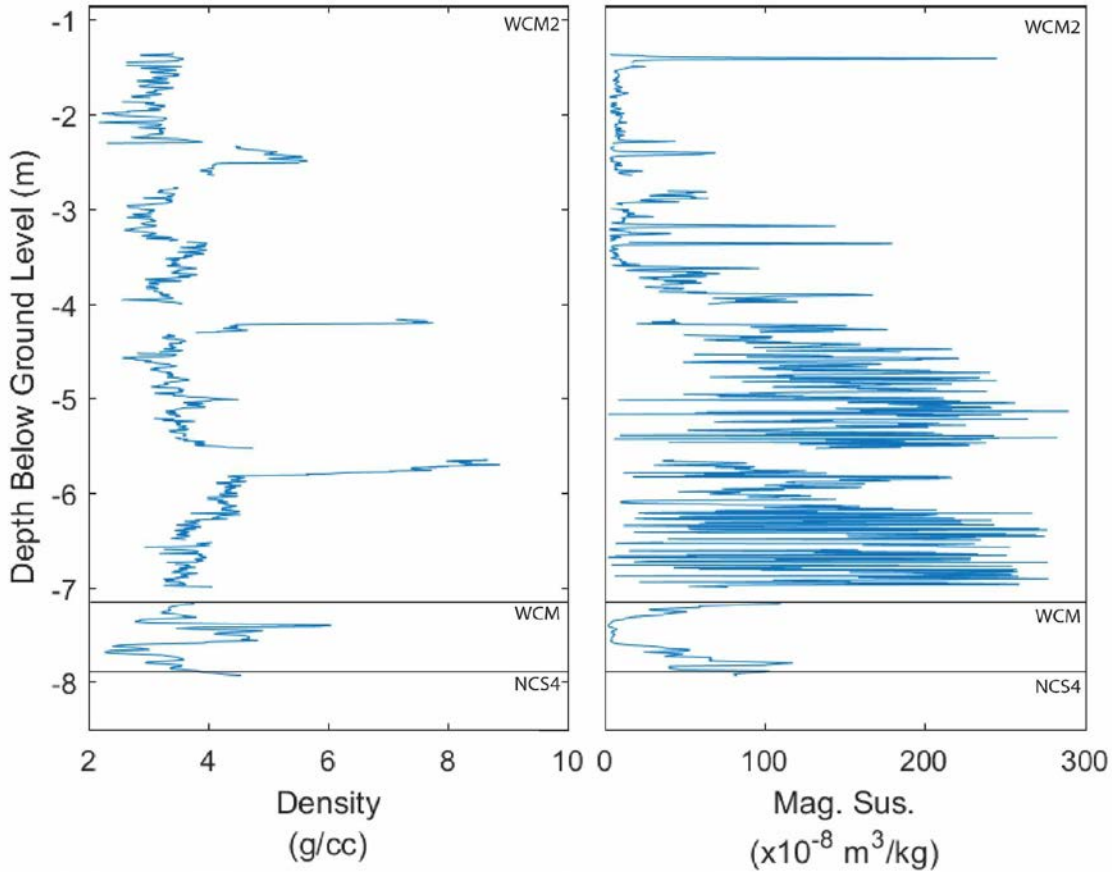

Figure 71: Geotek data for M3H5 showing density and magnetic susceptibility. Units within the core are labelled to the right of each graph.

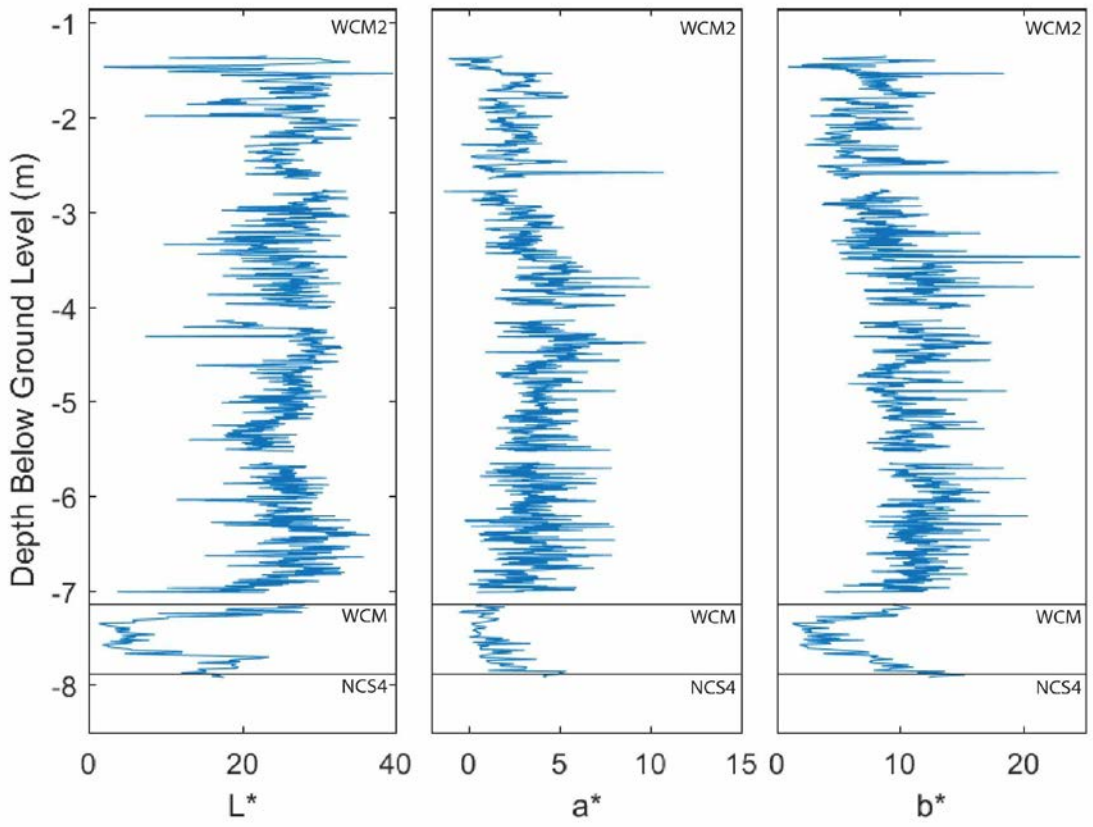

Figure 72: CIE values L*, a* and b* for M3H5. Units identified on the right of each the graphs.

4.4 pXRF Results

4.4.1 M1H1

The pXRF data collected for M1H1 shows that the concentrations of individual elements generally fluctuate uniformly across all elements within a specific unit. The elemental distribution of Unit BCS does not vary greatly between measured samples, apart from Mn, Mo, and Pb. Ti is only measured in one sample site for Unit BCS. The distribution of elements found in Unit NCS varies, although there is no significant change down the sample. Unit WCS is less varied than NCS. At 13.6 m a significant change occurs in the concentration of Ti and Nb. Initially, the concentration of both elements decreases down the unit to 13.6 m, at which point there is an abrupt increase in concentrations that stabilises for the rest of the unit. This change at 13.6 m is also observed as an increase in Rb and a decrease in Sr and Zr. Sample points below 16.3 m are more likely to contain Pb. 16.3 m corresponds with a sandstone lens containing mottles. However, mottles are only observed for 6 cm and are not seen for the rest of the unit. Unit STM has similar

results to the bottom of Unit WCS, although at 15.1 m the variation within concentration increases, except for Mn, which varies and is not found in all measured sites. No samples were taken for B2 and LSQ because the units were too small to be tested by the pXRF. The concentration of Y, Mn, and Fe increases down the core, which is most clearly seen in the last 3 samples sites. The concentration of Ti, Zr and Nb decreases down the core. Pb is only detected in the top of B1 (Figure 73).

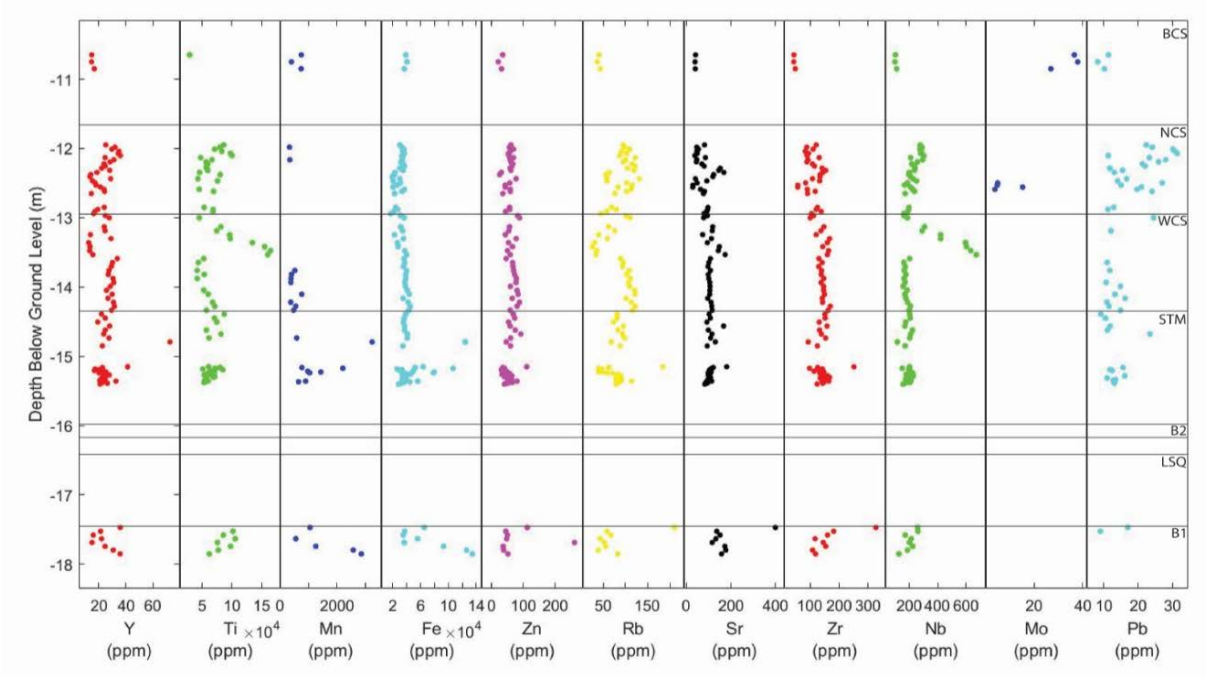

Figure 73: pXRF data for M1H1

4.4.2 M1H2

Data collected for M1H2 shows similar patterns of variation within each unit. From the top of unit NCS2 to 14.1 m, most elements examined by the pXRF are scattered, except for Fe, Sr, and Nb which increase, and Zr, which remains relatively constant. At the bottom of Unit NCS2 the elemental distribution is consistently scattered. Fe and Zn increase in concentration following a similar pattern to the unit below with variability increasing at the bottom. WCS2 shows less variation than Unit NCS2. Y and Ti decrease down the unit whereas Fe, Zn, Rb, Sr, Zr, and Nb increase. Unit WCS2 has a higher concentration of Y, Fe, Zr, Rb and Sr than the other two units but an average lower concentration of Ti. The concentration of elements is relatively consistent throughout Unit B3; however, variability increases down the unit. Unit B3 is the only unit which contains Mn. However, Mn is not found

consistently throughout the unit. M1H2 has similar Zr and Pb throughout the whole core (Figure 74).

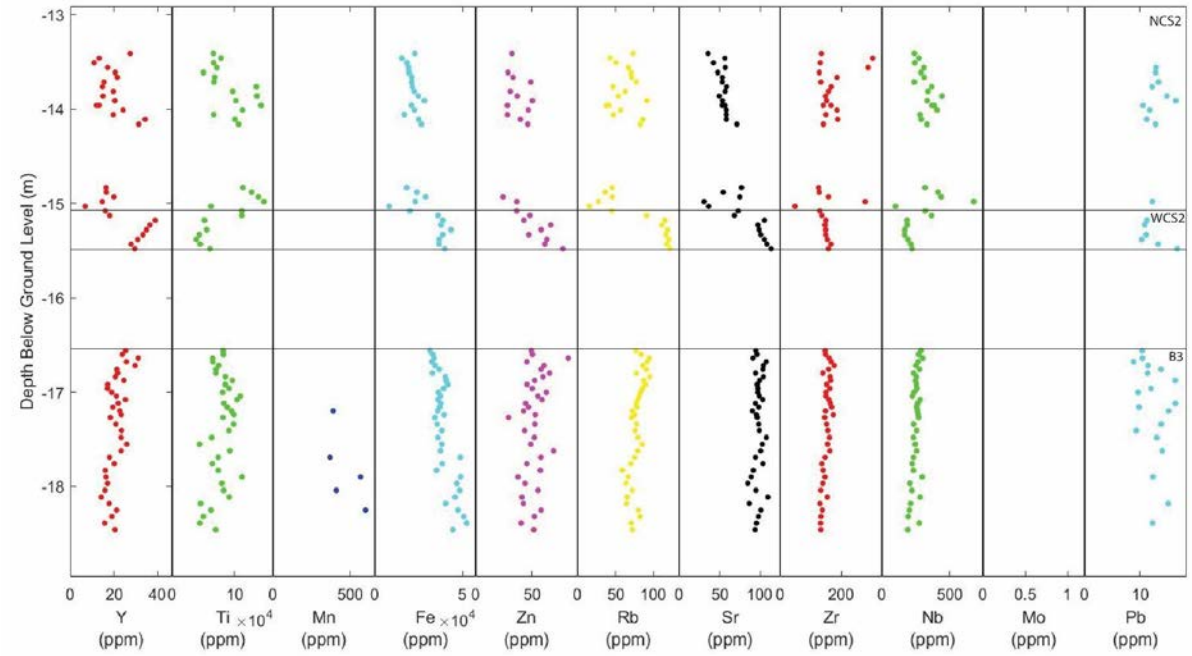

Figure 74: pXRF data for M1H2

4.4.3 M3H1

The elemental distribution for M3H1 shows that some elements are variable throughout the deposits, while others show little to no variability. No elemental data was acquired for the soil unit in M3H1. There is little variation in the concentration of Zn for all deposits found within the units. In Unit WCS3 the concentration of Ti, Fe, Sr, and Nb increases slightly down the unit and shows little variation. The concentration of Zr remains stable for many of the deposits. At 5.75 m the concentration decreases slightly and stabilises. Rb concentration decreases throughout the unit in a series of stages. The concentration of Y and Pb is variable throughout the deposit. However, Pb is detected less towards the bottom of the core. In Unit B4 the concentration of Ti, Fe, Zr, Sr and Nb increases towards the bottom of the deposit. Variability also increases with depth for these elements. The concentration of Rb decreases in B3. No Pb was detected in Unit B4 (Figure 75).

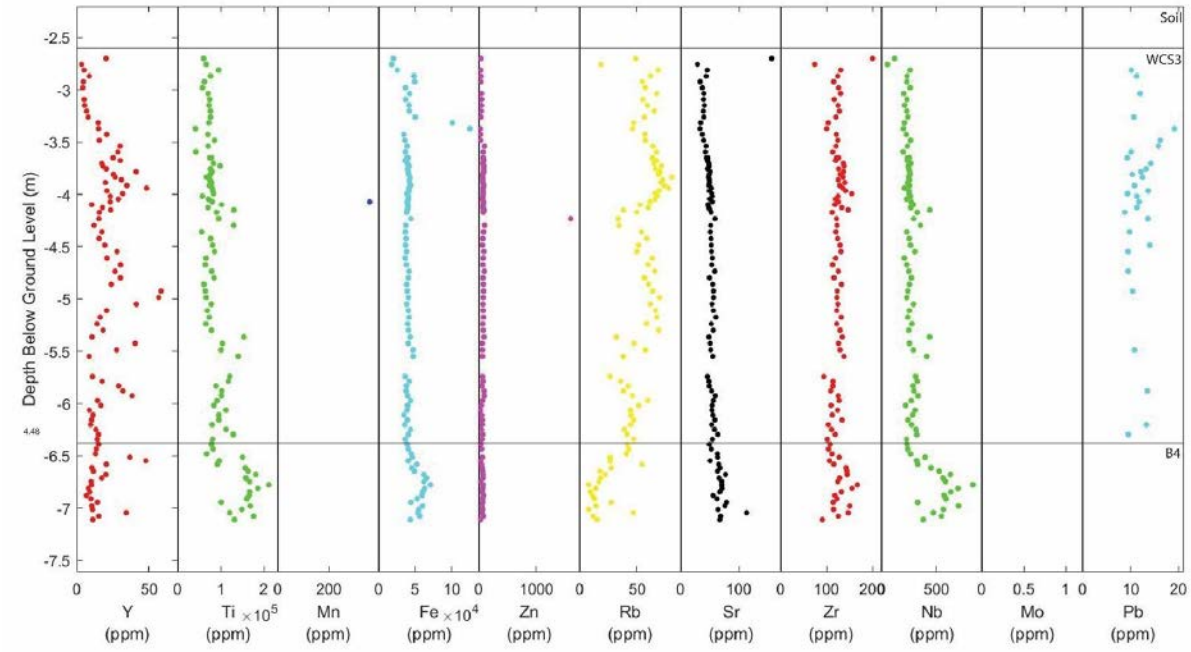

Figure 75: pXRF data for M3H1

4.4.4 M3H3

The elemental data for M3 H3 shows variation down the core with some units having greater variability than others. Only one pXRF measurement was taken for Unit BCS, and 2 measurements were taken for NCS3 due to the small size of the sample. BCS and NCS3 yielded similar results for Y, Ti, Fe, Zr, Sr, and Nb. Both deposits also measured Mo and Pb in all samples taken. The lowest measurement taken in NCS3 had higher Mn, Mo and Pb than the other measurements (Figure 76). Only one measurement was taken for WSC4, which produced similar results to unit MS. WCS4 contained Mn and high Pb in relation to deposits found in M3H3. MS had lower Y, Ti, Zn, Zr, and Nb in relation to other units measured in M3H3, however, the concentration of Y and Zn increases down the unit.

Unit NM has elevated concentrations of Y, Ti, Zr, and Nb and a relative decrease of Fe. Mo is also detected in NM; however, the concentration is less than that observed in the previous unit and is not detected in all measurements. The concentration of Sr does not vary from Unit NM to Unit B5.

Within Unit MS the concentration of Y is varied. It initially decreases to 14.2 m, increases suddenly to 14.9 m, and then decreases. The concentration of Ti in Unit MS initially decreases to 14.75 m, stabilises and then at 15.75 m increases in concentration. Mn is not found constantly throughout Unit MS and is only detected in two locations, at approximately 14.5 m and 15.4 m. The concentration of Fe, Zn, Zr, and Nb is similar throughout the core, however variation decreases down the

core and Zr and Nb initially decreased. Pb is found sporadically throughout MS, increasing throughout the unit. The concentration of Rb in Unit MS shows a similar pattern to the concentration of Rb in WCS3 found in M3H1.

In Unit WCS4 the concentration of elements does not vary. The concentration of Rb is much higher than in other units and the concentration of Nb is lower. Both Mn and Pb were detected within the measurement, but not consistently.

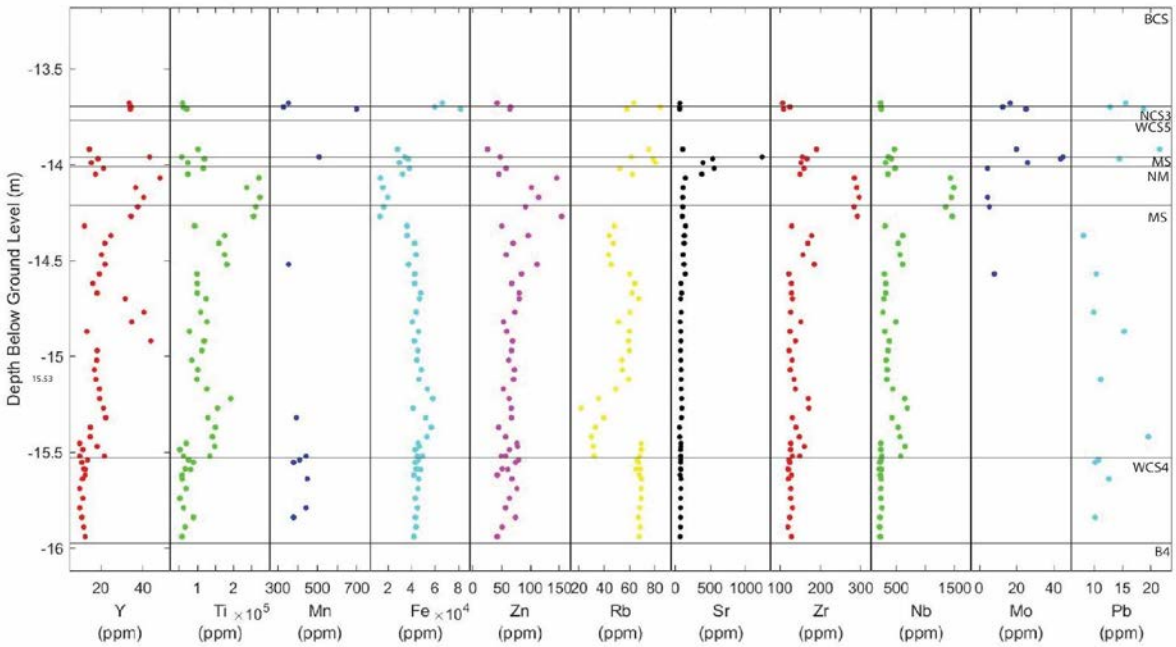

Figure 76: pXRF data for M3H3

4.4.5 M3H5

The overall elemental distribution for M3H5 shows that all elements behave similar to one another down the core. Elemental analysis of Unit WCM2 shows little change in the concentration of Y and Rb. At approximately 4 m there is a change in concentration for several of the elements. Ti, Zn, Zr, and Nb have a slight decrease in concentration that continues for the rest of the deposit. At 4.1 m the concentration of Fe decreases whereas the concentration of Sr increases. At 6.3 m the variability of Mn increases (Figure 77).

Only one data point was collected for Unit WCM, because the deposit was highly fragmented, and one for NCS4, because the deposit too small. The concentration of Y, Ti, Fe, Zr, and Nb are similar for Unit WCM and WCM2. No Rb is detected for WCM and Sr is higher than the other deposits. Unit NCS4 has similar Y, Mn, Ti, Sr, Zr, and Nb to WCM2. The concentration of all elements is less than the concentration of elements found in WCM2. The concentration of Zn found in NCS4

is lower than what is detected in other deposits. Mo and Pb are not detected in any of the deposits within M3H5.

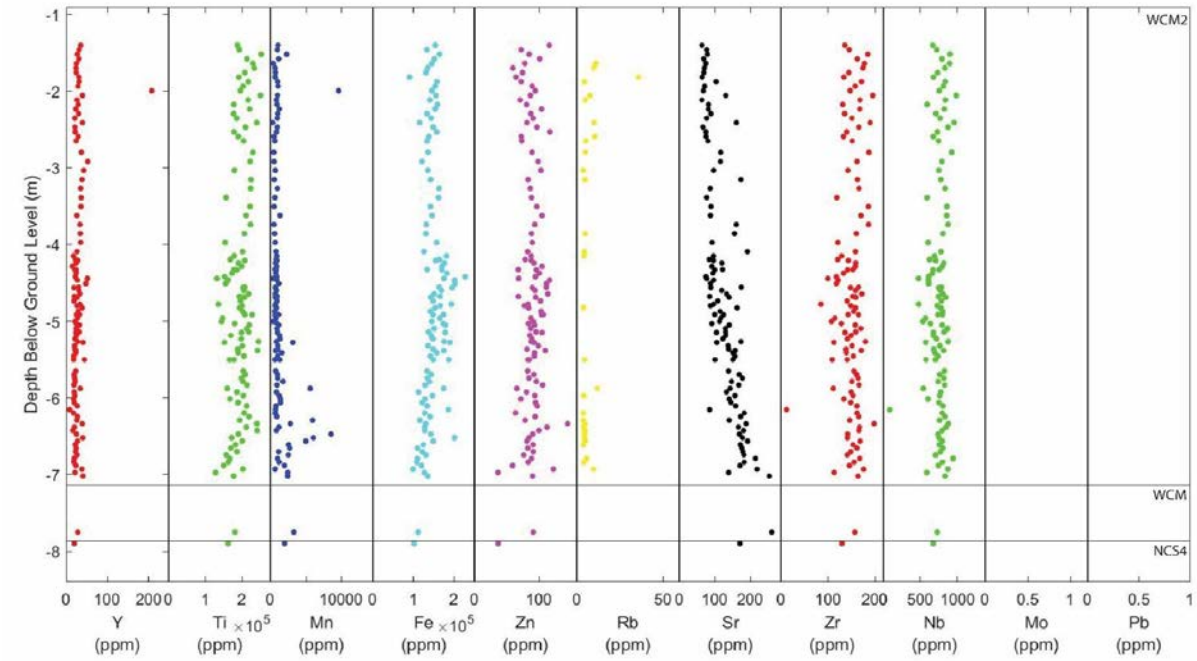

Figure 77: pXRF data for M3H5

4.4.6 Boulder field pXRF

pXRF analysis was conducted on 6 basalt boulders found within the boulder field on the surface of Maar 3 (Figure 78). The boulders have a higher Mn, Sr and Nd than the deposits in M3H5, however all other elements have similar concentrations.

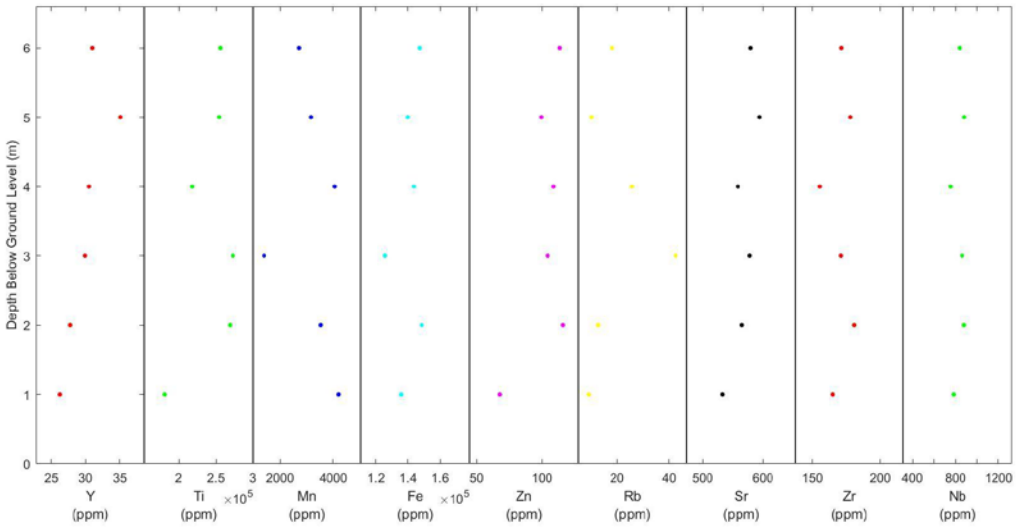

Figure 78: pXRF for the boulder field

4.4.7 Volcanic rock type

The volcanic rocks modified Pearce model is here used to classify the sediments in Unit WCM, WCM2 and NCS5, M3H5. This was done because the colour and elemental distribution of this unit indicated a potential volcanic parent rock. This model uses the ratio of Zn/Ti to Nb/Y to determine volcanic rock type. The model determines that the deposits found within M3H5 are consistent with ultra-alkaline basalt precursors (Figure 79).

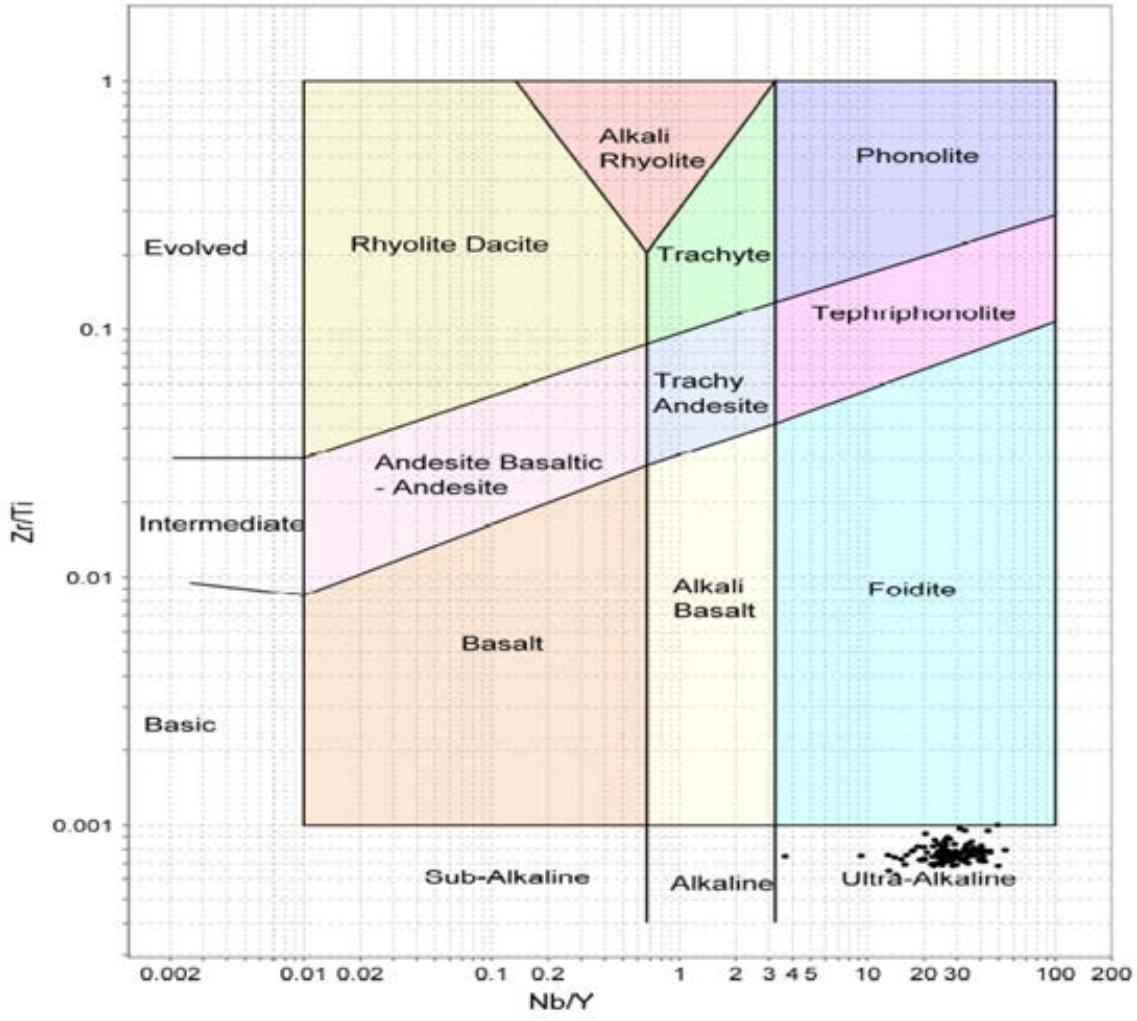

Figure 79: Volcanic rock modified model showing that the pXFR data plots to ultra-alkaline basalt (Floyd & Winchester, 1975).

4.5 XRD Results

XRD results are summarised below (Table 1). The XRD plots can be found in the Appendix-XRD. Several samples have clays from the illite and kaolinite group. XRD analysis does not show clear peaks in samples from M3H5, therefore interpretations of these results are less robust.

Table 1: XRD results for unit WCS4, NM, MS, WCM2 and WCM

Unit Name	Name and Location	Chlorite Group	Illite Group	Kaolinite Group
WCS4	M3H3 1 (13.75 m)	Chlorite	Regularly interstratified illite– chlorite	Kaolinite
NM	M3H3 2 (14.1 m)			Halloysite
MS	M3H3 3 (core catcher 13.0 - 14.62 m)		Illite and/or mica muscovite	Kaolinite
WCM2	M3H5 5 (core catcher 1.35 – 2.65 m)			Halloysite

4.6 Grain Size Analysis

Grain-size distributions for samples from the non-consolidated units are shown in Appendix-Grain Size Analysis. Table 2 shows a summary of the proportions of different grain sizes in these units. These grain-sizes are consistent with those derived from thin section analysis. Grain size analysis identifies Unit NCS as a silty sand deposit. NCS2 is a sandy silt, with the sand proportion of the deposit increasing down the unit. Unit NM is a clayey silt and has the highest clay proportion of any of the other nonconsolidated samples. WCM2 is a sandy silt and has a decrease in silt concentration in the middle of the deposit. All samples for WCM2 are identified as a silt. WCM and NCS are identified as sands, with NCS having a higher silt concentration.

Table 2: Grain size analysis for nonconsolidated samples.

			% of sample		
Core	**Depth**	**Unit**	**Clay**	**Silt**	**Sand**
M1H1	9.25	NCS	5.06	44.87	50.05
M1H2	13.30	NCS2	19.83	62.42	17.75
M1H2	13.48	NCS2	9.04	47.05	43.93
M1H2	15.08	WCS2	11.42	61.12	27.44
M3H3	14.10	NM	34.26	43.00	22.72
M3H5	1.45	WCM2	20.50	32.16	47.35
M3H5	2.95	WCM2	24.79	56.87	18.34
M3H5	3.21	WCM2	32.13	42.93	24.93
M3H5	5.35	WCM2	19.78	58.79	21.44
M3H5	7.60	WCM	16.39	26.65	56.94
M3H5	7.95	NCS4	16.18	39.30	44.53

4.7 Scanning Electron Microscope Results

SEM was performed on two samples from unit NM at 14.1 m. The first sample was a thin section sample and the second was a small sample directly placed in the SEM without surface preparation. Elemental data show high concentrations of Al, Si, O, C and Fe. The combination of Al, Si and O is likely to indicate the presence of clays (Table 3). Batiferrite has a similar chemical formula to the elements identified within unit NM. Photos taken under SEM show aggregated clays and particles with a similar morphology to halloysite tubes, which was identified in XRD (Table 1). Titanium oxide is likely present as the morphology of particles were spherical and nano-sized. Titanium oxide is consistent with the high abundance of titanium found by pXRF analysis (Figure 76).

4.7.1 Mottles

SEM was conducted on mottles in an attempt to identify their composition. Because there was limited material that could be cleanly removed from the cores, the mottles examined were a combination of several mottles over the course of a metre of a core. Samples from the mottles were placed directly in SEM without surface preparation. The morphology of the particles shown in the SEM images, combined with the elemental distribution, indicates a composition of volcanic glass and clays of the smectite and montmorillonite groups (Figure 80; Figure 81; Table 3). Crystals

of quartz and feldspar are also observed in some samples. Titanomagnetite and iron oxides are also present (Figure 80; Figure 81). Overall, the mottles are not identical to one another. For example, volcanic glass shards are not found in all mottles. However, extensive clay overgrowth is found throughout the mottles sampled here.

4.7.2 M3H5

Thin section samples from 2.08, 4.2 and 5.6 m were analysed under SEM. Elemental distributions showed a high percentage of Si, Al, C and O (Table 3), and a low percentage of Fe (consistent with pXRF findings (Figure 80; Figure 81)), indicating a composition dominated by clay minerals. At 5.6 m the sample comprised of quartz crystals, aggregated clays and spherical nano-sized particles.

Table 3: Shows average elemental distribution of samples scanned under SEM. Elemental distribution is are obtained through scanning for field view

Element	M3H5 (3 samples averaged) (2.5 , 4.2& 5.6 m)	Mottles – M3H3 Unit NM 14.1 m	Mottles – M3H3 14.30 to 14.60 m	Mottles – M1H1 17.13 to 18.48 m	Mottles – M1H1 17.59 to 17.85 m	Mottles – M1H1 15.58 to 16.35 ,	Mottles – M3H3 5.4 to 6.4 m
C	15	22	5	8	1	7	12.82
O	31	22	32	30	29	26	33.24
Na					3	0	
Mg	0	1					0.615
Al	20	10	13	9	11	5	8.21
Si	31	28	27	30	27	15	32.02
P		1			4	7	
S						0	
K		1	1				
Ca		3			10	9	
Ti	2	3	19	11	9	20	7.625
Cr		1					
Fe	2	11	1	12	4	11	5.46

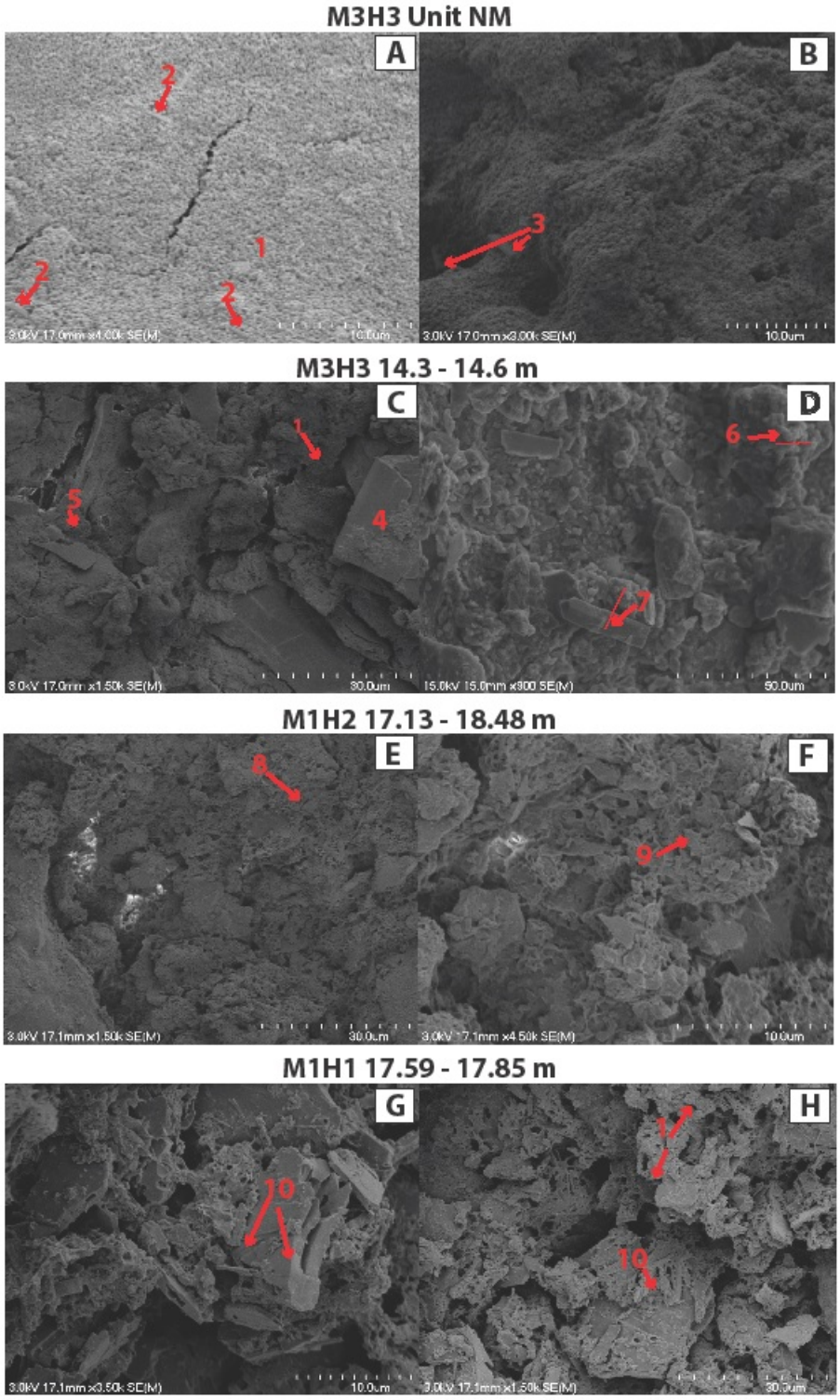

Figure 80: Photos of samples under SEM. A - B M3H3 unit NM at 14.1 m. C - D M3 H3 14.3 – 14.6 m sample of mottles. E – F M1H2 17.13 – 18.48 m sample of mottles. G - H M3H1 17.59 – 17.85 m sample of mottles. 1) spherical nanoparticles. 2) Halloysite tubes. 3) Clay overgrowth. 4) Quartz grain. 5) clay sheet. 6) clay aggregate. 7) Alkaline feldspar crystal. 8) smectite with montmorillonite. 9) Platy clay. 10) volcanic glass.

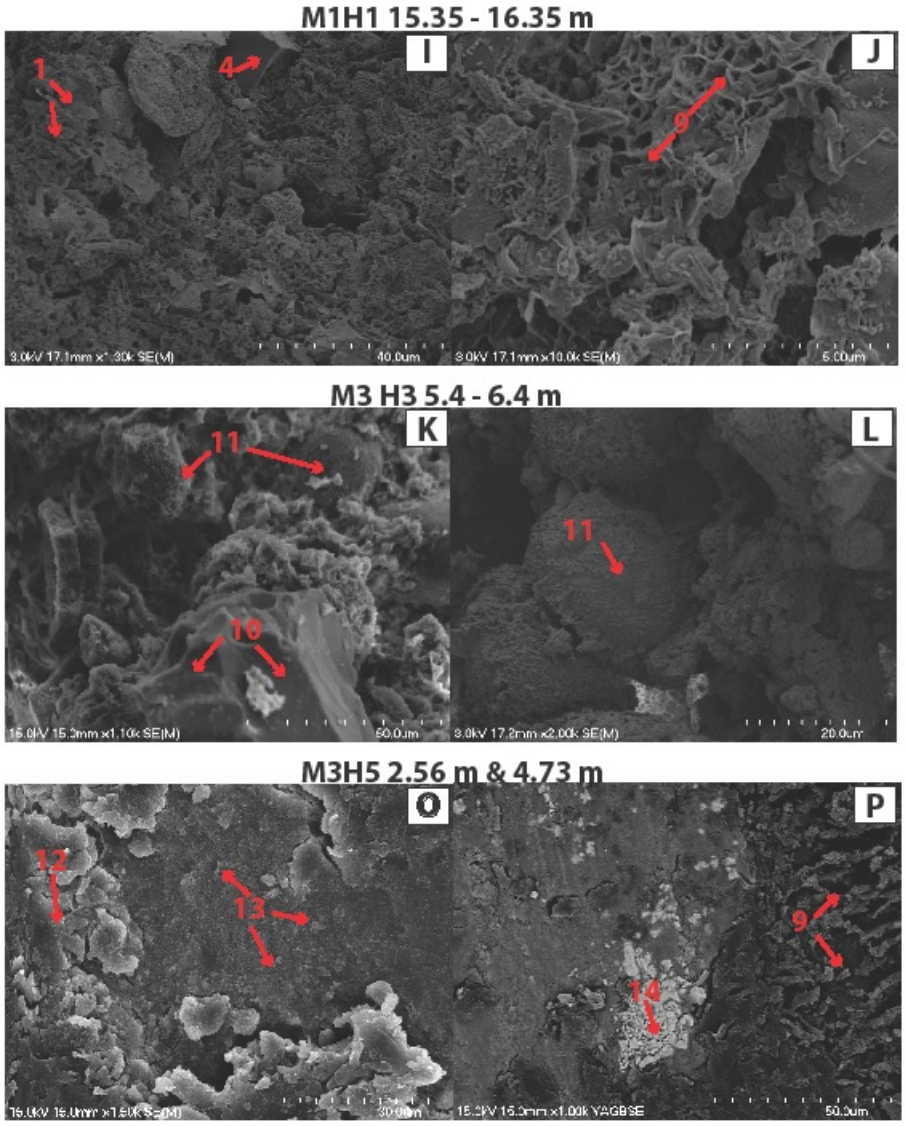

Figure 81: Photos are sample under SEM. I – J M1H1 5.35 – 16.35 m sample of mottles. K – L M3 H3 5.4 – 6.4 m sample of mottles. O – P M3H5 2.6 m & 4.73 m sample taken from core. 1) spherical nanoparticles. 2) Halloysite tubes. 3) Clay overgrowth. 4) Quartz grain. 5) clay sheet. 6) clay aggregate. 7) Alkaline feldspar crystal. 8) smectite with montmorillonite. 9) Platy clay. 10) volcanic glass. 11) ilmenite. 12) aggregated spherical nanoparticles. 13) Titanomagnetite.

4.8 Geomorphological Map

The geomorphology of the three maars is shown on Figure 23 and Figure 83, using standard geomorphological symbols. The greater geomorphology of the region is consistent with a peneplain, which is apparent just south of Maar 3 (Figure 82). The greater region also has many stream-cut valleys, which are evident throughout Maars 2 & 3 (Figure 83). The geomorphology of Maar 1 (Figure 82) and Maar 2

& 3 (Figure 83) vary from one another: Maar 1 occurs within a small basin, while Maar 2 and 3 vary greatly in elevation. The geomorphology of both mapping areas is expressed largely in changes in slope, with very few slope breaks or cliffs observed.

4.8.1 Maar 1

Gravity anomaly identification has been used to indicate the location of Maar 1(red line, Figure 82). A slope break has been identified where the land slopes inwards towards the centre of this anomaly. All slopes surrounding the maar slope towards the centre. In the centre of the maar, flat land has been observed with swampy land feeding towards the centre.

4.8.2 Maar 2 and 3

The geomorphology of Maars 2 and 3 is more complicated than Maar 1. The gravity anomalies used to identify Maars 2 and 3 form a NNE linear alignment (purple and orange lines, Figure 83). Maar 3 is located on a slope in the SW of the mapping area. Maar 2 is found in the NE of the mapping area and forms a positive feature in the landscape. In between Maars 2 and 3, where M3H1 and M3H3 were drilled, the land forms a small depression, as evident in the elevation cross-section (Figure 83). Furthermore, the SW facing slope of Maar 2 is significantly shallower than its NE facing slope. On either side of the maars are stream-cut valleys which are significantly deeper in the north and east of the mapping area.

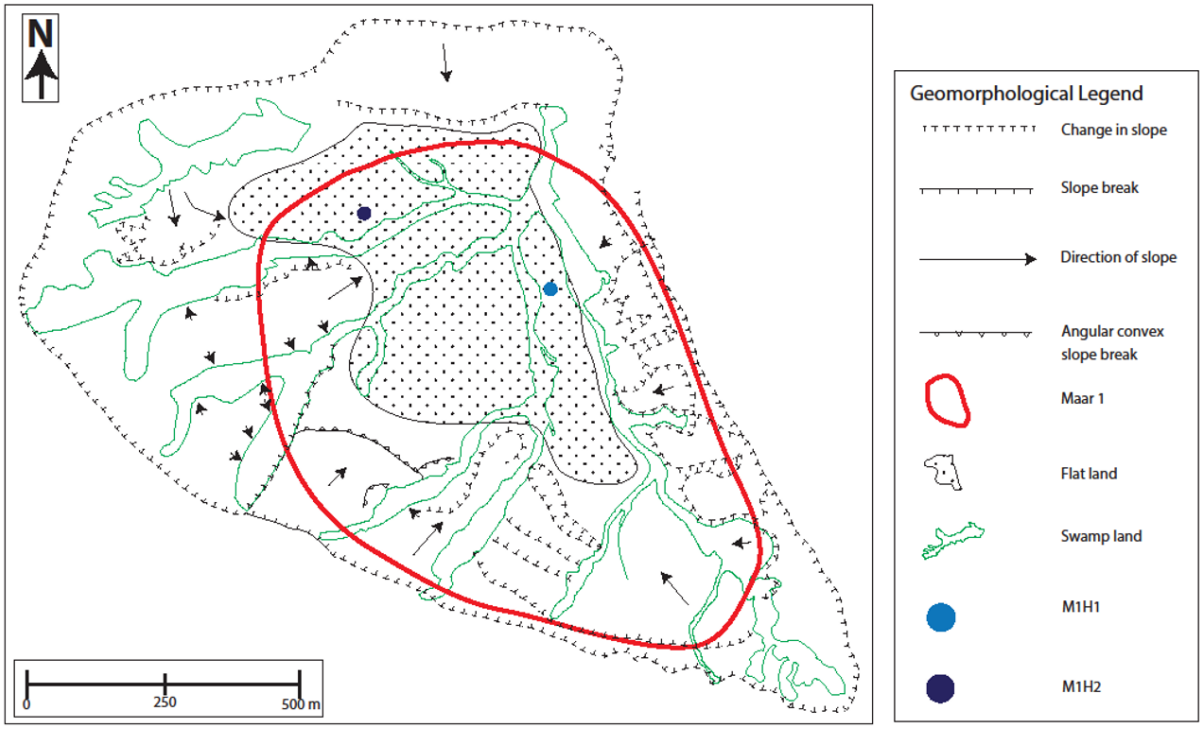

Figure 82: Geomorphic map of Maar 1. Geomorphological features were identified by visual interpretation in the field.

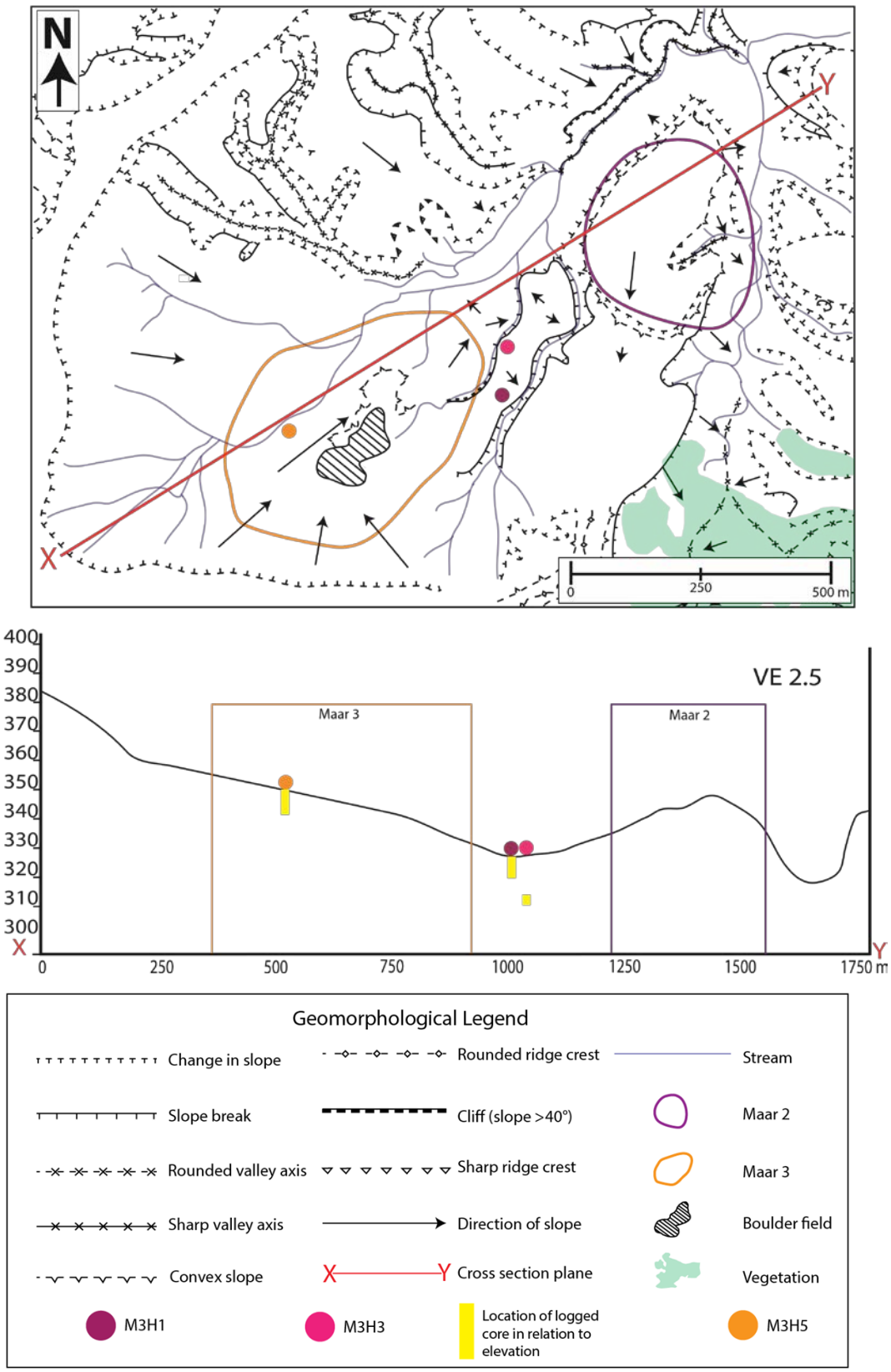

Figure 83: Geomorphic map of Maar 2 and Maar 3. With elevation graph along X and Y line. Geomorphological features were identified by visual interpretation in the field.

Chapter 5

Facies Description and Interpretation

This chapter comprises of the descriptions and interpretations of the ten facies identified in this thesis. Descriptions are based on the results described in Chapter 4. Interpretations combine the descriptions along with peer reviewed studies to interpret depositional processes.

Based on sediment composition, sedimentary structures, grain size and mottle concentration, a total of 10 facies have been identified within M1H1, M1H2, M3H1, M3H3 and M3H5. Analysis of the vertical distribution of facies along with physical sediment properties has allowed depositional processes to be inferred. Units in M3H1 and M3H3 differ from one to another, despite the holes only being 70 m apart. The facies identified in M3H5 are exclusive to this hole and consist of Facies 8 to 10.

5.1 Facies in Maar 1 and Maar 3

A total of seven facies were found within Maars 1 and 3 (Table 4), excluding M3H5. The composition of Facies 1 to 6 is dominated by mica and quartz, which are major components of the area's country rock, the Otago Schist (Németh & White, 2003). Mottles are found in Facies 2 to 5. As these appear in multiple facies, they are discussed separately below.

Table 4: Facies present in each core

Facies	M1H1	M1H2	M3H1	M3H3	M3H5
1	✓	✓		✓	
2	✓	✓		✓	
3	✓	✓	✓	✓	
4	✓	✓	✓	✓	
5	✓		✓		
6	✓				
7	✓				
8					✓

9	✓
10	✓

5.1.1 Mottles

The origin of the mottles has been determined largely through SEM analysis, which showed that some of the mottles contain volcanic glass. Smectite and montmorillonite have also been identified through SEM analysis, predominantly by examining the morphology of the mottles (4.5 XRD Results). Feldspar and quartz crystals were also found in some of the mottles (4.1 Core Description).

Smectite and montmorillonite form from the weathering of olivines, pyroxenes, and amphiboles, which occur in both igneous and metamorphic rocks (Churchman & Lowe, 2012). However, the country rock of the Hindon area is biotite-mica schist (Forster & Lister, 2003), which is not known to contain olivine. Furthermore, olivine is found with the boulder-field samples (4.2.6 Boulder Field). It is therefore here inferred that the clays identified within the mottles are the result of weathering of igneous olivines. Therefore, the mottles are interpreted as extensively weathered remnants of pyroclastic material.

It is unlikely that the mottles are the result of tephra fall-out into the lake resulting from nearby volcanic eruptions, for two reasons. Firstly, the mottles appear in zones of graded material; and secondly, the mottle-rich units found in the various maars are not at a comparable stratigraphic depth, nor are they similar enough to be regarded as representing the same deposit. It is therefore likely that this material would have come from the tephra ring or upper crater wall of the maars.

Mottles are often accompanied by coarser-grained material, which is consistent with the hypothesis that the mottles originated outside the lake and were transported to the lake bed by subaqueous gravity flows (Talling et al., 2012). Had the mottles entered into the lake because of tephra fallout from a nearby volcanic eruption, they would have not been accompanied by coarse-grained schist and quartz fragments (country rock). Furthermore, they would not have been extensively weathered. The extreme weathering of the mottles indicates the mottles must have gone through a period of weathering before entering into the lake. In addition, the high proportion of the country rock indicates that the failure which produced the emplacement of the mottles must have occurred within the crater wall.

5.1.2 Facies 7

Description

Facies 7 is a white non-consolidated clay-rich silt found only in M3H3. The split core surface of Facies 7 has a swirly structure, interpreted as an example of convolute bedding (Figure 39). Grains were too small to be identified by visual assessment, so laser sizer analysis was used. Grain sizes for Facies 7 were 43% silt, 34.26% clay and 22.72% sand. The density of Facies 7 is similar to that of Facies 4 and Facies 2, at 2.12 g/cc (Figure 87). Facies 7 had the second lowest magnetic susceptibility at 3.03 $x10^{-8}$ m^3/kg (Fig. 62), and the highest L* and lowest a* values of all facies, at 50.15 and -1.57 CIELAB units, respectively (Figure 89 and Figure 90). The b* was similar to other facies (Figure 91). XRD identified the clay minerals within Facies 7 as halloysite. Halloysite was also identified under SEM. SEM analysis also showed nano-sized spherical material which has been interpreted as titanium oxides, due to the high concentration of titanium observed within the sample. No diatoms or other evidence of biogenic sedimentation was observed within this facies. pXRF data indicates a relatively high concentration of Ti, but a low concentration of Fe (Figure 94).

Interpretation

Facies 7 is interpreted as a localised slump deposit. This is based on the swirly pattern observed in the core log as an example of convolute bedding. No organics have been observed in this facies, therefore deposition into the lake must have been rapid (Zolitschka et al., 2015). Geochemically, this facies is different to all other facies examined. It is probable that this facies was formed by processes different to the other sediments within the maar and was then redeposited locally. M3H1 was drilled in close proximity (70 m) to M3H3 but no evidence of Facies 7 was found, indicating a very local distribution. Because this deposit has high Ti, it is likely that the nanoparticles observed under SEM are titanium oxides (Vijayalakshmi & Rajendran, 2010). Titanium oxides can form from the weathering of various parent materials, such as schist (Churchman & Lowe, 2012; Force, 1976). Therefore, it is possible that Facies 7 formed by the weathering of schist under normal soil-forming processes and, at some point after the maar eruption, entered into the lake and was preserved from subsequent erosion.

5.1.3 Facies 6

Description and Interpretation

Facies 6 consists of loose schist and quartz grains which range from fine gravel to medium pebbles in size. These grains are angular to sub-angular and are poorly sorted. No Geotek analysis was performed on Facies 6. Facies 6 consists entirely of schist and quartz, which is the country rock of the region. Finer grained material may have been washed out during drilling. The recovery of this facies was poor and therefore it is difficult to interpret the environmental origin of this facies. However, Facies 6 is interpreted as being formed as a result of a failure of the crater wall material, derived mostly from country rock which has entered into the lake as a rock fall rather than a mass flow. Rock falls occur early after the initial maar eruption; therefore, this deposit likely occurred within a time frame of 0 to 25 years after the eruption (Pirrung et al., 2008).

5.1.4 Facies 5

Description

Facies 5 is a fine gravel sized grey breccia. The matrix of this breccia consists of fine to coarse sand which is angular to sub-angular. Gravel grains consist of schist and quartz and are angular to sub-angular. Overall this deposit is poorly sorted and often appears normally graded. Facies 5 contains less than 4% mottles. Facies 5 is found in M1H1 and M3H1 near or at the bottom of the hole (Figure 45 and Figure 47). It is poorly consolidated and in M3H1 has been fragmented by drilling. The overall density of this deposit is 2.44 g/cc (Figure 87). The magnetic susceptibility is elevated, at 8.51 $x10^{-8}$ m^3/kg. Both these values show high variability (Figure 88) Facies 5 had a similar L* and a* to several other facies (2, 3 and 4) at 31.62 and -0.70 CIELAB units respectively (Figure 89;Figure 90). The average b* is 7.55 CIELAB units, which is relatively high (Figure 91). The pXRF measurements show that Facies 5 contains no Mo, low Pb and varies in concentration for other elements (Figure 92 to Figure 95).

Interpretation

The density of Facies 5 is increased from Facies 7, but is consistent with other deposits which have similar mica and quartz content in the Hindon Maar complex. The variability in density and magnetic susceptibility indicates heterogeneity of the facies and is consistent with breccias (Pirrung et al., 2008). Facies 5 has a density

similar to schist, despite being highly fragmented after drilling. This indicates that the deposit must contain some pyroclastic material, which would account for the heavier density despite lack of consolidation. Furthermore, elevated iron concentration is likely due to pyroclastic material. The coarse-grained nature of Facies 5 indicates that the facies is a result of gravity flows producing a turbidity current. Normal grading can be observed within this deposit, with coarser grains concentrated at the bottom and finer grains towards the top (Pirrung et al., 2003; Talling et al., 2012). The grain size found within Facies 5 is coarser than in previously described facies, indicating a less stable slope (Pirrung et al., 2008).

5.1.5 Facies 4

Description

Facies 4 is a fine-grained bluish-grey breccia. The matrix of the facies is comprised of fine to coarse sand and the gravel fraction consists of fine to medium sized clasts of schist and quartz. Gravel grains are angular to sub-angular. Vesicular mottles are found throughout this facies at an abundance of greater than 5% but less than 35% of the deposit. However, mottles appear in concentrated zones. Overall this deposit is massive, although laminations and grading are observed in discrete lenses in thin sections and visually in the core log (Figure 84; Figure 85). The overall density of this facies is 2.6 g/cc, which is high compared to many of the other facies (Figure 87). The average magnetic susceptibility for Facies 4 is 3.59 $x10^{-8}$ m^3/kg, which is midrange (Figure 88). The CIE colour values are like those of several of the other Facies: 2,3 and 5 (Figure 89 to Figure 91). pXRF measurements show variation in Y and Ti; Pb is detected in most measurements within the facies. The concentration of Sr varies little throughout the facies, and Rb concentration changes in a step-like fashion (Figure 95). Average pXRF data shows that Facies 4 has low Mn, Nb and Sr and high Zn and Rb (Figure 93).

Interpretation

Facies 4 is also interpreted to be the result of mass flows (Figure 84; Figure 85). Mass flows from Facies 4 would have occurred when the crater wall was relatively unstable, as indicated by the fine gravel-sized grains (Pirrung et al., 2008). Facies 4 is interpreted as the result of a series of debris flows and turbidity currents. In thick Facies 4 deposits, such as those in M1H2 and M3H3, the breccia contains fine gravel that does not show grading. It is supported within a silt sand matrix, which

is consistent with a debris flow origin (Talling et al., 2012). However, where thinner deposits occur, such as in M1H1, normal grading can be observed, indicating a turbidity current (Talling et al., 2012). Turbidite divisions such as the T_C and T_D are not observed; it is possible that they were destroyed during drilling, eroded by overlying flows, or were never deposited at all in that location, depending on flow conditions. There is a further decrease in density from Facies 5, which I interpret as being due to a decrease in overburden pressure and therefore compaction. The magnetic susceptibility is less than Facies 5, and so is the concentration of iron. This may be a result of continued weathering of iron-bearing minerals between the deposition phases of these two facies.

As Facies 4 contains the highest proportion of mottles of all facies, it is concluded that the mass flow failures resulting in Facies 4 occurred higher in the crater wall than other facies, where the percentage of country rock is less (Lorenz, 2003). As the mottles are interpreted as weathered pyroclastic deposits, they would have likely been concentrated in the upper sequences of the maar crater wall and possibly associated with the tephra ring (Bertrand et al., 2014).

5.1.6 Facies 3

Description

Facies 3 is a bluish grey, weakly consolidated, poorly sorted sandstone, ranging in grain size from fine to coarse sand with some gravel lenses. Discrete intervals of normal grading and laminations can be observed, although most of this deposit is massive. Facies 3 is found within all cores except for M3H5 and underlies Facies 1 in all holes where it occurs, except M3H1, where Facies 1 does not appear and Facies 3 is found below a soil deposit (Figure 84; Figure 85). Facies 3 generally overlies and/or is interbedded with Facies 4. Less than 2% of Facies 3 is made up of mottles. Mottles are found sporadically throughout the facies. The overall average density of Facies 3 is 1.97 g/cc and, compared with other facies, is relatively low (Figure 87). The average magnetic susceptibility is 6.36 $x10^{-8}$ m^3/kg, (Figure 88). The CIELAB measurements showed that Facies 3 is light in comparison to other facies (high L*) and is bluish green in colour (Figure 89 to Figure 91). pXRF data shows little change in elemental data over the facies, except for Rb which decreases in steps in M3H1 and M3H2. Average pXRF data shows

that Facies 3 has low Mn, Nb and Sr and high Zn and Rb. The key pXRF and Geotek data for Facies 3 are similar to those of Facies 2.

Interpretation

Facies 3 is believed to be the result of a series mass flows occurring in the lake. These mass flows are interpreted from the data as turbidity currents. This is because of the normal grading of coarse grains observed throughout the log. The mass flows are identified through core logging and thin sections where normally graded sediment is overlain by laminations. Sharp contacts between coarse material below and fine material above are interpreted to represent the base of mass flows. Furthermore, the density and magnetic susceptibility and the Rb concentration show step-like changes down the entirety of Facies 3 in M3H1 (Figure 84). These step-changes may indicate contacts between individual mass flows.

The density is lower than the underlying Facies 4; this is likely a result of a lesser degree of compaction and a lower abundance of gravel grains. The magnetic susceptibility along with the concentration of iron indicates a small population of ferro-magnetic minerals. Overall, the variability in density and magnetic susceptibility is mostly low, indicating relatively homogenous sediment between mass flows (Pirrung et al., 2008).

Crater wall failures generally result in the deposition of coarser grained material than other types of mass flows in maars (Pirrung et al., 2008). The presence of coarse grained material in the form of gravel-sized grains suggests that the slope of the crater wall was not entirely stable during deposition of this facies. Bedding in this facies is observed on the split core surface and has an apparent horizontal dip. This is interpreted as evidence that the maar had a flat floor at the time of deposition (Kaulfuss, 2017).

5.1.7 Facies 2

Description

Facies 2 is a non-consolidated bluish grey clay-rich silt with minor sand and gravel, predominantly laminated. The highest mineral abundance identified in the thin sections is mica at 38.8%, followed by quartz at 37%. Overall, Facies 2 is 35% clay, 54% silt and 11% sand (Table 2). Facies 2 underlies Facies 1 in M1H1, M1H2 and M3H1 (Figure 84; Figure 85). The average density of this deposit is 1.74 g/cc, which is relatively low compared to other facies (Figure 87). The average magnetic

susceptibility is 22.40 x10^{-8} m^3/kg, which is higher than all other facies, excluding Facies 8–10. Overall, Facies 2 has the second highest L* value, a mid-range a* value and a low b* value (Figure 89 to Figure 91). There were not many pXRF measurements for Facies 2, as limited continuous measurements were taken due to poor core quality. Where continuous measurements were taken in M1H1 and M1H2, they showed that the elemental distribution for Facies 2 displayed little change in concentration over depth. When compared to other facies, Facies 2 had low Mn, Sr, Fe, and Ti but high Pb and Rb (Figure 92 to Figure 95).

Interpretation

No organic matter was detected in Facies 2, nor were any burrowing or tracks observed that may indicate faunal activity. Such burrowing and tracks may have been destroyed by the drilling process. However, as there is no indication of faunal or floral remnants in Facies 2, it is unlikely that these were ever present. The elevated magFigure 93netic susceptibility is believed to be a product of the high clay content rather than influence of weathered pyroclastic material. This is because Facies 2 has low iron, indicating a small to no basaltic input, despite the deposit having elevated magnetic susceptibility. Clays are paramagnetic, and their magnetic susceptibility is much less than that of iron bearing minerals (Filimonova et al., 2016). However, clays still have a weak positive magnetic signature. Facies 2 comprises approximately 35% clay, which is sufficient to increase the magnetic susceptibility compared to the clay-poor Facies 3 and 4 (Dearing, 1994). The L* shows reflectivity and lightness within the core consistent with mica and quartz grains, which is backed up by observations made in the thin sections (Baykan & Yılmaz, 2010).

Facies 2 likely accumulated in the maars after some stabilisation of the crater wall through vegetation cover. Vegetation cover can limit the input of coarse granular material into the maar through slope stabilisation (Pirrung et al., 2008). Therefore, inputs into the maar at this stage are likely to have been the result of gradual weathering and erosion along the crater wall and the crater rim rather than the destabilisation of the crater wall face. This is because Facies 2 is comprised of fine grains with no outsize clasts, which indicates low-energy depositional processes and/or derivation from fine-grained parent sediment (Talling et al., 2012). Stratigraphic position of the facies and inferred revegetation of crater walls suggests a relatively long period of time has passed since the eruption. Also, relatively low

mottle content indicates little tephra input. The most likely explanation that is consistent with all these factors is background erosion of extensively weathered soil material around the crater. Relatively long exposure of pyroclastic materials may have resulted in complete disappearance. Heavy vegetation prevents all but the finest grains from being eroded. However, there is no indication of organic matter in Facies 2.

The laminations in the material indicate that the deposit formed by layer-by-layer deposition. It is likely that any mass flows that formed part of this deposit would have been debris flows rather than turbidity currents. This is because of the high percentage of clay particles identified (35%) (Table 2). The presence of even small amounts of clay in mass flows increases the cohesion within that flow through electrostatic bonds, therefore decreasing the likelihood of a turbidity current (Talling et al., 2012). Some flows form debrites with as little as 4% clay (Talling et al., 2012). However, debrites freeze *en masse* and do not produce primary sedimentary structures. Therefore, the combination of layer-by-layer deposition and high clay content suggests gradual background deposition rather than mass-flow processes. There was no obvious difference in grain size between laminations, nor was there any discernible pattern that could be associated with their occurrence.

Structureless sections of Facies 2 may have resulted from suspension of material following the re-sedimentation of material by wind or wave action on a debris fan (Pirrung et al., 2003). Similar deposits were found within Ukinrek East Maar, Alaska (Pirrung et al., 2008).

Another possible explanation for these structureless sections found within Facies 2 is that structure was destroyed during drilling. Significant sections of the core have been liquefied, for example 11.85–12.65 m. In M1H1, sections of laminated core are found interbedded with sections of liquefied core (Figure 27). Structureless sections may also be the result of deposition of a clean sand debrite (Talling et al., 2012). It is likely that Facies 2 was deposited in the timescale of a hundred years post maar eruption due the grain size and lack of organic matter (Pirrung et al., 2003).

5.1.8 Facies 1

Description

Facies 1 consists of highly organic black laminated carbonaceous sediments. This deposit was found at the top of all holes except for M3H1 and M3H5 (Figure 84; Figure 85). Facies 1 had the overall lowest average density, at 0.99 g/cc, and the second lowest magnetic susceptibility at 1.27 $x10^{-8}$ m^3/kg (Figure 87; Figure 88). When compared with other facies, Facies 1 has a low L* and b* and a slightly high a*, at 17.44, 0.0 and 1.53 CIELAB units respectively (Figure 89 to Figure 91). Geochemically, Facies 1 is different to other facies found in Maar 1 and 3, with high Mn and Rb and Low Y compared to other facies. Facies 1 also has higher Mo and lower Sr, Zn, Zr and Ti concentrations than other facies (Figure 92 to Figure 95).

Interpretation

Facies 1 consists of carbonaceous lake sediments which would have accumulated after the crater slope stabilised, most likely after the crater wall and tephra ring had accumulated sufficient vegetation cover to prevent mass flows and soil erosion occurring, preventing significant terrigenous input (Pirrung et al., 2003). Lack of terrigenous input is indicated by the low magnetic susceptibility. Organic matter has a weak negative magnetic susceptibility, while terrigenous material containing any ferrimagnetic component at all has a relatively strong positive signature. Therefore, a magnetic susceptibility as low as 1.27 $x10^{-8}$ m^3/kg indicates derivation from only a small concentration of terrigenous material (Dearing, 1994; Thompson et al., 1975). Furthermore, analysis of the organic matter plant and pollen has shown that the wider area was heavily vegetated (Möller et al., 2017). Extensive vegetation means that the area must have revegetated since the eruption, indicating sufficient time for vegetation between the eruption and the accumulation of lake sediments.

Facies 1 consists almost entirely of organic matter, which indicates that the bottom of the lake during the accumulation of Facies 1 must have been anoxic (Zolitschka et al., 2015). This organic-rich composition is reflected in the data by the low density, which is similar to that of other lake sediments consisting largely of organic matter (Timperley & Allan, 1974). Facies 1 is also laminated and there is no indication of bioturbation, indicating that the lake must have been permanently stratified while the 10 m of Facies 1 was deposited in each lake (Möller et al., 2017).

It is thus likely the maar lakes were monomictic or meromictic (Paternoster et al., 2016).

The carbonaceous lake sediment has preserved many fossils, including leaves, fish and insects (Kaulfuss & Moulds, 2015; Möller et al., 2017). Therefore, this deposit is significant for paleoclimate reconstruction, and likely shows seasonal variation in biogenic accumulation from which climate variability may be inferred. It is likely that the carbonaceous lake sediments represent thousands of years of lake deposition (Brauer et al., 1999; Lindqvist & Lee, 2009; Fox et al., 2015; Czymzik et al., 2016; Martin-Puertas et al., 2017). Carbonaceous lake sediments would have continued into swamp deposits which would have represented the final stages of lake infilling (Pirrung et al., 2003).

5.2 Facies of M3H5

5.2.1 Facies 10

Description and Interpretation

Facies 10 is a brownish orange, non-consolidated fine to coarse silt facies found at the bottom of M3H5. Medium gravel fragments are also present and are sub-angular to sub-rounded. Overall, this facies is poorly sorted. Facies 10 has a distinctive orange colour not seen in Facies 1–9 (Figure 42). The average density of Facies 10 is higher than any of the other facies, at 4.19 g/cc, although only slightly higher than Facies 8 and Facies 9. This density seems unlikely to be correct, as basalt only has an average density ~3 g/cc (McCanta et al., 2015). The absolute density measurement is likely poorly calibrated. However, I believe that the density is still high. The magnetic susceptibility of Facies 10 is less than Facies 8 and 9 but significantly more than Facies 1 to 7 (Figure 88), at 87.17 $x10^{-8}$ m^3/kg. The CIE colour values show extremes within Facies 10: L* is low compared to other facies at 15.78 CIELAB units, a* is higher than any other facies at 4.73 CIELAB units, and b* is also higher than all other facies tested at 13.28 CIELAB units. Overall the colour of Facies 10 is similar to Facies 9 and 8. Only a short interval of Facies 10 was retrieved through drilling, and therefore, limited data points were obtained. Due to the lack of information, it is difficult to determine the environmental deposition of Facies 10. However, it is likely associated with Facies 9 and Facies 8, as it is similar both in terms of geochemical data, density and magnetic susceptibility

5.2.2 Facies 9

Description and Interpretation

Facies 9 is a weakly consolidated grey sandstone found only in M3H5. Grain-size analysis indicates 57% sand, 26% silt and 16% clay. However, visual inspection defined this facies as a mudstone. The difference between the grain size observed in the split core versus the laser grain size analysis is attributed to aggregation of silt and clay particles, as with Facies 8.

No minerals could be identified in thin sections of this facies, as the sample was highly weathered and comprised mostly unidentified material. The density of this facies is similar to those of Facies 10 and Facies 10: 3.55 g/cc (Figure 87). Magnetic susceptibility is much less then Facies 8 and 10 at 35.77 $x10^{-8}$ m^3/kg although higher than Facies 1 to 7. The L* value is average compared to other facies, at 15.44 CIELAB units. a* is 1.81 CIELAB units and is significantly lower than Facies 8 and 10. b* is less than that of Facies 8 and 10. A similar environment of deposition is assumed as for Facies 8 and Facies 10. This is because Facies 9, much like Facies 8, has a high density, although the magnetic susceptibility is lower. The density is similar to basalt and the decrease in magnetic susceptibility is still significantly higher than the siliciclastic sediments. Also, Facies 9 has the second highest concentration of iron in the geochemical analysis, indicating the presence of mafic minerals. Facies 9 is located below Facies 8, therefore, it is likely that they have the same parent material.

5.2.3 Facies 8

Description

Facies 8 is a purplish-brown silt. The laser sizer identified the grain sizes for this deposit as 44.6% silt, 31.2% sand and 24.1% clay. It was not possible to identify any minerals present within the deposit in thin section because the particles were too fine grained.

The laser sizer findings were inconsistent with grain-size observations made on the core and in thin section. The laser sizer overestimated the proportion of silt and sand grains within the facies. Although the deposit does have some sand and silt grains, most of the grains are clay -sized. This observation is supported by both thin section analysis and the settling out of clay particles for XRD. Therefore, most of sand-

sized grains identified in the laser sizer must have been aggregated clay and silt size particles.

XRD analysis did not clearly identify clay minerals within Facies 8. Therefore, it is concluded that the deposits contain clay size particles but not necessarily many clay minerals. However, halloysite and interstratified illite-montmorillonite were tentatively identified in samples from this facies by XRD. XRD analysis produced noisy peaks making interpretation difficult. However, XRD did indicated some clay minerals. Facies 8 has a density of 3.77 g/cc, which is similar to other facies found in M3H3 but is higher than Facies 1–7. The magnetic susceptibility is higher than any other facies tested, at 91.10 $x10^{-8}$ m^3/kg. The L* value is relatively low, at 15.44 CIELAB units, but higher than that of Facies 9 and 10. Unlike the previously described facies, a* is positive, at 3.5 CIELAB units. The average b* is 10.91 CIELAB units and is higher than many of the other facies (Figure 91). Fe and Ti are higher in Facies 8 than in the previously described facies (Figure 94).

Interpretation

Facies 8 was drilled near a boulder field of largely basaltic boulders. The thin sections from these boulders indicated that they were not highly weathered, and minerals could be easily identified in thin sections (4.2 Thin Sections). By comparison, the thin sections of Facies 8 were highly weathered. However, some crystals were identified as being of a similar appearance to feldspars such as plagioclase, which were also seen as phenocrysts in the basaltic boulders. Secondary infilling of vesicles found within the basalt is similar to infilling of vesicles found within Facies 8. Both infillings were of a yellow amorphous material; however, the basalt infilling was spherulitically formed. Furthermore, the basalt was a bluish reddish-purple colour, similar in appearance to Facies 8. The extreme degree of weathering of Facies 8 is interpreted to mean that the material found in this facies is phreatomagmatic, which is different to that of the boulder field, which is magmatic. The boulder field has been $^{40}Ar/^{39}Ar$ dated to 14.603 ± 0.093 Ma old (Daphne Lee, pers. comm., March 2018). However, fossil pollen assemblages analysed within the Hindon Maar lake sediments date the maars to the early Miocene, 23–16 Ma (Kaulfuss & Moulds, 2015). If the pollen age is reliable, the boulder field is slightly to significantly younger than the Hindon Maars and may not be related to the maar craters.

No evidence of quartz or mica was found in Facies 8, unlike Facies 1 to 7. This indicates that Facies 8 was influenced by something other than the surrounding country rock. It is impossible to determine the exact environment of deposition for Facies 8 due to the high degree of weathering. However, M3H5 is interpreted as most likely volcanically derived from the tephra ring. This is because there is no indication that the material has been derived from the country rock and therefore must have a different parent material. Furthermore, the high density and magnetic susceptibility is consistent with mafic minerals. Analysis on tephra from Moon Lake, China, concluded that basaltic tephra found within the lake had a magnetic susceptibility of 80. This is similar to the magnetic susceptibility found within M3H5 (Sun et al., 2017). However, SEM analysis found mostly silica and aluminium with very little iron in samples from Facies 8. Both aluminium and silica are mobile elements and not suitable for rock classification (Floyd & Winchester, 1975). Silica and aluminium are the main component of clays, further indicating clays within the deposit. Furthermore, pXRF analysis indicates that Facies 8 is likely basaltic in origin because of elevated Fe and Rb concentrations.

Maar eruptions are phreatomagmatic and produce fine-grained pyroclastic material which forms much of the tephra ring (Agustín-Flores et al., 2015; Zimanowski et al., 2015). The fine-grained material has a high surface area and weathers quickly; weathering occurs more rapidly in low silica magma (Churchman & Lowe, 2012). Although felsic maars exist, they are uncommon and generally result in larger maar structures than that observed at Hindon (Ross et al., 2017). Furthermore, the basalt boulder field is evidence that basaltic activity has occurred nearby. Additionally, the age of the Hindon Maars is consistent with that of the Waipiata Volcanic Field, which is basaltic (Coombs et al., 2008; Möller et al., 2017). Finally, no juvenile pyroclasts are observed.

Based on the above considerations, I propose that the parent materials for Facies 8 were basaltic pyroclasts which have weathered into clays since the early Miocene. The boulder field has been dated to approximately 15 Ma and overlies the maar deposits, indicating a minimum age for Facies 8 of 15 Ma (Churchman & Lowe, 2012).

5.3 Primary Pyroclastic Materials

No primary pyroclastic material was observed in any facies of the Hindon Maar complex. This is unusual, as most maar lakes have pyroclastic material in the lower deposits (Eichhorn et al., 2017; Kaulfuss, 2017; White, 1990). Deposition of volcanic material can occur immediately following the formation of the crater and can continue for hundreds of years (Pirrung et al., 2003). Pyroclastic material is usually more heavily concentrated within the lower deposits of maars, such as the eruptive breccia and diatreme deposits (White & Ross, 2011). However, it is not uncommon to find some material throughout the siliciclastic deposits of maars (Lefebvre et al., 2013; Manville et al., 2009;Pirrung et al., 2003).

Water accumulates rapidly within maar craters and forms anoxic environments which prevent the weathering of material (Pirrung et al., 2008; Zolitschka et al., 2015). If pyroclastic material had been deposited into the lake immediately, it might be expected to have been preserved. Therefore, any pyroclastic material that was present in the maar catchment must have been weathered prior to its deposition into the presumed maar lakes in Maars 1 and 3 (Pirrung et al., 2003). Here, it is proposed that Facies 8–10 and the mottles found in Facies 2–6 represent the remnants of pyroclastic materials that were weathered on land before being deposited into the maar crater lakes.

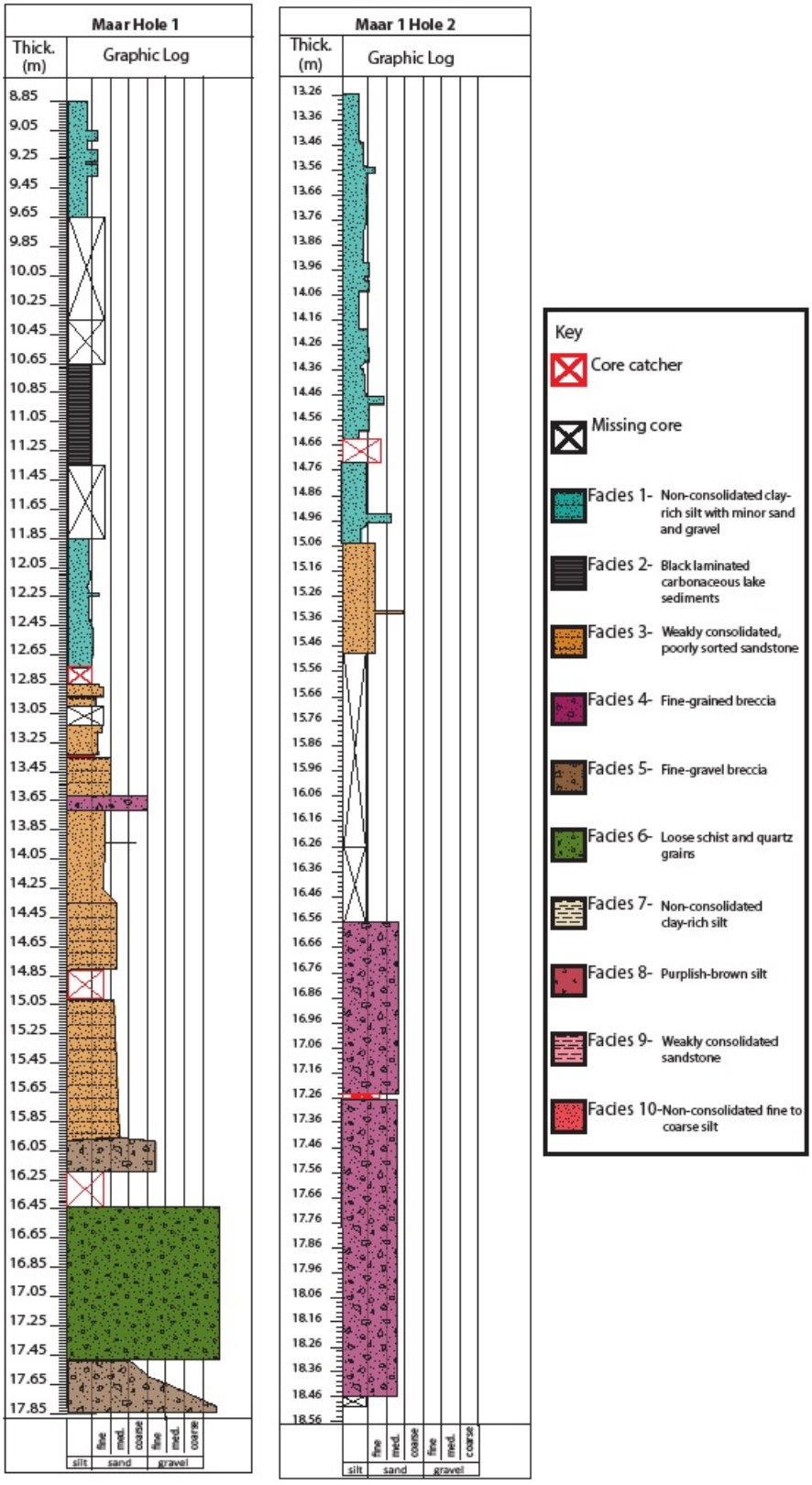

Figure 84: Facies in M1H1 (left) and M1H2 (right) showing Facies 1 to 6.

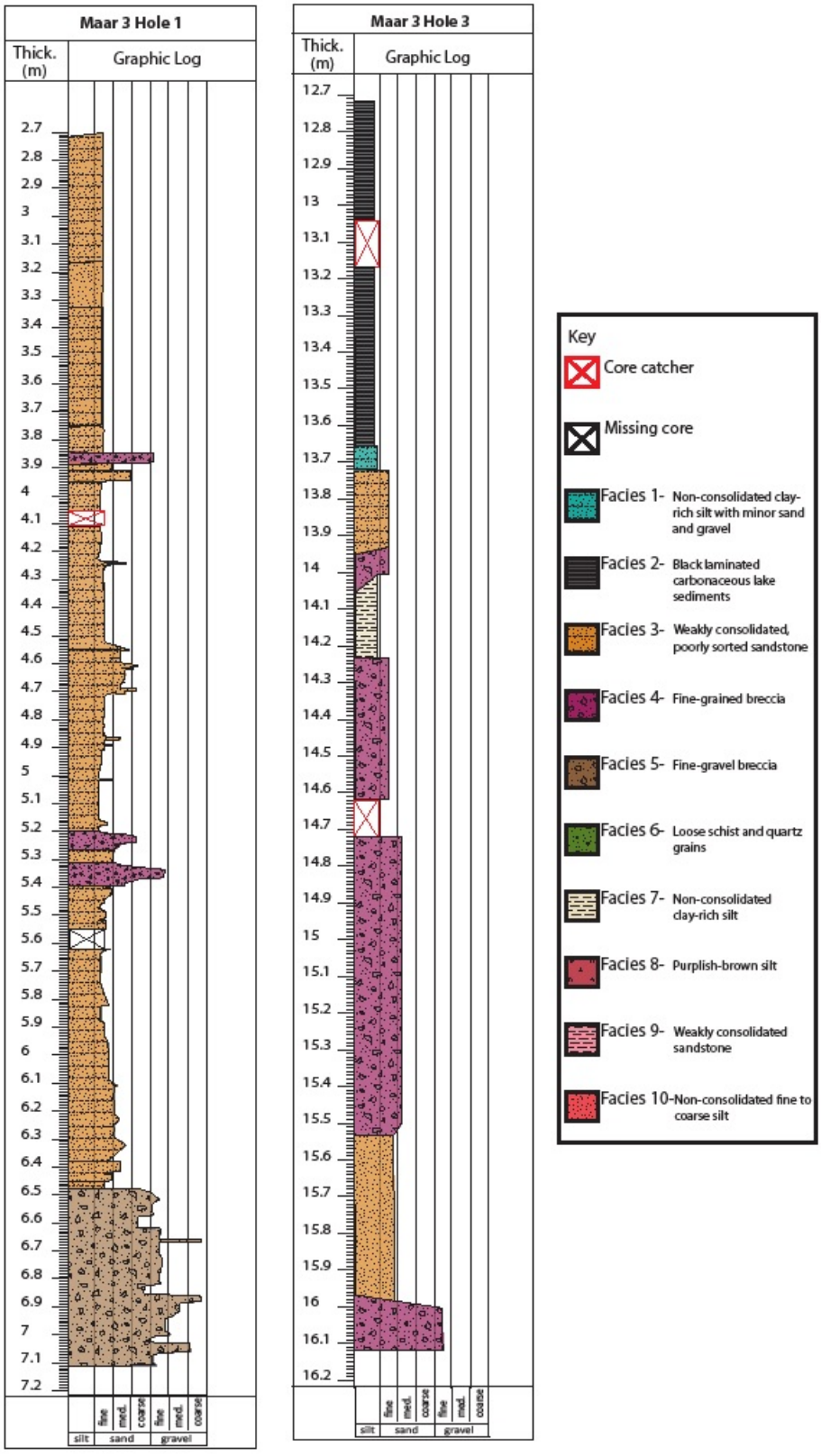

Figure 85: Facies in M3H1 (left) and M3H3 (right) showing Facies 1 to 7, excluding 6.

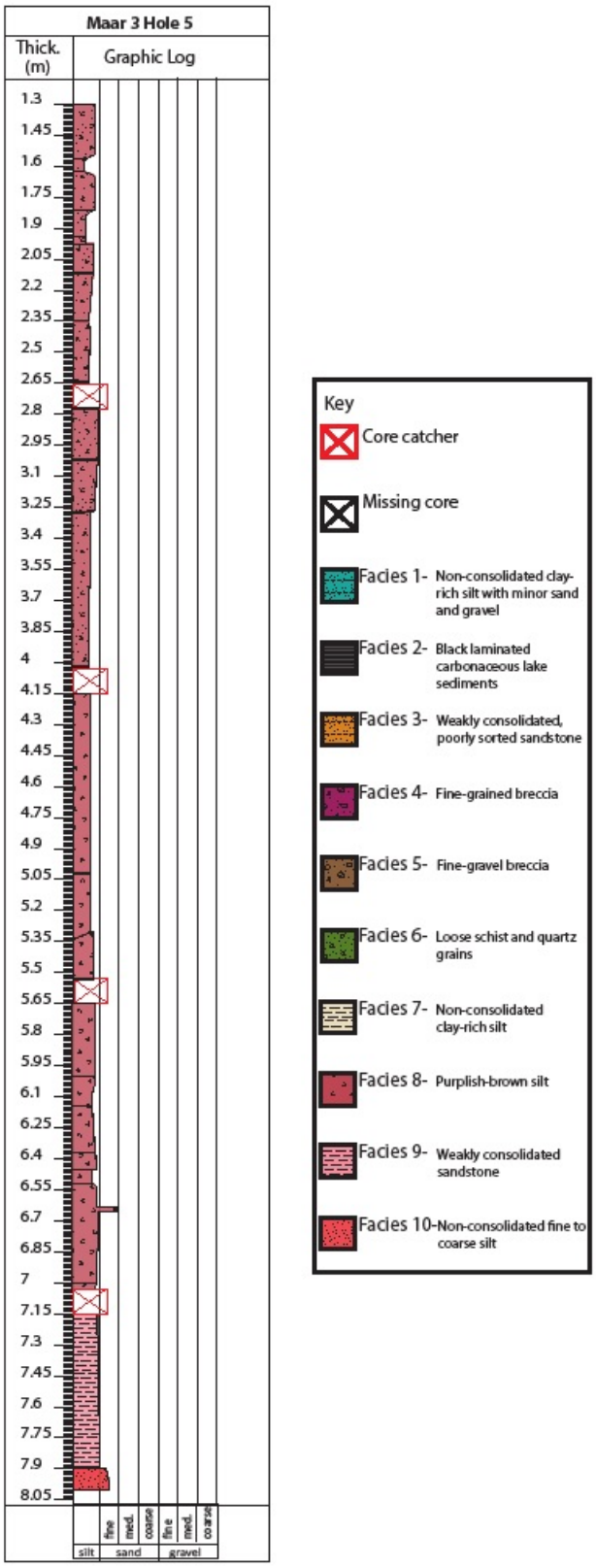

Figure 86: Facies in M3H5 showing Facies 8 to 10.

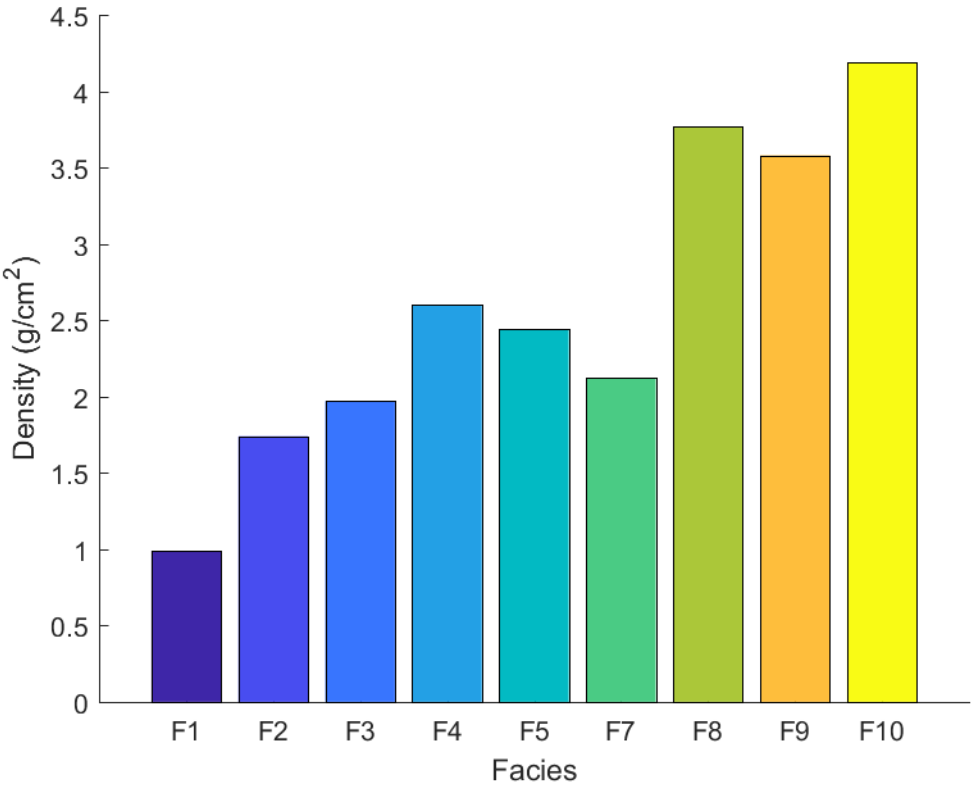

Figure 87: Average density across facies.

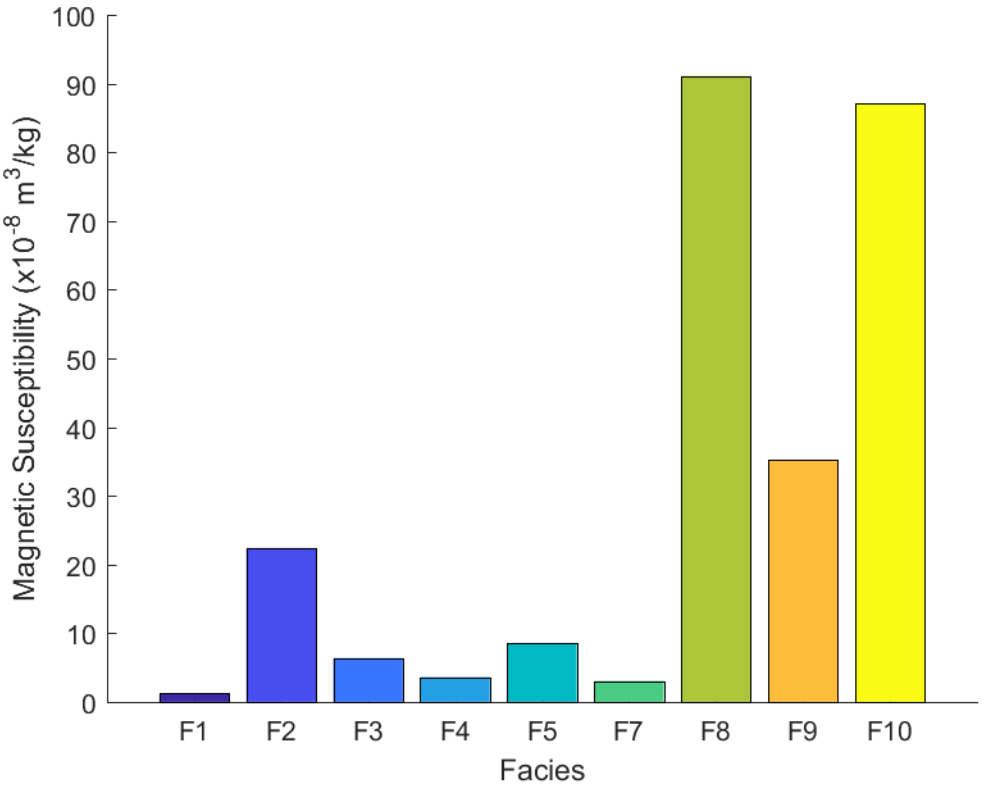

Figure 88: Average magnetic susceptibility across all facies

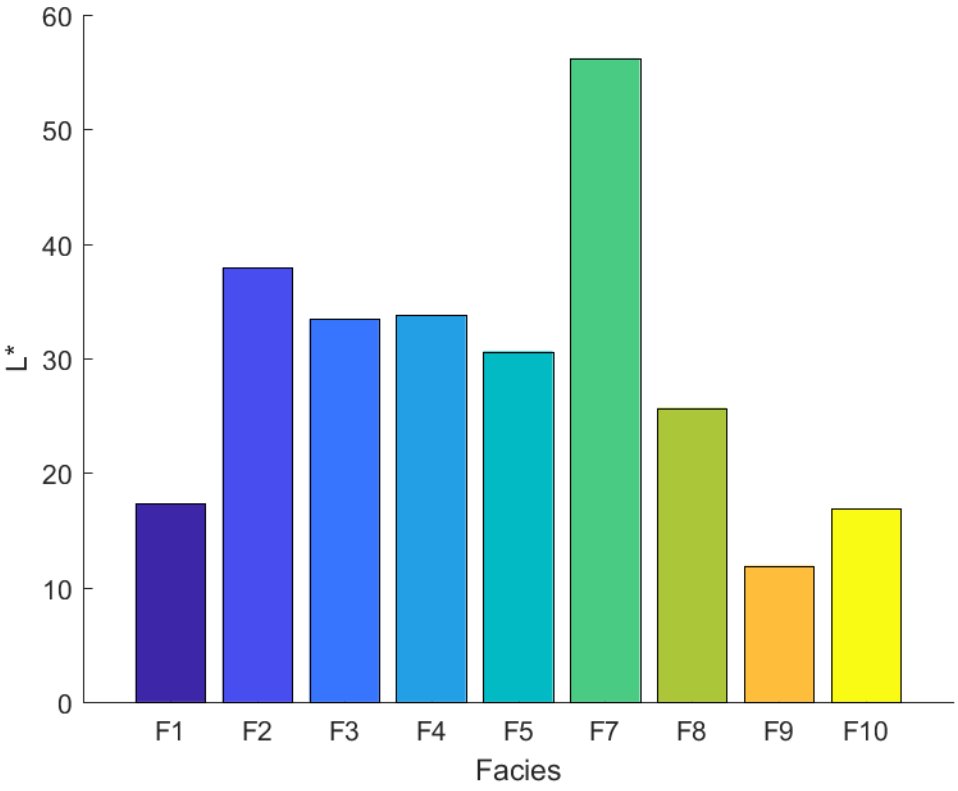

Figure 89: Average L* across all facies

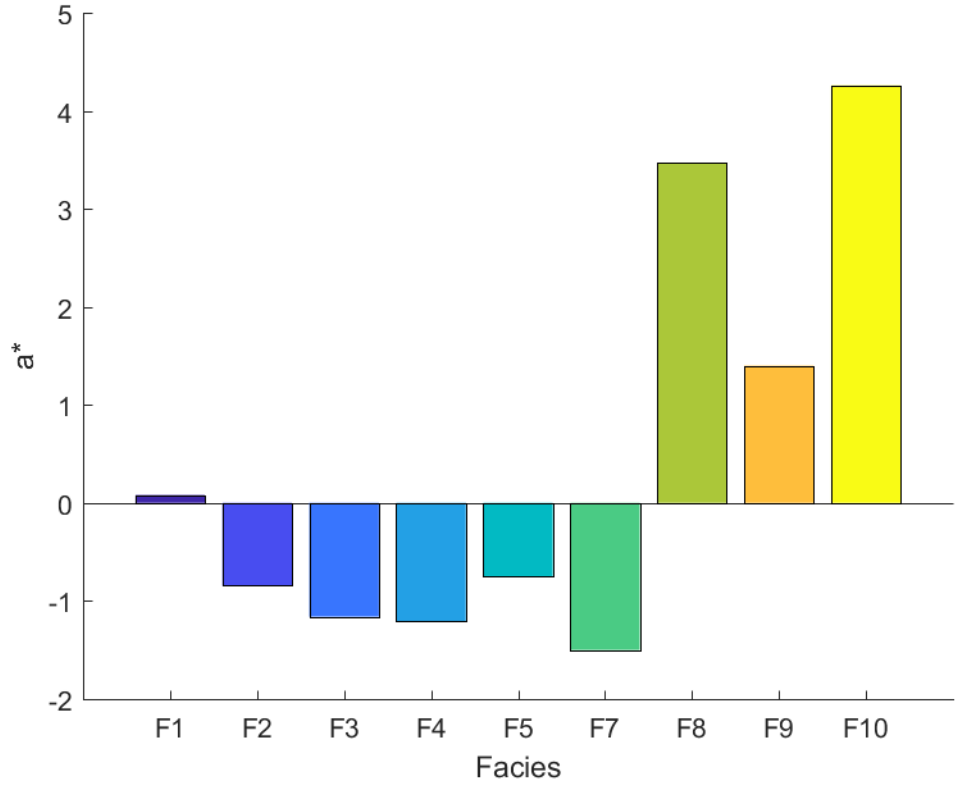

Figure 90: Average a* across all facies.

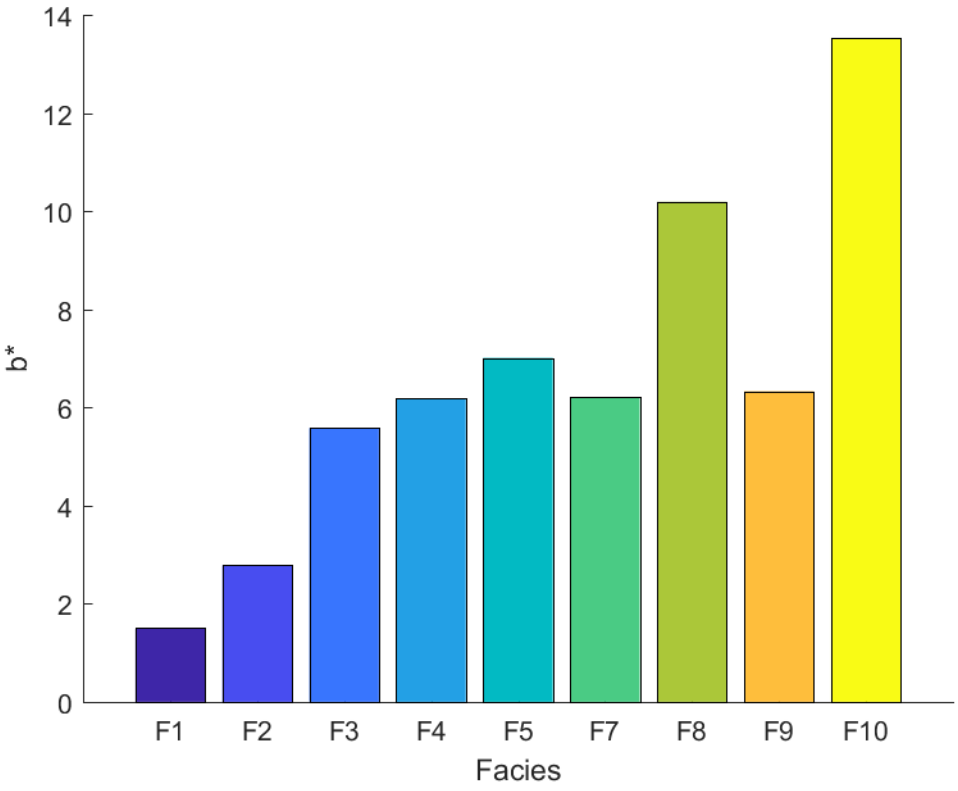

Figure 91: Average b* across all facies.

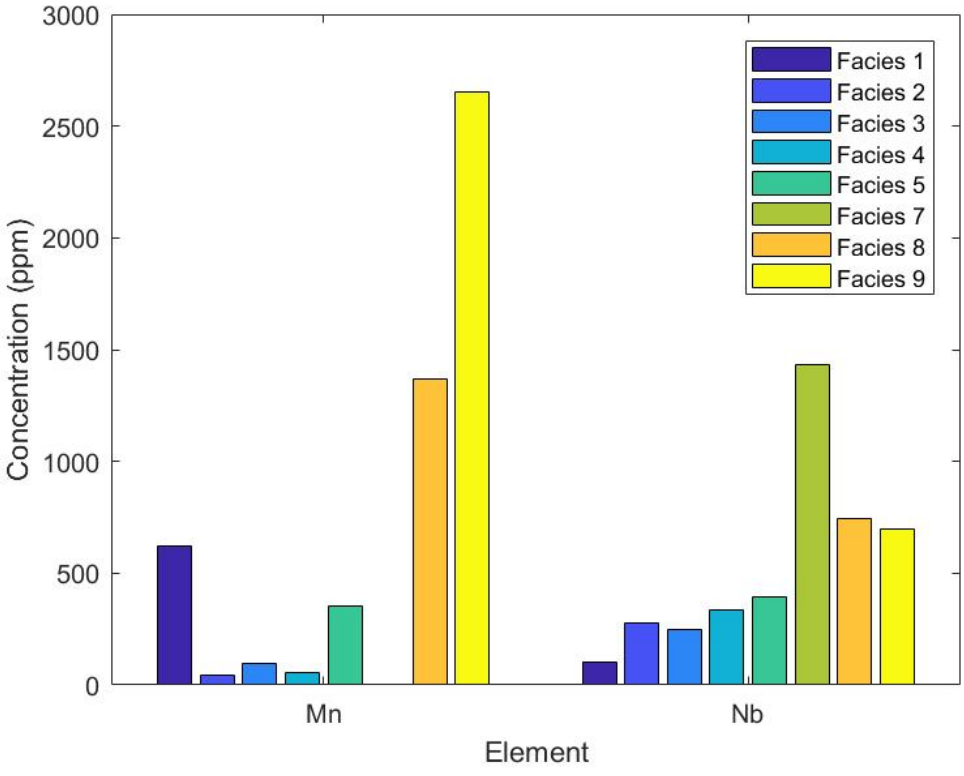

Figure 92: Averaged pXRF Mn and Nb for all facies.

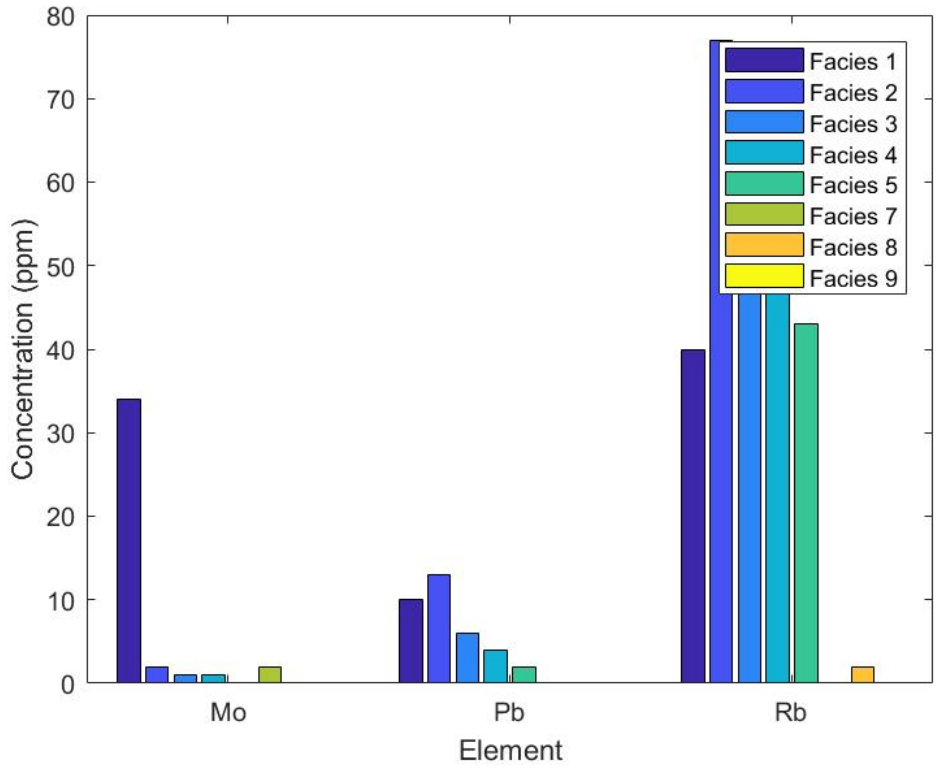

Figure 93: Averaged pXRF Mo, Pb and Rb across all facies.

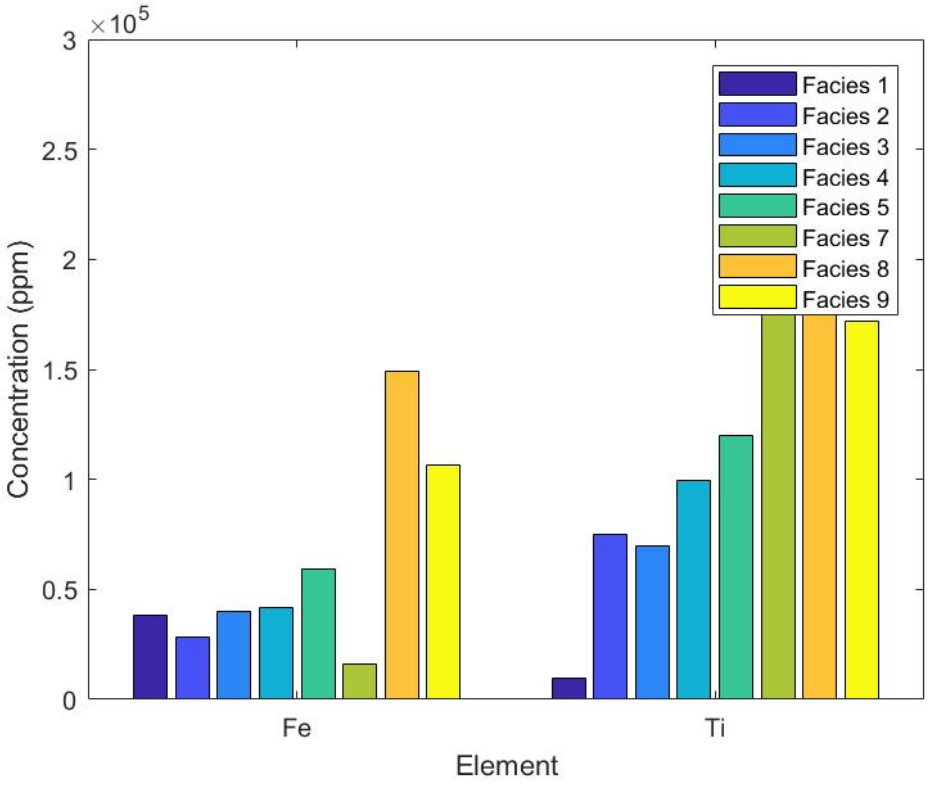

Figure 94: Averaged pXRF Fe and Ti across all facies.

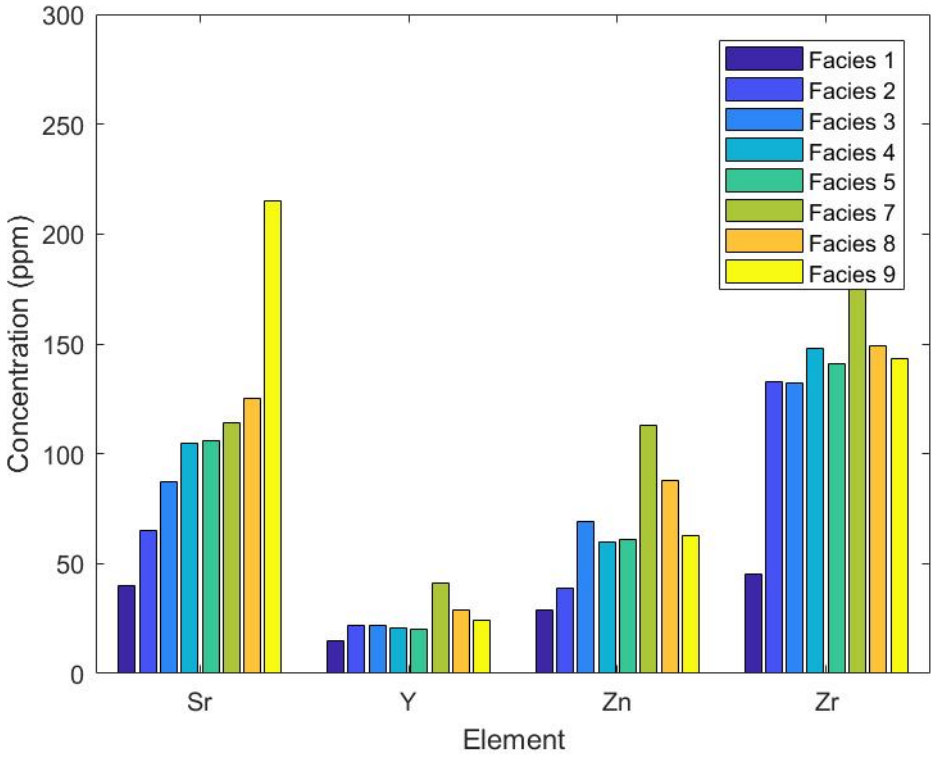

Figure 95: Averaged pXRF Sr, Y, Zn and Zr across all facies.

Chapter 6

Discussion

This chapter covers the geological evolution of the Hindon Maar Complex.

6.1 The Hindon Maar Complex Eruption Phase

The Hindon Maar complex erupted sometime between the beginning of the Miocene and 15 Ma, resulting in 4 maar craters (Möller et al., 2017). The length of the eruption is unknown. However, maar-forming eruptions generally last less than one year (Kurszlaukis & Fulop, 2013; Németh & Kereszturi, 2015). During the eruption of a typical maar, an area of 2–5 km surrounding each eruption site is covered in pyroclastic deposits. The tephra ring deposits are thinly bedded and thickest near the crater rim (Lorenz et al., 2017). The thickness of the tephra ring is dependent on the size of the eruption, with larger tephra rings corresponding with larger eruptions (White & Ross, 2011). The tephra ring usually dips between 5° and 20° away from the maar crater (Carrasco-Núñez et al., 2007; White & Ross, 2011), and consists of interstratified pyroclastic deposits comprising tephra, lapilli, tuff breccia and scoria blocks. These deposits are commonly found within tephra rings associated with maars (Self et al., 1980; Carrasco-Núñez et al., 2007; Németh et al., 2008). The tephra can consist of up to 90% country rock material, which I believe to be the case for the Hindon Maar complex as no primary pyroclastic material has been preserved.

Maar eruptions which occur in hard-rock environments produce steep sided craters, where the lower section of the crater wall is exposed country rock (Lorenz, 2003; Lorenz et al., 2017). The initial depth of the maar craters would have likely been between 10 and 200 m (Valentine et al., 2017).

Maars found within hard rock environments generally have lower water availability (Lorenz et al., 2017). Often, such maars transition into magmatic eruptions due to low water availability. Therefore, maars sometimes are accompanied with scoria cones, lava lakes and lava flows (Kereszturi et al., 2010; White & Ross, 2011).

No evidence of a tephra ring is observed in the field associated with either Maar 3 or Maar 1, although M3H5 has been interpreted as the highly weathered remnants of a tephra ring for Maar 3 (5.2 Facies of M3H5). No scoria cone or significant

pyroclastics, which could indicate magmatic activity, have been observed anywhere in the complex.

Maar eruptions are phreatomagmatic, and produce pyroclastic material that weathers quickly due to its small particle size, high surface area and unstable mineral content (Churchman & Lowe, 2012). Additionally, tephra rings often erode away early in the development of a maar crater (White & Ross, 2011). As the HMC is assumed to be Miocene in age, it is likely that the tephra ring existed but has subsequently been eroded (Németh et al., 2008; Kaulfuss & Moulds, 2015). A boulder field near M3H5 was determined to consist largely of basaltic boulders and is here interpreted as the remnants of a lava flow. These boulders are lying on the present-day ground surface overlying Maar 3. However, the author believes this lava flow was not formed as a result of the Hindon Maar eruptions, because it overlies the maar lake deposits. Although there is very little evidence of eruption style and no evidence of eruption intensity, there is no evidence to indicate that the Hindon Maar Complex differs from the generalised model of maar-forming eruptions described above.

6.2 The Structure of the Hindon Maar Complex

All four maars within the Hindon Maar Complex are within 1.5 km of one another, and at its greatest extent the complex is 3.5 km wide. The four maars have been identified through gravity surveys and are not thought to form one large maar structure (Martin et al., 2007), because 3.5 km would be abnormally large for a maar (Begét et al., 1996; Jordan et al., 2013). Although such a size is possible, this generally only occurs in areas with soft substrates or high water availability. This is unlikely for the Hindon Maar Complex, which is hosted in a hard-rock environment (Begét et al., 1996).

The deposits found within the three maars examined in this thesis are similar but not the same, and are here considered to have been deposited in different craters. Furthermore, the difference in elevation between Maar 3 and Maar 1 is approximately 80 m. Differential subsidence can occur within a maar, with greater subsidence occurring in the centre (Suhr et al., 2006; Kurszlaukis & Fulop, 2013). However, the overall topography is not consistent with a model in which all four maars are part of the same crater, with the elevation difference due to differential subsidence; Maar 3 has the lowest elevation yet is not in the centre, and the

surrounding topography does not indicate one large depression structure. I therefore conclude that the Hindon Maar Complex does not represent one single crater.

The coalescence of multiple maar vents has occurred at the Hindon Maars. Coalescence often results in shallow craters (Carrasco-Núñez et al., 2007; Jordan et al., 2013); however, Möller et al (2017) concluded that organic-rich sediments, such as those found in Maar 1 and Maar 3, indicate that the maars formed stratified lakes. The HMC also does not show the characteristics of known coalesced maar craters. For example, the coalescence of Lake Purrumbete, Australia, was a result of a migrating multiple vent system. This ultimately formed a 3 km maar structure with one diatreme (Jordan et al., 2013). However, the gravity anomalies for Hindon Maar indicate 4 separate diatremes (Bowie, 2015). Furthermore, the coalescence of multiple maar vents often results in one large maar structure (Begét et al., 1996; Jordan et al., 2013). As stated previously, this is not consistent with the present-day geomorphology at the site. Though coalescence is possible, it is thought to be unlikely at the Hindon Maar complex.

It is possible that the Hindon Maar complex is an example of a polycyclic monogenetic volcano, as described in Chapter 2 Literature Review. This could account for the proximity of the maar craters to each other. However, the gravity anomalies indicate that the maars are between 1 km and 1.5 km apart, which may exceed the defined distance between maar craters for polycyclic maars (Németh et al., 2010). As the actual size of the maar volcanoes is impossible to determine with the information currently available, whether the maars are within half the width of one volcanic edifice or not cannot be determined (Németh, 2010). The elemental distribution of lake sediments shows some variation in chemical composition. However, as this analysis is on clastic lake sediments and not on pyroclastic eruptive material, it is unknown whether the volcanic complex is polymagmatic or not. Without dates, the time between eruptions in the Hindon Maar complex cannot be determined. Polycyclic monogenetic volcanoes can have as little as a year between eruptions (Németh et al., 2001), or eruptions may be separated by tens of thousands of years (Kereszturi et al., 2010). Both scenarios are possible for the Hindon Maar complex.

As no primary pyroclastic materials was preserved in the maar sediments, it is unlikely that an eruption of one of the maars occurred whilst another maar was a lake. If this had been the case, the pyroclastic material produced from the eruption

event would likely have been deposited in the nearby lake and been preserved (Lowe, 1988; Haberle & Lumley, 1998; Schneider et al., 2017). Although this project did not drill to depths greater than 18 m, Facies 5, found in both Maar 1 and Maar 3, would have accumulated early in the evolution of the lakes (Chapter 5 Facies Description). This implies that the eruptions did not occur during the depositional period of the maar lakes, as they are preserved today. Facies 5 was likely deposited 10 to 100 years after the eruption (Chapter 5 Facies Description), and the lifespan of maar lakes can exceed 150,000 years; although, the thickness of carbonaceous sediment observed indicates the lake lifespan is likely 10,000 years (Pirrung et al., 2008; Fox et al., 2015); therefore, the eruptions may have been separated by more than a thousand years. Alternatively, all four eruptions in the Hindon Maar complex may have occurred within a ten to hundred year window.

It is possible that pyroclastic material was deposited into surrounding maar lakes and was subsequently eroded. Alternatively, one eruption could have produced the four craters over a short eruptive period. This would be similar to the Ukinrek Maars, Alaska, where two craters were produced within the space of four days (Kienle et al., 1980).

6.3 Maar 1

The results from Maar 1 show a typical succession of sediments that is consistent with other maars found throughout the world. Sediments fine upwards, beginning with breccia and finishing with carbonaceous lake sediment. Morphologically, Maar 1 is straightforward in comparison to Maars 2 and 3. Maar 1 is located within a shallow depression. Based on the present-day geomorphology, which shows an elongated depression at the location of the maar, the crater of Maar 1 is elliptical (section Map).

Deposition within the crater would have begun during the eruption, resulting in syneruptive deposits. These deposits would have consisted of mostly material from the crater wall and tephra ring (Pirrung et al., 2008). Maar craters can yield hundreds of metres of material (Mertz et al., 2000; Kaulfuss, 2017), but Maar 1 was only drilled to a depth of 17.85 m; therefore, it is unlikely that the syneruptive deposits were collected in the core. It is unclear how deep Maar 1 is, or how many metres of material are below 17.85 m. Previous research has included geophysical analysis of Maar 1, and it was hypothesised that there was 300 m of diatomite

preserved in Maar 1 (Bowie, 2015). This was found not to be the case during this drilling project.

It is likely that the deposits collected and tested within Maar 1 were deposited sub aqueously. Water accumulates in maars immediately following eruption, and therefore it is assumed that a lake would have formed very early in the evolution of the maar (Pirrung et al., 2008).

6.3.1 First phase of evolution for Maar 1

The first phase of evolution of Maar 1 consisted of a series of rock falls and rock slides (Figure 96; Chapter 5 Facies Description). No primary pyroclastics were observed, therefore it is assumed that the tephra ring consisted of a high proportion of country rock material and was stabilised before the first unit was deposited (Lorenz, 2007). Furthermore, the time between the eruption and the deposition of the first unit was probably insufficient for extensive weathering of fine-grained pyroclastic materials (Chapter 5 Facies Description) (Churchman & Lowe, 2012). The stabilisation of the tephra ring likely began in part due to the recolonization of exposed slopes by vegetation, the effect of stabilisation would increase with time (Pirrung et al., 2008).

Rock falls occurred frequently in the early evolution stage as a result of crater wall instability (Pirrung et al., 2008). Both the breccia and the gravel (Chapter 5 Facies Description) are indicative of instability of the crater wall. Due to the high proportion of country rock in these facies, I believe that the crater wall failures were lower in the crater, where country rock was exposed. Rock falls would have been localised, as evidenced by Facies 6, which is only observed in M1H1.

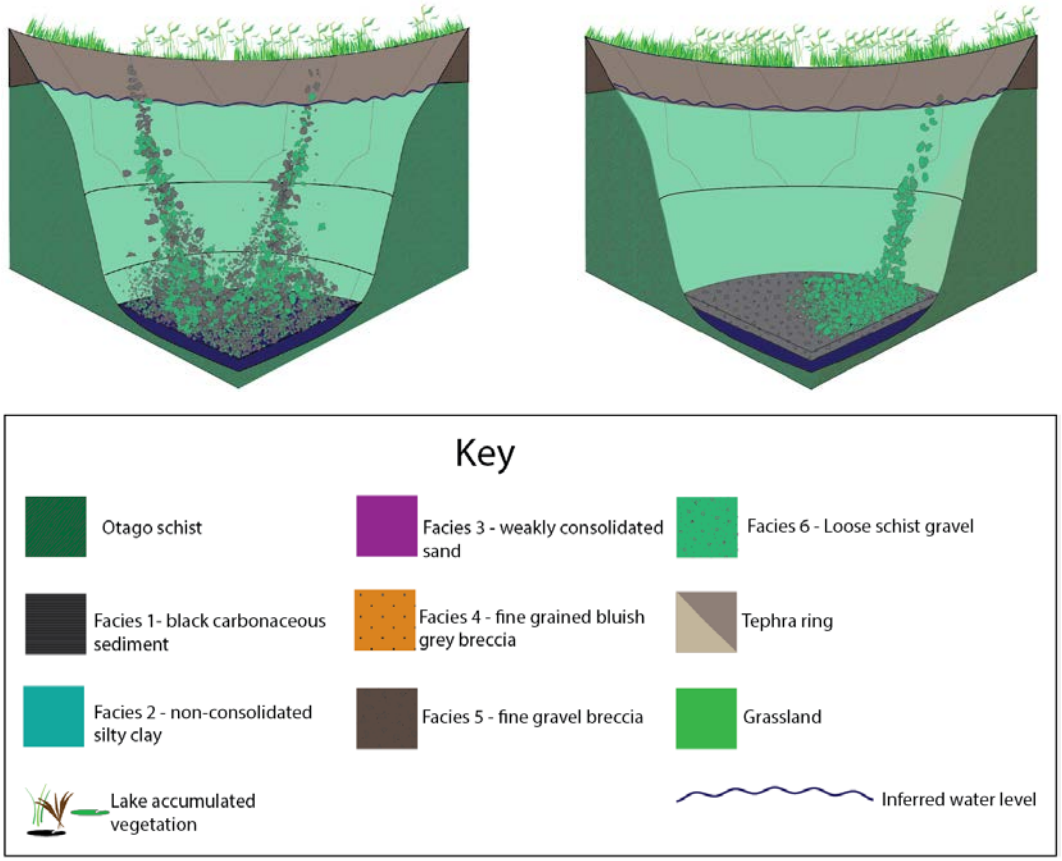

Figure 96: Infilling of Facies 5 and 6 into Maar 1, predominantly through rockfalls

6.3.2 First phase of evolution for Maar 1

The second phase of evolution consisted mostly of a series of mass flows into the maar

(

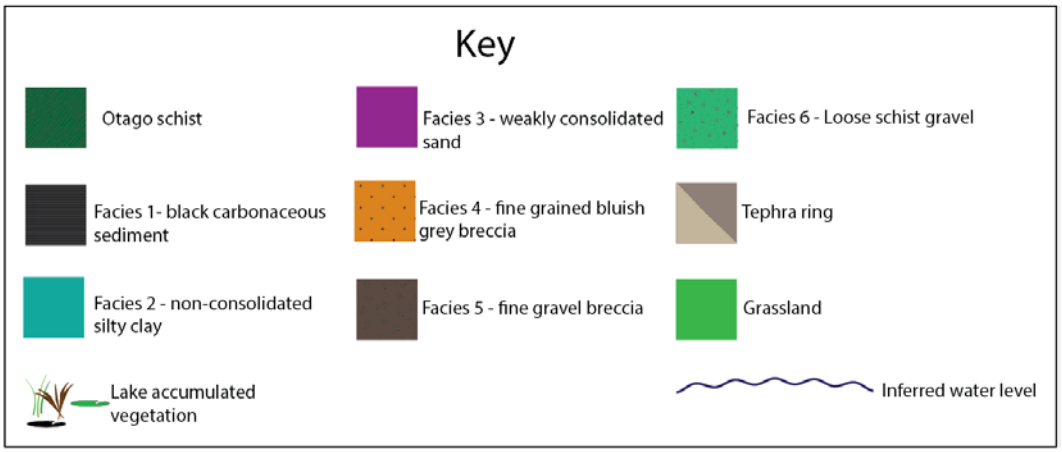

Figure 97; Chapter 5 Facies Description). Minor rock falls would have occurred near the crater walls and background sedimentation from erosion of the crater wall would have also occurred. The mass flows consisted of turbidity currents and debris

flows (Facies 2, 3 and 4). The overall grain size decreased in size across this phase from fine gravel breccias to silty clays. The decrease in overall grain size suggests that crater wall stability during the second phase of evolution was higher than in the first phase (Pirrung et al., 2008). However, the presence of a series of mass flow deposits is an indication of some crater wall and tephra ring instability. During the second phase, multiple debris fans would most likely have been found at the outer margins of the maar, as this is a feature observed in other maars (White, 1992; Pirrung et al., 2008). Debris fans were probably concentrated in areas where the crater wall was the steepest, with coarser grains observed closer to the crater wall. Debris fans can be a source of distal sedimentation in maars. Failures on the surface of these fans result in turbidity currents and debris flows (White, 1992; Pirrung et al., 2008; Schindler & Wuttke, 2015).

The mottles which occur in Facies 3, 4 and 5 have been interpreted in Chapter 5 Facies Description as weathered pyroclastic material. Their increased presence in Facies 4 compared to Facies 3 indicates that the failures that resulted in the deposition of Facies 4 occurred higher up the crater wall and into the tephra ring, as this is where the juvenile (and subsequently weathered) pyroclastic material is likely to have been located. After the crater wall became stable, Facies 2 is the result of background sedimentation.

Mass flows within maars behave in similar ways to mass flows in other systems (see Talling et al., 2012, for a detailed review). However, maars are usually small, closed basins, and therefore cannot have long runouts like those observed in marine subaqueous flows. As a result, flows with considerable energy reflect on impact with the opposite crater wall. This can occur multiple times until the energy of the flow has dissipated (Németh et al., 2008). Evidence for this has been found in Pula Maar, Hungary, and has been described by Németh et al. (2008), who found that this process produces soft sediment deformation and dewatering structures. Although no obvious soft sediment deformation and dewatering structures have been observed within Maar 1, it is possible that liquefied areas of core which have been interpreted as caused by drilling fluid injection may in fact be soft sediment deformation and dewatering structures (Figure 27). Liquefaction of the core appears in both M1H1 and M1H2 at similar depths (11.85–12.7 m and 13.26–14 m, respectively). If sections of liquefied core are in fact evidence of dewatering

structures, one reflected turbidite may have occurred, but the rest of the mass flow deposits observed within Maar 1 formed discrete deposits.

All but two of the mass flow deposits found in the Maar 1 cores are alike, but not similar enough to be regarded as being from the same flow. Thus, I here interpret them as representing discrete flows rather than multiple deposits from a reflected flow. Consequently, it is likely that most of these mass flows were small and did not have long runouts. This implies that no larger scale crater wall failures occurred during the second phase of evolution.

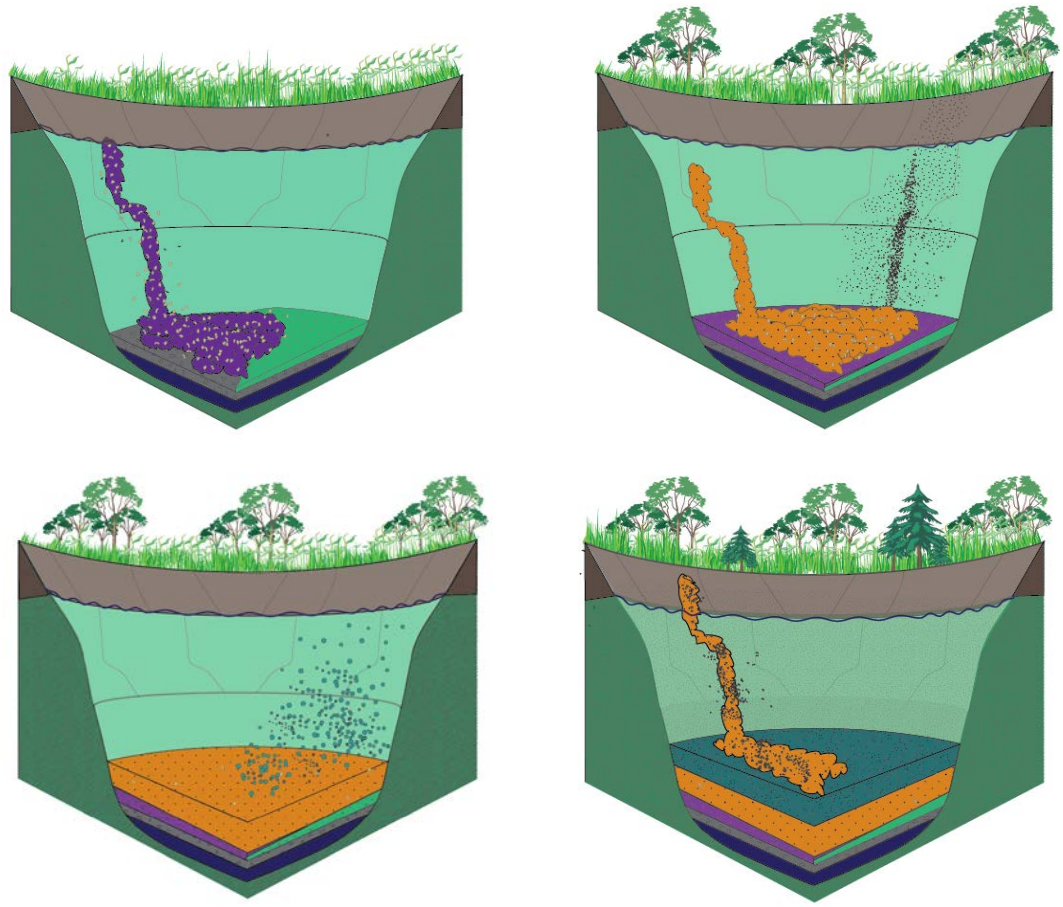

Figure 97: Showing a series of mass flows into the Maar crater consisting of Facies 2 to 4.

6.3.3 First phase of evolution for Maar 1

At the end of the second phase, the crater wall became stable and mass flows stopped occurring (Figure 98). This marked the beginning of the third phase of evolution. During this time, large quantities of organic matter accumulated, resulting in Facies 1. Facies 1 is a laminated organic mudstone and diatomite, which indicates a calm deep permanently stratified lake where leaves and pollen from surrounding forests accumulate (Möller et al., 2017). These deposits likely reflect seasonal variation in vegetation growth and would have accumulated for thousands of years (Pirrung et al., 2003; Fox et al., 2015). As organic matter accumulated, the maar would have eventually turned into a swamp, after which the maar would become completely infilled (Pirrung et al., 2003). However, no swamp deposits have been preserved.

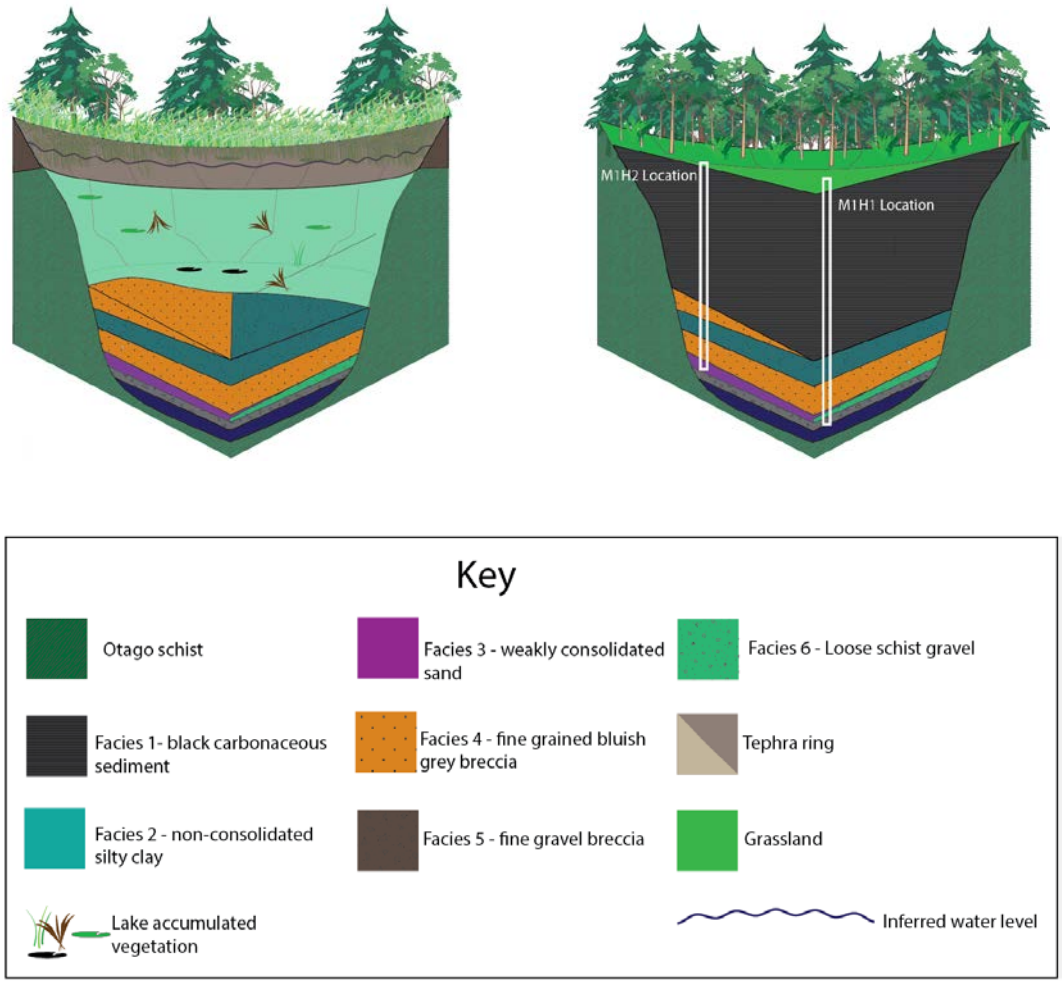

Figure 98: Showing the final depositional phase of Maar 1 where organic matter accumulated, ultimately forming the topography seen today.

6.4 Maar 3

The lake sediments associated with Maar 3 do not occur in a circular depression like Maar 1. However, they do occur in a depression between Maar 2 and M3H5 (Figure 83). The gravity anomaly assumed to represent the Maar 3 diatreme is centred around M3H5. There is no significant gravity anomaly located underneath the lake sediments in M3H1 and M3H3 (Figure 4).

Gravity and magnetic anomalies have been successfully used in many cases to determine the location of maars (Mrlina et al., 2009; Blaikie et al., 2014). This is because diatremes host dense material with is dense than the surrounding rock. However, in some cases the gravity anomaly is offset from volcanic landforms observed in the field; all calculations tend assume homogeneity of below ground volcanic structures (Cassidy et al., 2007; Blaikie et al., 2012). Domain Maar in the Auckland Volcanic Field has an offset gravity anomaly, however this has been attributed to a nearby scoria cone, and not an offset between the Maar diatreme and Maar crater. (Cassidy et al., 2007). It is important to note that the diatreme found underneath maars is what forms the gravity anomaly used to detect them. There is no evidence in literature which shows a diatreme not in the centre of the maar crater. Geophysical analysis has been conducted extensively on the subsurface morphology of maars but there are few studies of the geophysical data comparing the subsurface morphology to eruptive histories and above ground volcanic features (Cassidy et al., 2007).

It is assumed that the lake sediments associated with Maar 3 are offset from the gravity anomaly. If the boulder field is larger than what was expressed at the surface it may have been enough to offset the gravity anomaly. This does not explain why lake sediments are found adjacent to the gravity anomaly. Therefore, there must have been other geological processes which have occurred. The lake sediments located in between M3H5 and Maar 2 are associated here with Maar 3 rather than Maar 2 because the gravity anomaly over Maar 2 neatly covers the positive feature of Maar 2. M3H5 is here interpreted to have drilled through the tephra ring of Maar 3 (see Chapter 5 Facies Description for further discussion of this interpretation). As

mentioned above, the intensity of the eruptions is unknown; therefore, it is possible that the deposit associated with the tephra ring at M3H5 continued downwards for several metres.

6.4.1 Evolution of Maar 3

Maar 3 follows the same three evolution phases as Maar 1 (Figure 99: Showing a simplified model for sediment accumulation within Maar 3, starting with rockfalls, later showing mass flows and ending with lake sediment accumulation.). The first phase of evolution of Maar 3, represented by Facies 5 and 4, is a series of rock falls associated with crater wall instability. The second phase is a series of mass flows of gradually decreasing grain size, represented by Facies 2, 3 and 4. However, unlike in Maar 1, there is no evidence of reflective turbidity currents. Facies 4 is also thicker in Maar 3 (Figure 99).

During the second phase, a localised slump deposit occurred in Maar 3, forming Facies 7 (Figure 99). Slump deposits are often found within biogenic sediments in maars, but are not limited to these sediments (Pirrung et al., 2003; Kaulfuss, 2017). The formation of slump deposits is often the result of subsidence within the maar crater due to diatreme compaction (Suhr et al., 2006).

The third phase of evolution is the accumulation of black carbonaceous sediment. No published studies have been conducted on the carbonaceous sediment of Maar 3. However, it is similar to the carbonaceous sediment of Maar 1 and is therefore assumed to represent a similar environment. This indicates that Maar 3 produced a deep lake that would have ultimately infilled, producing a swamp (Figure 99) (Pirrung et al., 2003).

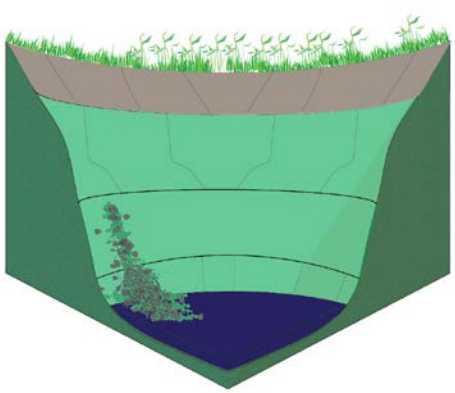

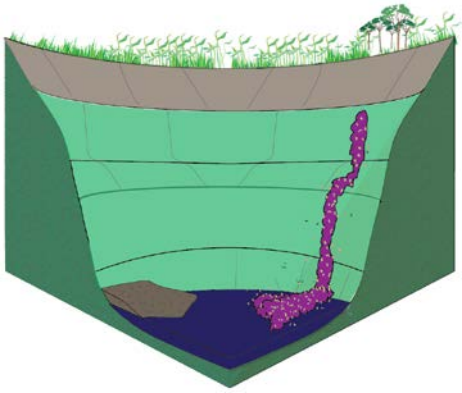

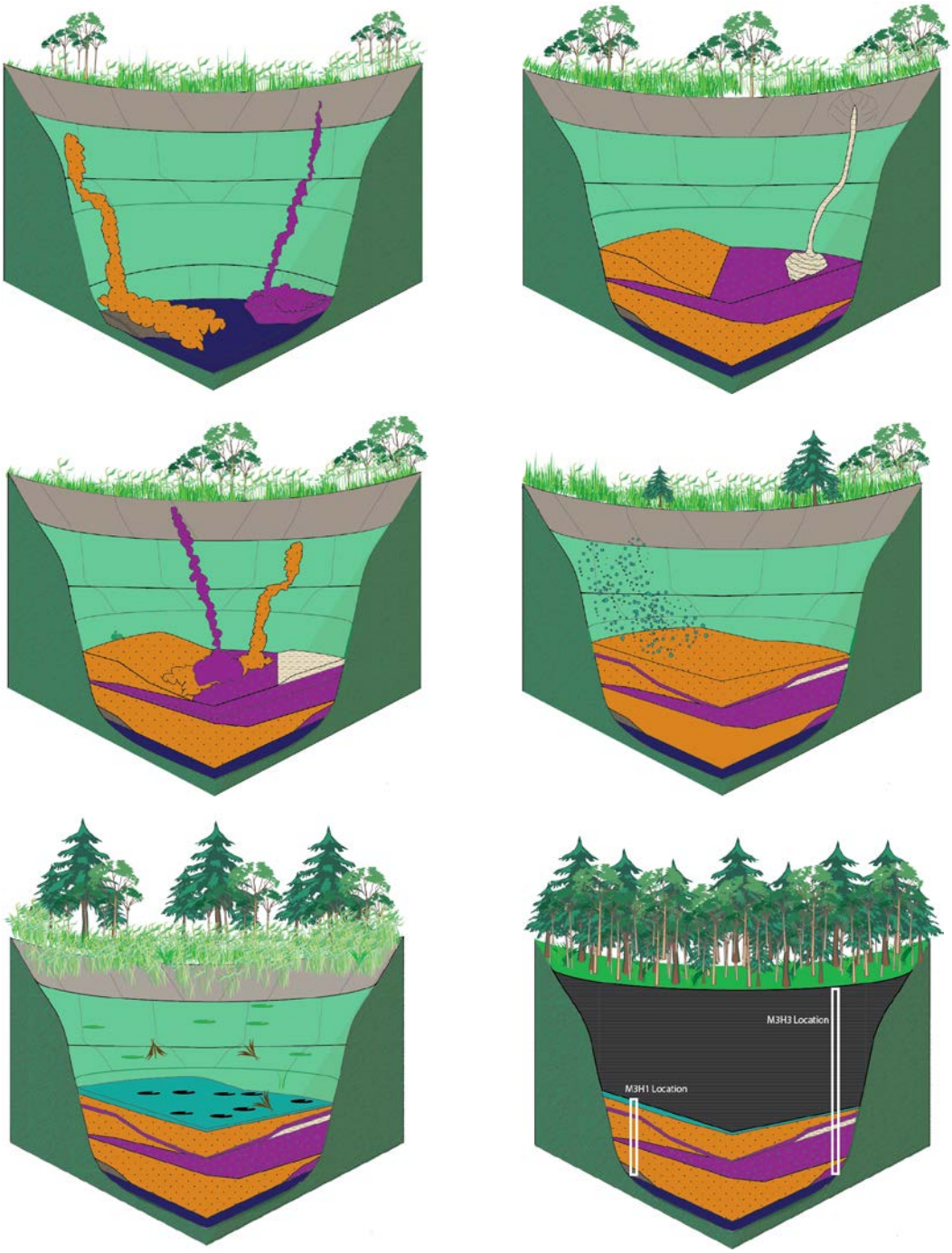
M3H3 Location
M3H1 Location

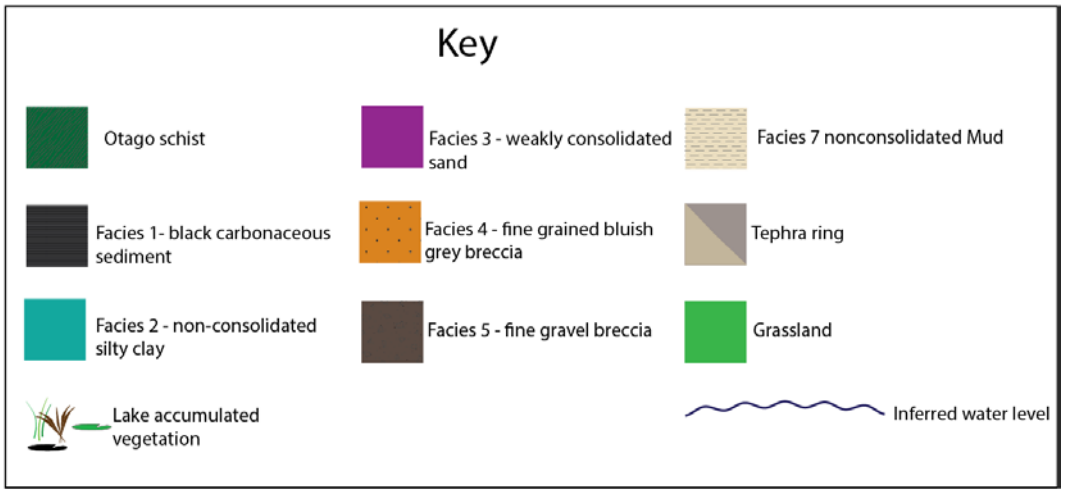
Key
Otago schist
Facies 3 - weakly consolidated sand
Facies 7 nonconsolidated Mud
Facies 1- black carbonaceous sediment
Facies 4 - fine grained bluish grey breccia
Tephra ring
Facies 2 - non-consolidated silty clay
Facies 5 - fine gravel breccia
Grassland
Lake accumulated vegetation
Inferred water level

Figure 99: Showing a simplified model for sediment accumulation within Maar 3, starting with rockfalls, later showing mass flows and ending with lake sediment accumulation.

The basic model of sedimentation described in Maar 1 partially applies to Maar 3, as shown in Figure 98. However, it does not adequately account for the differences in deposits found between M3H1 and M3H3. No lake sediments are found in M3H1, and lake sediments are found in M3H3 to a depth of 13.65 m, despite M3H1 and M3H3 having been drilled approximately 70 m away from each other (Figure 83). Sediments within maars can vary spatially, especially between crater wall and distal deposits (Pirrung et al., 2008). The lack of lake sediments in M3H1 indicates that either the lake sediments have been eroded from the top of M3H1, or they were never deposited in the first place. It is possible that M3H1 represents a debris fan building out from the edge of the crater. Debris fans are commonly found in maars (Pirrung et al., 2008). The building up of a debris fan could infill the side of the maar crater, which would therefore prevent lake sediment accumulation. However, debris fans produce distinct bedding, none of which has been observed (White, 1992). Furthermore, the grain sizes observed in M1H3 are predominantly silt to fine sand which are generally deposited further away from the crater wall (Pirrung et al., 2003). Lastly where M3H1 was drilled, the debris fan would have to have extended to the top of the crater wall to prevent depositions of lake material before the crater wall became stable where lake sediments would have been deposited. Therefore, it is concluded that it is unlikely that M3H1 is a debris fan. Two other possible origins for this spatial variability are discussed below

6.4.2 Fault Within Maar 3

If lake sediments were originally deposited at the site of M3H1, this part of the lake bed may subsequently have been uplifted or subsided due to faulting, resulting in the removal of the lake sediments by erosion (Figure 100). Maars in a monogenetic field are often aligned with and occur along identified faults, and ring faults may form around maar diatremes (Lorenz, 1986; Jordan et al., 2013). Active faulting has occurred in Otago since the Hindon Maars were formed (Jackson et al., 1996). Therefore, it is possible that faulting could have occurred in between M3H1 and M3H3. Resulting in M3H3 being downthrown. However, the deposits found in M3H1 and M3H3 do not correlate well with one another (Figure 100), therefore

comparing the deposits in M3H1 to M3H3 in order to determine the presence or absence of a fault is difficult. Furthermore, faults within maar basins generally result in subsidence (Suhr et al., 2006; Kurszlaukis & Fulop, 2013).

During the early Miocene, the reactivation of Oligocene-aged normal faults resulted in high angle reverse faulting within the Otago region (Alder et al., 2016; Smith et al., 2017). However, exact the age of the Hindon Maar complex is unknown. It is early Miocene in age and may be as young as 15 Ma (Kaulfuss & Moulds, 2015; Möller et al., 2017), and the reactivation of normal faulting occurred for only 5 million years from the start of the Miocene. It is therefore possible that the maars formed after early Miocene faulting (Alder et al., 2016).

It is difficult to establish the presence or absence of faults by field observations, as there is very little rock exposure. Where rock is exposed, it is greenschist, which does not allow for easy observation of offsets. However, given that the age of the maars most likely post-dates the reactivation of Otago faults, it is unlikely that faulting which resulted in uplift is the reason for the lack of black carbonaceous sediment in M3H1.

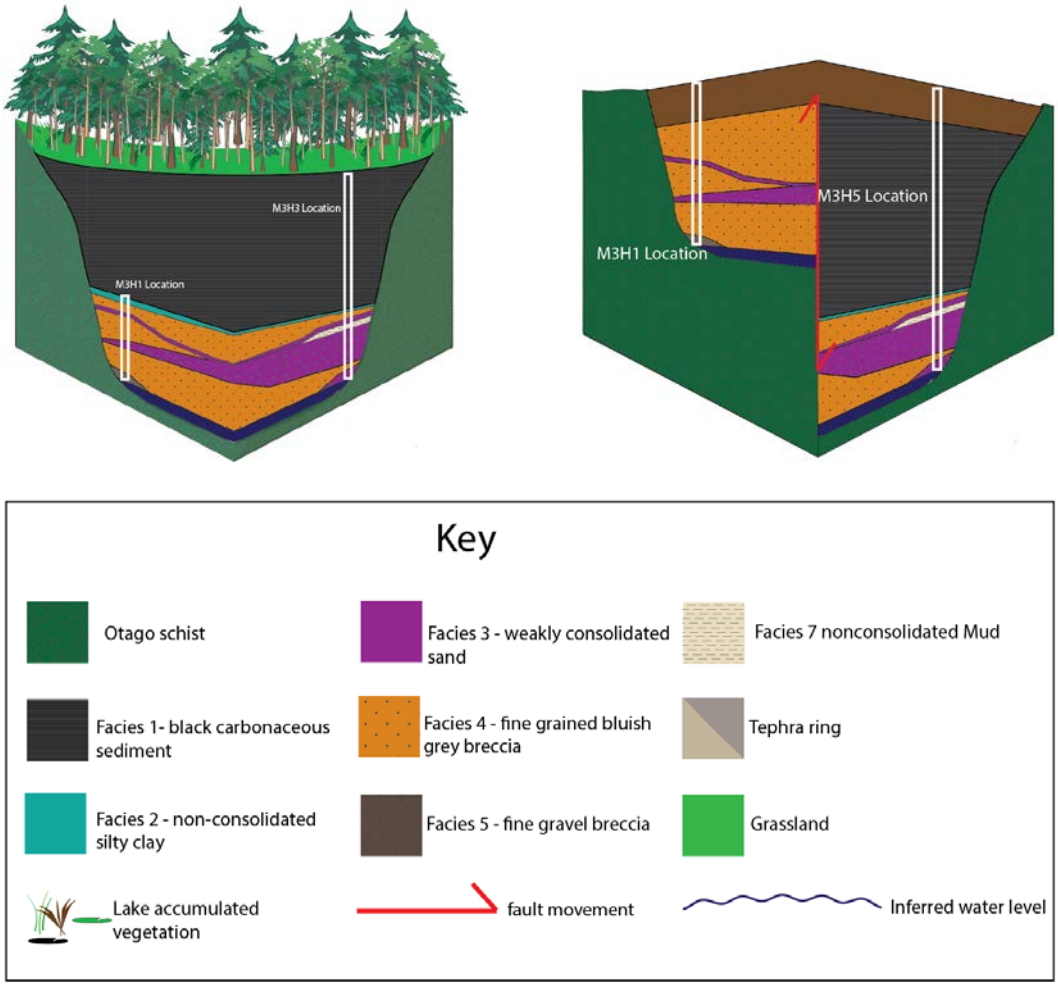

Figure 100: Showing the final outcomes of lake sediment deposition using the simple model versus the scenario of a fault.

6.4.3 Differential Subsidence of the Diatreme

It is possible that no or very little lake sediment accumulated at the site of M3H1. This may have been the result of differential subsidence of the maar basin. Subsidence within maar basins can exceed 1 km and can last for millions of years (Suhr et al., 2006; Delpit et al., 2014). The subsidence within the maar crater creates accommodation space, allowing for continuous deposition of material (Figure 101) (Manville et al., 2009; Schindler & Wuttke, 2015; Fristad et al., 2017). Subsidence is generally greater in the centre of the maar, resulting in greater deposition at that point (Suhr et al., 2006). Therefore, it is possible that M3H3 occurred closer to the centre of the maar, allowing for greater accumulation of lake sediments. However, the differential subsidence between the two holes would have been at least 10 m over 70 m. Furthermore, although the gravity anomaly is offset from the lake sediments, it is still the likely location of the diatreme. This is significant because subsidence in maars generally occurs in the diatreme (Suhr et al., 2006; Delpit et al., 2014). Subsidence within maar diatremes is often the result of the compaction of material within the diatreme which, over the space of millions of years, results in subsidence of the above ground crater (Suhr et al., 2006). As the lake sediments in Maar 3 are offset from the diatreme, subsidence in the crater would be of a lesser extent and both M3H1 and M3H5 would be on the outer edge of the diatreme, rather than M3H5 occurring at the outer extent of the diatreme and M3H5 occurring closer to the centre of the diatreme. Neither of these two scenarios adequately explains what is occurring in Maar 3. It is possibly a combination of both processes, as both subsidence and faults occur regularly in maars. However, a satisfactory conclusion cannot be made with the information available.

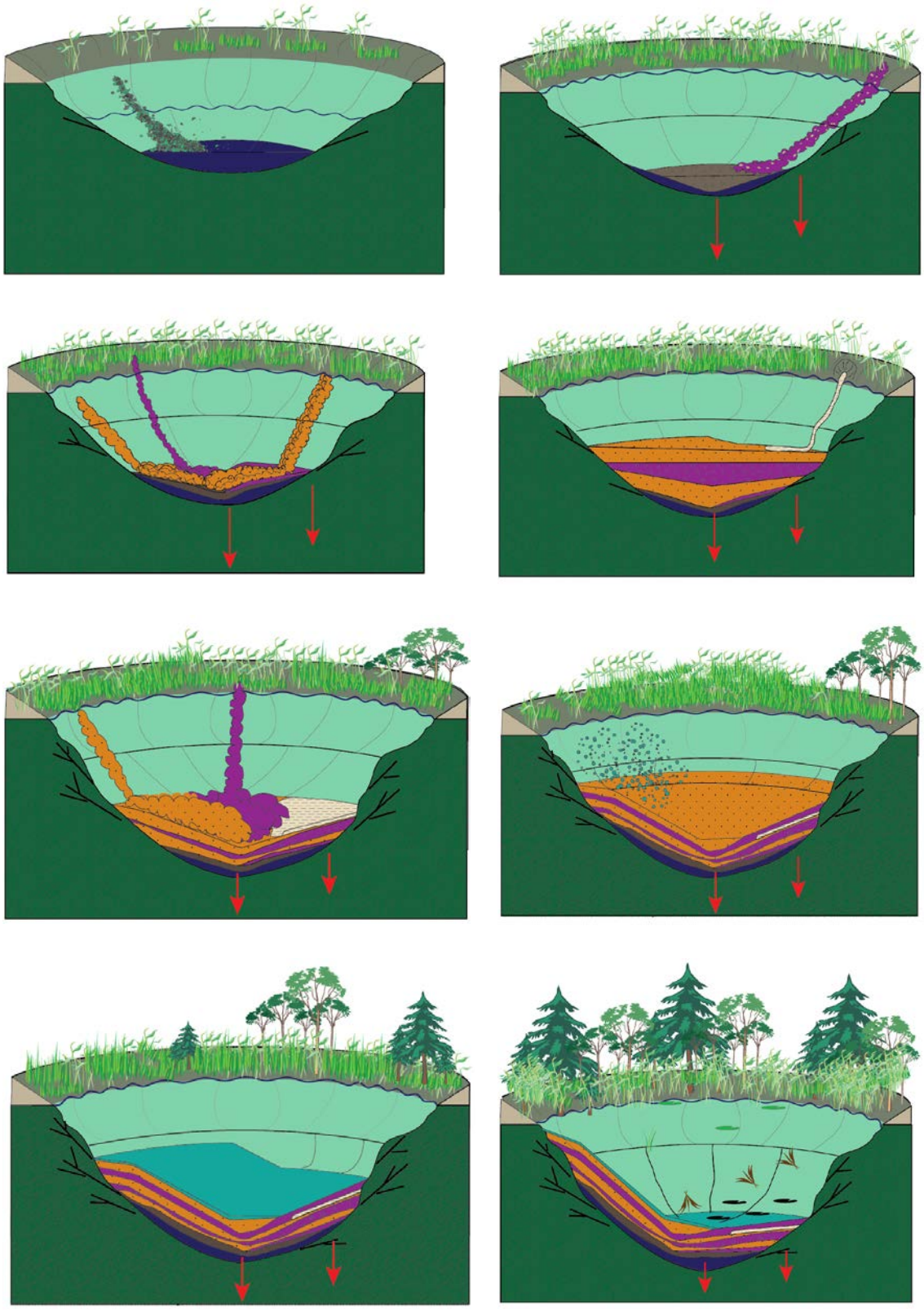

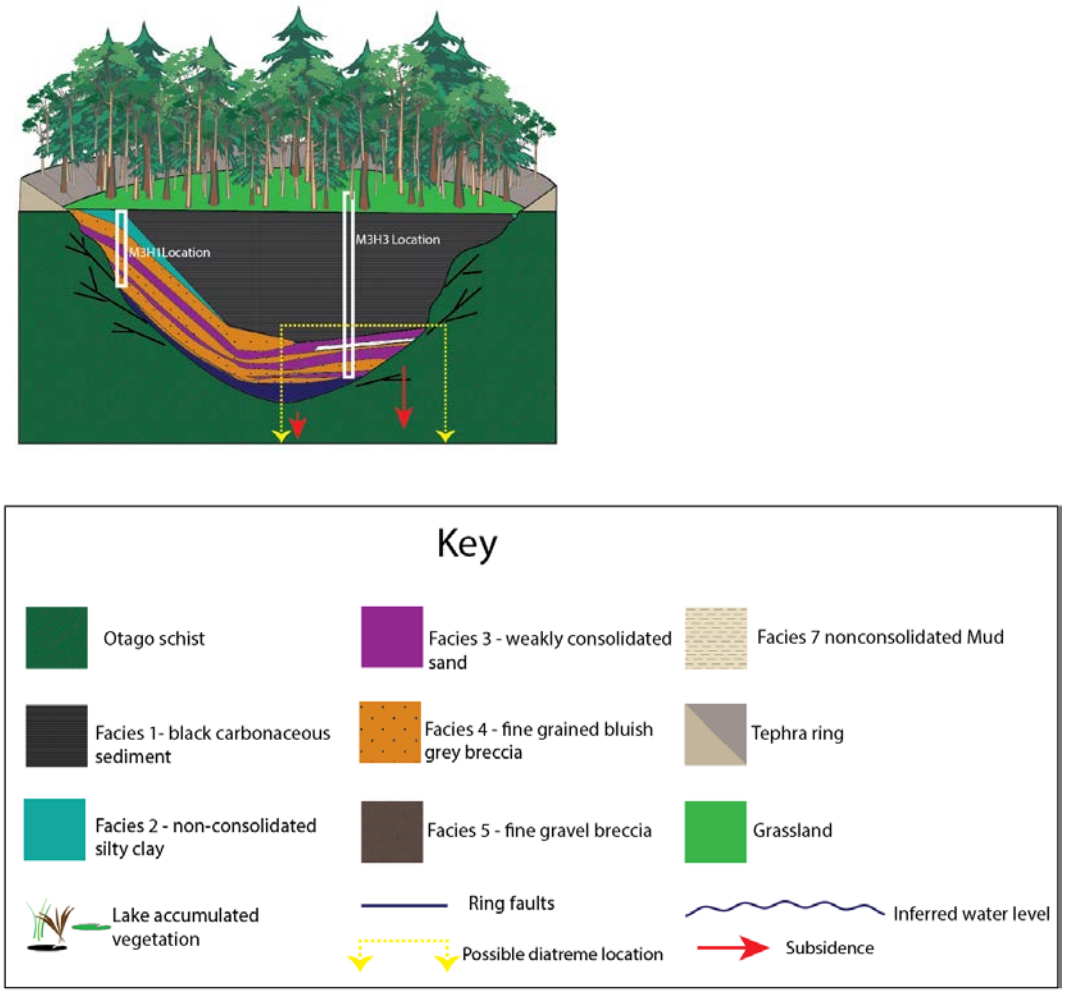

Figure 101: Showing sediment accumulation with ongoing subsidence of the maar diatreme for Maar 3.

6.5 Maar 2

Maar 2 is a positive feature and is therefore unlike a typical maar, which forms a depression. Limited analysis conducted on Maar 2 indicates similar deposits to Maar 1 and Maar 3. Unit 2 is a bluish grey fine sand with extensive mottles found throughout the deposit. This is similar to Facies 4, identified in Maar 1 and Maar 3. Also, Unit 1 and Facies 2 are both fine-grained sandy silts with no mottles. Furthermore, thin section analysis of Maar 2 indicates that the majority of the exposed outcrops are made up of mica and quartz grains, much like the siliciclastic sediment observed in Maar 1 and Maar 3. In addition, no primary pyroclastics were observed in Maar 2.

Although Maar 2 is a positive feature in the landscape, the deposits were poorly consolidated and had relatively minor components of weathered volcanic material,

and there is no indication that the structure is a tuff cone in origin. For example, no bedded lapilli or tephra are present in exposed outcrops.

Few conclusions can be drawn from Maar 2 due to the lack of availability of sample material. This is because only small samples were collected and rock outcrop exposures were limited in the field. What is known about Maar 2 is that the positive feature in the landscape resides above the gravity anomaly detected, and that deposits found in outcrops of Maar 2 seem likely to be sediments from the early evolution of a maar crater, based on their similarity to those found in Maars 1 and 3. Further research is needed to confirm these assumptions and explain why Maar 2 is a positive feature rather than a depression.

Maar 2 may have been uplifted along a normal fault that runs between Maar 2 and Maar 3; this could have resulted in the rotation of the block containing M3, which is why the slope exists between the site of the anomaly and the edge of M2. This could also explain why M3H1 is higher up the slope. M3H1 could be further back from the fault, and therefore have dropped down less, resulting in no lake sediments due to erosion. Whereas M3H3 could be closer to the fault, and therefore downthrown more, resulting in more accommodation space for carbonaceous lake sediments to accumulated.

The geomorphological positive anomaly of Maar 2 could be the result of the reactivation of ring faults resulting in uplift. During the Miocene, the area underwent a reversal of many faulting systems (Alder et al., 2016), and perhaps something similar occurred at Maar 2. However, this was not observed in any of the other maars. Further research is required to establish the presence or absence of faulting and direction of any offset.

6.6 Further Research

The Hindon Maar Complex is relatively unstudied, leaving a large scope of possible further research. This research can be broken down into 2 categories: adding to the knowledge of Maar 1 and Maar 3, and analysis of Maar 2 and Maar 4.

Firstly, longer drill holes in Maars 1 and 3 into the diatreme deposits would enable analysis of the entire maar depositional sequence. This could also uncover pyroclastic material that could be used to infer eruption type and intensity. Furthermore, multiple holes in different locations would help with the correlation of sediments found within each of the maars. Geophysical surveys could identify the below-ground architecture of the maars. This would be useful for Maar 3, and could help explain the offsets found between the gravity anomaly and the sediments. Detailed geochemical and clay analysis of M3H5 would yield insight into the depositional environments, and may confirm whether M3H5 is the product of the weathered tephra ring.

As no real analysis has been conducted on Maars 2 and 4, there is significant potential for further research into these two maars. Drilling in Maar 2 and Maar 4 would not only help to determine the depositional and evolutional settings of the maar, but could also shed light into the Hindon Maar Complex as a whole. Drilling in Maar 2 could confirm whether or not the sediments were deposited in a lake, and why the maar is a positive feature.

Chapter 7

Conclusion

7.1 Section

Maar eruptions are phreatomagmatic and form as the result of magma interaction with water, creating steep sided craters. Maar craters form unique sediment traps and as a result are often used in paleoclimate reconstruction studies. There are limited studies into the early siliciclastic sedimentation within maars, which often incorporate pyroclastic and country rock material.

The Hindon Maar Complex resulted from a series of maar forming eruptions, creating four separate explosion craters, Maars 1 to 4. Five cores were obtained from Maar 1 and Maar 3, ranging in depth from 8–18 m. A limited outcrop survey was conducted in Maar 2 and geomorphological mapping was conducted in the area which encompassed Maars 1, 2 and 3. Geomorphologically there is little evidence of the maars existing. Maar 1 is situated in a shallow depression, Maar 3 is found along a slope, and Maar 2 is a positive feature in the landscape. It is assumed that the maars were formed by typical maar eruptions producing a tephra ring of 2–5 km in diameter surrounding each of the vents. The close proximity of the vents to one another indicates that the Hindon Maar Complex is an example of either a polycyclic maar complex or a clustered maar complex.

A total of 10 facies have been identified within the Hindon Maar complex as a series of mass flows or extremely weathered tephra deposits. Nonconsolidated mottles are found throughout facies 2–5 and are interpreted as weathered pyroclastic material. No primary pyroclastics were observed in any of the facies within the Hindon Maar complex; this is assumed to be due to weathering.

Facies 1 is laminated black carbonaceous sediment which consists almost entirely of organic matter. Facies 1 was deposited into the Hindon Maar lakes once the crater had become stable due to vegetation along the crater rim and has formed a deep stratified lake with an anoxic bottom.

Facies 2 is a nonconsolidated bluish grey clay rich silt with minor sand and gravel lenses. Facies 2 is predominantly laminated, comprising mostly mica and quartz grains. Facies 2 has elevated magnetic susceptibility, which is believed to be a

product of the high clay content of 35% within this deposit. Facies 2 resulted from the weathering of the crater wall after significant stabilisation.

Facies 3 is a bluish grey weakly consolidated poorly sorted sandstone which ranged in size from fine sand to coarse sand with discrete gravel lenses. Normal grading was observed in the lenses. Facies 3 is believed to result from turbidity currents.

Facies 4 is a fine-grained bluish grey breccia with a matrix consisting of fine to coarse subangular sand. Facies 4 included up to 35% mottles and is interpreted as the result of mass flows originating from the tephra ring.

Facies 5 is a fine-grained gravel breccia with a matrix of fine to coarse, angular to subangular sand. Lithics within this deposit are schist and quartz. Overall this deposit is poorly sorted with normal grading observed. Within Facies 5 there is significant variability in magnetic susceptibility, which has been interpreted as a result of the heterogeneity of the unit. Facies 5 was deposited when the crater wall was unstable.

Facies 6 consists of loose schist and quartz grains ranging from fine gravel to medium pebbles, is sub angular and poorly sorted. Facies 6 is the result of localised rockfalls into Maar 1, and would have occurred early in the sedimentation of the maar.

Facies 7 is a result of a localised sump deposit found in Maar 3. Facies 7 is a white nonconsolidated clay-rich silt with a high proportion of titanium. It shows convoluted bedding and no organics, and is interpreted as having been deposited rapidly within the maar. Tthere is no evidence of mica or quartz grains within this deposit and therefore it is believed to have different parent material from other local facies.

Facies 8, 9 and 10 are found in Maar 3 and have been interpreted as extremely weathered pyroclastic material, likely originating from the tephra ring. These facies are similar to one another, having high densities and magnetic susceptibilities greater than 80 $x10^{-8}$ m^3/kg, consistent with basaltic material. Furthermore, there is no evidence of country rock within this deposit. Pyroclastic material weathers rapidly and as the maar is a minimum of 15 million years old, sufficient time has passed for pyroclastic material to be completely weathered to clays. It is assumed that the tephra ring was exposed at the surface for long enough for weathering to be complete before being buried below the present-day ground surface.

The facies succession observed in Maar 1 is consistent with studies of other early post-eruptive maar sediments. Firstly, Facies 5 and 6 were deposited, which were the result of crater wall collapses and rock falls into the crater. Facies 5 and 6 would have been deposited days to years following the eruption, with the frequency of such rock falls decreasing with time. This was followed by Facies 4, which was the result of failures within the upper crater wall and tephra ring. This is indicated by the higher percentage of mottles within Facies 4. Facies 3 was then deposited and formed a series of mass flows within the maar basin. During the deposition of Facies 3 debris fans would have formed around the crater wall. After this, the crater wall became stabilised and significant vegetation cover prevented coarse grains entering the lake. Facies 2 was deposited as a result of erosion of crater wall material. Facies 2 formed debris flows within the maar basin. Finally, Facies 1 would have been deposited after the lake became stratified, forming an anoxic bottom layer. Ultimately, the crater basin would have filled up, producing a swamp and later the current day topography.

Facies accumulated within Maar 3 in a similar succession. However, the presence of significant organic matter in M3H3 and the absence of organic matter in M3H1 indicates that additional geological processes must have occurred. These processes may have involved significant subsidence of the diatreme, or faulting. It is believed that M3H5 represents weathered tephra ring deposits and is therefore not part of the siliciclastic crater-floor sedimentation.

Analysis of outcrop sediments in Maar 2 show that the deposits are similar to Facies 2 to 4. As Maar 2 is a positive feature in the landscape, it does not conform to normal maar diatremes. The reason for this morphological abnormality is unknown. However, it is likely that the sediments have originally accumulated in a similar depositional setting to Facies 1 to 4.

References

Hitachi S-4700 SEM Training and Reference Guide. (2007). In.

Abdullah, E. C., & Geldart, D. (1999). The use of bulk density measurements as flowability indicators. Powder Technology, 102(2), 151-165. doi:https://doi.org/10.1016/S0032-5910(98)00208-3

Adams, C. (1981). Migration of late Cenozoic volcanism in the South Island of New Zealand and the Campbell Plateau. Nature, 294(5837), 153.

Adams, C. J., & Graham, I. J. (1997). Age of metamorphism of Otago Schist in eastern Otago and determination of protoliths from initial strontium isotope characteristics. New Zealand Journal of Geology and Geophysics, 40(3), 275-286. doi:10.1080/00288306.1997.9514760

Agustín-Flores, J., Németh, K., Cronin, S. J., Lindsay, J. M., & Kereszturi, G. (2015). Shallow-seated explosions in the construction of the Motukorea tuff ring (Auckland, New Zealand): Evidence from lithic and sedimentary characteristics. Journal of Volcanology and Geothermal Research, 304, 272-286. doi:https://doi.org/10.1016/j.jvolgeores.2015.09.013

Alder, S., Smith, S. A. F., & Scott, J. M. (2016). Fault-zone structure and weakening processes in basin-scale reverse faults: The Moonlight Fault Zone, South Island, New Zealand. Journal of Structural Geology, 91, 177-194. doi:https://doi.org/10.1016/j.jsg.2016.09.001

Arnaud, F., Magand, O., Chapron, E., Bertrand, S., Boës, X., Charlet, F., & Mélières, M.-A. (2006). Radionuclide dating (210Pb, 137Cs, 241Am) of recent lake sediments in a highly active geodynamic setting (Lakes Puyehue and Icalma—Chilean Lake District). Science of the Total Environment, 366(2-3), 837-850.

Baykan, N. A., & Yılmaz, N. (2010). Case study in effects of color spaces for mineral identification. Scientific research and essays, 5(11), 1243-1253.

Bebbington, M. S., & Cronin, S. J. (2011). Spatio-temporal hazard estimation in the Auckland Volcanic Field, New Zealand, with a new event-order model. Bulletin of Volcanology, 73(1), 55-72.

Begét, J. E., Hopkins, D. M., & Charron, S. D. (1996). The largest known maars on Earth, Seward Peninsula, northwest Alaska. Arctic, 62-69.

Bertrand, S., Daga, R., Bedert, R., & Fontijn, K. (2014). Deposition of the 2011–2012 Cordón Caulle tephra (Chile, 40 S) in lake sediments: Implications for tephrochronology and volcanology. Journal of Geophysical Research: Earth Surface, 119(12), 2555-2573.

Black, D. L., McQuay, M. Q., & Bonin, M. P. (1996). Laser-based techniques for particle-size measurement: a review of sizing methods and their industrial applications. Progress in energy and combustion science, 22(3), 267-306.

Blaikie, T. N., Ailleres, L., Betts, P. G., & Cas, R. A. F. (2014). A geophysical comparison of the diatremes of simple and complex maar volcanoes, Newer Volcanics Province, south-eastern Australia. Journal of Volcanology and Geothermal Research, 276, 64-81. doi:https://doi.org/10.1016/j.jvolgeores.2014.03.001

Blaikie, T. N., Ailleres, L., Cas, R. A. F., & Betts, P. G. (2012). Three-dimensional potential field modelling of a multi-vent maar-diatreme — The Lake Coragulac maar, Newer Volcanics Province, south‐eastern Australia. Journal of Volcanology and Geothermal Research, 235-236, 70-83. doi:https://doi.org/10.1016/j.jvolgeores.2012.05.002

Boggs Jr, S. (2006). Sedimentology and Stratigraphy: Pearson Education.

Boldt, B., Kaufman, D., & Briner, J. (2012). Decadally resolved quantitative temperature reconstruction spanning 5.6 ka at Kurupa Lake, Arctic Alaska. Paper presented at the AGU Fall Meeting Abstracts.

Boris, Ohba, T., Kereszturi, G., Németh, K., Aka, F. T., Youmen, D., . . . Hell, J. V. (2015). Towards the reconstruction of the shallow plumbing system of the Barombi Mbo Maar (Cameroon) Implications for diatreme growth processes of a polygenetic maar volcano. Journal of Volcanology and Geothermal Research, 301(Supplement C), 293-313. doi:https://doi.org/10.1016/j.jvolgeores.2015.06.004

Bouma, A. (1962). Sedimentology of some Flysch deposits; a graphic approach to facies interpretation, Published Ph. D. thesis, Elsevier,

Bouma, A. H. (1963). Sedimentary facies model of turbidites. AAPG Bulletin, 47(2), 351-351.

Bowie, E. (2015). Geophysical Characterisation of the Hindon Maar Complex. (Degree of Post Graduate Diploma in Science), University of Otago, Dunedin.

Bowie, E. (2015). Geophysical Characterisation of the Hindon Maar Complex. Post graduate diploma in science. The University of Otago. Dunedin.

Brauer, A., Endres, C., Günter, C., Litt, T., Stebich, M., & Negendank, J. F. W. (1999). High resolution sediment and vegetation responses to Younger Dryas climate change in varved lake sediments from Meerfelder Maar, Germany. Quaternary Science Reviews, 18(3), 321-329. doi:https://doi.org/10.1016/S0277-3791(98)00084-5

Büchel, G., & Lorenz, V. (1993). Syn-and post-eruptive mechanism of the Alaskan Ukinrek maars in 1977. In Paleolimnology of European Maar Lakes (pp. 15-60): Springer.

C. A. LANDIS, H. J. CAMPBELL, J. G. BEGG, D. C. MILDENHALL, A. M. PATERSON, & TREWICK, S. A. (2008). The Waipounamu Erosion Surface: questioning the antiquity of the New Zealand land surface and terrestrial fauna and flora. Geological Magazine, 145(2), 173-197. doi:10.1017/S0016756807004268

Carrasco-Núñez, G., Ort, M. H., & Romero, C. (2007). Evolution and hydrological conditions of a maar volcano (Atexcac crater, Eastern Mexico). Journal of Volcanology and Geothermal Research, 159(1), 179-197. doi:https://doi.org/10.1016/j.jvolgeores.2006.07.001

Carter, R. M. (1988). Plate boundary tectonics, global sea-level changes and the development of the eastern South Island continental margin, New Zealand, Southwest Pacific:‘The existence of the widely acclaimed Vail (sea-level) curves seems to be encouraging a circularity in arguments about local correlation… and is certainly discouraging attempts to investigate local departures from the so-called global standard’.(Miall, 1986, p. 131). Marine and petroleum geology, 5(2), 90-107.

Cassidy, J., France, S. J., & Locke, C. A. (2007). Gravity and magnetic investigation of maar volcanoes, Auckland volcanic field, New Zealand. Journal of Volcanology and Geothermal Research, 159(1), 153-163. doi:https://doi.org/10.1016/j.jvolgeores.2006.06.007

Chapman, M. R., & Shackleton, N. J. (1998). What level of resolution is attainable in a deep ‐ sea core? Results of a spectrophotometer study. Paleoceanography, 13(4), 311-315.

Chassiot, L., Chapron, E., Di Giovanni, C., Albéric, P., Lajeunesse, P., Lehours, A.-C., & Meybeck, M. (2016). Extreme events in the sedimentary record of maar Lake Pavin: Implications for natural hazards assessment in the French Massif Central. Quaternary Science Reviews, 141, 9-25.

Churchman, G. J., & Lowe, D. J. (2012). Alteration, formation, and occurrence of minerals in soils: CRC press.

Churchman, G. J., Pasbakhsh, P., Lowe, D. J., & Theng, B. (2016). Unique but diverse: some observations on the formation, structure and morphology of halloysite. Clay Minerals, 51(3), 395-416.

Coombs, D. S., Adams, C. J., Roser, B. P., & Reay, A. (2008). Geochronology and geochemistry of the Dunedin Volcanic Group, eastern Otago, New Zealand. New Zealand Journal of Geology and Geophysics, 51(3), 195-218. doi:10.1080/00288300809509860

Coombs, D. S., Cas, R., Kawachi, Y., Landis, C., McDonough, W., & Reay, A. (1986). Cenozoic volcanism in north, east and central Otago. Royal Society of New Zealand Bulletin, 23, 278-312.

Cooper, A., Barreiro, B., Kimbrough, D., & Mattinson, J. (1987). Lamprophyre dike intrusion and the age of the Alpine fault, New Zealand. Geology, 15(10), 941-944.

Covault, J. A., Kostic, S., Paull, C. K., Ryan, H. F., & Fildani, A. (2014). Submarine channel initiation, filling and maintenance from sea‐floor geomorphology and morphodynamic modelling of cyclic steps. Sedimentology, 61(4), 1031-1054.

Croudace, I. W., Rindby, A., & Rothwell, R. G. (2006). ITRAX: description and evaluation of a new multi-function X-ray core scanner. Geological Society, London, Special Publications, 267(1), 51-63.

Cunningham, M. J. (2012). Sensitive rhyolitic pyroclastic deposits in the Tauranga region: mineralogy, geomechanics and microstructure of peak and remoulded states. University of Waikato,

Czymzik, M., Adolphi, F., Muscheler, R., Brauer, A., Mekhaldi, F., Martin-Puertas, C., . . . Possnert, G. (2016). Atmospheric production signal in 10Be from varved sediments of Lake Meerfelder Maar during the late glacial-early Holocene transition. Paper presented at the EGU General Assembly Conference Abstracts.

Dearing, J. (1994). Environmental magnetic susceptibility. Using the Bartington MS2 system. Kenilworth, Chi Publ.

Delannay, R., Valance, A., Mangeney, A., Roche, O., & Richard, P. (2017). Granular and particle-laden flows: from laboratory experiments to field observations. Journal of Physics D: Applied Physics, 50(5), 053001.

Deligne, N., Lindsay, J., & Smid, E. (2015). An integrated approach to Determining Volcanic Risk in Auckland, New Zealand: the multi-disciplinary DEVORA project. Global Volcanic Hazards and Risk, 233.

Delpit, S., Ross, P.-S., & Hearn, B. C. (2014). Deep-bedded ultramafic diatremes in the Missouri River Breaks volcanic field, Montana, USA: 1 km of syn-eruptive subsidence. Bulletin of Volcanology, 76(7), 832.

Dorren, L. K. (2003). A review of rockfall mechanics and modelling approaches. Progress in Physical Geography, 27(1), 69-87.

Douglas S. Coombs, Christopher J. Adams, Barry P. Roser, & Anthony Reay. (2008). Geochronology and geochemistry of the Dunedin Volcanic Group, eastern Otago, New Zealand. New Zealand Journal of Geology and Geophysics, 51(3), 195-218. doi:10.1080/00288300809509860

Eichhorn, L., Pirrung, M., Zolitschka, B., & Büchel, G. (2017). Pleniglacial sedimentation process reconstruction on laminated lacustrine sediments from lava-dammed Paleolake Alf, West Eifel Volcanic Field (Germany). Quaternary Science Reviews, 172, 83-95.

Filimonova, S., Kaufhold, S., Wagner, F. E., Häusler, W., & Kögel-Knabner, I. (2016). The role of allophane nano-structure and Fe oxide speciation for hosting soil organic matter in an allophanic Andosol. Geochimica et Cosmochimica Acta, 180, 284-302.

Floyd, P. A., & Winchester, J. A. (1975). Magma type and tectonic setting discrimination using immobile elements. Earth and Planetary Science Letters, 27(2), 211-218. doi:https://doi.org/10.1016/0012-821X(75)90031-X

Force, E. R. (1976). Metamorphic source rocks of titanium placer deposits: a geochemical cycle: US Department of the Interior, Geological Survey.

Forster, M., & Lister, G. (2003). Cretaceous metamorphic core complexes in the Otago Schist, New Zealand. Australian Journal of Earth Sciences, 50(2), 181-198.

Fox, B. R., Wartho, J., Wilson, G. S., Lee, D. E., Nelson, F., & Kaulfuss, U. (2015). Long‐term evolution of an Oligocene/Miocene maar lake from Otago, New Zealand. Geochemistry, Geophysics, Geosystems, 16(1), 59-76.

Fox, B. R. S., D'Andrea, W. J., Wilson, G. S., Lee, D. E., & Wartho, J. A. (2017). Interaction of polar and tropical influences in the mid-latitudes of the Southern Hemisphere during the Mi-1 deglaciation. Global and Planetary Change, 155, 109-120. doi:https://doi.org/10.1016/j.gloplacha.2017.06.008

Fristad, K. E., Svensen, H. H., Polozov, A., & Planke, S. (2017). Formation and evolution of the end-Permian Oktyabrsk volcanic crater in the Tunguska Basin, Eastern Siberia. Palaeogeography, Palaeoclimatology, Palaeoecology, 468, 76-87. doi:https://doi.org/10.1016/j.palaeo.2016.11.025

Gani, M. R. (2004). From turbid to lucid: a straightforward approach to sediment gravity flows and their deposits. The Sedimentary Record,, 2(3), 4-8.

Genesis, A. Controls on the Rates of Weathering and Clay Mineral Genesis in Airfall Tephras: a Review and New Zealand Case Study.

Geotek, L. (2014). Multi-Sensor Core Logger. Northamptonshire.

Glassey, P., Barrell, D., Forsyth, J., & Macleod, R. (2003). The geology of Dunedin, New Zealand, and the management of geological hazards. Quaternary International, 103(1), 23-40. doi:https://doi.org/10.1016/S1040-6182(02)00139-8

Goldich, S. S. (1938). A Study in Rock-Weathering. The Journal of Geology, 46(1), 17-58. doi:10.1086/624619

Goldstein, J. I., Newbury, D. E., Michael, J. R., Ritchie, N. W., Scott, J. H. J., & Joy, D. C. (2017). Scanning electron microscopy and X-ray microanalysis: Springer.

Goodale, N., Bailey, D. G., Jones, G. T., Prescott, C., Scholz, E., Stagliano, N., & Lewis, C. (2012). pXRF: A study of inter-instrument performance. Journal of Archaeological Science, 39(4), 875-883.

Haberle, S. G., & Lumley, S. H. (1998). Age and origin of tephras recorded in postglacial lake sediments to the west of the southern Andes, 44 S to 47 S. Journal of Volcanology and Geothermal Research, 84(3-4), 239-256.

Hayden B. Dalton, James M. Scott, Jingao Liu, Tod E. Waight, D. Graham Pearson, Marco Brenna, . . . Palin, J. M. (2017). Diffusion-zoned pyroxenes in an

isotopically heterogeneous mantle lithosphere beneath the Dunedin Volcanic Group, New Zealand, and their implications for intraplate alkaline magma sources. Lithosphere, 9(3), 463-475. doi:10.1130/L631.1

Hoernle, K., White, J. D. L., van den Bogaard, P., Hauff, F., Coombs, D. S., Werner, R., . . . Cooper, A. F. (2006). Cenozoic intraplate volcanism on New Zealand: Upwelling induced by lithospheric removal. Earth and Planetary Science Letters, 248(1), 350-367. doi:https://doi.org/10.1016/j.epsl.2006.06.001

Jackson, J., Norris, R., & Youngson, J. (1996). The structural evolution of active fault and fold systems in central Otago, New Zealand: evidence revealed by drainage patterns. Journal of Structural Geology, 18(2), 217-234. doi:https://doi.org/10.1016/S0191-8141(96)80046-0

Jordan, S., Cas, R., & Hayman, P. (2013). The origin of a large (> 3 km) maar volcano by coalescence of multiple shallow craters: Lake Purrumbete maar, southeastern Australia. Journal of Volcanology and Geothermal Research, 254, 5-22.

Joussein, E., Petit, S., Churchman, J., Theng, B., Righi, D., & Delvaux, B. (2005). Halloysite clay minerals–a review. In: De Gruyter.

Joy, D. C. (2006). Scanning electron microscopy: Wiley Online Library.

Jugum, D., Norris, R. H., & Palin, J. M. (2013). Late Jurassic detrital zircons from the Haast Schist and their implications for New Zealand terrane assembly and metamorphism. New Zealand Journal of Geology and Geophysics, 56(4), 223-228. doi:10.1080/00288306.2013.815639

Kahle, M., Kleber, M., & Jahn, R. (2002). Review of XRD-based quantitative analyses of clay minerals in soils: the suitability of mineral intensity factors. Geoderma, 109(3), 191-205. doi:https://doi.org/10.1016/S0016-7061(02)00175-1

Kalnicky, D. J., & Singhvi, R. (2001). Field portable XRF analysis of environmental samples. Journal of hazardous materials, 83(1-2), 93-122.

Kaulfuss, U. (2017). Crater stratigraphy and the post-eruptive evolution of Foulden Maar, southern New Zealand. New Zealand Journal of Geology and Geophysics, 60(4), 410-432.

Kaulfuss, U., & Moulds, M. (2015). A new genus and species of tettigarctid cicada from the early Miocene of New Zealand: Paratettigarcta zealandica (Hemiptera, Auchenorrhyncha, Tettigarctidae). ZooKeys(484), 83.

Kereszturi, G., Csillag, G., Németh, K., Sebe, K., Balogh, K., & Jáger, V. (2010). Volcanic architecture, eruption mechanism and landform evolution of a Plio/Pleistocene intracontinental basaltic polycyclic monogenetic volcano from the Bakony-Balaton Highland Volcanic Field, Hungary. Central European Journal of Geosciences, 2(3), 362-384.

Khripounoff, A., Crassous, P., Lo Bue, N., Dennielou, B., & Silva Jacinto, R. (2012). Different types of sediment gravity flows detected in the Var submarine canyon (northwestern Mediterranean Sea). Progress in Oceanography, 106, 138-153. doi:https://doi.org/10.1016/j.pocean.2012.09.001

Kienle, J., Kyle, P. R., Self, S., Motyka, R. J., & Lorenz, V. (1980). Ukinrek Maars, Alaska, I. April 1977 eruption sequence, petrology and tectonic setting. Journal of Volcanology and Geothermal Research, 7(1), 11-37. doi:https://doi.org/10.1016/0377-0273(80)90018-9

Kimsey, M. J., Garrison-Johnston, M. T., & Johnson, L. (2011). Characterization of Volcanic Ash-Influenced Forest Soils across a Geoclimatic Sequence All rights reserved. No part of this periodical may be reproduced or transmitted in any form or by any means, electronic or mechanical, including photocopying, recording, or any information storage and retrieval system, without permission in writing from the publisher. Permission for printing and for reprinting the material contained herein has been obtained by the publisher. Soil Science Society of America Journal, 75(1), 267-279.

Kjarsgaard, B., Harvey, S., Zonneveld, J., Heaman, L., White, D., & MacNeil, D. (2006). Volcanic stratigraphy, eruptive sequences and emplacement of the 140/141 kimberlite, Fort à la Corne field, Saskatchewan. Paper presented at the Long abstracts, Kimberlite Emplacement Workshop, Saskatoon, Sask. Available at http://www. venuewest. com/8IKC/files/21% 20Kjarsgaard, Harvey. pdf [accessed 18 June 2008].

Kluger, M. O., Moon, V. G., Kreiter, S., Lowe, D. J., Churchman, G. J., Hepp, D. A., . . . Mörz, T. (2017). A new attraction-detachment model for explaining flow sliding in clay-rich tephras. Geology, 45(2), 131-134.

Konert, M., & Vandenberghe, J. (1997). Comparison of laser grain size analysis with pipette and sieve analysis: a solution for the underestimation of the clay fraction. Sedimentology, 44(3), 523-535.

Kurszlaukis, S., & Fulop, A. (2013). Factors controlling the internal facies architecture of maar-diatreme volcanoes. Bulletin of Volcanology, 75(11), 761.

Larter, R. D., Cunningham, A. P., Barker, P. F., Gohl, K., & Nitsche, F. O. (2002). Tectonic evolution of the Pacific margin of Antarctica 1. Late Cretaceous tectonic reconstructions. Journal of Geophysical Research: Solid Earth, 107(B12).

Lee, D. (2016).

Lefebvre, N., White, J., & Kjarsgaard, B. (2013). Unbedded diatreme deposits reveal maar-diatreme-forming eruptive processes: Standing Rocks West, Hopi Buttes, Navajo Nation, USA. Bulletin of Volcanology, 75(8), 739.

Lehndorff, E., Wolf, M., Litt, T., Brauer, A., & Amelung, W. (2015). 15,000 years of black carbon deposition–a post-glacial fire record from maar lake sediments (Germany). Quaternary Science Reviews, 110, 15-22.

Lindqvist, J. K., & Lee, D. E. (2009). High-frequency paleoclimate signals from Foulden Maar, Waipiata Volcanic Field, southern New Zealand: an Early Miocene varved lacustrine diatomite deposit. Sedimentary Geology, 222(1-2), 98-110.

Liu, L., Chen, H., Zhong, Y., Wang, J., Xu, C., Chen, A., & Du, X. (2017). Sedimentological characteristics and depositional processes of sediment gravity flows in rift basins: The Palaeogene Dongying and Shahejie formations, Bohai Bay Basin, China. Journal of Asian Earth Sciences, 147, 60-78. doi:https://doi.org/10.1016/j.jseaes.2017.07.021

Lorenz, V. (1973). On the formation of maars. Bulletin of Volcanology, 37(2), 183-204.

Lorenz, V. (1986). On the growth of maars and diatremes and its relevance to the formation of tuff rings. Bulletin of Volcanology, 48(5), 265-274.

Lorenz, V. (2003). Maar-diatreme volcanoes, their formation, and their setting in hard-rock or soft-rock environments. Geolines, 15, 72-83.

Lorenz, V. (2007). Syn-and posteruptive hazards of maar–diatreme volcanoes. Journal of Volcanology and Geothermal Research, 159(1-3), 285-312.

Lorenz, V., Suhr, P., & Suhr, S. (2017). Phreatomagmatic maar-diatreme volcanoes and their incremental growth: a model. Geological Society, London, Special Publications, 446(1), 29-59.

Loubser, M., & Verryn, S. (2008). Combining XRF and XRD analyses and sample preparation to solve mineralogical problems. South African Journal of Geology, 111(2-3), 229-238.

Loughlin, S. C., Sparks, R. S. J., Brown, S. K., Jenkins, S. F., & Vye-Brown, C. (2015). Global volcanic hazards and risk: Cambridge University Press.

Lowe, D. J. (1986). Controls on the Rates of Weathering and Clay Mineral Genesis in Airfall Tephras: a Review and New Zealand Case Study. In S. M. Colman & D. P. Dethier (Eds.), Rates of Chemical Weathering of Rocks and Minerals: Academic Press

Lowe, D. J. (1988). Late Quaternary volcanism in New Zealand: towards an integrated record using distal airfall tephras in lakes and bogs. Journal of Quaternary Science, 3(2), 111-120.

Lowe, D. J., & Nelson, C. S. (1983). Guide to the nature and methods of analysis of the clay fraction of tephras from the South Auckland region, New Zealand. Retrieved from

Lowe, D. R. (1976). Grain flow and grain flow deposits. Journal of Sedimentary Research, 46(1).

Macorps, É., Graettinger, A. H., Valentine, G. A., Ross, P.-S., White, J. D., & Sonder, I. (2016). The effects of the host-substrate properties on maar-diatreme volcanoes: experimental evidence. Bulletin of Volcanology, 78(4), 26.

Manville, V., Németh, K., & Kano, K. (2009). Source to sink: a review of three decades of progress in the understanding of volcaniclastic processes, deposits, and hazards. Sedimentary Geology, 220(3-4), 136-161.

Marchetto, A., Ariztegui, D., Brauer, A., Lami, A., Mercuri, A. M., Sadori, L., . . . Guilizzoni, P. (2015). Volcanic lake sediments as sensitive archives of climate and environmental change. In Volcanic Lakes (pp. 379-399): Springer.

Martin, A. P., Kellett, R. L., Henderson, S., Davies, B., & Coote, J. A. (2007). The Central Otago helicopter-borne magnetic and electromagnetic regional survey: a preliminary geological interpretation.

Martin‐Puertas, C., Tjallingii, R., Bloemsma, M., & Brauer, A. (2017). Varved sediment responses to early Holocene climate and environmental changes in Lake Meerfelder Maar (Germany) obtained from multivariate analyses of

micro X‐ray fluorescence core scanning data. Journal of Quaternary Science, 32(3), 427-436.

McCanta, M. C., Hatfield, R. G., Thomson, B. J., Hook, S. J., & Fisher, E. (2015). Identifying cryptotephra units using correlated rapid, nondestructive methods: VSWIR spectroscopy, X‐ray fluorescence, and magnetic susceptibility. Geochemistry, Geophysics, Geosystems, 16(12), 4029-4056.

McDaniel, P. A., Lowe, D. J., Arnalds, O., & Ping, C.-L. (1999). Andisols. In Handbook of soil science: CRC press.

Meiburg, E., & Kneller, B. (2010). Turbidity Currents and Their Deposits. Annual Review of Fluid Mechanics, 42(1), 135-156. doi:10.1146/annurev-fluid-121108-145618

Mertz, D., Swisher, C., Franzen, J., Neuffer, F., & Lutz, H. (2000). Numerical dating of the Eckfeld maar fossil site, Eifel, Germany: a calibration mark for the Eocene time scale. Naturwissenschaften, 87(6), 270-274.

Mildenhall, D. C., Kennedy, E. M., Lee, D. E., Kaulfuss, U., Bannister, J. M., Fox, B., & Conran, J. G. (2014). Palynology of the early Miocene Foulden Maar, Otago, New Zealand: Diversity following destruction. Review of Palaeobotany and Palynology, 204, 27-42.

Möller, A. L., Kaulfuss, U., Lee, D. E., & Wappler, T. (2017). High richness of insect herbivory from the early Miocene Hindon Maar crater, Otago, New Zealand. PeerJ, 5, e2985.

Moorhouse, B., White, J., & Scott, J. (2015). Cape Wanbrow: A stack of Surtseyan-style volcanoes built over millions of years in the Waiareka–Deborah volcanic field, New Zealand. Journal of Volcanology and Geothermal Research, 298, 27-46.

Mortimer, N. (2000). Metamorphic discontinuities in orogenic belts: example of the garnet–biotite–albite zone in the Otago Schist, New Zealand. International journal of earth sciences, 89(2), 295-306.

Mosher, T. (2007). Chapter 10 - Magnetic Resonance Imaging in Osteoarthritis A2 - Sharma, Leena. In F. Berenbaum (Ed.), Osteoarthritis (pp. 143-177). Philadelphia: Mosby.

Mrlina, J., Kämpf, H., Kroner, C., Mingram, J., Stebich, M., Brauer, A., . . . Seidl, M. (2009). Discovery of the first Quaternary maar in the Bohemian Massif, Central Europe, based on combined geophysical and geological surveys.

Journal of Volcanology and Geothermal Research, 182(1), 97-112. doi:https://doi.org/10.1016/j.jvolgeores.2009.01.027

Németh, K. (2010). Monogenetic volcanic fields: origin, sedimentary record, and relationship with polygenetic volcanism. Geological Society of America Special Papers, 470, 43-66.

Németh, K., Cronin, S. J., Haller, M. J., Brenna, M., & Csillag, G. (2010). Modern analogues for Miocene to Pleistocene alkali basaltic phreatomagmatic fields in the Pannonian Basin: “soft-substrate” to “combined” aquifer controlled phreatomagmatism in intraplate volcanic fields Research Article. Central European Journal of Geosciences, 2(3), 339-361. doi:10.2478/v10085-010-0013-8

Németh, K., Goth, K., Martin, U., Csillag, G., & Suhr, P. (2008). Reconstructing paleoenvironment, eruption mechanism and paleomorphology of the Pliocene Pula maar, (Hungary). Journal of Volcanology and Geothermal Research, 177(2), 441-456. doi:https://doi.org/10.1016/j.jvolgeores.2008.06.010

Németh, K., & Kereszturi, G. (2015). Monogenetic volcanism: personal views and discussion. International journal of earth sciences, 104(8), 2131-2146.

Nemeth, K., Martin, U., & Csillag, G. (2002). Pliocene crater lake deposits and soft sediment deformation structures associated with a phreatomagmatic volcano, Pula maar, western Hungary.

Németh, K., Martin, U., & Harangi, S. (2001). Miocene phreatomagmatic volcanism at Tihany (Pannonian Basin, Hungary). Journal of Volcanology and Geothermal Research, 111(1), 111-135. doi:https://doi.org/10.1016/S0377-0273(01)00223-2

Nemeth, K., & White, J. (2009). Miocene phreatomagmatic monogenetic volcanism of the Waipiata volcanic field, Otago, New Zealand; field guide (Vol. 128B).

Németh, K., & White, J. D. (2003). Geochemical evolution, vent structures, and erosion history of small-volume volcanoes in the Miocene Intracontinental Waipiata Volcanic Field, New Zealand. Paper presented at the Geolines J AS Czech Repub (Proceedings for the Hibsch 2002 Prague meeting on ‘‘Alkaline basaltic continental rift related magmatism’’).

Németh, K., & White, J. D. (2003). Reconstructing eruption processes of a Miocene monogenetic volcanic field from vent remnants: Waipiata Volcanic Field,

South Island, New Zealand. Journal of Volcanology and Geothermal Research, 124(1-2), 1-21.

Newnham, R. M., Lowe, D. J., & Alloway, B. V. (1999). Volcanic hazards in Auckland, New Zealand: a preliminary assessment of the threat posed by central North Island silicic volcanism based on the Quaternary tephrostratigraphical record. Geological Society, London, Special Publications, 161(1), 27-45. doi:10.1144/gsl.sp.1999.161.01.04

Okaya, D., Stern, T., & Davey, F. (2013). A Continental Plate Boundary: Tectonics at South Island, New Zealand (Vol. 175): John Wiley & Sons.

Ollier, C. D. (1967). Maars their characteristics, varieties and definition. Bulletin Volcanologique, 31(1), 45-73.

Paternoster, M., Mongelli, G., Caracausi, A., & Favara, R. (2016). Depth influence on the distribution of chemical elements and saturation index of mineral phases in twins maar lakes: The case of the Monticchio lakes (southern Italy). Journal of Geochemical Exploration, 163, 10-18. doi:https://doi.org/10.1016/j.gexplo.2016.01.001

Pirrung, M., Buchel, G., & Jacoby, W. (2001). The Tertiary volcanic basins of Eckfeld, Enspel and Messel (Germany). ZEITSCHRIFT-DEUTSCHEN GEOLOGISCHEN GESELLSCHAFT, 152(1), 27-60.

Pirrung, M., Büchel, G., Lorenz, V., & TREUTLER, H. C. (2008). Post‐eruptive development of the Ukinrek East Maar since its eruption in 1977 AD in the periglacial area of south‐west Alaska. Sedimentology, 55(2), 305-334.

Pirrung, M., Fischer, C., Büchel, G., Gaupp, R., Lutz, H., & Neuffer, F. O. (2003). Lithofacies succession of maar crater deposits in the Eifel area (Germany). Terra Nova, 15(2), 125-132.

R.Vijayalakshmi, & Rajendran, K. V. (2010). Influence of Surfactants on the Synthesis of TiO2 Nanoparticles. The AZo Journal of Minerals Online. doi:10.2240/azojomo0304

Rach, O., Engels, S., Kahmen, A., Brauer, A., Martín-Puertas, C., van Geel, B., & Sachse, D. (2017). Hydrological and ecological changes in western Europe between 3200 and 2000 years BP derived from lipid biomarker δD values in lake Meerfelder Maar sediments. Quaternary Science Reviews, 172, 44-54.

Reed, S. J. B. (2005). Electron microprobe analysis and scanning electron microscopy in geology: Cambridge University Press.

Reichgelt, T., Kennedy, E. M., Jones, W. A., Jones, D. T., & Lee, D. E. (2016). Contrasting palaeoenvironments of the mid/late Miocene Dunedin Volcano, southern New Zealand: Climate or topography? Palaeogeography, Palaeoclimatology, Palaeoecology, 441, 696-703.

Reichgelt, T., Kennedy, E. M., Mildenhall, D. C., Conran, J. G., Greenwood, D. R., & Lee, D. E. (2013). Quantitative palaeoclimate estimates for early Miocene southern New Zealand: evidence from Foulden Maar. Palaeogeography, Palaeoclimatology, Palaeoecology, 378, 36-44.

Rochette, P. (1987). Magnetic susceptibility of the rock matrix related to magnetic fabric studies. Journal of Structural Geology, 9(8), 1015-1020.

Ross, P. S., White, J. D. L., Valentine, G. A., Taddeucci, J., Sonder, I., & Andrews, R. G. (2013). Experimental birth of a maar–diatreme volcano. Journal of Volcanology and Geothermal Research, 260, 1-12. doi:https://doi.org/10.1016/j.jvolgeores.2013.05.005

Ross, P.-S., Núñez, G. C., & Hayman, P. (2017). Felsic maar-diatreme volcanoes: a review. Bulletin of Volcanology, 79(2), 20.

Rouillon, M., & Taylor, M. P. (2016). Can field portable X-ray fluorescence (pXRF) produce high quality data for application in environmental contamination research? Environmental Pollution, 214, 255-264.

Schiffman, P., Spero, H. J., Southard, R. J., & Swanson, D. A. (2000). Controls on palagonitization versus pedogenic weathering of basaltic tephra: Evidence from the consolidation and geochemistry of the Keanakako'i Ash Member, Kilauea Volcano. Geochemistry, Geophysics, Geosystems, 1(8), n/a-n/a. doi:10.1029/2000GC000068

Schindler, T., & Wuttke, M. (2015). A revised sedimentological model for the late Oligocene crater lake Enspel (Enspel Formation, Westerwald Mountains, Germany). Palaeobiodiversity and Palaeoenvironments, 95(1), 5-16.

Schneider, L., Alloway, B. V., Blong, R. J., Hope, G. S., Fallon, S. J., Pain, C. F., . . . Haberle, S. G. (2017). Stratigraphy, age and correlation of two widespread Late Holocene tephras preserved within Lake Kutubu, Southern Highlands Province, Papua New Guinea. Journal of Quaternary Science, 32(6), 782-794.

Scott, J. M. (2013). A review of the location and significance of the boundary between the Western Province and Eastern Province, New Zealand. New Zealand Journal of Geology and Geophysics, 56(4), 276-293. doi:10.1080/00288306.2013.812971

Self, S., Kienle, J., & Huot, J.-P. (1980). Ukinrek Maars, Alaska, II. Deposits and formation of the 1977 craters. Journal of Volcanology and Geothermal Research, 7(1), 39-65. doi:https://doi.org/10.1016/0377-0273(80)90019-0

Shanmugam, G., & Wang, Y. (2015). The landslide problem. Journal of Palaeogeography, 4(2), 109-166. doi:https://doi.org/10.3724/SP.J.1261.2015.00071

Smith, R. (1986). Sedimentation and palaeoenvironments of Late Cretaceous crater‐lake deposits in Bushmanland, South Africa. Sedimentology, 33(3), 369-386.

Smith, S. A. F., Tesei, T., Scott, J. M., & Collettini, C. (2017). Reactivation of normal faults as high-angle reverse faults due to low frictional strength: Experimental data from the Moonlight Fault Zone, New Zealand. Journal of Structural Geology, 105, 34-43. doi:https://doi.org/10.1016/j.jsg.2017.10.009

Sohn, Y. K., & Park, K. H. (2005). Composite tuff ring/cone complexes in Jeju Island, Korea: possible consequences of substrate collapse and vent migration. Journal of Volcanology and Geothermal Research, 141(1-2), 157-175.

Sprung, P., Schuth, S., Münker, C., & Hoke, L. (2007). Intraplate volcanism in New Zealand: the role of fossil plume material and variable lithospheric properties. Contributions to Mineralogy and Petrology, 153(6), 669-687.

Suhr, P., Goth, K., Lorenz, V., & Suhr, S. (2006). Long lasting subsidence and deformation in and above maar-diatreme volcanoes–a never ending story [Lang anhaltende Subsidenz und Deformation in und über Maar-Diatrem-Vulkanen–eine unendliche Geschichte]. Zeitschrift der deutschen Gesellschaft für Geowissenschaften, 157(3), 491-511.

Sun, C., Liu, Q., Wu, J., Németh, K., Wang, L., Zhao, Y., . . . Liu, J. (2017). The first tephra evidence for a Late Glacial explosive volcanic eruption in the Arxan-Chaihe volcanic field (ACVF), northeast China. Quaternary Geochronology, 40, 109-119.

Sweeney, M. R., & Valentine, G. A. (2015). Transport and mixing dynamics from explosions in debris-filled volcanic conduits: Numerical results and implications for maar-diatreme volcanoes. Earth and Planetary Science Letters, 425, 64-76. doi:https://doi.org/10.1016/j.epsl.2015.05.038

Talling, P. J. (2014). On the triggers, resulting flow types and frequencies of subaqueous sediment density flows in different settings. Marine Geology, 352, 155-182. doi:https://doi.org/10.1016/j.margeo.2014.02.006

Talling, P. J., Masson, D. G., Sumner, E. J., Kamp, & Malgesini, G. (2012). Subaqueous sediment density flows: Depositional processes and deposit types. Sedimentology, 59(7), 1937-2003. doi:10.1111/j.1365-3091.2012.01353.x

Thompson, R., Battarbee, R. W., O'sullivan, P., & Oldfield, F. (1975). Magnetic susceptibility of lake sediments. Limnology and Oceanography, 20(5), 687-698.

Thompson, R., & Oldfield, F. (1986). Mineral magnetic studies of lake sediments. In Environmental Magnetism (pp. 101-123): Springer.

Timm, C., Hoernle, K., Werner, R., Hauff, F., den Bogaard, P. v., White, J., . . . Garbe-Schönberg, D. (2010). Temporal and geochemical evolution of the Cenozoic intraplate volcanism of Zealandia. Earth-Science Reviews, 98(1), 38-64. doi:https://doi.org/10.1016/j.earscirev.2009.10.002

Timperley, M., & Allan, R. J. (1974). The formation and detection of metal dispersion halos in organic lake sediments. Journal of Geochemical Exploration, 3(2), 167-190.

Ugolini, F. C., Dahlgren, R., LaManna, J., Nuhn, W., & Zachara, J. (1991). Mineralogy and weathering processes in Recent and Holocene tephra deposits of the Pacific Northwest, USA. Geoderma, 51(1), 277-299. doi:https://doi.org/10.1016/0016-7061(91)90074-4

Vacca, A., Adamo, P., Pigna, M., & Violante, P. (2003). Genesis of tephra-derived soils from the Roccamonfina volcano, south central Italy. Soil Science Society of America Journal, 67(1), 198-207.

Valentine, G. A., Shufelt, N. L., & Hintz, A. R. (2011). Models of maar volcanoes, Lunar crater (Nevada, USA). Bulletin of Volcanology, 73(6), 753-765.

Valentine, G. A., & White, J. D. L. (2012). Revised conceptual model for maar-diatremes: Subsurface processes, energetics, and eruptive products. Geological Society of America, 40(12), 1111-1114. doi:10.1130/G33411.1

Valentine, G. A., White, J. D. L., Ross, P.-S., Graettinger, A. H., & Sonder, I. (2017). Updates to Concepts on Phreatomagmatic Maar-Diatremes and Their Pyroclastic Deposits. Frontiers in Earth Science, 5(68). doi:10.3389/feart.2017.00068

van der Meer, Q. H. A., Storey, M., Scott, J. M., & Waight, T. E. (2016). Abrupt spatial and geochemical changes in lamprophyre magmatism related to Gondwana fragmentation prior, during and after opening of the Tasman Sea. Gondwana Research, 36, 142-156. doi:https://doi.org/10.1016/j.gr.2016.04.004

Varnes, D. J. (1978). Slope movement types and processes. Special report, 176, 11-33.

von Bohlen, A. (2009). Total reflection X-ray fluorescence and grazing incidence X-ray spectrometry—tools for micro-and surface analysis. A review. Spectrochimica Acta Part B: Atomic Spectroscopy, 64(9), 821-832.

Wellman, P. (1983). Hotspot volcanism in Australia and New Zealand: Cainozoic and mid-Mesozoic. Tectonophysics, 96(3), 225-243. doi:https://doi.org/10.1016/0040-1951(83)90219-6

White, J. D. (1992). Pliocene subaqueous fans and Gilbert‐type deltas in maar crater lakes, Hopi Buttes, Navajo Nation (Arizona), USA. Sedimentology, 39(5), 931-946.

White, J. D., & Ross, P.-S. (2011). Maar-diatreme volcanoes: a review. Journal of Volcanology and Geothermal Research, 201(1), 1-29.

White, J. D. L. (1990). Depositional architecture of a maar-pitted playa: sedimentation in the Hopi Buttes volcanic field, northeastern Arizona, U.S.A. Sedimentary Geology, 67(1), 55-84. doi:https://doi.org/10.1016/0037-0738(90)90027-Q

Whitton, J., & Churchman, G. (1987). Standard methods for mineral analysis of soil survey samples for characterisation and classification in NZ Soil Bureau, New Zealand. In: Wellington, NZ, DSIR, Soil Bureau.

Wilson, C., Rogan, A., Smith, I., Northey, D. J., Nairn, I., & Houghton, B. (1984). Caldera volcanoes of the Taupo volcanic zone, New Zealand. Journal of Geophysical Research: Solid Earth, 89(B10), 8463-8484.

Wright, N. M., Seton, M., Williams, S. E., & Müller, R. D. (2016). The Late Cretaceous to recent tectonic history of the Pacific Ocean basin. Earth-Science Reviews, 154, 138-173. doi:https://doi.org/10.1016/j.earscirev.2015.11.015

Xian, B., Liu, J., Dong, Y., Lu, Z., He, Y., & Wang, J. (2017). Classification and facies sequence model of subaqueous debris flows. Acta Geologica Sinica (English Edition), 91(2), 751-752.

Youngson, J. H. (1993). Mineralized Vein Systems and Miocene Maar Crater Sediments at Hindon, East Otago, New Zealand: A Thesis Submitted for the Degree of Master of Science at the University of Otago, Dunedin, New Zealand, July, 1993. University of Otago,

Ziegler, K., Chadwick, O. A., Brzezinski, M. A., & Kelly, E. F. (2005). Natural variations of δ30Si ratios during progressive basalt weathering, Hawaiian Islands. Geochimica et Cosmochimica Acta, 69(19), 4597-4610. doi:https://doi.org/10.1016/j.gca.2005.05.008

Zimanowski, B., Büttner, R., Dellino, P., White, J. D. L., & Wohletz, K. H. (2015). Chapter 26 - Magma–Water Interaction and Phreatomagmatic Fragmentation A2 - Sigurdsson, Haraldur. In The Encyclopedia of Volcanoes (Second Edition) (pp. 473-484). Amsterdam: Academic Press.

Zolitschka, B., Francus, P., Ojala, A. E. K., & Schimmelmann, A. (2015). Varves in lake sediments – a review. Quaternary Science Reviews, 117, 1-41. doi:https://doi.org/10.1016/j.quascirev.2015.03.019

Abdullah, E. C., & Geldart, D. (1999). The use of bulk density measurements as flowability indicators. *Powder Technology*, *102*(2), 151-165. doi:https://doi.org/10.1016/S0032-5910(98)00208-3

Alder, S., Smith, S. A. F., & Scott, J. M. (2016). Fault-zone structure and weakening processes in basin-scale reverse faults: The Moonlight Fault Zone, South Island, New Zealand. *Journal of Structural Geology*, *91*, 177-194. doi:https://doi.org/10.1016/j.jsg.2016.09.001

Arnaud, F., Magand, O., Chapron, E., Bertrand, S., Boës, X., Charlet, F., & Mélières, M.-A. (2006). Radionuclide dating (210Pb, 137Cs, 241Am) of recent lake sediments in a highly active geodynamic setting (Lakes Puyehue and Icalma—Chilean Lake District). *Science of the Total Environment*, *366*(2-3), 837-850.

Blaikie, T. N., Ailleres, L., Betts, P. G., & Cas, R. A. F. (2014). A geophysical comparison of the diatremes of simple and complex maar volcanoes, Newer Volcanics Province, south-eastern Australia. *Journal of Volcanology and Geothermal Research*, *276*, 64-81. doi:https://doi.org/10.1016/j.jvolgeores.2014.03.001

Chapman, M. R., & Shackleton, N. J. (1998). What level of resolution is attainable in a deep - sea core? Results of a spectrophotometer study. *Paleoceanography*, *13*(4), 311-315.

Churchman, G. J., & Lowe, D. J. (2012). *Alteration, formation, and occurrence of minerals in soils*: CRC press.

Dearing, J. (1994). Environmental magnetic susceptibility. *Using the Bartington MS2 system. Kenilworth, Chi Publ.*

Filimonova, S., Kaufhold, S., Wagner, F. E., Häusler, W., & Kögel-Knabner, I. (2016). The role of allophane nano-structure and Fe oxide speciation for hosting soil organic matter in an allophanic Andosol. *Geochimica et Cosmochimica Acta*, *180*, 284-302. doi:https://doi.org/10.1016/j.gca.2016.02.033

Floyd, P. A., & Winchester, J. A. (1975). Magma type and tectonic setting discrimination using immobile elements. *Earth and Planetary Science Letters*, *27*(2), 211-218. doi:https://doi.org/10.1016/0012-821X(75)90031-X

Geotek, L. (2014). *Multi-Sensor Core Logger*. Northamptonshire.

Kaulfuss, U. (2017). Crater stratigraphy and the post-eruptive evolution of Foulden Maar,

southern New Zealand. *New Zealand Journal of Geology and Geophysics*, *60*(4), 410-432.
Kaulfuss, U., & Moulds, M. (2015). A new genus and species of tettigarctid cicada from the early Miocene of New Zealand: Paratettigarcta zealandica (Hemiptera, Auchenorrhyncha, Tettigarctidae). *ZooKeys*(484), 83.
Lee, D. (2016).
Lefebvre, N., White, J., & Kjarsgaard, B. (2013). Unbedded diatreme deposits reveal maar-diatreme-forming eruptive processes: Standing Rocks West, Hopi Buttes, Navajo Nation, USA. *Bulletin of Volcanology*, *75*(8), 739.
Lorenz, V. (2007). Syn-and posteruptive hazards of maar–diatreme volcanoes. *Journal of Volcanology and Geothermal Research*, *159*(1-3), 285-312.
McCanta, M. C., Hatfield, R. G., Thomson, B. J., Hook, S. J., & Fisher, E. (2015). Identifying cryptotephra units using correlated rapid, nondestructive methods: VSWIR spectroscopy, X‐ray fluorescence, and magnetic susceptibility. *Geochemistry, Geophysics, Geosystems*, *16*(12), 4029-4056.
Mosher, T. (2007). Chapter 10 - Magnetic Resonance Imaging in Osteoarthritis A2 -

Sharma, Leena. In F. Berenbaum (Ed.), *Osteoarthritis* (pp. 143-177). Philadelphia: Mosby.

Mrlina, J., Kämpf, H., Kroner, C., Mingram, J., Stebich, M., Brauer, A., . . . Seidl, M. (2009). Discovery of the first Quaternary maar in the Bohemian Massif, Central Europe, based on combined geophysical and geological surveys. *Journal of Volcanology and Geothermal Research*, *182*(1), 97-112. doi:https://doi.org/10.1016/j.jvolgeores.2009.01.027

Nemeth, K., & White, J. (2009). *Miocene phreatomagmatic monogenetic volcanism of the Waipiata volcanic field, Otago, New Zealand; field guide* (Vol. 128B).

Pirrung, M., Buchel, G., & Jacoby, W. (2001). The Tertiary volcanic basins of Eckfeld, Enspel and Messel (Germany). *ZEITSCHRIFT-DEUTSCHEN GEOLOGISCHEN GESELLSCHAFT*, *152*(1), 27-60.

Pirrung, M., Büchel, G., Lorenz, V., & TREUTLER, H. C. (2008). Post‐eruptive development of the Ukinrek East Maar since its eruption in 1977 AD in the periglacial area of south‐west Alaska. *Sedimentology*, *55*(2), 305-334.

Pirrung, M., Fischer, C., Büchel, G., Gaupp, R., Lutz, H., & Neuffer, F. O. (2003).

Lithofacies succession of maar crater deposits in the Eifel area (Germany). *Terra Nova*, *15*(2), 125-132.

Rochette, P. (1987). Magnetic susceptibility of the rock matrix related to magnetic fabric studies. *Journal of Structural Geology*, *9*(8), 1015-1020.

Scott, J. M. (2013). A review of the location and significance of the boundary between the Western Province and Eastern Province, New Zealand. *New Zealand Journal of Geology and Geophysics*, *56*(4), 276-293. doi:10.1080/00288306.2013.812971

Talling, P. J., Masson, D. G., Sumner, E. J., Kamp, & Malgesini, G. (2012). Subaqueous sediment density flows: Depositional processes and deposit types. *Sedimentology*, *59*(7), 1937-2003. doi:10.1111/j.1365-3091.2012.01353.x

Timperley, M., & Allan, R. J. (1974). The formation and detection of metal dispersion halos in organic lake sediments. *Journal of Geochemical Exploration*, *3*(2), 167-190.

White, J. D. (1992). Pliocene subaqueous fans and Gilbert - type deltas in maar crater lakes, Hopi Buttes, Navajo Nation (Arizona), USA. *Sedimentology*, *39*(5), 931-946.

White, J. D., & Ross, P.-S. (2011). Maar-diatreme volcanoes: a review. *Journal of*

Volcanology and Geothermal Research, 201(1), 1-29.

Youngson, J. H. (1993). *Mineralized Vein Systems and Miocene Maar Crater Sediments at Hindon, East Otago, New Zealand: A Thesis Submitted for the Degree of Master of Science at the University of Otago, Dunedin, New Zealand, July, 1993*. University of Otago,

Ziegler, K., Chadwick, O. A., Brzezinski, M. A., & Kelly, E. F. (2005). Natural variations of δ30Si ratios during progressive basalt weathering, Hawaiian Islands. *Geochimica et Cosmochimica Acta, 69*(19), 4597-4610. doi:https://doi.org/10.1016/j.gca.2005.05.008

Zolitschka, B., Francus, P., Ojala, A. E. K., & Schimmelmann, A. (2015). Varves in lake sediments – a review. *Quaternary Science Reviews, 117*, 1-41. doi:https://doi.org/10.1016/j.quascirev.2015.03.019